Interaction of some molecules with complex surfaces

Resta, Andrea

2007

Interaction of Some Molecules with Complex Surfaces

Andrea Resta

2008

Department of Synchrotron Radiation Research
Lund University

LUND
UNIVERSITY

To be presented with the permission of the Faculty of Science of Lund University,
for public criticism in Lecture Hall B at the Department of Physics,
18 January 2008, at 10:15.

Thesis for Degree of Philosophy Doctor in Physics
Department of Synchrotron Radiation Research
Institute of Physics
Lund University
BOX 118
SE-221 00 LUND, SWEDEN

Andrea Resta
ISBN 978-91-628-7361-5
Printed in Lund, Sweden by Mediatryck

Etiam capillus unus habet umbram suam.

Publilio Siro
I century A.C.

Sammanfattning för allmänheten

This thesis is within the surface science field. Surface science investigates phenomena occurring at boundaries and interfaces, where abrupt discontinuities are present e.g. between solid and gas phase or between two solids of different nature. Because of the subject treated it makes use of both chemical and physical knowledge. Surface science affects the daily life of all of us. Profound surface science knowledge is contained in many objects of common use such as mobile phones, computers, car catalysts or batteries and is involved for the production of a large amount of substances from paints to fertilisers and more.

More specifically, the work of this thesis is related to heterogeneous catalysis and surface chemistry. It explores the catalytic activity of Rh towards small molecules and the reduction of oxygen induced structures on Pd and Rh. The importance of surface chemistry is illustrated by the 2007 year Nobel Prize in Chemistry being awarded to Gerhard Ertl "for his studies of chemical processes on solid surfaces."

The motivation behind this thesis originates from the known and promising possibility to produce hydrogen from ethanol. Ethanol (C_2H_5OH) was therefore the starting molecule designed for the experiments, however simpler molecules as ethylene (CH_2CH_2) and carbon monoxide (CO) has also been used with the main intent to simplify the system and facilitate the interpretation of the ethanol data.

All the experiments were performed in vacuum under controlled conditions of temperature and pressure on single crystals. The vacuum guarantees the cleanliness of the samples while single crystals guarantee knowledge and control on the substrate initial conditions down to an atomic level. A combination of different techniques was used to study the molecules on the sample surface: High Resolution Core Level Spectroscopy (HRCLS), Low Energy Electron Diffraction (LEED), Reflection Adsorption Infra Red Spectroscopy (RAIRS) and Scanning Tunnel Microscopy (STM).

During the HRCLS experiments light is made to impinge on the sample, whereafter electrons bound in the sample are excited and emitted. The light energy is chosen and known, therefore it is possible to determine how strongly such electrons were bound inside the material by measuring the electrons kinetic energy. The electron binding energy depends firstly on the element and secondly on the local surrounding of the atom from which the electron is emitted. Therefore the same element placed in different surrounding can be distinguished. During the LEED experiments an electron beam impinges on the sample and the back-scattered electrons are collected on a fluorescent screen. The image on the fluorescent screen delivers information on the surface symmetry and ordering of the sample. Further surface geometrical information is obtained with a scanning tunnel microscope that can achieve atomic resolution and therefore enlighten the surface structure. Infra

red spectroscopy has been used because of its strong capability to recognise organic molecules. Each technique provides a different set of information and the final model must be consistent with of all the aspects collected with the different techniques.

The hope is that this work contributed to the scientific knowledge on how reactivity can be influenced by the local atomic structure and that it may also be useful in the future for some specific processes.

Preface

This thesis reports results concerning the catalytic activity of Rh towards organic molecules and the reduction of oxygen induced surface structures on Pd and Rh. The experimental work is mainly based on photoemission experiments but also uses techniques such as low energy electron diffraction, Infra-Red spectroscopy and scanning tunnelling microscopy. In part of the work, density functional theory based simulations proved vital.

The photoemission experiments were performed at the MAX-lab synchrotron radiation facility, Lund university, Sweden. The infra-red experiments were carried out in collaboration with Per Uvdal and Jakob Blomquist from Chemical Physics, Department of Chemistry, Lund university. The scanning tunneling microscopy measurements were performed in collaboration with the Technical University of Vienna, Austria. Density functional theory simulations were performed by collaborators at the Technical University of Vienna, Austria, at the university of Aarhus, Denmark and at the Dalian Institute of Chemical Physics, China.

I *CO - hydrogen coadsorption on stepped Rh surfaces with A and B type facets.*
Jesper N Andersen, Andrea Resta, Edvin Lundgren, Johan Gustafson, Xiu-Fang Ma, Wei-Xue Li, Jianguo Wang and Bjørk Hammer.
In manuscript

II *Mechanism of CO oxidation reaction on O-covered Pd(111) surfaces studied with fast x-ray photoelectron spectroscopy: Change of reaction path accompanying phase transition of O domains.*
Ikuyo Nakai, Hiroshi Kondoh, Toru Shimada, Andrea Resta, Jesper N. Andersen and Toshiaki Ohta.
J. Chem. Phys. **124** 224712 (2006)

III *Acetate formation during the ethanol oxidation on Rh(111).*
A. Resta, J. Blomquist, J. Gustafson, H. Karhu, A. Mikkelsen, E. Lundgren, P. Uvdal and J. N Andersen.
Surf. Sci. **600** 5136 (2006)

IV *Step induced increased dehydrogenation of ethanol on Rh.*
Andrea Resta, Johan Gustafson, Anders Mikkelsen, Edvin Lundgren, Jesper N Andersen, Ming-Mei Yang and Wei-Xue Li.
In manuscript

V *Step dependent hydrocarbon decomposition.*
Andrea Resta, Edvin Lundgren and Jesper N Andersen.
In manuscript

VI *Kinetics of the reduction of the Rh(111) surface oxide: Linking spectroscopy and atomic-scale information.*
J. Klikovits, M. Schmid, J. Gustafson, A. Mikkelsen, A. Resta, E. Lundgren, J. N. Andersen and P. Varga.
J. Phys. Chem. B **110** 9966 (2006)

VII *The surface oxide as a source of oxygen on Rh(111).*
E. Lundgren, J. Gustafson, A. Resta, J. Weissenrieder, A. Mikkelsen, J. N. Andersen, L. Köhler, G. Kresse, J. Klikovits, A. Biederman, M. Schmid, and P. Varga.
J. Electron Spectrosc. Relat. Phen. **144-147** 367 (2005)

The articles presented below are related to the work presented in the thesis but not included.

Oxidation of Pd(553): from ultrahigh vacuum to atmospheric pressure.
R. Westerström, J. Gustafson, A. Resta, A. Mikkelsen, J. N. Andersen, E. Lundgren, N. Seriani, F. Mittendorfer, M. Schmid, J. Klikovits, P. Varga, M. D. Ackermann, J. W. M. Frenken, N. Kasper and A. Stierle.
Phys. Rev B **76** 155410 (2007).

Growth and reactivity of titanium oxide ultrathin films on Ni(110).
A.C. Papageorgiou, G. Cabailh, Q. Chen, A. Resta, E. Lundgren, J.N. Andersen and G. Thornton.
J. Phys. Chem. C **111** 7704 (2007)

Complex interaction of hydrogen with the RuO_2(110) surface.
M. Knapp, D. Crihan, A.P. Seitsonen, E. Lundgren, A. Resta, J.N. Andersen and H. Over.
J. Phys. Chem. **111** 5363 (2007)

Unusual process of water formation on RuO_2(110) by hydrogen exposure at room temperature.
M. Knapp, D. Crihan, A. P. Seitsonen, A. Resta, E. Lundgren, J.N. Andersen, M. Schmid, P. Varga and H. Over.
J. Phys. Chem. B, **110** 14007 (2006)

Oxygen-induced step bunching and faceting of Rh(553): experiment and ab initio calculations.
J. Gustafson, A. Resta, A. Mikkelsen, R. Westerström, J.N. Andersen, E. Lundgren,

J. Weissenrieder, M. Schmid, P. Varga, N. Kasper, X. Torrelles, S. Ferrer, F. Mittendorfer and G. Kresse.
Phys. Rev. B **74** 35401 (2006)

Comments on my own contribution to the papers

For all the papers where I am the first author I have been responsible for the measurements, the analysis of the experimental results and the writing of the manuscript. For the papers where I am not the first author, my contribution is reflected by the position in the author list.

Contents

Abstract

This thesis investigates the adsorption, decomposition and reactions of small molecules on flat, oxidised and vicinal surfaces of late transition metals. The main technique for these studies is high resolution core level spectroscopy (HRCLS). All the studies presented in the thesis are performed in Ultra High Vacuum (UHV). The articles can be divided into three groups.

The first three articles deal with co-adsorption on flat and stepped surfaces. The first article is focused on the adsorption thermodynamics that determines the adsorption sites. Adsorption of CO is performed on two surfaces vicinal to the Rh(111) surface which exhibit different step geometry to investigate the influence of the local step geometry on the adsorption process. The experiments proceed further to study CO co-adsorption with H_2. The measurements and conclusions are supported by Density Functional Theory (DFT) calculations.

The second article deals with the CO co-adsorption with oxygen and a kinetic analysis of the reaction occurring between CO and oxygen as function of the temperature. In this system, the two adsorbates create separate domains on the surface and the reaction proceeds with two different mechanisms depending on the temperature. The time evolution of the reactions has been followed by in-situ high resolution core level spectroscopy.

The third article studies the co-adsorption of ethanol (C_2H_5OH) and oxygen on Rh(111). Due to a larger number of atoms the ethanol molecule allows a rich chemistry on the surface. Via high resolution core level spectroscopy it is shown that acetate ($CH_3COO - Rh$) is formed during the ethanol oxidation process. This is confirmed by Infra Red Reflection Absorption Spectroscopy.

The second group of articles, article four and five, investigates the interaction of small hydrocarbons such as ethanol and ethylene (C_2H_4) with flat and stepped Rh surfaces. Article four studies the adsorption of pure ethanol on Rh(111) and Rh(553). Here use is made of the HRCLS chemical sensitivity to identify the hydrocarbon species on the surfaces. DFT calculations proved to be an invaluable tool in this identification. Clear differences in the ethanol dissociation on a flat and a vicinal surface are observed.

The fifth article investigates the effects of the steps and their local geometry on the decomposition of ethylidyne (C_2H_3) generated on the surface from ethylene. Rh(111) is used as reference to compare to the two different step geometries present on Rh(553) and Rh(322). Clear indications that the local step geometry influences the ethylidyne decomposition are found.

The last group of articles, article six and seven, investigates the interaction between CO and H_2 respectively and a pre-oxidised Rh(111) surface. The reduction of the oxide thin film is measured in real time while the reductive reagent is introduced in the chamber. Both articles compare the microscopic information obtained from scanning tunnelling microscope and the laterally averaged information typical of HRCLS.

Chapter 1

Introduction

This thesis work is within the Surface Science field. This subject indicates a wide and interdisciplinary area that spans from solid state physics to molecular quantum mechanics, from thermodynamics to micro-electronics. It studies phenomena occurring at boundaries and interfaces, where abrupt discontinuities are present e.g. between solid and gas phase or between two solids of different nature. Surface science affects the daily life of all of us. Profound surface science knowledge is contained in many objects of common use such as mobile phones, computers, car catalysts or batteries and is involved for the production of a large amount of substances from paints to fertilisers and more.

Surface science tries to understand and explain surface processes down to the atomic scale. This aim presents some difficulties, both in the modelling and in the data acquisition. The surface only constitutes a small fraction of a macroscopic sample, thus the signal from the surface may in many cases be very small relative to that of the bulk, even though the surface properties are vital in determining the interaction with the surroundings. Moreover the environment around the sample can rapidly contaminate the surface thereby changing its properties. As answer to these problems, specific surface science experimental techniques were developed. In order to reduce the complexity of e.g. polycrystalline materials and small particles present in real catalysts, single crystal surfaces are often used as a model systems.

More specifically, the work of this thesis is related to heterogeneous catalysis. Surface chemistry, including adsorption, fragmentation and reaction of molecules on catalytically important metals is of major importance for obtaining an atomistic based understanding of heterogeneous catalysis. The importance of this is for example illustrated by the 2007 year Nobel Prize in Chemistry being awarded to Gerhard Ertl "for his studies of chemical processes on solid surfaces".

Surface chemistry on the flat, low-index single crystal surfaces typically used as model systems in surface science may, however, not provide a complete description of the surface chemistry occurring on the small particles often used in real catalysts. One reason for this is that the surfaces of small particles contain a large fraction of edge and corner atoms which are under-coordinated compared to atoms on low-index surfaces. These under-coordinated atoms may provide active sites, i.e. specific local atomic arrangements responsible for most of the activity of the catalysts, as

suggested at the beginning of the last century [1]. One way to address this issue is, as suggested previously [2], to use high-index, so-called vicinal, surfaces. Vicinal surfaces consist of low-index terraces separated by periodically arranged mono-atomic steps containing atoms with a lower coordination number, whereby they provide possibilities for monitoring the local adsorption and reaction behaviour in the vicinity of low-coordinated atoms. This thesis contains a number of studies on vicinal surfaces where clear differences in adsorption and reaction between flat and vicinal surfaces have been found.

This thesis explores the behavior of C_2H_5OH, C_2H_4 and $CO+H_2$ on stepped metallic surfaces and the reduction of some oxygen induced surface structures. The initial motivation for the ethanol (C_2H_5OH) dehydrogenation studies was its applications in hydrogen reforming [3]. During the ethanol studies it was found that several of the hydrocarbon fragments formed were strongly affected by the surface morphology. In order to study this morphology dependence in a simpler system studies were performed of ethylene (C_2H_4) adsorption and reaction on Rh(111) and on two of its vicinal surfaces. The two vicinal surfaces that were chosen to contain different micro facets at the steps thereby facilitating a more detailed study. Carbon monoxide is historically one of the most used molecules for adsorption studies, but is also a catalysts poison for hydrogen fuel cells. The present study concentrates on CO adsorption on stepped Rh surfaces and how the affinity of the CO to the steps is influenced by co-adsorption of hydrogen.

Oxidation is a process of high technological interest because of the wide range of applications spanning from car catalytic converters to fertiliser production. Despite their economical importance the active phases and mechanisms for several processes are still open questions. The studies included in the thesis aim to identify the active phase involved in the reaction and at least part of the time evolution.

In the experimental work we have made use of a powerful way to investigate surfaces: High Resolution Core Level Spectroscopy (HRCLS) applied on single crystals. Beamline I311 at MAX-lab in Lund provides world class photon flux and energy resolution, which permits detailed studies of surface phenomena. Ultra High Vacuum (UHV) conditions, e.g. pressures below 10^{-9} Torr., are used to guarantee the sample cleanliness during the analysis. These techniques have been combined with Reflection Adsorption Infra Red Spectroscopy (RAIRS), Scanning Tunnel Microscopy (STM) and Low Energy Electron Diffraction (LEED). The hope is that this work contributed to the scientific knowledge on how reactivity and adsorption can be influenced by the local atomic structure and that it may also be useful for some specific processes like hydrogen or hydrocarbon reforming.

Chapter 2

Crystal Surfaces

This chapter briefly describes some fundamentals of surface crystallography and of the surface induced changes on the electronic structure of a d-band metal.

2.1 Surfaces

The experiments performed for this thesis always make use of single crystals in Ultra High Vacuum (UHV). Single crystals are used in order to increase the knowledge of the starting system. Single crystals with known orientation of the surface represent more well defined situations in terms of atomic positions than the surfaces of poly-crystalline or amorphous samples. UHV conditions, i.e. pressures below 10^{-9} Torr., are also used to obtain more control on the system. These low pressures are needed in order to keep the surface free from unwanted contamination by molecules from the surrounding gas. Depending on the material in question various methods, e.g. Argon ion sputtering, are used to obtain atomically clean surfaces as starting point for the experiments. Relevant for this thesis are lattices with a cubic structure, see Fig. 2.1, particularly the face centred cubic (FCC).

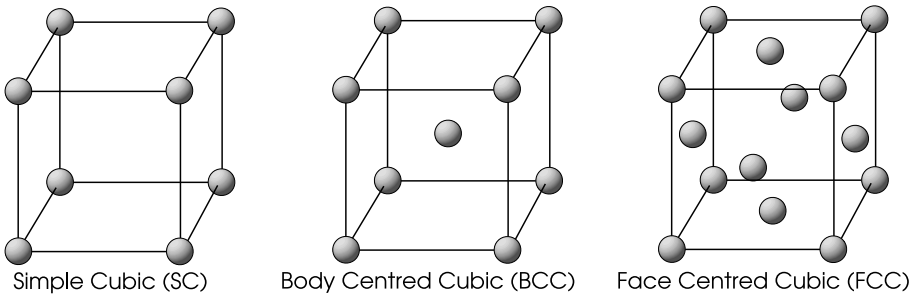

Figure 2.1: Cubic structures.

The orientation of a surface is defined by the relative orientation of the surface plane with respect to the bulk lattice. The used system is the Miller index. The Miller indices are determined by the inverse of the intercept of the plane with the

crystallographic axes and define the vector normal to a family of planes, see Fig. 2.2. Planes in a crystal are indicated with (hkl) and directions by [hkl].

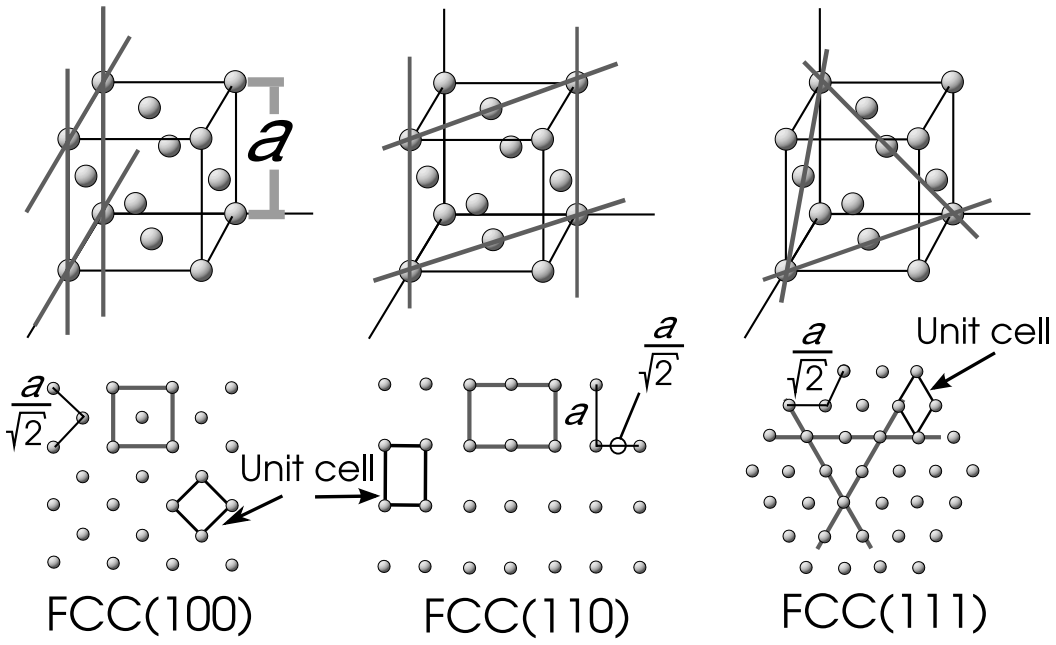

Figure 2.2: Crystal planes and related low Miller index surfaces.

For an FCC lattice the low Miller index planes (111), (100), (110), see Fig. 2.2, are essentially smooth on the atomic scale. These planes are also called singular planes. To mimic defects and under-coordinated atoms high Miller index surfaces are used, see Fig 2.3 B and C as examples. Rh(553) and Rh(322) have been used during the experimental work summarised here. Both surfaces are vicinal to the (111) surface. They present five atoms wide (111) terraces separated by single atomic steps. The (553) and (322) FCC surfaces differ in the step geometry, (553) surfaces exhibit (111) micro facets (B type step), while instead (322) exhibits (100) micro facets.

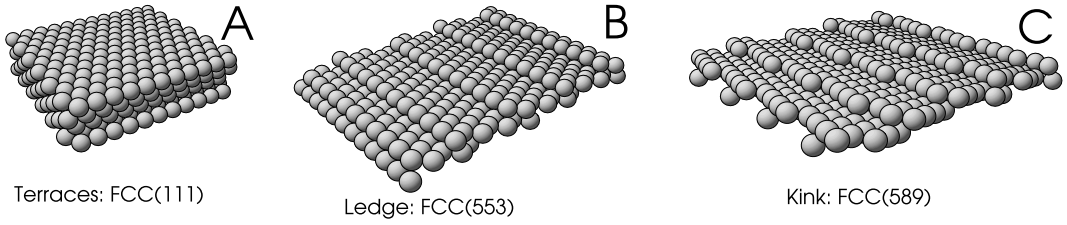

Figure 2.3: Example: a flat surface and two stepped FCC surfaces.

Atoms placed at the surface have fewer neighbours than atoms in the bulk. The coordination number quantifies the number of first neighbours and for the surface atoms of an FCC lattice is 9 for the (111) plane, 8 for the (100) plane and 7 for the (110) plane. Atoms in the bulk have coordination number 12 for FCC lattices.

On a vicinal surface the atoms right at the step in fact have lower coordination in comparison to the terrace atoms near by. In the used (553) and (322) Rh surfaces the atoms right at the step have 7 as coordination number. The presence of kinks goes even further in decreasing the number of first neighbours, see Fig. 2.3 C, containing not only straight ledges but also pronged ledges between terraces.

The surface contribution to the total energy of the system becomes relevant when the ratio surface over volume increases. For a liquid the total surface energy is proportional to the surface area. Since liquids are isotropic media: $\gamma_h = \gamma_s S$ where γ_h is the surface contribution to the total energy, γ_s is the energy per surface unit area and S is the surface area. Therefore minimising the surface area also minimises the surface free energy. The resulting shape in absence of other forces is a sphere. For crystals the surface energy also depends on which plane is exposed therefore the previous equation is modified: $\gamma_h = \sum^i \gamma_i S_i$, where γ_h is the surface contribution to the total energy, γ_i is the energy per surface unit area for the facet i and S_i is the surface area of the i^{th} facet. Therefore the shape of the small particle can be obtained by minimising the total surface free energy [4]. The entity γ_i depends on the chemical potential of the exposed surface. In the presence of adsorbates, γ_i depends also on the chemical potential of the adsorbate on that specific surface [5]. Therefore the presence of adsorbates can change the particle shape. The adsorbates can induce wide modifications of the surface morphology and mass redistribution, step bunching on vicinal surfaces is one example [6].

2.2 Wood Notation

Until now the surface atoms were always considered to be in the bulk truncated positions. On a real surface this is not always the case. For metals a relaxation is often observed. It consists in modification of the inter-planes distances along the axis orthogonal to the surface, while instead the two dimensional periodicity is preserved for most of the clean metal surfaces. However, there exist cases where even a clean surface reconstructs in order to minimise the surface contribution to the total energy. A common way to describe ordered surface structures as reconstructions or adsorbate layers is the Wood notation. It consist into finding a set of basis vectors that describe the structure periodicity and relate them to the bulk terminated surface of the substrate [7, 8], see Fig 2.4 for some examples. The information contained in the Wood notation starts defining the material M and the surface (hml). After, it defines the new structure unit vector in relation to the bulk truncated positions. The relationship between substrate lattice (a, b) and adsorbate lattice (a', b') is expressed as ratio between the unit vectors length for the two basis $p = |\mathsf{a}'|/|\mathsf{a}|$ and $q = |\mathsf{b}'|/|\mathsf{b}|$ and the angle θ of rotation between the two basis. Also the number n of adsorbates molecules A per unit cell must be specified if present and different from one. Thus the full notation appear as: $M(hml)\ (p \times q)\ R\theta\ n - A$.

The notation $c(4 \times 2)$ used for the last structure indicate that the unit cell so defined is not the primitive, the c stands for centred. In some cases a p is added in order to explicitly point out that the unit cell is primitive, e.g. (2×2) is sometimes written as $\mathrm{p}(2 \times 2)$ [7, 8].

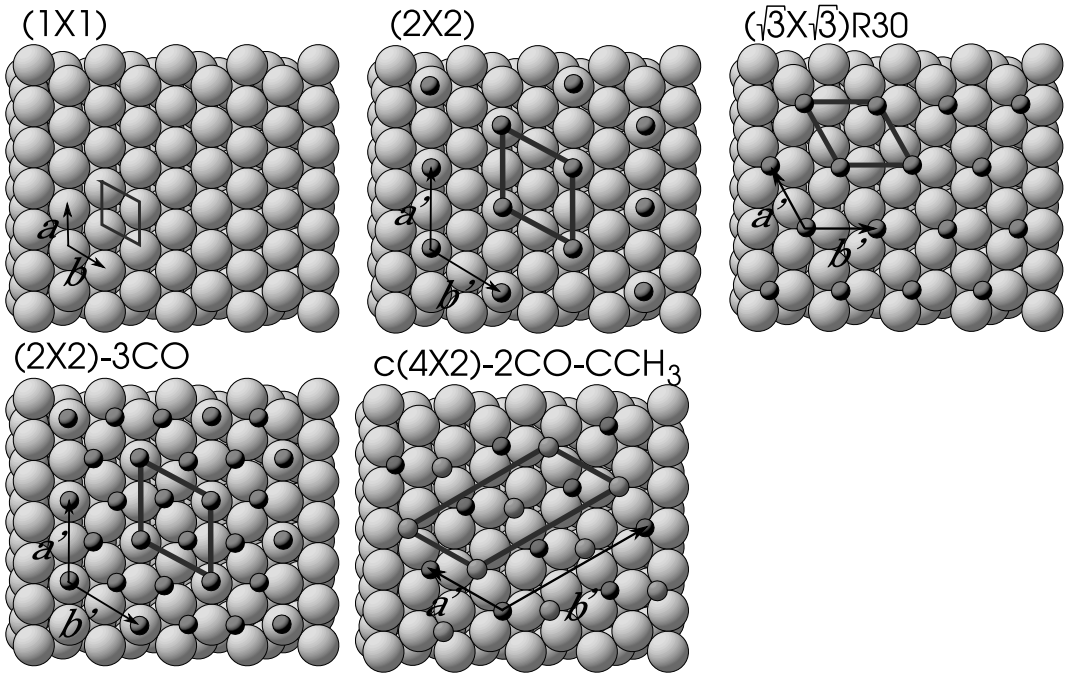

Figure 2.4: Some examples of how adsorbate structures are described in terms of the FCC (111) (1×1) unit cell. The (2×2)-1CO has been found for both oxygen and CO adsorbed on Rh(111). The (2×2)-3CO represents the Rh(111) CO surface saturation. The $(\sqrt{3}\times\sqrt{3})$R30°-1O is one of the reactive oxygen compressed phases found on Pd(111). The c(4 × 2)-2CO-2C_2CH_3 has been found for ethylidyne co-adsorbed with CO on Rh(111). All these phases are relevant to this thesis.

2.3 Surface Band Narrowing

The Local Density of States (LDOS) in solids can be interpreted as the result of the superposition of the orbitals involved in the bonds and therefore its width is related to the number of orbitals shared in bonds. Thus differences between bulk and surface are expected. The main qualitative effect for metals with d-valence states is the reduction of the root mean square (rms) width of the LDOS [9] at the surface. Using the tight binding approximation [10, 11] it has been shown that the rms width varies as $\sqrt{z}$ where z is the number of nearest neighbours [9].

As this narrowing occurs around the d-band centre, it would for a more (less) than half filled d-band result in the filling (emptying) of the d-band states of the surface atoms (see Fig 2.5 for the case of a more than half filled band.). Since we deal with metals where practically there is no charge accumulation [12] the narrowed surface d-band has to shift in order to maintain charge neutrality; for a more (less) than half filled d-band the shift towards (away from) the Fermi level. If it is assumed that the energy difference between the d-band and the core level is constant the d-band shift also causes a shift of the core levels, see Fig 2.5. The surface atoms are different from the bulk atoms, but also surface atoms can differ from each other. This is for instance the case on stepped surfaces where the atoms at the steps have

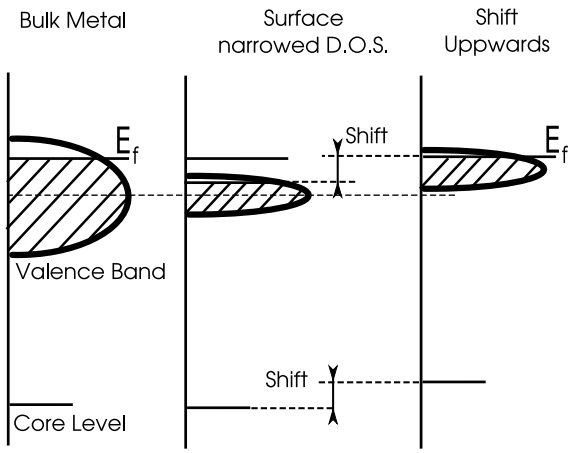

Figure 2.5: Illustration of the narrowing of the d band in metals at the surface. The illustrated case is for a d-band being more than half filled. The figure also illustrates how the narrowing and shifting of the surface valence band leads to a core level shift, if the core level is assumed to be rigidly fixed to the valence band.

lower coordination. The presence of steps and therefore of under-coordinated atoms makes the band at the step even narrower than on the terraces; the local surface morphology modifies the local electronic properties.

Chapter 3

Molecules

Together with surfaces, molecules are the other ingredient used in this experimental work. This chapter briefly describes some fundamentals of molecules.

3.1 Orbitals and Bonds

From the International Union of Pure and Applied Chemistry (IUPAC), a molecule is defined as: "An electrically neutral entity consisting of more than one atom (n > 1). Rigorously, a molecule, in which n > 1 must correspond to a depression on the potential energy surface that is deep enough to confine at least one vibrational state." Therefore a molecule refers to the smallest unit, composed of atoms, that presents properties that will be lost considering only a fraction of it. The molecules used during the experiments had only covalent bonds. A covalent bond can be qualitatively described as the sharing of electrons between two atoms, in order to reach the valence electronic state of the nearest noble gas. When the shared electrons are equally localised on both atoms involved in the bond one gets the so called pure covalent bond. When the electrons are not equally localised on both atoms a polar covalent bond forms. A dipole is associated with each polar bond and the vector sum over all the single dipoles will give the molecular dipole. Other types of bonds exist but they are usually not involved in molecules, as the metal bond, typical of metals, and the ionic bond, typical of salts [13].

An appropriate description of molecular bonds requires quantum mechanics and was proposed in 1927 by Walter Heinrich Heitler. Unfortunately quantum mechanics can not provide an exact solution for the Schrödinger equation even for the simplest molecular entity: H_2^+. To overcome this difficulty simplifications must be introduced. The Born-Oppenheimer approximation [14] takes into consideration the large mass difference between electrons and nuclei. Because of this difference the electrons respond almost instantaneously to nuclear displacements. Under this assumption it is possible to consider the nuclei as fixed and solve the remaining part of the Schrödinger equation. As a result, the total molecular Hamiltonian can be treated as composed of two parts acting on different time scales: one nuclear and one electronic. We consider first the electronic part. A linear combination of atomic orbitals can be used to design the molecular orbitals, this approach is named Linear

Combination of Atomic Orbitals (LCAO) [14]. For instance hydrogen (H_2) molecular orbitals can be constructed starting from two 1s hydrogen orbitals: $1\sigma = \psi_{N1} + \psi_{N2}$ and $2\sigma = \psi_{N1}$ - ψ_{N2} [14]. The subscript $_{N1}$ and $_{N2}$ distinguishes between the two atoms. The molecular mixing energy schema can be visualised, as in Fig 3.1 which shows the H_2 and CO molecules as representative examples. For the H_2 molecule,

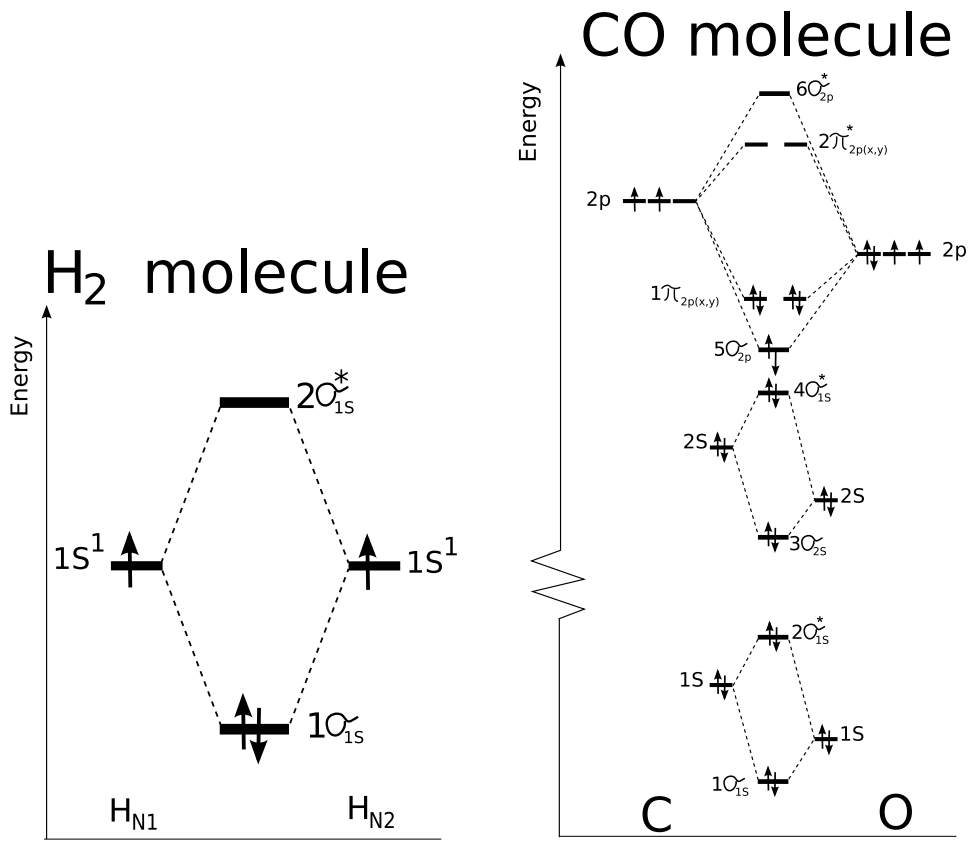

Figure 3.1: Energy diagram for two diatomic molecules: hydrogen on the left and carbon monoxide on the right. The atomic orbitals combine to generate the molecular orbitals. The orbitals marked with an asterisk are anti-bonding states.

electrons in the 1σ molecular orbital lower the total energy thereby stabilising the molecule. Instead the presence of any electron in the 2σ molecular orbitals would destabilise the molecule by increasing the total energy of the system. The orbital contributions to the total energy discriminate between bonding and anti-bonding orbitals: bonding orbitals stabilise the system while anti-bonding do not. Why this is so becomes more clear by plotting the H_2 electron density resulting from the 1σ and 2σ generated molecular orbital. A non zero electron density is visible between the nuclei for the bonding state (1σ), while for the anti-bonding 2σ there is a point in between the nuclei with zero density of electron charge, see Fig 3.2 B. Therefore the 1σ molecular orbital minimises the nuclear repulsion because of the electron charge localised between them, while instead the 2σ does not reduce the nuclei repulsion. Extrapolating from this behaviour, a bonding state minimises the electrostatic re-

pulsion between the nuclei because of the electron density localised between them. For an anti-bonding state the electron density between nuclei is reduced resulting in an increased electrostatic repulsion and thus a destabilization of the molecule.

With σ and π are specified the symmetry and the electron density spatial distribution of the molecular orbitals. The spatial distribution attributed to them is represented in Fig. 3.3. The populated level with highest energy (σ_{1s} for H_2 and π_{2p} for CO) is also named Highest Occupied Molecular Orbital (HOMO). The first empty state after the HOMO (σ^*_{1s} for H_2 and π^*_{2p} for CO) is named Lowest Unoccupied Molecular Orbital (LUMO). These orbitals are often called the frontier orbitals.

We now turn to the dependence on the nuclei position. The molecular potential energy versus the distance between the nuclei for the two molecular orbitals of hydrogen is plotted with solid curves in Fig 3.2 A. The presence of a minima in the molecular potential curve for the 1σ electronic state means that the molecule is stable with an equilibrium distance r_0 between the nuclei. The distance r_0 corresponds to the minimum in the 1σ potential, see Fig 3.2 A. The potential generated from the 2σ is without minima and when populated will lead to dissociation if not contrasted by the 1σ potential. Anti-bonding states contribute to the system with a dissociative potential and their contribution to the total energy depends on their state.

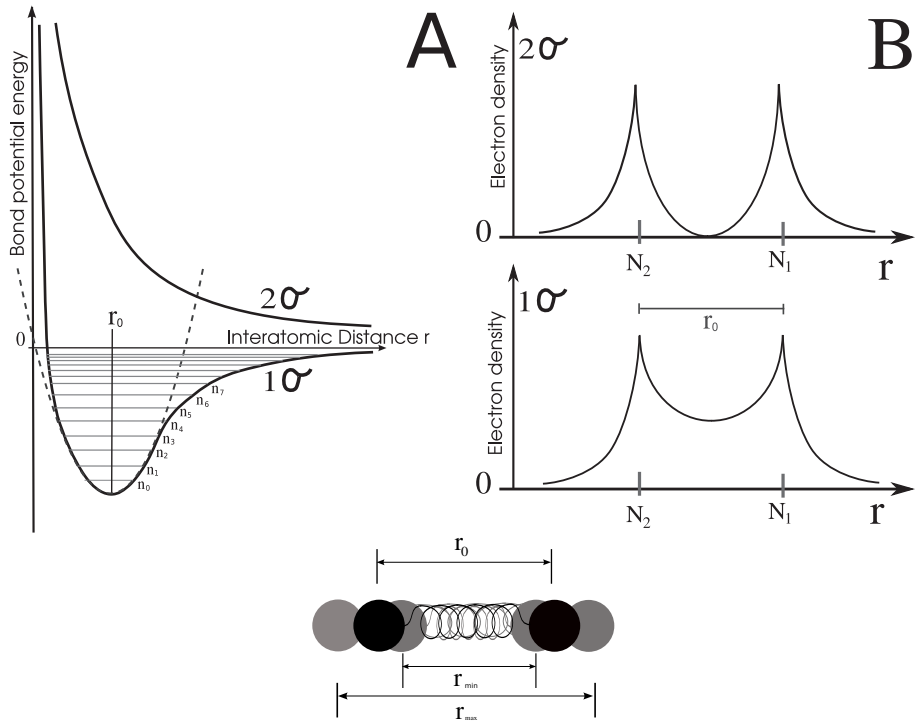

Figure 3.2: A Molecular potential energy as function of the atomic distance for the two first electronic levels. One bonding (1σ) and one dissociative (2σ). Vibrational levels are represented as lines across the binding potential. The parabolic line represents the harmonic oscillator potential showing that the molecule for lower vibrational levels can be treated as a harmonic oscillator. In B are represented the electron densities related to the two electronic states.

3.2 Molecular Vibrations

The potential minimum of the bonding state in Fig. 3.2 can be fitted with a parabola and therefore described with the harmonic oscillator model. The atoms vibrate around the equilibrium distance r_0.

Inserting the potential from a spring $V(x) = \frac{1}{2}\left(\frac{d^2V}{dx^2}\right)$ in the Shrödinger equation, the vibrational levels for the harmonic potential can be calculated. The vibrational levels are spaced according to $E_v = (v + \frac{1}{2})\hbar\omega$ with $\omega = \left(\frac{k}{m_{eff}}\right)^{\frac{1}{2}}$ where k is the constant of the spring [15, 16] and m_{eff} is the effective mass defined by $\frac{1}{m_{eff}} = \frac{1}{m_1} + \frac{1}{m_2}$.

The energy distance between the levels is a function of the force that keeps the atoms together and of the masses involved in the vibration. This explains the differences in the vibrational frequencies among the organic groups. These properties are used in any vibrational techniques. The harmonic approximation works until the real potential starts to differ from the harmonic one. After this point the spacing between the levels is not constant and anharmonic contributions must be considered, see Fig. 3.2. In most cases this however corresponds to highly excited vibrational states. In case of more extended molecules composed of more than two atoms the vibrations can be more complicated. Collective movements can preserve the symmetry during the vibration or deform the structure around the equilibrium positions. If one bond is vibrationally excited the energy of that vibration can propagate across the molecule. The potential energy in a polyatomic molecule depends on all the displacements of the atoms from their equilibrium positions [14].

3.3 Organic Molecules

The chemistry involving molecules where the main elements are carbon and hydrogen is called organic chemistry. In the beginning this name was used for the chemistry of the substances present in living systems, but now it is also used for compounds synthesised artificially. The molecules involved in organic chemistry are obviously

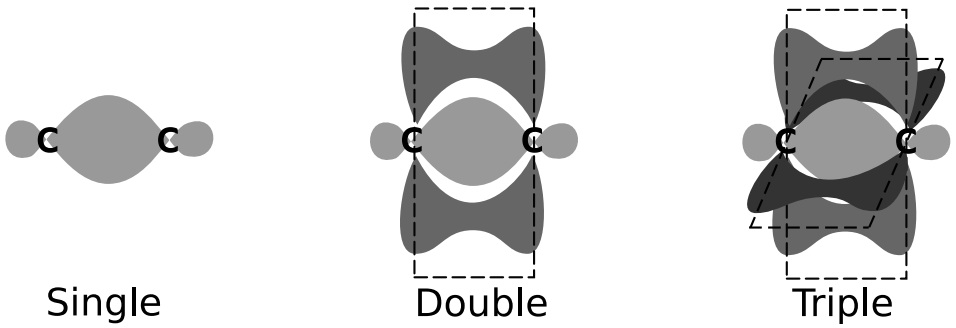

Figure 3.3: Schematic picture illustrating the three bond orders between two carbon atoms. From the left: single bound as in H_3CCH_3(Ethane), double bond as in H_2CCH_2 (Ethene), triple bond as in $HCCH$ (Ethyne).

called organic molecules. The electronic structure of carbon is $1s^2, 2s^2, 2p^2$. The rich chemistry of carbon is due to the easiness with which it hybridises [17]. With hybridization is meant the linear combination of the valence atomic orbitals inside one atom. For carbon this means linear combinations of the 2s and the three 2p orbitals, the result of the possible linear combination are: the s orbital and one p orbital (sp), the s orbital and two p orbitals (sp_2), the s orbital and three p orbitals (sp_3).

Three orders of bonds are found in organic molecules: single, double and triple. The single bond is axial to the straight line between the atoms involved in the σ bond, relative rotations of the two carbon atoms are allowed around the single bond axis. A molecule representative for this bond is ethane (C_2H_6). The double bond is composed of a σ bond and a π bond, rotations are not permitted along the double bond axis. A representative molecule for this bond is ethene (C_2H_4). The triple bond is composed by a σ bond and a two π bond lying in planes orthogonal to each other, rotations are not permitted along the triple bond axis, see Fig.3.3. A representative molecule for this bond is ethyne (C_2H_2). The π orbital requires sp_2 or sp hybridization of the carbon atoms involved. The π bond is formed by the overlap between the p_i orbitals not involved in the hybridization. The overlap generating such a bond is less efficient than the overlap between the orbitals generating the σ bond, therefore the π bonds are somewhat weaker than the σ. This is reflected in the reactivity, that is higher for the π bonds. Thus intuitively the reactivity of an organic compound is a function of the bonds present in the molecule. An approximative reactivity scale can be listed from lower to higher: pure covalent bond, polar covalent, double, triple bond. Organic molecules can be classified by the presence of groups that induce specific chemical reactivity. The most common groups are listed in Table 3.1. Each group is characterized by a particular reactivity

Table 3.1: Basic organic functional group

formula	Functional group name	example name	example formula
C-C	alkanes	ethane	CH_3-CH_3
C=C	alkenes	ethene	CH_2=CH_2
C≡C	alkynes	ethyne	CH≡CH
-OH	alcohol	ethanol	CH_3-CH_2OH
-CHO	aldehyde	ethanal	CH_3-CHO
-CON	amide	ethanamide	CH_3-$CONH_2$
-NR_2	amine	ethylamine	CH_3-CH_2NH_2
-COOH	carboxylic acid	ethanoic acid	CH_3-COOH
-COO-R	ester	ethyl ethanoate	CH_3-COO-CH_2-CH_3
-O-R	ether	di-ethyl ether	CH_3-CH_2-O-CH_2-CH_3
-CO-R	ketone	di-ethyl ketone	CH_3-CH_2-CO-CH_2-CH_3

The letter R indicates a general fragment of molecule, considered not relevant for the description of the group.

and vibrational frequency.

Chapter 4

Gas - Surface Interactions

The intent of this chapter is to briefly introduce some models of phenomena occurring when molecules come into contact with surfaces.

4.1 Adsorption

The first step in the adsorption process is the gas impingement on the surface. The atoms or the molecules composing the gas phase impact on the surface. The degrees of freedom available in this picture are the particle kinetic energy, the impact angle, and in the molecular case also the molecular orientation with respect to the surface at the impact. After the impact the molecule (atom) can bounce back into gas phase or remain on the surface. In the latter case the particle is said to be adsorbed on the surface.

Common denominator between adsorption processes is the presence of an attractive force between gas and surface that leads to energy gain. Even without going into the specific details it is possible to define some general behaviour.

The interaction between surface and adsorbates is not equal in every point of the surface, therefore some adsorption sites are more favourable than others. With the term "adsorption site" is indicated the position of the adsorbates relative to the surface atoms. Experience shows that high symmetry sites are preferred. A short list of high symmetry sites is presented in Fig. 4.1. The 111 FCC surface lattice has two different three fold hollow sites, the hexagonal close packed (HCP) site and the face centred cubic (FCC) site. In the hcp site an atom is present in the layer just underneath, while instead underneath the fcc site no atom is present. On stepped surfaces at the step ledge the normal site symmetry is broken opening new possibilities.

Adsorbates often extend their influence also to adjacent adsorption sites. If the interaction between molecules is sufficiently repulsive, the occupancy of two neighbouring sites does not occur. Therefore the density of surface adsorbates can be lower than the number of available sites. The amount of adsorbates present on the surface can be given in relation to the number of atoms that compose the outermost layer in the substrate, see eq.(4.1), or to the total amount of that specific adsorption site available on the bare surface, see eq.(4.2).

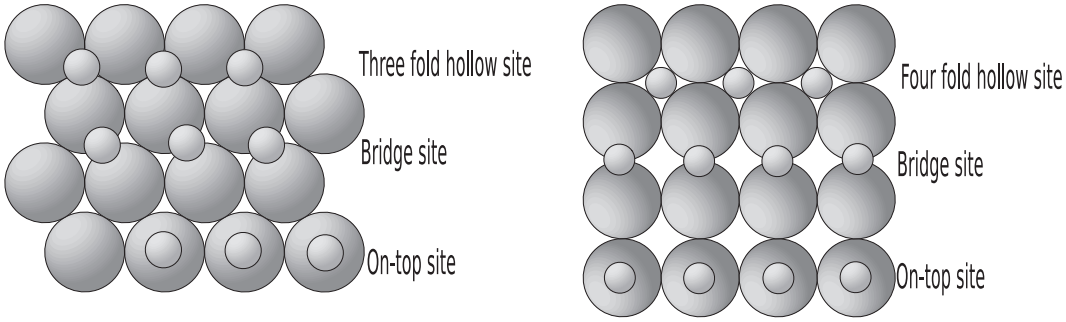

Figure 4.1: High symmetry adsorption sites for hexagonal and square symmetry surfaces.

$$\Theta_m = \frac{\text{Number of adsorbates on the surface for unit of area}}{\text{Number of surface substrate atoms for unit of area.}} \tag{4.1}$$

$$\Theta_s = \frac{\text{Number of adsorbate on the surface for unit of area}}{\text{Number of available site for the adsorbate for unit of area}} \tag{4.2}$$

Only a fraction of the molecules that hit the surface adsorbs on it. The probability that a given incident molecule adsorbs is called the sticking probability (s). Sticking probability '$s(\Theta)$' relates the flux of molecule that hit the surface to the coverage $\Theta = \int_0^t s(\Theta) \cdot \text{Flux(t)} \cdot \text{dt}$. The flux of molecules on the surface is defined by pressure, molecular mass and gas phase temperature: Flux $\propto \frac{P}{\sqrt{2\pi mkT}}$.

Two simple models are here described for the sticking probability behaviour in relation with the surface coverage Θ_s: proportional to $(1-\Theta_s)$ and constant with Θ_s. The case of the sticking probability proportional to $(1-\Theta_s)$ corresponds to molecules adsorbing only when they hit directly an empty site otherwise no adsorption occurs, see Fig. 4.2 A. This proportionality is represented with a dashed line in Fig. 4.3 A. If we consider the dissociative adsorption of a molecule AB instead of a non dissociative adsorption the $(1-\Theta_s)$ behaviour changes into a $(1-\Theta_s)^2$ behaviour, as the molecules now need to find two empty adjacent sites. This case is shown in Fig.4.3 A and B by the dotted lines.

The constant sticking probability model can be imagined with the help of a mobile precursor state, see Fig. 4.2 B. The molecules hit the surface and are then able to move freely across the surface until they adsorb in empty sites. The molecules that hit the surface therefore can be adsorbed until saturation without any change in the sticking probability. This case is represented in Fig. 4.3 with a solid line. The coverage is increasing linearly until saturation of the surface Fig. 4.3 B, at that point the sticking probability goes to zero Fig. 4.3 A. The dash dotted line consider the case for an adsorption via a mobile precursor state with limited lifetime. Limiting the lifetime limits the distance that the molecules can cover on the surface and therefore limits also the probability to find an empty site for the adsorption.

Equilibrium has not been mentioned until now since the experimental conditions used during the thesis mostly do not involve it. The main difference is that at equilib-

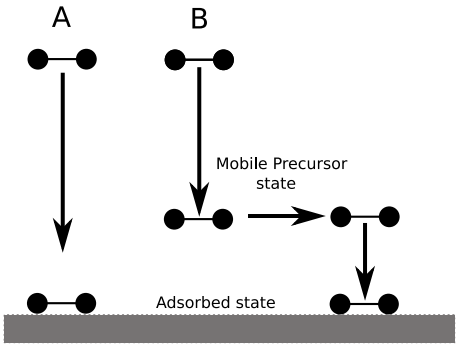

Figure 4.2: Two different adsorption mechanism possibilities. A) Direct adsorption on the available site. B) A mobile precursor state that allows the adsorbate to move across the surface and adsorbs in an empty preferred adsorption site.

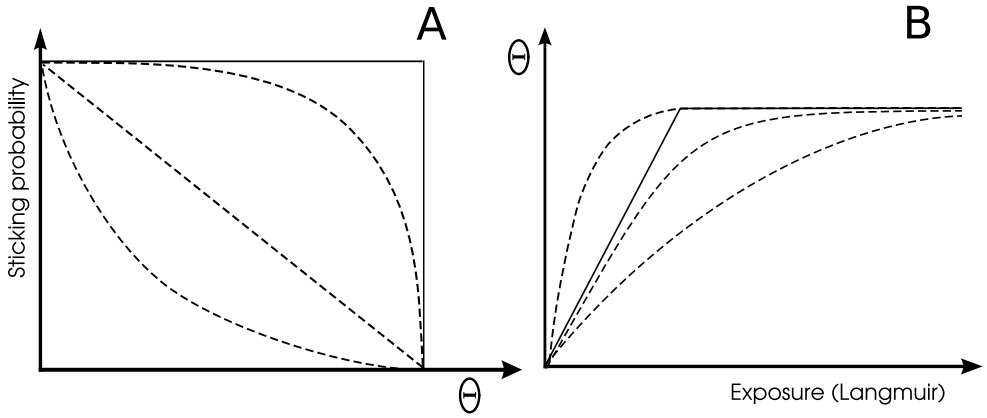

Figure 4.3: A) Shows the sticking probability versus the coverage. The described adsorption behaviours are only qualitative: solid line: constant up to Θ max, zero thereafter. Dashed line: $\propto (1 - \Theta)$. Dash-dotted line: limited mobility precursor. Dotted line: dissociative adsorption. In B) is shown the resulting coverage versus Langmuir exposure.

rium the coverage does not depend on the exposure time and the desorption process must be considered. The equilibrium conditions are defined as the point where the number of molecules that adsorb on the surface is equal to the number of molecules that desorb. The speed of the desorption depends on the surface temperature and how strongly the molecules are bound. The desorption process is described by an Arrhenius equation. Since the adsorption process is related to the pressure and the desorption depends on the sample temperature, the coverage Θ_s at the equilibrium point is a function of both sample temperature and gas pressure.

The attractive force between adsorbates and a surface is described via a potential similarly to the one used for a bond between two atoms presented in chapter. 3.1. Only if the potential presents a minimum there is a possibility to trap the molecule.

Probably the most common potential used for describing adsorption is the Lennard-

Jones, see Fig. 4.4. In this model the interaction energy between surface and adsorbates is merely a function of the distance between the adsorbates and the surface. The use of a one dimensional potential is to some extent oversimplified but useful for a qualitative description. For a more detailed picture of the phenomena the potential energy surface (PES) of the system must be used. The PES is a hyperplane that describes the energies over the surface atomic coordinates. Therefore it includes information on the adsorption sites, molecular orientations, adsorption energies and barrier for adsorption and mobility [18].

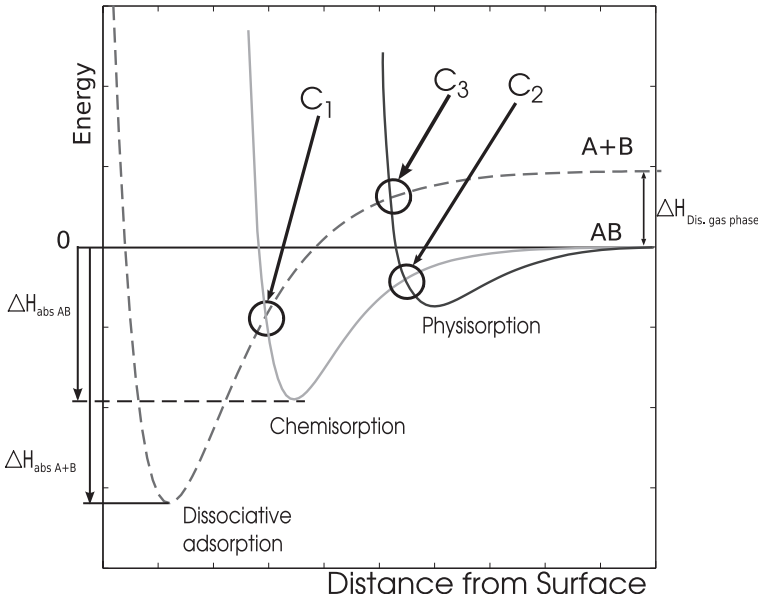

Figure 4.4: Qualitative shape of the Lennard-Jones potential which is experienced by molecules approaching a surface. The solid lines are for non dissociative adsorption and the dashed line for the dissociative adsorption. With ΔH_{absAB} is indicated the enthalpy of the adsorption process for the molecule, with ΔH_{absA+B} is indicated the enthalpy of the adsorption process for the fragments, and with $\Delta H_{Dis.gas.phase}$ the enthalpy of the dissociation of the molecule in gas phase. For the interpretation of C_1, C_2 and C_3 refer to the text.

The cases proposed until now do not discern between different adsorption states. The well depth and the state of the molecules during a generic adsorption process allow to discern between different adsorption states: physisorption, chemisorption and dissociative adsorption, see Fig. 4.4 and later paragraphs.

4.1.1 Physisorption

Physisorption is characterized by a small adsorption energy meaning a shallow minimum in the potential and by an adsorbate-surface distance which is larger than for chemisorption, see solid line in Fig. 4.4. The attraction between surface and adsorbates can be explained via van der Waals forces. The adsorbate and surface electronic structures are only weakly affected, all the bonds of the original and not

interacting systems are preserved. This kind of attractive forces come from the interaction between induced dipoles [18]. On the other hand Pauli repulsion between the molecular HOMO and the surface electron density is responsible for the repulsive force generating the rapid increase of the potential with decreasing surface-adsorbate distance. From the physisorbed state it is possible to move towards the chemisorption state via overcoming the cross point "C_2", see Fig. 4.4. The energy position of such a point defines the energy barrier (if present) to reach the other state. In the same manner the cross point "C_3" separates the physisorbed state from the dissociative adsorption. The position of the cross points in Fig. 4.4 are just representative. Such points can lie above or below the zero energy line (the adsorbate in the gas phase). If present, the activation energy to pass from one adsorption state to the other is the vertical distance from the local minimum that is trapping the molecule and the cross point with the potential of the final state.

4.1.2 Chemisorption

Chemisorption is characterized by the creation of a proper chemical bond between adsorbate and surface. Electrons are shared or exchanged between substrate and adsorbates, see Fig. 4.4. The electronic structure of both surface and adsorbate is perturbed from the interaction. The electron density of the final state gives information on the character of the bond formed between surface and adsorbate. Electron density localised in between the two parts involved in the bond suggests a covalent bond while charge transfer between them indicates an ionic bond.

However the spatial information on the charge redistribution is not enough to gain insight on the energy balance between band-structure and electrostatic contribution. Information on the energy density of states must be considered to obtain a more complete picture [18], see paragraph 4.2.

The heat of adsorption for the chemisorption process also depends on the surface coverage, because of the adsorbate-adsorbate interactions. The presence of ordered adsorbate structures for instance can destabilise further adsorption. This reflected in a decrease of the heat of adsorption [19].

4.1.3 Dissociative Adsorption

As the name suggests the interaction between substrate and adsorbates affects not only the electronic configuration but also modifies the molecular structure of the adsorbates. If the energy potential for the dissociate molecule present a minimum lower than the other adsorption states, the spontaneity of the process depends on the energy position of the crossing points with the other adsorption curves, C_1 and C_3 in Fig. 4.4. In the presence of energy barriers in the process it is also clear that the kinetic energy and the impact angle of the impinging molecules affect the efficiency of the process [20]. As seen from Fig. 4.4 the dashed potential line does not converge to zero for infinite surface-adsorbate distance as the other two. Instead it converges to the dissociation energy for the molecule in gas phase $\Delta H_{Dis\ gas\ phase}$.

The thermodynamic of the dissociation process is of course relevant to predict spontaneous events, but also the detailed surface mechanism plays a role. The

presence of moieties on the surface can affect the process via blocking the active sites or limiting the availability of neighbour sites for the adsorption. The importance of this scenario has been recently theoretically described [21].

4.2 Hammer-Nørskov Model

Transition metals are extensively used in heterogeneous catalysis. The Hammer-Nörskov model provides a qualitative understanding of the interaction between the adsorbate levels and the electronic structure of the substrate and in particular highlights the influence of the d-band of the metal.

The bonding between free molecules in gas phase is characterized by the mixing of well defined discrete energy levels, as described briefly in paragraph 3.1. Moreover, it has been found that most chemical properties of gas phase reagents are determined by the Highest Occupied Molecular Orbitals (HOMO) and the Lowest Unoccupied Molecular Orbitals (LUMO) [18, 20] of the molecules. To transfer this picture to the adsorbate case, HOMO and LUMO equivalents for the surface must be found. For the transition metals, the d-band solves this role. In these metals, the d-band has a narrow energy distribution and is only partially filled. It can therefore provide filled and empty states in a narrow and defined energy range that can work as HOMO (the filled part of the band) and as LUMO (the empty part of the band). The interaction between the molecular levels and the d-band therefore reflects the two levels interaction problem, known from chemistry [22, 23]. Fig.4.5 shows the case of

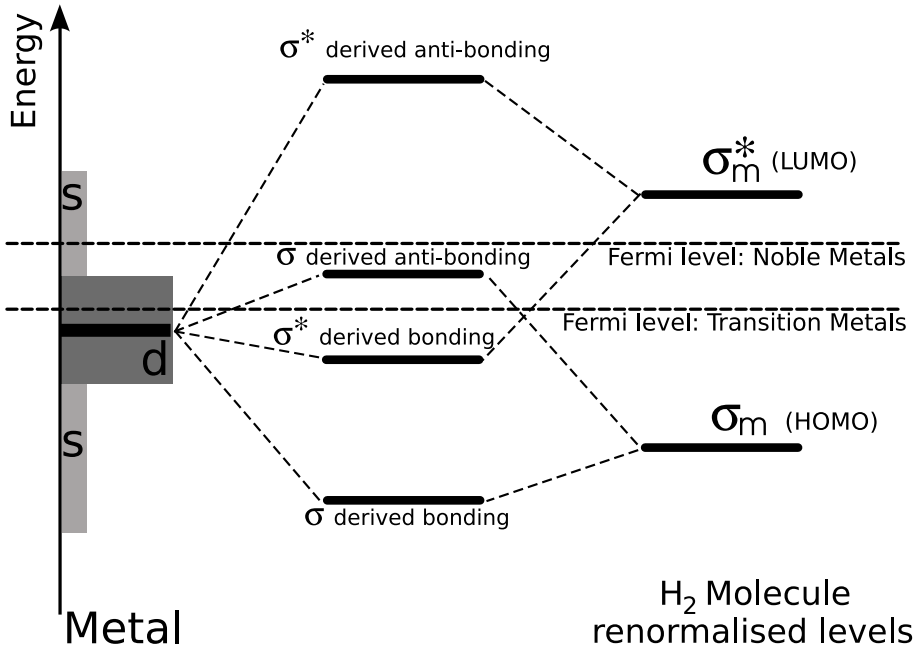

Figure 4.5: Schematic representation of the surface electron density and the hydrogen molecule levels. The interaction between the surface and the molecule induces new levels typical of bond formation, see paragraph 3.1. With S and d are indicated the S and d-band of the metallic substrate.

a hydrogen molecule bonding to a d-band metal. The interaction of the molecular adsorbate levels with the sp-band of the metal leads first to the broadening and then to an energy shift of the HOMO and the LUMO of the molecule, this is termed renormalisation. The interaction between the molecule and the d-band is influenced by three important factors: (1) The position of the molecular bonding and anti-bonding states relatively to the d-band. (2) The magnitude of the matrix element representing the orbital overlap between the molecular orbitals and the d-band. (3) The filling of the molecule-surface anti-bonding states which is determined by the position of the Fermi level. This is rationalized in the following formula for the change in total energy ΔE caused by the adsorption:

$$\Delta E = -2\frac{V_{dm}^2}{\varepsilon_{\sigma_m^*} - \varepsilon_d} - 2(1-f)\frac{V_{dm}^2}{\varepsilon_d - \varepsilon_{\sigma_m}} + \alpha V^2 \tag{4.3}$$

The term ε_d is the energy position of the d-band centre relative to the Fermi level. The term ε_m is the energy position of the bonding molecular orbital relative to the Fermi level after the renormalization process. The term ε_m^* is the energy position of the anti-bonding orbital referred to the Fermi level after the renormalization process. [22, 18]. The term f is the filling factor for the d-band. The term V_{dm} is the coupling matrix element between the molecular orbitals and the d-band. The energy variation described by eq. 4.3 is also a good descriptor for estimating the energy barrier involved in dissociation [24, 22, 25]. Furthermore, it has been shown that in many cases, e.g. for H_2 [22] and CO adsorption [26] the first term of Eq. 4.3 dominates the molecule-surface attraction. This underlines the importance of the position of the centre of the d-band relative to the Fermi level; assuming no change of the matrix element, a shift of the d-band centre towards the Fermi-level will lead to a larger energy gain.

As described in chapter 2.3, the extension and the centre of the d-band can be modified by the surface morphology. For a late transition metal, the d-band at a step is narrower than on the terraces and its centre is closer to the Fermi-level, causing e.g.CO to bond stronger at a step than on the terrace for such metals. These differences in adsorption energy has been probed during the CO adsorption experiments performed in [I]; the difference in reactivity was investigated in [IV, V].

4.3 Mobility

Mobility explains the surface atomic and molecular motion and diffusion. Mobility therefore is relevant for all surface processes that involve mass transport. In surface chemistry it is responsible for the mass transport towards and away from the active sites.

After a molecule is adsorbed it can meet limits while it is trying to move across the surface. A common description of the adsorbate motion involves hopping between adsorption sites. For non-interacting particles this leads to a random walk.

Experimentally it is well established that the rate of the process follows an Arrhenius behaviour: the rate is a function of the temperature:

$$k = Cexp\left(-\frac{E_a}{k_b T}\right) \tag{4.4}$$

k is the number of successful events, C is the number of attempts to overcome the barrier E_a at the temperature T, k_b is the Boltzmann constant.

On the other hand, a directed flux of adsorbates across the surface can be induced by a variation of their density or chemical potential.

Mobility is a thermally activated process, two different diffusion regimes can be distinguished: (1) $kT \ll E_a$ and (2) $kT \sim E_a$ and $kT \geq E_a$. In the first case the adsorbates are mainly localised at the adsorption sites where they are vibrating. This regime is characterised by random jumps between adsorption sites, a hopping rate can be defined. For the second scenario the adsorbates translational energy is always of the same order of magnitude as the energy barrier, therefore the adsorbates move almost freely across the surface. A two dimensional Brownian motion is more appropriate to describe the latter case [27].

The presence of steps inserts further barriers which influence the surface mobility [28, 27]. The presence of such barriers can alter the hopping rate and therefore

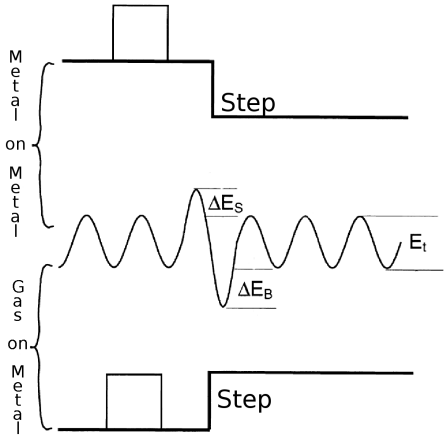

Figure 4.6: Ehrlich Schwoebel Barrier for the case of metal ad-atoms on metals and gases on metals. The term ΔE_S indicates the Schwoebel Barrier, ΔE_B indicates the minimum of the potential near the Schwoebel barrier, and ΔE_t indicates the potential corrugation on the terraces.

the diffusion length [29, 30].

The model proposed by Schwoebel and Ehrlich was assigning the mobility limits to the presence of barriers. Later it was understood that the presence of the minimum after the barrier also played an important role in the mobility and in the kinetic of the system [31]. For a metal adatom on metallic surfaces the potential barrier is at the top of the step and the trapping minima is placed at the bottom of the step, see Fig. 4.6. For molecules adsorbed on metals the potential just described is inverted, molecules feel the barrier at the step bottom and the trapping minima at the top of the step [30], see Fig. 4.6.

Chapter 5

Reactions

Reactions are an important part of this thesis, the intent of this chapter is to provide a brief description of reaction related phenomena relevant for heterogeneous catalysis.

5.1 Reactions and The Effect of Catalysts

A chemical reaction is the process that results in the conversion of chemical species. Chemical reactions may be elementary reactions or stepwise reactions. Chemical reactions normally involve a set of molecular entities but may also contain only single molecular entities [32]. Good examples of the latter possibility are ethanol and ethylene dissociation processes studied in this thesis [IV, V]. Having a detailed knowledge of a reaction means to know the system while the reagents are transforming into products: the intermediates, the energy state of the system while going from the reagent to the product and the transformation rate. Thermodynamics is the tool that describe the system energy using physical conditions such as temperature, pressure, composition and volume.

The so called *Gibbs free energy* contains the information to describe the energy state of the system at constant pressure. The Gibbs free energy is defined as $G = H - TS$ but it is usually considered in the form that refers to transformations at constant temperature:

$$\Delta G = \Delta H - T\Delta S \tag{5.1}$$

where H is the enthalpy involved in the reaction occurring at temperature T and S is the entropy. The enthalpy is defined as $H = U + pV$ where U is the internal energy of the system [16]. If $\Delta G < 0$ the reaction is exothermic.

But even if a reaction is thermodynamically favourable ($\Delta G < 0$) that does not mean that it will occur. It is common experience that a fire needs to be ignited. This behaviour is explained by the presence of an energy barrier separating reactants and products, which must be overcome in order for the reaction to occur. Thermodynamics acts as a driving force that moves the system towards the most stable condition. The influences of energy barriers are taken in account by the reaction kinetics.

Reagents are in a local minimum and need a push to overcome an energy barrier (activation energy $E_{att.}$) to move towards the products, see Fig. 5.1. Kinetics studies the relation between the reaction speed and the experimental conditions. The reaction mechanism also influences the speed since it represents the path taken to go from reagents to products. Different mechanisms might involve different energy barriers and must be considered to explain the time evolution of the system, see Fig. 5.1. The speed of a reaction from a kinetic point of view depends on the

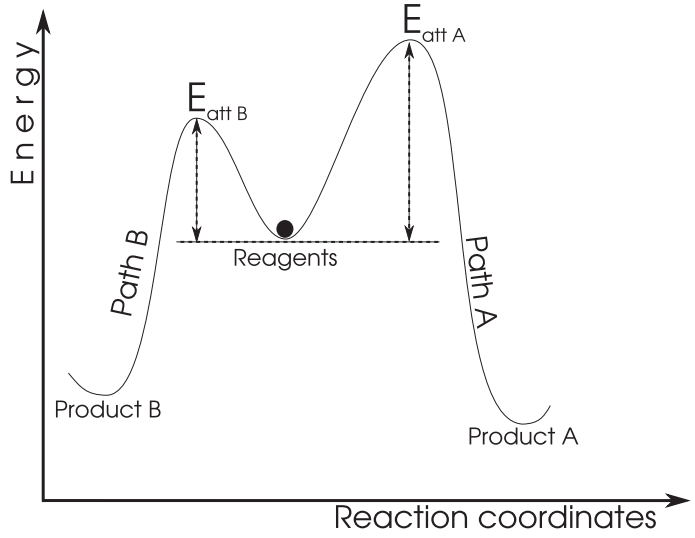

Figure 5.1: Cartoon description of a reaction. The reagents located in a local minima need to overcome an energetic barrier to evolve towards the products. Depending on which barrier that is overcome the reaction paths and the products will be different.

concentration and temperature. The concentration affects the hitting probability between reagents and therefore the reaction speed. The temperature influences the possibility to overcome energy barriers.

The speed of a specific reaction can be drastically increased by lowering the activation barrier involved in the process. This is obtained with the help of catalysts. The general influence of a catalyst is to lower the activation barrier between reagents and products. However to decrease the activation barriers is not enough, in fact also the thermodynamics of the surface intermediate can influence the reaction path and mechanism. The presence of even a single endothermic step along the surface intermediate chain can block a reaction.

There are two main reasons why catalysts are used in industry. Firstly, the use of a catalyst decreases the transformation time from reagents to products at a given temperature. Secondly catalysts give higher selectivity and higher yield. If a number of competitive reactions exists, decreasing the energy barrier for one of them will lead to a selective speed improvement. This will change the ratio between the products in favour of the enhanced reaction. The catalyst is involved in the reaction but is not consumed thus at the end of the reaction its conditions are unchanged. The amount of catalyst necessary for a reaction is a function of its efficiency. In

heterogeneous catalysis, the reaction takes place at the surface of the catalyst. This fact strongly motivates the study of surface reactions.

5.2 Surface Reactions

Reactions occurring on a surface can be described through a three steps sequence. At first adsorption together with surface mobility regulates the incoming flux of matter on the surface. The second step is the chemical transformation, that takes place according to thermodynamics and kinetics. In the last step, the products have to be desorbed from the surface. Each step can present thermodynamic and kinetic barriers characteristic for the specific reaction considered.

For surface reactions the surface coverage takes the same role that the concentration has, for instance, in solutions or in the gas phase reactions. This assumes that the contact area between the reagents is proportional to the molecular concentration on the surface and therefore it assumes that the reagents are mixing down to a molecular scale on the surface. But it is known that adsorbates might not mix, e.g. [33, 34], segregating instead into islands. In this second scenario, the contact between the reagents is limited to the contact perimeter between different islands. The limitation in the contact between the reagents is reflected in the time evolution of the system that becomes proportional to the square root of the reagent coverages. Therefore it is possible to extract from the time evolution of the average surface coverage informations on the kinetics[II].

There are a few basic models for to describe reactions dynamics on surfaces: the Langmuir-Hinshelwood (L-H), the Eley-Rideal (E-L) and the Mars van Krevelen, which could be said to be a special case of the Langmuir-Hinshelwood dynamics.

5.2.1 Langmuir-Hinshelwood mechanism

This model is based on the assumption that the reagents are adsorbed on the catalyst and after diffusing on the surface they interact and react, see Fig. 5.2. It is considered a common mechanism, often preferred to the Eley-Rideal [35]. In the classical and general description the reactants are mixed on the surface [34] but as already introduced this is not always the case. This mechanism was firstly proposed by Langmuir at the beginning of the past century.

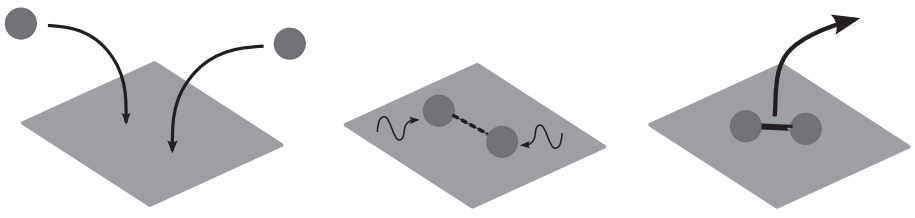

Figure 5.2: Langmuir Hinshelwood mechanism model.

The ethanol oxidation studied in [III] has shown that the acetate formation does not depend on how the reagents are supplied to the surface. In fact the formation is

happening in both cases: either if one reagent is already present on the surface while the other is introduced in the chamber or if they are dosed together. Therefore it can be speculated that the reaction occurs between adsorbed oxygen and adsorbed ethanol in a Langmuir-Hinshelwood mechanism.

5.2.2 Eley-Rideal mechanism

The basic assumption in this model is that only one of the species involved in the reaction is adsorbed on the surface. The reaction occurs when the second reagent impacts directly on the adsorbate from the gas phase, see Fig. 5.3. Thus the reaction speed is related to the surface coverage of one reactant and to the pressure of the other in the gas phase. This mechanism was proposed for the first time in the late forties [36]. It is commonly considered as less frequent compared to the Langmuir-Hinshelwood. For a long time the real existence of it was debated until Rettner provided some convincing experiment [37].

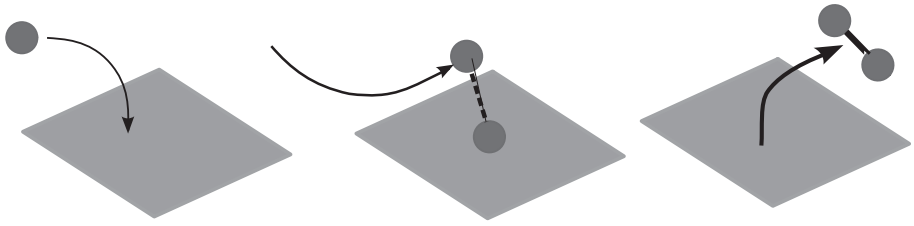

Figure 5.3: Eley-Rideal mechanism model.

5.2.3 Mars-van Krevelen mechanism

In this mechanism one of the reagents is stored in a "solid" phase on the catalyst, see Fig. 5.4. For instance, oxygen may be stored in surface oxides and then supplied during the reaction to the incoming reagent. In this process the reagent is oxidised and the surface reduced. To maintain a steady state reaction the stored reagent must be continuously supplied to replace the fraction consumed from the reaction. This mechanism also holds for sulfides, halides and hydrides [38]. It takes its name

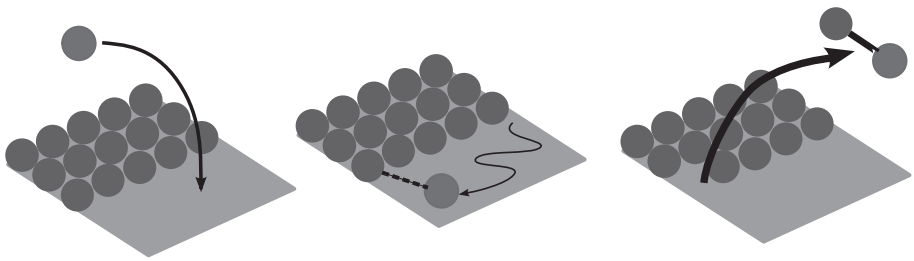

Figure 5.4: Mars-van Krevelen mechanism model.

from the authors that discovered the process during the fifties [39], it is also known as a red-ox or regenerative mechanism.

The mechanism has been recently addressed as responsible for the oxidation activity of Ru(110) thin oxide films on Ru(001) [40].

5.3 Active Sites

As already mentioned in chapter 4, not all surface sites are equivalent. The morphology can influence the LDOS, which implies a different reactivity for different sites. The influence of the morphology on the catalytic activity was observed at the beginning of the last century and Taylor [1] introduced the concept of an active site. The term active site makes a distinction between the fraction of the catalyst (surface) active in the chemical process and the fraction which does not take part in the reaction.

The maximum in the catalytic rate is often argued to be a compromise between having a low activation barrier for the adsorbate dissociation (favoured by strong metal-adsorbate bond) and being able to further react the adsorbate reagents to adsorbate products (favoured by a weak adsorbates-surface bond). This is known as the Sabattier principle. Weak metal-adsorbate bonds lead to a simple adsorption and no dissociation, strong metal-adsorbate bond favourites the dissociation but may inhibit diffusion and the realising of the active site. As example of such principle can be taken the different behaviour between the type A step of the Rh(322) and type B of the Rh(553) presented in [V].

5.3.1 The Step Activity

The band narrowing introduced for surfaces in paragraph 2.3 also affects the LDOS of the steps differentiating them from the terraces, resulting in a different d-band width and centre as compared to the terraces. The Hammer-Nørskov model presented in paragraph 4.2 relates such properties to adsorption energy and catalytic activity. A different activity is therefore expected from the steps as compared to the terraces. Enhanced step activity is generally attributed to the local decrease of the dissociation barrier, moreover the trapping potential present at the steps withhold the molecules for longer time in such sites [28, 41]. The enhanced activity towards molecular dissociation at steps is widely supported from theory and experimental observations e.g. hydrogen, oxygen, nitrogen, nitrogen monoxide dissociate at steps [42, 41, 43, 44, 45, 46]. In addition, molecules adsorbed at steps experience a higher degree of freedom allowing movements of otherwise sterically blocked molecules on the terraces, providing new possibilities for reaction channels otherwise not feasible [47, 48].

Article [V] contributes to the idea of steps as bond opener but it also put in evidence the site activity dependence on the local geometry.

Chapter 6

High Resolution Core Level Photoemission

High Resolution Core Level Photoemission is the main techniques used in this experimental work and it deserves a dedicated chapter to shortly introduce it.

6.1 Introduction

High resolution core level spectroscopy (HRCLS) is based on the photoelectric effect: the phenomenon that shining light of sufficiently short wavelength onto an object leads to electron emission. The explanation of the photoelectric effect was given by Einstein in 1905.

HRCLS is a technique based on X-ray Photoelectron Spectroscopy (XPS) which is very sensitive to the elemental composition of the sample. The photon energy used is typically 50-1000 eV. This technique is intrinsically surface sensitive due to the short mean free path of low kinetic energy electrons in solids. According to the literature [49, 50] for electrons with kinetic energy in the range 20-1000 eV, the mean free path is about two to six monolayers, see Fig. 6.1. As seen from Fig. 6.1, the mean free path for most elements fall on a so called universal curve with a minimum around a kinetic energy of 50 eV. By making use of this variation with the kinetic energy, the surface sensitivity can be tuned.

6.2 Core Level Binding Energies

Electromagnetic radiation excites electrons and induces their emission. The number of emitted electrons is related to the number of photons of the incoming beam. The kinetic energy of the emitted electrons depends on the frequency of the radiation and how strongly the electrons were bound in the material. For a photon of energy $h\nu$ absorbed by an electron that leaves the material with a kinetic energy E_{Kin}, the binding energy of the electron in the material ($E_{Binding}$) is given by:

$$E_{Binding} = h\nu - E_{kin} \tag{6.1}$$

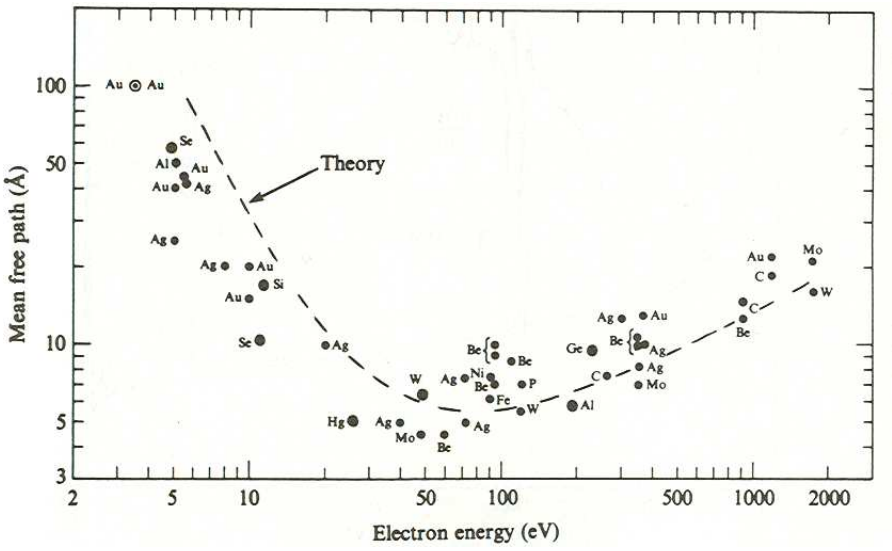

Figure 6.1: Universal curve for electron mean free path in solids a function of their kinetic energy[51].

The binding energy is also defined as the energy which must be supplied to the material in order to extract the electron, thus:

$$E_{Binding} = E_{final} - E_{initial} \tag{6.2}$$

where $E_{initial(final)}$ is the total energy of the system before (after) the electron was emitted. In this latter definition it is more evident that both the initial and the final state contribute to the resulting binding energy. Each element has a unique series of energy levels [52]. In a first approximation the energy of each core level is related to the nuclear charge. However, the environment also plays a role being responsible for minor energy contributions. It is these minor contributions which contain information about the local surroundings of the probed atom. The shift induced from inequivalent surroundings is called a chemical shift.

In Fig. 6.2A it is shown the shift between bulk and surface atoms. The first measurements of such a chemical shift between surface and bulk atoms, normally called the surface core level shift, were performed in 1979 on tungsten [53]. The Rh $3d_{5/2}$ spectra have the bulk signal at 307.2 eV and the surface peak at 306.7 eV in binding energy. The surface sensitivity was changed by tuning the photon energy, thus the intensity ratio between surface and bulk peak changes. In this way it was possible to determine which peak belongs to the bulk and which to the surface. The second spectrum, Fig. 6.2B, is measured from a Rh(111)(9×9) thin surface oxide. In this spectrum there is a signal at the same binding energy as for the Rh(111) clean surface due to the bulk, the other main signal is due to the Rh atoms in the oxide layer [54]. In Fig. 6.2C it is reported as example the chemical shift observed between the two carbon atoms of the ethylidyne (C-CH_3) moiety adsorbed on Rh(111). The carbon directly bonded to the Rh surface has a binding energy of 283.45 eV while the carbon in the methyl group has a binding energy of 284.06 eV. The additional structure seen in the emission from the methyl group C-atom is due to the excitation

of the C-H stretch vibrations, see paragraph 6.3.2.

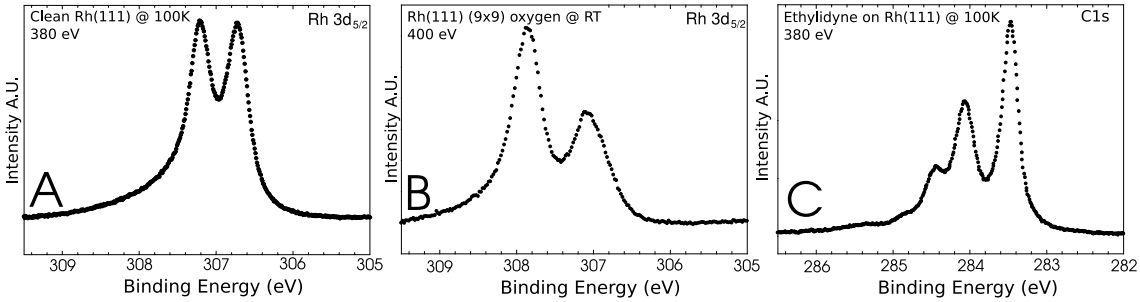

Figure 6.2: A) The clean Rh(111) surface shows two well resolved $3d_{5/2}$ peaks: at lower binding energy the surface signal and at higher binding energy the signal from the bulk. B) Spectra of Rh(111)(9×9) surface oxide structure. At lower binding energy the bulk signal and at higher energy the signal of the Rh atoms in the oxide layer. C) HRCLS distinguishes between the two carbons in C-CH_3 adsorbed on Rh(111) at 283.47 eV the carbon bonded to the metal surface and right after the signals of the methyl group (CH_3).

If we want to calculate the chemically shifted components of a particular atom in a sample what is needed are calculations of the initial system total energy and the various final states corresponding to the hole being localised on the various chemically inequivalent atoms [55]. This is the idea used in the calculations performed using Density Functional Theory.

The contributions to the binding energy shift can be divided into initial and final state effects, see e.g. [12]. The initial state effects influence the energy position of the core levels and therefore the starting point for the ionisation. An intuitive electrostatic picture suggests that differences in the initial state charge density affect the potential in the atom core, thus shifting the core levels. In a simple model the electronegativity of the elements bonding to the probed atom can be used to predict changes in the valence charge density and thus the core level shift. Also the surface band narrowing mentioned in 2.3 affects the initial state charge density of the surface atoms, thus it induces a chemical shift from the bulk binding energy. For a centroid narrowing of the d-band its degree of filling will influence the surface core level shift. For d-bands more (less) than half filled, surface core level shifts towards lower (higher) binding energies are expected as seen from Fig. 2.5.

Final state effects basically are contributions that can not be accounted for by the initial state effects. They reflect the response of the system to the creation of a core hole. These final state effects may depend on the chemical surroundings of the emitting atoms thereby changing conclusion made from only initial state reasoning.

Finally it is important to note that different binding energy implies a different chemical surrounding of the probed atom, but it is not always true that equal binding energy corresponds to equal surrounding.

6.3 Features and Lineshapes in Photoemission

6.3.1 Traditional Lineshape Decomposition

Various factors come together in influencing the shape of a core level photoemission peak. Each effect must be convoluted with the others in order to obtain the spectra. Two basic shapes are used as starting point to rationalise a spectrum: Lorentzian and Gaussian. The excited state lifetime generates the Lorentzian shape via the Heisenberg principle. The exponential decay in time can be shown, via a Fourier transform, to correspond to a Lorentzian shape in the energy domain [15]. The phonon excitation generated during the photoemission is responsible for a Gaussian contribution. Electronic transitions in molecules are often accompanied by vibrational excitations with distributions governed by the Franck Condon principle, see paragraph 6.3.2. A similar phenomenon also occurs in solids, with the main differences that the initial state is usually not in the lowest vibrational state and the energy separations between the vibrational levels is smaller. Because of such differences the same distribution that leads to a Poisson distribution for molecules leads here to a Gaussian distribution of unresolved levels [56].

During the photoemission process the creation of plasmons, quantized oscillation of the electron gas, might be observed. These excitation are typically in the order of 10 eV, and appear on the high binding energy side of the spectra as a broadened replica of the adiabatic peak. The photoemission process that ionised the atom can also excite a second electron into a empty state (shake up) or into the continuum (shake off). These phenomena manifest themselves as broad structures on the high binding energy side of the adiabatic peak [12].

The creation of electron-hole pairs around the Fermi level is typical for metals and it requires infinitesimally small amounts of energy because of the continuous density of states in that region. This effect makes the line shape asymmetric adding to the peak a tail towards high binding energy. The resulting shape is called a Doniach Šunjić [57] line shape.

Finally, the theoretical line shape must be convoluted with a function describing the finite experimental resolution. As experimental function a Gaussian is commonly used.

6.3.2 Including Vibrational Components

The photoemission process is very fast and it can be considered to occur within a stationary nuclear framework. The initial state is considered to be in the ground vibrational state with the nuclei around the equilibrium distance r_0. The constant nuclei spatial distribution during the vertical transition defines the so called Franck Condon region, see Fig 6.3. Since the nuclei equilibrium distance between initial and excited state might differ, the final state can end up not only in the ground vibrational state. Thus a vibrational structure can arise in the core photoemission spectra due to vibrations in the excited state. The quantum mechanical description is based on the evaluation of the transition dipole moment between the initial state

$|\varepsilon\upsilon\rangle$ and the final $|\varepsilon'\upsilon'\rangle$ [14].

$$\langle\varepsilon'\upsilon'|\mu|\varepsilon\upsilon\rangle = \mu_{\varepsilon'\varepsilon}\underbrace{\int \psi_{\upsilon'}(R)\psi_{\upsilon}(R)d\tau_{\upsilon}}_{\text{F-C Term}} = \mu_{\varepsilon'\varepsilon}S(\upsilon',\upsilon) \tag{6.3}$$

The total transition probability between electronic states is therefore divided among the vibrational states of the final electronic state [58]. The intensities of the vibrational lines, see Fig. 6.3, depends on the Franck Condon factors, that are the square of the term $|S(\upsilon',\upsilon)|$. However this picture can be simplified even further. By applying the linear coupling model [59, 60, 61] the final state can be considered as having the same harmonic potential as the initial state but with different equilibrium distances between the nuclei, see Fig. 6.3. This approximation expresses the Franck Condon factors as:

$$I(0-n_1,\ldots,0-n_q) = I(0-0,\ldots,0-0)\cdot\prod_{r=1}^{q}\frac{S_r^{n_r}}{n_r!} \tag{6.4}$$

where $I(0-n)$ describes the intensity for the transition from $\upsilon = 0$ in the initial electronic state to $\upsilon = n$ in the excited state. The term n_r is the vibrational quantum number of the r^{th} mode and S^{n_r} is the Franck-Condon Factor between the levels considered. Thus using the harmonic oscillator and the linear coupling model the intensities (F-C factors) can be related to each other via a Poisson distribution allowing a decrease in the number of free parameters in the fit.

This phenomenon is analogous to the one mentioned in section 6.3.1 for phonons in a lattice. The molecular vibrational energies are often larger than the phonon energies, thus the Franck Condon region covers a smaller number of vibrational states in the excited state, see Fig 6.3.

In the fitting of ethylidyne C1s spectra [IV, V], we describe the vibrational components by such a Poisson distribution using a value for S (S factor) determined by the intensity ratio between the $I(0-0)$ and $I(0-1)$ components. For the peaks attributed to vibrations it is assumed the same peak shape as the adiabatic.

Within the linear coupling model, the F-C factors for stretching modes can be expressed as function of the bond length change upon the core ionisation (Δr), reduced mass(μ) and vibrational frequency (ω) as: $S \propto \Delta r^2\mu\omega$ [62, 60]. As mentioned in chapter 3.2, the vibrational frequency depends on the reduced mass for the vibrating bond. The reduced mass relation between oscillators that involve deuterium instead of hydrogen is: $\mu_D \approx 2\mu_H$. Thus the vibrational frequencies and the F-C factors for hydrogen and deuterium are related by:

$$\omega_D \approx \frac{1}{\sqrt{2}}\omega_H \qquad \text{and} \qquad S_D \approx \sqrt{2}S_H \tag{6.5}$$

Knowing the moiety and the initial F-C factors it is therefore possible to predict the modification in the spectra induced by isotope substitutions. This procedure has been applied in [IV] to discern between chemical shifts and vibrations of the ethanol generated moieties on Rh(111), see Fig. 6.4.

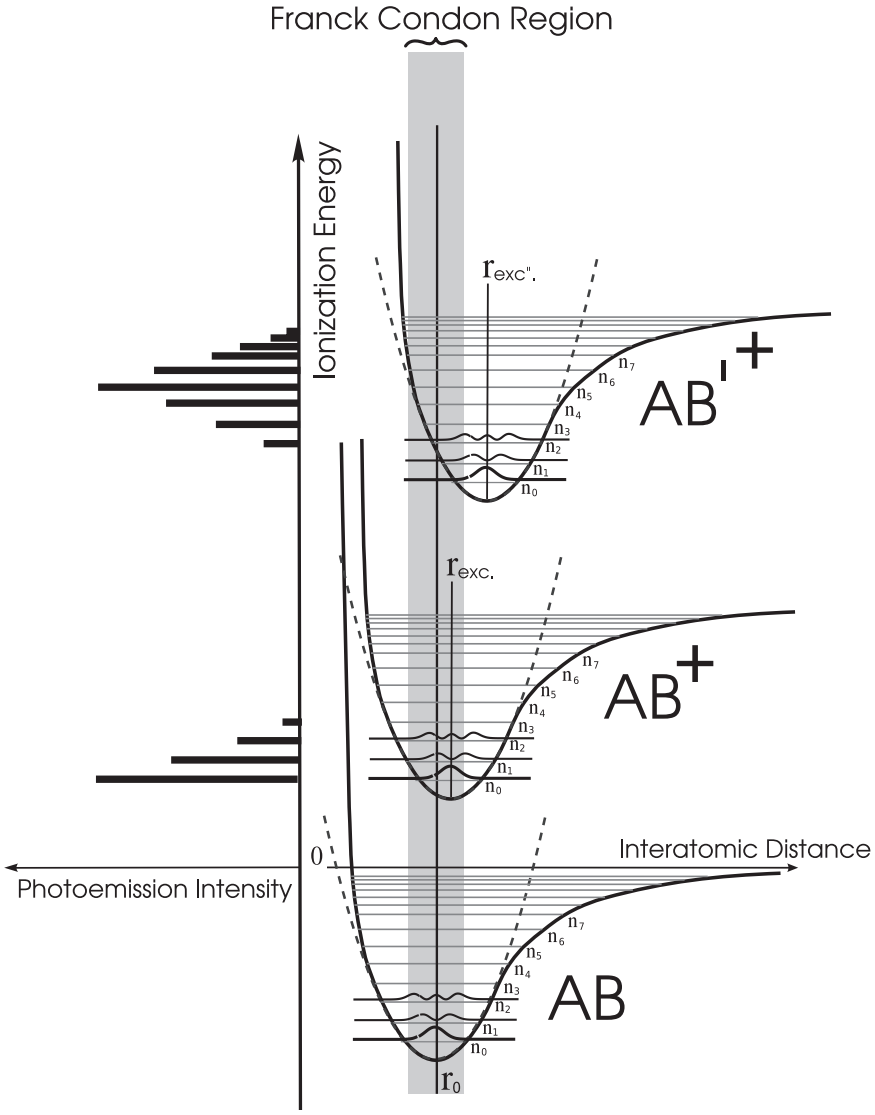

Figure 6.3: The transition between the initial state and one of the excited states can be described as a vertical transition. For molecule in the ground state is considered starting from the lowest vibrational state and therefore within the grey zone marked as Franck Condon Region. The potential in the excited state can have a different equilibrium distance between the nuclei compared to the ground state. Because the electronic transition is much faster than the nuclei relaxation the final nuclei state is the projection of the initial nuclei distribution on the vibrational levels of the final state.

6.4 Photolectron Diffraction

The emitted electron may be described as a wave originating from the excited atom. This wave expanding from its origin will be scattered by the neighbouring atoms, see Fig. 6.5 A. The elastically scattered wave will interfere with the directly emitted, see Fig. 6.5. In photoelectron diffraction there are two different ways to change the phase difference between the various scattering paths. One is collecting the photoemitted

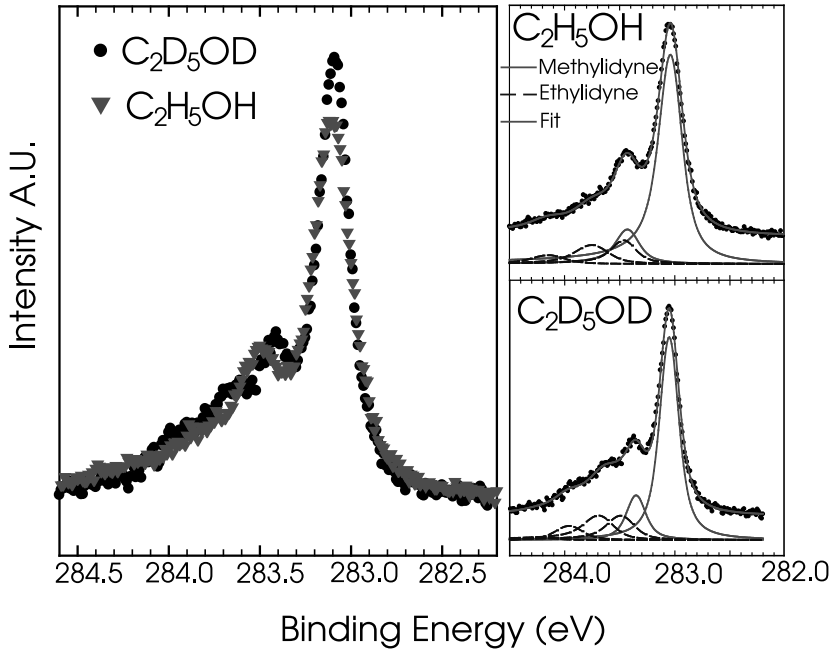

Figure 6.4: Comparison between the spectra of methylidyne (CH) and deuterated methylidyne (CD). In this specific experiment it was found that the vibrational frequency changes by a factor $\frac{\omega_H}{\omega_D} = 1.345$, while the S factor changes by: $\frac{S_D}{S_H} = 1.375$. Both changes agree with the model described in eq. 6.5.

electrons as function of their emission angle, the "angle" scanning mode. The second is collecting the photoelectrons along a fixed emission direction and changing the electron wavelength, the "energy" scanning mode [63, 64, 65]. The kinetic energy of the photoemitted electrons is scanned by using different photon energies for the excitation, see eq. (6.1). By changing the ratio between spectra components via the diffraction effect, one component or the other can be emphasised and better isolated and resolved. In Fig. 6.5 B as an example is reported the strong variations that diffraction effects can induce on the C1s ethylidyne spectra [66].

In the work performed here excitation energy changes were routinely used as a tool to emphasise the contrast between different chemical shifts and distinguish chemical shifts from vibrations. The ratio between the adiabatic peak and the vibrational peaks is constant versus the photon energy and depends only on the F-C factors while instead between different species the ratio is normally not constant but changes with the excitation energy, e.g. Fig. 6.5B.

The intensity as function of the photon energy depends on the local environment, therefore each species has its typical fingerprint. The energy scanning was the tool that in [IV, V] was used to recognise the characteristic ethylidyne fingerprint namely the variation of intensity ratio between outer and inner carbon versus excitation energy. Because of that fingerprint, the presence of ethylidyne on the surface could be confirmed.

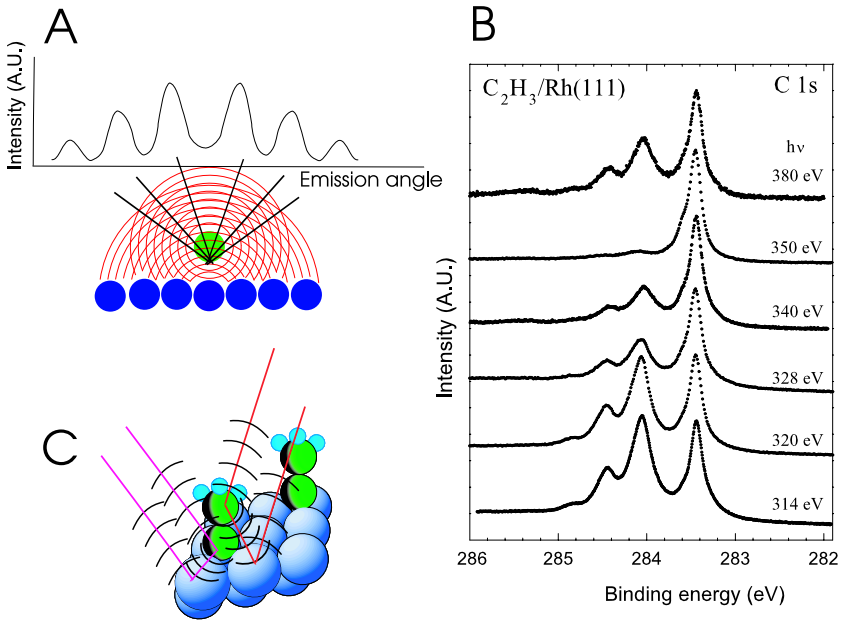

Figure 6.5: A) Cartoon description of the diffraction behaviour of an electron emitted from an adsorbate. B) The intensities from the ethylidyne moiety are strongly affected by the photon energy used for the excitation and can be associated to the CH_3 signals affected by photoelectron diffraction. The ratio between the two carbon signals versus the excitation energy generates a fingerprint specific for ethylidyne [66]. C) Cartoon of the diffracting ethylidyne moiety.

6.5 The Light Source

Historically X-ray radiation was first produced by colliding accelerated electrons with a metal target, X-ray tubes are based on this idea. Negative aspects for this device are the brilliance (photons s^{-1} mm^{-2} $mrad^{-2}$) which is in the order of 10^7 photons s^{-1} mm^{-2} $mrad^{-2}$ [67] and the discrete nature of the spectra, partially compensated by the low cost and small size of the device.

Higher brilliance, photon flux, and continuous nature of the emitted spectra are advantages achieved by making use of synchrotron radiation, nowadays normally obtained from electron storage rings. In a storage ring the electron beam is made to circulate in a closed orbit. The radial acceleration needed to keep the beam in the closed orbit is provided by magnetic elements named bending magnets. As the electrons are accelerated they emit electromagnetic radiation. The characteristics of the emitted radiation depends on the electron kinetic energy and on the magnetic field spatial distribution and intensity. The radiation is emitted in a narrow cone in the forward direction of the moving electrons and extracted in the proximity of the bending magnets. The resulting light has a continuous spectrum and is polarised in the plane of the ring. The energy range available from storage rings goes from Infra-Red to hard X-ray. Typical brilliance for a bending magnet source is five orders of magnitude higher than for an X-ray tube [67]. In addition, the

continuous spectrum of the synchrotron radiation gives large freedom in the photon energy choice for the experiments. Of course, the continuous spectrum requires a monochromator for experiments that require a mono-energetic photon beam.

To further improve the brilliance and the photon flux, dedicated magnetic structures are inserted in the straight sections of the storage rings: the insertion devices. Such insertion devices generally consist of periodic array of magnets designed to make the electrons oscillate around the straight path they would otherwise have followed. At each magnetic pole of the array the electrons make a small turn and therefore emit synchrotron radiation. Depending on the insertion devices used the brilliance increase two to six orders of magnitude from that of a bending magnets [67]. Also the radiation produced at insertion devices requires a monochromator for experiments with monochromatic light.

6.6 Beam Line I311

Beam line I311 is placed at the third-generation storage ring MAX II in which electrons are stored with a kinetic energy of 1.5 GeV. The beam line and end station were designed to achieve high energy resolution and high intensity in photoemission experiments from solids. The monochromator operates in the energy range between 30 to 1500 eV [68]. Typical working conditions at high photon flux allow 100 meV resolution at 400 eV photon energy.

The end station is composed of two chambers, one for sample treatment as cleaning, preparation and low energy electron diffraction (LEED) analysis and one dedicated to the photoemission analysis. An array of leak valves, each with its own gas reservoir, enables the introduction of accurate gas doses. The samples are held with tungsten wire and can be cooled to liquid nitrogen temperature and heated by running current through the wire and the sample itself. The temperature is measured by a thermocouple spot-welded directly on the sample.

The SCIENTA-SES200 electron energy analyser is the heart of this beam line. It is a hemispherical analyser, see Fig. 6.6, which is composed of two main parts, the electrostatic lens and the hemisphere for the energy analysis. The lens collects the electrons from the sample, focusing them at the slits just before the hemispheres. The lens is also responsible for retarding (accelerating) the electrons to the desired pass energy. The pass energy is the energy that will keep the electrons in the ideal path midway between the two charged hemispheres, see Fig. 6.6. The field present between the two hemispheres provides energy analysis of the electrons. The electrons with kinetic energy lower than the pass energy move towards the inner hemi-sphere while instead electron with higher energy will move towards the outer hemi-sphere. If the energy of the electrons is too different from the pass energy they will hit one of the hemispheres. The electrons that reach the end of the hemispheres are now dispersed in energy and ready to be collected, their shift from the central path is proportional to their energy difference from the pass energy. The electrons that pass through the hemispheres will impinge on the channelplate where the electrons are multiplied and then accelerated towards a phosphorus screen preserving the spatial distribution. The light emitted from the phosphorus screen is collected by a CCD

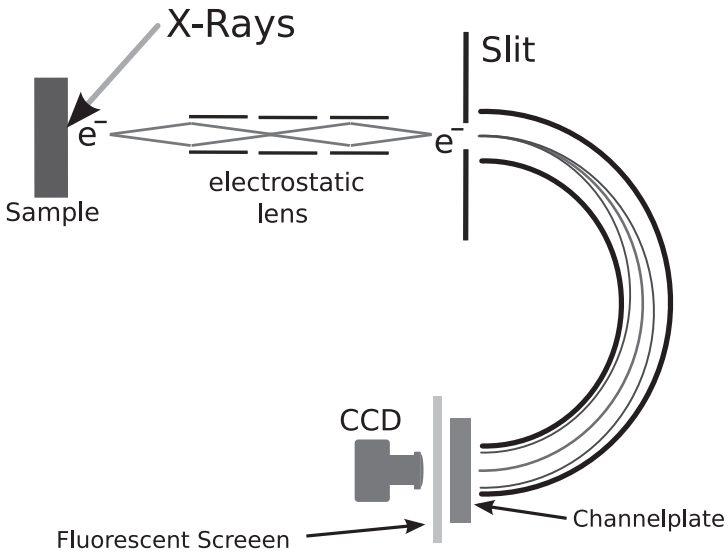

Figure 6.6: Schematic representation of a hemispherical electron analyser using a CCD based multichannel detector.

camera.

The energy range collected by the channelplate corresponds approximately to 10% of the pass energy. This energy window is divided into the number of channels present on the CCD chip of the TV camera. Each channel collects an electron intensity and is associated to a specific energy in the window.

Chapter 7

Other Techniques

The previous chapter describes the main techniques used, however it is not the only one adopted. To confirm some of the conclusions made from the HRCLS experiments, Reflection Absorption InfraRed Spectroscopy (RAIRS) was also used. Low Energy Electron Diffraction (LEED) and Scanning Tunnelling Microscopy supplied surface structural information complementary to the two spectroscopy techniques.

7.1 Infrared Spectroscopy

Infrared spectroscopy (IR Spectroscopy) uses electromagnetic radiation in the spectral region between microwave and visible light. Conventionally in this field the unit of measure for the photon energy is the wavenumber $[cm^{-1}]$, the conversion factor between $[cm^{-1}]$ and eV is 8065.5 $[cm^{-1}/eV]$. The infra red region is divided into three regions: far infrared (400-10 cm^{-1}), the mid infrared (4000-400 cm^{-1}) and the near infrared (14000-4000 cm^{-1}). An infrared spectrum shows the sample absorption as function of the wavenumber, the absorption is expressed as absorbance or transmittance. The transmittance is defined as the ratio between the radiation intensity transmitted through the instrument with the sample (I) and without the sample (I_0), the absorbance is the negative logarithm of the transmittance:

$$Transmittance = I/I_0 \qquad Absorbance = -\log(I/I_0) \tag{7.1}$$

Infrared spectroscopy is widely used in organic chemistry to identify compounds. Nowadays it finds application also in surface science to probe adsorbed molecules. In this text only the mid infrared region is taken in consideration. The photon energy in the mid infrared is between 0.5 eV and 0.05 eV. In this energy interval the electric field of the radiation interacts with the molecule exciting vibrational modes.

The vibrational energy level spacing depends on the potential where the atoms move, as was shortly presented in paragraph 3.2. In the case of organic molecules, the vibrational modes can be summarised as: symmetric stretching, asymmetric stretching, scissoring, rocking, wagging and twisting, see Fig. 7.1. Each organic group is characterised by a different set of atoms and bonds (see Table 3.1), which is reflected in different resonance frequencies in the infrared region. According to this, it is possible to assign a general absorption region for the different groups and

their modes. The frequency ranges for stretching modes of some organic groups are shown in Fig. 7.1 [13]

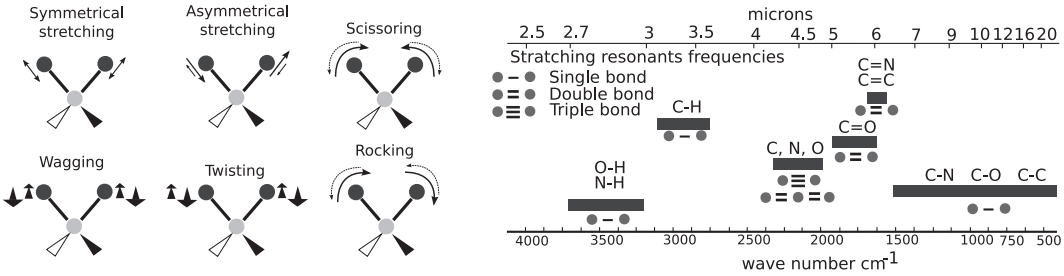

Figure 7.1: Vibrational modes for ligands on an sp_3 hybridised carbon atom and vibrational frequency region for the stretching of some organic groups.

The vibrational selection rules for Infra-Red can be summarised by one gross selection rule: the molecular dipole must change during the transition [16]. The Infra Red measurements performed during this experimental work were performed in Reflection Absorption Infra Red Spectroscopy (RAIRS) geometry, see Fig. 7.2. The infrared radiation is made to impinge with grazing angle on the sample surface and the reflected beam is collected by the detector [69].

The RAIRS geometry applied to metals influences the selection rule just mentioned. The radiation electric field component parallel to the surface is mirrored by the free electrons present in the metal, nullifying the electric field parallel to the surface. This component (S-polarised) therefore does not generate an effective field on metallic surfaces. The component orthogonal to the surface (P-polarised) is able to generate an electric field on the surface, see Fig. 7.2. Since the dipole transition is parallel to the electric field only adsorbates with a dipole component orthogonal to the surface can be excited [70]. Therefore by working at grazing angle the p-polarised component is preserved and the sensitivity increased [69, 70].

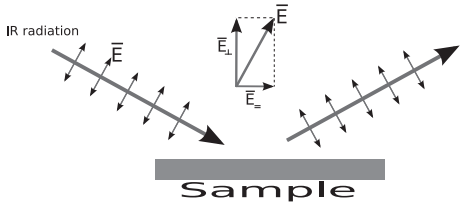

Figure 7.2: RAIRS geometrical configuration for incoming IR radiation and reflected beam at the sample. The electric field is decomposed in the components parallel and orthogonal to the sample surface.

7.2 Scanning Tunnelling Microscopy

Scanning tunnelling microscopy was invented in 1982 by Gerd Binnig and Heinrich Rohrer at the IBM Zürich laboratory and it won them the Physics Nobel prize in

1986 [71]. The technique is based on electrons tunnelling through a barrier and on the tunnelling probability dependence from the barrier thickness. The idea exploited start with a sharp metal tip brought close to the surface until it is possible to have tunnelling current through the gap separating tip and surface. By applying a bias between tip and surface the tunnelling current is driven through the gap and its intensity depends exponentially on the tip surface distance S: $I \propto e^{-A\Psi^{\frac{1}{2}}S}$ where A is a constant depending on electron mass and Planck constant, Ψ is the barrier height. The images are obtained by mapping the tunnelling current over the sample surface, the tip probe point by point all the area of interest. It is possible to obtain these images with sufficiently good resolution to have atomically resolved images of surface structures. There are two main image recording modes: constant current and constant height.

In the constant current mode the microscope user sets sample-tip bias and tunnelling current. Then for each point probed by the tip the electronics will adapt the tip height to obtain the set point current. The image is composed of the tip height versus the x-y array of surface points probed.

In the constant height imaging mode the microscope user sets sample-tip bias and tip height. Then the tip scans the desired area while recording the current intensity. The image now is composed of the tunnelling current versus the x-y array of surface point probed.

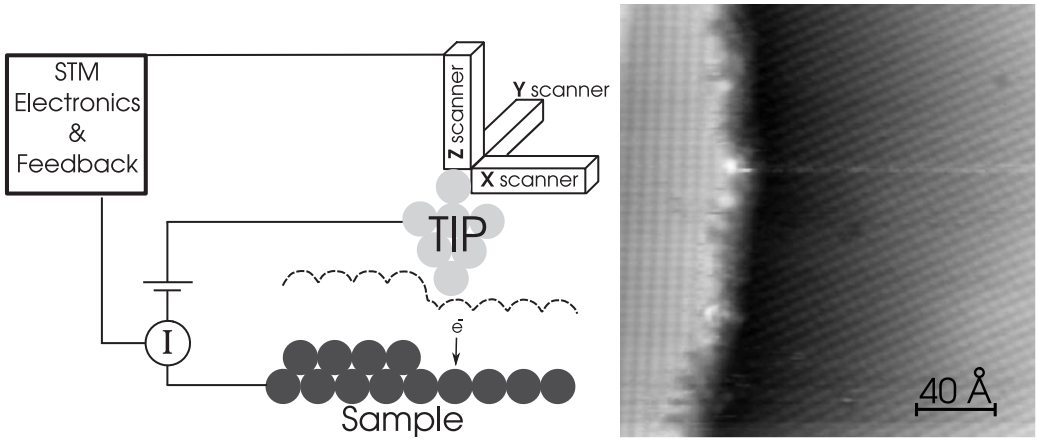

Figure 7.3: Schematic representation of the STM operation. Room temperature STM image of a adsorbate Rh(111)(4×2) structure.

The tunnelling resistance is proportional to the local density of states in the proximity of the Fermi level belonging to the surface at the tip position [72]. Thus STM experiments are a map of the overlap between the surface density of states and the tip density of states. This might not strictly agree with the sample morphology.

The bias direction influences the imaging results: when the electrons are flowing from the tip to sample one probes the overlap between the tip occupied states and the sample empty states. By reversing the bias the electrons will now flow from the sample to the tip and the image is now given by the overlap between the occupied states of the sample and the empty states of the tip.

7.3 Low Energy Electron Diffraction

Low Energy Electron Diffraction (LEED) has been used during this work to obtain qualitative information on the surface morphology and adsorbate lattice. This technique is based on the de Broglie wavelength of electrons that are impinging on the sample surface, the electron waves are then scattered from the sample and recorded. The electron energy is typically in the order of 100 eV. Because the electron mean free path in solids is limited to a few Ångström for these energies the backscattered electrons come only from a few surface layers, making LEED a surface sensitive technique.

The spatial distribution of elastically scattered electrons contains information on the substrate and adsorbate lattice, this was clear since the early experiments [73]. Because the sample information is contained in the electron angular distribution the instrument is constructed to preserve the trajectories of the scattered electrons.

The incident electron beam is directed onto the sample surface. The sample is in the center of the hemisphere so that all the back-diffracted electrons travel towards the LEED optics on radial trajectories. Before the electrons reach the screen they must pass through a retarding field energy analyser. Such an analyser is typically composed of 4 grids, see Fig. 7.4, the fist grid is grounded together with the sample providing a field free region to the travelling electrons. Grids two and three are the retarding grids, they filter away all electrons with kinetic energy below a certain threshold. Grid four mainly shields the field of the screen which is in the order of a few kV to make the diffracted spot visible [70].

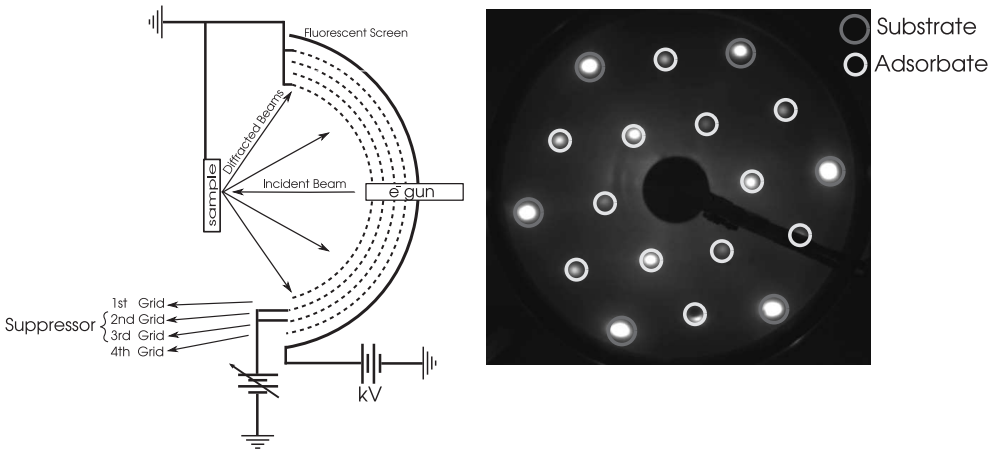

Figure 7.4: Instruments schematic of a four-grids LEED display system, image collected at 57 eV electron kinetic energy at room temperature from a Rh(111) surface exhibiting a (2×2) structure.

Because the electrons do not penetrate into the bulk and fully experience the three dimensional periodicity, the diffraction pattern is determined by the surface two dimensional periodicity. The diffraction condition is $\overline{R}\Delta\overline{k} = 2\pi n$, which leads to that the $\Delta\overline{k}$ component parallel to the surface must be equal to a reciprocal lattice vector $\Delta\overline{k_{\shortparallel}} = \overline{G}$ [10, 74]. Thus the LEED image provides information on the two

dimensional reciprocal space and because of the relation between real and reciprocal space it is possible to have information on the sample surface.

The LEED spot size and the intensity of the diffuse background give information on the state of the surface. An ideal instrument measuring an ideal sample will produce infinitely sharp spots, however in a real experiment the spots are broadened. The surface often contains different domain orientations and sizes, ordered and disordered areas. All forms of disorder or inhomogeneity are generally not directly visible but contribute to the spot broadening and to the background. Further broadening is induced by the thermal vibrations. In Fig. 2.4 as example is shown the LEED image of a Rh(111)(2×2) structure.

Chapter 8

Summary of Papers

Paper I

CO - hydrogen coadsorption on stepped Rh surfaces with A and B type facets.

In the present work we study the influence of co-adsorbed hydrogen on the adsorption of CO at the steps of two vicinal Rh surfaces; Rh(553) which has (111)-type micro-facets at the steps and Rh(322) which has (100)-type facets. These stepped surfaces are used to mimic the behavior of small particles.

We use a combination of experimental high resolution core level spectroscopy (HRCLS) and theoretical modeling based on density functional theory (DFT). With this combination of techniques it was possible to determine the adsorption dynamics of the system. On Rh(553), with (111)-type micro-facets at the steps, CO is found to occupy atop sites at the steps for pure low coverage CO overlayers. Low coverages of H are found to induce a site change from atop to bridge at the steps whereas high H-coverage is found to force the CO away from the steps and into atop terrace sites. For Rh(322), with (100)-type micro-facets at the steps, CO is found to occupy atop and bridge sites at the steps for pure low coverage CO overlayers. At both low and high H-coverages, CO remains at the steps but now exclusively in bridge sites.

Paper II

Mechanism of CO oxidation on O-covered Pd(111) surfaces studied with fast x-ray photoelectron spectroscopy: Change of reaction path accompanying phase transition of O domains.

In paper II, the oxidation of CO on an oxygen pre-covered Pd(111) surface has been investigated by HRCLS. The $p(2 \times 2)$ formed by the initial oxygen adsorption is found to be compressed first into a $\sqrt{3} \times \sqrt{3}R30^\circ$ and further into a $p(2 \times 1)$ by adding CO. The $p(2\times2)$ phase is not a reactive phase for CO oxidation while the two compressed phases are. The experiments were performed at a constant temperature and CO pressure. Above 200 K the reduction of the $\sqrt{3} \times \sqrt{3}R30^\circ$ phase is faster than the $p(2 \times 1)$ formation. By monitoring the atomic oxygen and the CO signals as a function of time, but at different temperatures, the order of the reaction and the

activation energies for the reactions could be estimated. It could be shown that the reaction between CO-oxidation has different reaction orders and activation energies for the two compressed phases.

Paper III

Acetate formation during the ethanol oxidation on Rh(111).

In this paper the co-adsorption of oxygen and ethanol at room temperature on Rh(111) has been studied with the intent to determine some of the intermediates in the ethanol oxidation process. The techniques used were HRCLS and RAIRS. The RAIRS experiments were accompanied by cluster calculations of the expected vibrational frequencies. In the first part of the paper, room temperature ethanol adsorption on the clean Rh(111) surface is studied in order to provide necessary background information on the adsorption system. Ethanol was found to dissociate when adsorbed at room temperature and by comparing the C1s and O1s binding energies to literature data, some of the dissociation products could be identified, such as CO. In particular, the formation of atomic oxygen as a dissociation product could be excluded. From these observations it was concluded that the Rh(111) surface rather breaks the C-C than the C-O bond of the ethanol molecule.

In the second part of the paper, the effect of co-adsorbed oxygen is investigated. Particular attention is paid to the identification of the molecular fragment responsible for a new and narrow C1s peak at 286.8 eV observed when ethanol and oxygen are co-adsorbed on Rh(111). It is found that this C1s component is always accompanied by another broad C1s component at about 284 eV binding energy. The approximately 1:1 C1s intensity ratio found for all preparations suggests that these two C1s signals derive from a single, intermediate fragment. The 286.8 eV binding energy implies that the intermediate contains a carbon atom that bonds to more than one oxygen atom. The binding energy of 284 eV is in the range expected for a hydrocarbon group, furthermore the 284 eV emission can be fitted with the C-H vibrational progression expected for a methyl group. Combining this information leads to acetate ($CH_3COO-Rh$). The presence of acetate was confirmed by RAIRS detection of the molecular vibrational modes by comparing to literature values from acetate on Cu. We therefore conclude that acetate is an important intermediate in the oxidation of ethanol on the Rh(111) surface.

Paper IV

Step induced efficient dehydrogenation of ethanol on Rh.

We have investigated the decomposition of ethanol on the Rh(111) and Rh(553) surfaces at room temperature using high resolution core level spectroscopy and density functional theory (DFT) based simulations. A detailed analysis of the C1s core level spectra, including analysis of the vibrational fine-structure and comparison to calculated C1s binding energy shifts, shows that the ethanol decomposes into CO, ethylidyne (C_2H_3), methylidyne (CH), atomic carbon (C) and hydrogen.

Both surfaces were found to predominantly dissociate the carbon-carbon bond and preserve the carbon-oxygen bond leading to adsorbed CO but no adsorbed atomic O. In addition to CO, also significant amounts of methylidyne and ethylidyne are formed on Rh(111). On Rh(553), the dominant surface species in addition to CO was shown to be atomic C adsorbed in the hcp sites on the lower side of the steps. In agreement with the experimental results, DFT-based simulations demonstrated that the activation barrier for CH dissociation was lower for Rh(553) than for Rh(111) and furthermore that the CH dissociation changes from endothermic on Rh(111) to exothermic on Rh(553).

It is therefore clear that a different dissociation pathway is induced by the presence of the steps on the Rh(553) surface. In particular, the atomic carbon produced by the Rh(553) surface suggests a higher dehydrogenation yield (or higher hydrogen production) of the hydrocarbons than on the Rh(111) surface.

Paper V

Step dependent hydrocarbon decomposition.

Here we study the influence of steps with different structural arrangements on the dissociation of a hydrocarbon molecule, specifically we have studied the adsorption and dissociation of ethylene on Rh(111), Rh(322) (A-step), and Rh(553) (B-step). Ethylene decomposes into ethylidyne, which subsequently decomposes into methylidyne, and atomic C at increasing temperatures. This study not only shows that the dissociation process is enhanced by the steps, but it also indicates that the different geometries exposed by the A and B-steps lead to decomposition differences.

The A-step promotes ethylidyne decomposition at low temperatures (low activation energy), but the resulting dissociation products adsorb strongly at the steps, preventing further decomposition. On the B-steps, the dissociation temperature is slightly higher (higher activation energy), but the products do not block the active sites. This results in the Rh(553) being more effective than the Rh(322) for ethylidyne decomposition.

Paper VI

Kinetics of the reduction of the Rh(111) surface oxide: Linking spectroscopy and atomic-scale information

The reduction of the (9x9) tri-layer surface oxide on Rh(111) by H_2 was studied by in-situ STM and in-situ fast HRCLS. At room temperature, H_2 does not adsorb on the oxide. However, the (9x9) can still be reduced, the reduction starting at defects in the oxide. The reaction can deliberately be started by creating a defect using the STM tip, which allows for detailed studies of the reduction kinetics. Two different reduction regimes depending of the size of the reduced area can be observed.

During the early phase of the oxide reduction the reaction is limited by hydrogen adsorption on the already reduced area. This leads to an exponential growth of the reduced area with time. At a later reduction stage, the processes at the border of the reduced area limit the reduction speed resulting in a constant speed of the

reaction front. Because of the random distribution of the reaction nuclei, the oxide defects, it is possible to use the JMAK theory [75] to describe the reduction process. The microscopic and local information from STM measurements agrees with the spatially averaged data as obtained by in-situ fast HRCL spectroscopy.

Paper VII

The surface oxide as a source of oxygen on Rh(111)

This paper reports on the reduction of the (2×1) chemisorbed oxygen structure and the (9x9) tri-layer surface oxide on Rh(111) by CO.

For the (2×1) oxygen structure the coverage of atomic surface oxygen rapidly decreases as CO is introduced in the experimental chamber. As the atomic oxygen is consumed, CO starts to adsorb on the surface. The surface oxide exhibits a different behaviour. It is shown, within the limits of detection of HRCLS, that CO does not adsorb on the (9x9) even at liquid nitrogen temperatures. However, the (9x9) can readily be reduced. At the beginning, the reduction process is very slow, but after an incubation period its speed increases drastically. Simultaneously with the speed increase, signals corresponding to the binding energy of atomic oxygen and CO can be detected.

The initial slow start of the reduction is due to the fact that the reduction starts at defects, as shown by STM. The reduction itself creates more defects which increases the speed of the reduction. Further, under the experimental (UHV) conditions the (9x9) surface oxide is not thermodynamically stable resulting in an oxygen transport to the already reduced areas in the vicinity of the surface oxide. Here, the reaction proceeds similarly to the (2×1) case.

Bibliography

[1] H. S. Taylor, Proc. R. Soc. (London) A **108**, 105 (1925).

[2] G. A. Somorjai, R. L. York, D. Butcher, and J. Y. Park, Phys. Chem. Chem. Phys. **9**, 3500 (2007).

[3] G. A. Deluga, J. R. Salge, L. D. Schmidt, and X. E. Verykios, Science **303**, 993 (2004).

[4] H. Conyers, Phys. Rev. **82**, 87 (1951).

[5] K. Reuter and M. Scheffler, Phys. Rev. B **65**, 035406 (2002).

[6] J. Gustafson, A. Resta, A. Mikkelsen, R. Westerström, J. N. Andersen, E. Lundgren, J. Weissenrieder, M. Schmid, P. Varga, N. Kasper, X. Torrelles, and S. Ferrer, Phys. Rev. B **74**, 035401 (2006).

[7] A. Bradshaw and N. Richardson, Pure & App. Chem **68**, 457 (1996).

[8] E. A. Wood, J. App. Phys. **35**, 1306 (1964).

[9] R. Haydock, V. Heine, M. J. Kelly, and J. B. Pendry, Phys. Rev. Lett. **29**, 868 (1972).

[10] N. W. Ashcroft and N. D. Mermin, *Solid State Physics* (Thomson Learning, Berkshire House 168-173 High Holborn London WC1 V7AA United Kingdom, ISBN: 0-03-083993-9, 1976).

[11] M. Desjonquéres and F. Cyrot-Lackmann, Surf. Sci. **53**, 429 (1975).

[12] W. F. Egelhoff, Surf. Sci. Rep. **6**, 253 (1986).

[13] R. J. Fessenden and J. S. Fessenden, *Organic Chemistry* (Brooks/Cole Pub Co, ISBN: 0534351999, 1998).

[14] P. W. Atkins and R. S. Friedman, *Molecular Quantum Mechanics* (Oxford university press, ISBN: 019855947, 2001).

[15] S. Gasiorowicz, *Quantum Physics* (John Wiley & Sons, Inc, ISBN: 0471857378, 1995).

[16] P. W. Atkins, *Physical Chemistry* (Oxford University Press, ISBN: 0198501021, 2001).

[17] A. P. Sutton, *Electronic Structure of Materials* (Oxford University Press, ISBN: 0198517548, 1993/4).

[18] A. Groß, *Theoretical Surface Science* (Springer-Verlag Berlin Heidelberg New York, ISBN: 3-540-43903-X, 2003).

[19] G. Attard and C. Barnes, *Surfaces* (Oxford university press, ISBN: 0198556861, 1998).

[20] A. Groß, Surf. Sci. Rep. **32**, 291 (1998).

[21] C. Stampfl, M. V. Ganduglia-Pirovano, K. Reuter, and M. Scheffler, Surf. Sci. **500**, 368 (2002).

[22] B. Hammer and J. K. Nørskov, Surf. Sci **343**, 211 (1995).

[23] B. I. Lundqvist, O. Gunnarsson, H. Hjelmberg, and J. K. Nørskov, Surf. Sci. **89**, 196 (1979).

[24] B. Hammer and J. K. Nørskov, Nature **376**, 238 (1995).

[25] A. Nilsson, L. G. M. Pettersson, B. Hammer, T. Bligaard, C. H. Christensen, and J. K. Nørskov, Cat. Lett. **100**, 111 (2005).

[26] B. Hammer, Y. Morikawa, and J. K. Nørskov, Phys. Rev. Lett **76**, 2141 (1996).

[27] J. V. Barth, Surf. Sci. Rep. **40**, 75 (2000).

[28] R. L. Schwoebel and E. J. Shipsey, J. App. Phys. **37**, 3682 (1966).

[29] J. Merikoski and S. C. Ying, Phys. Rev. B **56**, 2166 (1997).

[30] J. Ma, L. Cai, X. Xiao, and M. M. T. Loy, Surf. Sci. **425**, 131 (1999).

[31] K. Kyuno and G. Ehrlich, Surf. Sci **383**, L766 (1997).

[32] IUPAC Compendium of Chemical Terminology, 2nd edition 1997.

[33] H. Over, Prog. Surf. Sci. **58**, 249 (1998).

[34] F. Zaera, Prog. Surf. Sci. **69**, 1 (2001).

[35] R. J. Baxter and P. Hu, J. Chem. Phys. **116**, 4379 (2002).

[36] D. Eley and E. Rideal, Nature **146**, 401 (1946).

[37] C. T. Rettner, Phys. Rev. Lett. **69**, 383 (1992).

[38] C. Doornkamp and V. Ponec, J. Mol. Cat. A **162**, 19 (2000).

[39] P. Mars and D. W. Van Krevelen, Chem. Eng. Sci. Spec. Suppl. **3**, 41 (1954).

[40] H. Over, Y. D. Kim, A. P. Seitsonen, S. Wendt, E. Lundgren, M. Schmid, P. Varga, A. Morgante, and G. Ertl, Science **287**, 1474 (2000).

[41] R. A. Olsen, D. A. McCormack, and E. J. Baerends, Surf. Sci. **571**, L325 (2004).

[42] K. Christmann and G. Ertl, Surf. Sci. **60**, 365 (1976).

[43] P. Gambarella, *Ž. Šljivančanin*, B. Hammer, M. Blanc, K. Kuhnke, and K. Kern, Phys. Rev. Lett. **87**, 056103 (2001).

[44] S. Dahl, A. Logadottir, R. C. Egeberg, J. H. Larsen, I. Chorkendorff, E. Törnqvist, and J. K. Nørskov, Phys. Rev. Lett. **83**, 1814 (1999).

[45] B. Hammer, Phys. Rev. Lett. **83**, 3681 (1999).

[46] H. R. Claude, Surf. Sci. Rep. **31**, 231 (1998).

[47] Y. W. Tsang and L. M. Falicov, J. Phys. C **9**, 51 (1976).

[48] B. Hammer, O. H. Nielsen, and J. K. Nørskov, Cat. Lett. **46**, 31 (1997).

[49] M. P. Seah and W. A. Dench, Surf. Interface Anal. **1**, 2 (1979).

[50] A. Jablonski and C. J. Powell, Surf. Sci. Rep. **47**, 33 (2002).

[51] A. Zangwill, *Physics at Surfaces* (Cambridge Univ. Press, Cambridge, ISBN: 0 521 32147 6, 1998).

[52] A. C. Thompson, D. T. Attwood, E. M. Gullikson, M. R. Howells, J. B. Kortright, A. L. Robinson, J. H. Underwood, K. Kwang-Je, J. Kirz, I. Lindau, P. Pianetta, H. Winick, G. P. Williams, J. H. Scofield, A. C. Thompson, and D. Vaughan, *X-ray Data Booklet* (Lawrence Berkeley National Laboratory University of California Berkeley California 94720, University of California Berkeley California 94720, 2001).

[53] D. Tran Minh, C. Guillot, Y. Lassailly, J. Lecante, Y. Jugnet, and J. C. Vedrine, Phys. Rev. Lett. **43**, 789 (1979).

[54] J. Gustafson, A. Mikkelsen, M. Borg, E. Lundgren, L. Köhler, G. Kresse, M. Shmid, P. Varga, J. Yuhara, X. Torrelles, C. Quirós, and J. N. Andersen, Phys. Rev. Lett. **92**, 126102 (2004).

[55] J. N. Andersen and C.-O. Almbladh, J. Phys.: Condens. Matter **13**, 11267 (2001).

[56] P. H. Citrin, G. K. Wertheim, and Y. Baer, Phys. Rev. B **16**, 4256 (1977).

[57] S. Doniach and M. *Šunjić*, J. Phys. C **3**, 285 (1970).

[58] J. M. Hollas, *Modern Spectroscopy* (John Wiley & Sons, Ltd, ISBN 0 470 84416 7, 2004).

[59] L. S. Cederbaum and W. Domcke, J. Chem. Phys. **64**, 603 (1976).

[60] W. Domcke, L. S. Cederbaum, H. Köppel, and W. Niessen von, Mol. Phys **34**, 1759 (1977).

[61] S. J. Osborne, S. Sundin, A. Ausmees, S. Svensson, L. J. Sæthre, O. Sværen, S. L. Sorensen, J. Végh, J. Karvonen, S. Aksela, and A. Kikas, J. Chem. Phys. **106**, 1661 (1997).

[62] L. J. Sæthre, O. Sværen, S. Svensson, S. Osborne, T. D. Thomas, J. Jauhiainen, and S. Aksela, Phys. Rev. A **55**, 2748 (1997).

[63] S. D. Kevan, D. H. Rosenblatt, D. Denley, B.-C. Lu, and D. A. Shirley, Phys. Rev. Lett. **41**, 1565 (1978).

[64] D. P. Woodruff, D. Norman, B. W. Holland, N. V. Smith, H. H. Farrel, and M. M. Traum, Phys. Rev. Lett. **41**, 1130 (1978).

[65] C. Westphal, Surf. Sci. Rep. **50**, 1 (2003).

[66] M. Wiklund, A. Beutler, R. Nyholm, and J. N. Andersen, Surf. Sci. **461**, 107 (2000).

[67] D. E. Moncton, in *: TOWARD A FOURTH-GENERATION X-RAY SOURCE*, Argonne National Laboratory, Argonne, IL 60439 U.S.A. (XIX International Linear Accelerator Conference, Chicago, Illinois, USA, 1998).

[68] R. Nyholm, J. N. Andersen, U. Johansson, B. N. Jensen, and I. Lindau, Nucl. Instrum. Methods Phys. Res., Sect. A **467-468**, 520 (2001).

[69] Y. Chabal, Surf. Sci. Rep. **8**, 211 (1988).

[70] H. Burbert and H. Janett, *Surface and Solid Thin Film Analysis: Principles, Instrumentation, Application.* (Wiley Interscience Pubblication, ISBN: 3527304584, 2002).

[71] G. Binning, H. Roher, C. Gerber, and E. Weibel, Phys. Rev. Lett. **49**, 57 (1982).

[72] J. Tersoff and D. R. Hamann, Phys. Rev. B **31**, 805 (1985).

[73] C. Davisson and L. H. Germer, Phys. Rev. **30**, 705 (1927).

[74] C. Kittel, *Introduction to Solid State Physics* (John Wiley & Sons, ISBN 0-471-11181-3, 1996).

[75] M. Fanfoni and M. Tomellini, Il Nuovo Cimento **20**, 1171 (1998).

I

Paper I

CO - hydrogen coadsorption on stepped Rh surfaces with A and B type facets

Jesper N Andersen, Andrea Resta, Edvin Lundgren, Anders Mikkelsen, Johan Gustafson, Ming-Mei Yang, Wei-Xue Li, Jianguo Wang and Bjørk Hammer.

In manuscript

CO - hydrogen coadsorption on stepped Rh surfaces with A and B type facets

Jesper N Andersen, Andrea Resta, Edvin Lundgren, and Johan Gustafson

Department of Synchrotron Radiation Research, Institute of Physics, Lund University, Box 118, S-22100 Lund, Sweden

Xiu-Fang Ma and Wei-Xue Li

Center for Theoretical and Computational Chemistry, Dalian Institute of Chemical Physics, Chinese Academy of Sciences, 457 Zhongshan Road, Dalian 116023, China

Jianguo Wang and Bjørk Hammer

Department of Physics and Astronomy and Interdisciplinary Nano Science Center (iNANO), University of Aarhus, Building 1520, Ny Munkegade, 8000 Aarhus C, Denmark

Abstract

A combination of high resolution core level spectroscopy and density functional theory based simulations is used to investigate low coverages of CO and CO-H mixtures on two stepped Rh surfaces. On Rh(553), with 111-type microfacets at the steps, CO is found to occupy atop sites at the steps for pure low coverage CO overlayers. Low coverages of H are found to induce a site change at the steps from atop to bridge whereas high H-coverage is found to force the CO away from the steps and into atop terrace sites. For Rh(322), with 100-type microfacets at the steps, CO is found to occupy atop and bridge sites at the steps for pure low coverage CO overlayers. At both low and high H-coverages CO remains at the steps but now exclusively in bridge sites.

Introduction

Surface mediated catalytic processes often involve a reaction between several different adsorbed molecules/atoms where the detailed spatial distribution of these reactants on the surface may strongly influence the reaction. In many cases this spatial distribution differs between the co-adsorbed system and the adsorption systems of the individual reactants, e.g., the adsorption sites may differ between the co-adsorbed and the separate adsorption systems or phase separation may occur. In the case of an inhomogeneous surface, this may lead to a complicated situation as the co-adsorption behavior may differ amongst the various parts of the surface leading to spatial variations in the reactant distribution on the same length scale as that of the inhomogeneities. For instance, the reactant distribution in the vicinity of the edges and corners of a small particle may differ from that on the facets of the particle which, as these parts of the particle often have quite different reactivity, may strongly influence the total reaction.

In the present work we study the influence of co-adsorbed hydrogen on the adsorption of CO at the steps of two vicinal Rh surfaces, Rh(553) which has (111)-type micro-facets at the steps and Rh(322) which has (100)-type facets. These stepped surfaces are used to mimic the behavior of small particles with the step atoms taking the role of the particle's under-coordinated edge and corner atoms and the terraces that of the flat facets of the particle. We use a combination of experimental high resolution core level spectroscopy (HRCLS) and theoretical modeling based on density functional theory (DFT). By this combination of experiment and theoretical simulations we can study how CO adsorption at the steps is influenced by co-adsorbed hydrogen and demonstrate that this influence depends both on which micro-facet is present as well as on the hydrogen coverage.

Experimental and calculational

The measurements were performed at beam line I311 [1] at the synchrotron radiation source MAX II in Lund, Sweden. The Rh(553) and Rh(322) surfaces were cleaned by a combination of Ar^+ sputtering and annealing in O_2 and in vacuum. The surface cleanness was checked by HRCLS and the long range order by low energy electron diffraction (LEED) which showed the typical spot-splitting characteristic of these vicinal surfaces. The temperature was measured by Chromel-Alumel thermocouples spotwelded to the crystals. Typically CO was dosed at 273K and H_2 at 100K. Exposures are given in Langmuir (L) (1 L =10^{-6} torr sec) based on the gauge reading. The HRCL spectra were recorded at normal emission and at liquid nitrogen temperatures in order to reduce thermal broadenings. The spectra were decomposed using Doniach-Šunjić line shapes [2] convoluted with Gaussian functions that represent unresolved vibrations and the experimental broadening. A linear background was included in the fits.

For the slab-based modeling we used DFT as implemented in the DACAPO package [3] using ultrasoft pseudopotentials [4] for description of the ion-cores. For the core ionized C atoms, we used a pseudopotential constructed for a C atom where a 1s electron had been promoted to a 2p valence level [5,6]. The one-electron wave functions were expanded in a plane wave basis with an energy cutoff of 340 eV. We used the Generalized Gradient Approximation (GGA) as implemented in the revised Perdew, Burke, Ernzerhof (RPBE) form [7]. For the initial survey we used slabs

containing three (111) Rh layers and allowed the first two of these as well as the adsorbates to relax geometrically. For subsequent refinement of interesting structures we used five layers slabs. The slabs were separated by vacuum of thickness equivalent to eight (111) Rh layers. Sampling of k-space was done using a (4x2x1) mesh for the (2x1) unit cells typically used. Finally, the C1s core level binding energy shifts were calculated as total energy differences between systems where the appropriate C-atoms had been core-ionized.

Results and discussion

In Fig. 1 we show C1s spectra measured after 0.2L CO exposures of the Rh(553) and Rh(322) surfaces at a temperature of 273K, after these CO overlayers have been exposed to 5L of H_2 at 100K, and finally after these CO-hydrogen co-adsorbed surfaces have been flashed at 400K.

Starting with the CO-only dosed Rh(553) surface, we find two C1s components at binding energies of ~286.05 eV and ~285.7 eV, respectively. By comparison to Rh(111) [8], the component at 286.05 eV can directly be identified as due to CO in atop-positions on the 111 terraces of the Rh(553) surface. The C1s component at ~285.7 eV, however, has no counterpart on the Rh(111) surface. By analogy with C1s spectra from CO on a number of stepped Pt surfaces [6,9] this component is suggested to be due to CO molecules adsorbed atop Rh step atoms. This suggestion is confirmed by direct calculations of site resolved adsorption energies and C1s binding energy shifts in a similar fashion as in [6]. The calculational results show the atop at the step site to be the preferred site and that a CO molecule in this site has a C1s binding energy which is 0.43 eV lower than a CO in an atop site on the terrace in agreement with the experimental results. Using the atop CO intensity from the Rh(111)-(2x2)-3CO structure as reference we estimate a total CO coverage of ~0.05 monolayer (ML, 1ML equals the number of Rh surface atoms) for the situation in Fig.1.

Turning now to the CO-only dosed Rh(322) surface, we may directly identify the C1s component at ~285.7 eV as due to CO in atop-step sites. This assignment is confirmed by DFT calculations which also for this surface find the atop-step site as the most favorable CO adsorption site and a C1s shift (relative to the atop-terrace site) of -0.41 eV in good agreement with the experimental value of -0.33 eV. The Rh(322) C1s spectra also contain a component at a binding energy of 285.35 eV characteristic [8] of CO adsorbed in three-fold-hollow sites on Rh(111). From the coinciding binding energies, it would seem straightforward to assign this component to CO in three-fold-hollow sites on the Rh(322) terraces. Such an assignment would, however, mean that the three-fold sites are preferred over the atop-sites on the 111 terraces which conflicts with exactly the opposite ordering of sites being observed on Rh(111) [8]. The solution to this comes from DFT calculations which show that CO molecules adsorbed in bridge sites along the Rh(322) steps have a C1s binding energy which is 0.78 eV lower than that of atop-terrace CO, in good agreement with the experimental shift of ~0.68 eV. The simulations also show that the bridge-step site is preferred over the three-fold-hollow terrace sites by at least 0.2 eV per CO molecule in a Rh(322)-(2x1)-1CO structure. We therefore assign the 285.35 eV C1s component from Rh(322) to CO molecules adsorbed in bridge sites along the steps.

The C1s spectra from the co-adsorbed CO-hydrogen systems, shown in the middle curves of each panel in Fig.1, are distinctly different from those of the CO-only systems. After dosing of 5L H_2, all C1s intensity is for Rh(553) found at ~286 eV and for Rh(322) at 285.35 eV. As demonstrated by the upper curves in both panels measured after a short anneal at 400K in order to desorb the hydrogen, changes induced by hydrogen co-adsorption are reversible. Small differences between the upper and lower curves in the two panels are similar to what is expected for adsorption of a small additional CO amount (~0.005ML) which easily occurs during the measurements.

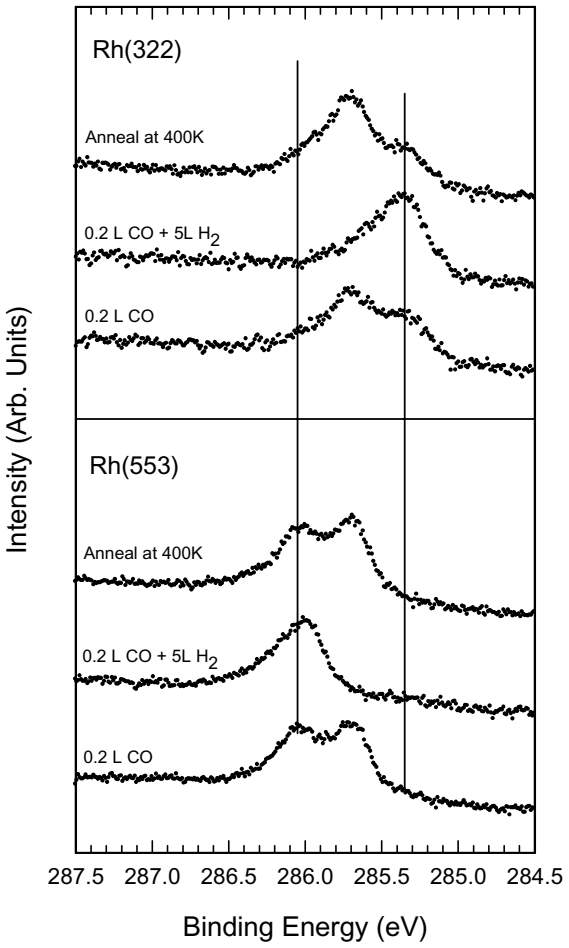

Figure 1. Lower panel: C1s after exposure of Rh(553) to the indicated CO and H_2 amounts. CO is dosed at 273K, H_2 at 100K. Upper curve shows C1s after an anneal at 400K of the middle situation. Upper panel is as lower panel but for Rh(322). The C1s binding energies for CO in atop (286.05 eV) and three-fold-hollow (285.35eV) sites, respectively, on Rh(111) [8] are indicated by vertical lines. Photon energy 380 eV.

Using the above assignments of C1s components to CO adsorption sites, the spectra of Fig.1 show that for Rh(553) the hydrogen forces CO away from the steps and into atop sites on the terraces. In contrast, on Rh(322) CO remains at the steps also in the co-adsorption system but now all CO is exclusively found in bridge sites.

In order to test this interpretation of the experimental data and to provide a more detailed understanding, an extensive set of calculations were performed for pure hydrogen adsorption as well as for CO-hydrogen co-adsorption systems. For a (2x1)-1H structure, i.e., a H-coverage of 0.1 ML, adsorption at the steps was found to be preferred. For Rh(553) the fcc site above the step is preferred and has 0.09 eV/H-atom more favorable adsorption energy than the fcc-terrace site which is the preferred site on the terraces. For Rh(322) the bridge site at the steps is preferred by 0.08 eV/H atom over the terrace fcc-site. Furthermore, the H-adsorption energy in the preferred step sites is about equal on both surfaces, 0.42 eV/H-atom on Rh(553) and 0.40 eV/H-atom on Rh(322). Thus at low H-coverage, the energetics of the step preference by H is the same for the two surfaces. However, for CO the atop-step site is preferred by ~0.11 eV for Rh(553) and ~0.17 eV for Rh(322) over the atop-terrace site. Thus considering only the

separate (non-co-adsorbed) systems at low H-coverage, the calculations indicate that H-induced CO removal from the steps is more likely on Rh(553) than on Rh(322) but they do not predict CO removal from the steps of Rh(553) as the energy gain by step adsorption is lower for H than for CO, albeit only by 0.02eV. At higher H-coverage,

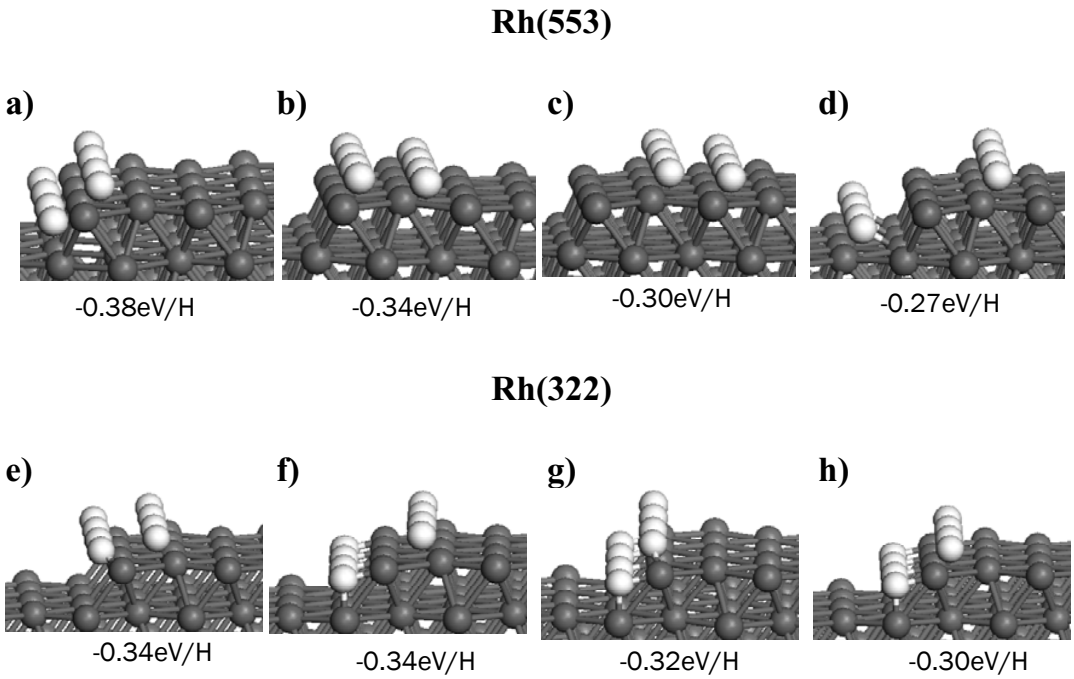

Figure 2. Adsorption energies per H-atom of the depicted overlayer structures on Rh(553) and Rh(322).

which is more appropriate for comparison to the experimental results in Fig.1, the step preference of hydrogen starts to differ for the two surfaces. This is illustrated in Fig.2 which shows the adsorption energies for selected structures at a H-coverage of 0.4ML. For these structures, no strong step preference is found for Rh(322) whereas on Rh(553) the step "hydride" structure of Fig.2a is preferred by at least 0.04 eV/H-atom (i.e. 0.16 eV per (2x1) unit cell) over the other structures shown. Thus, at high H-coverage the energy gain per (2x1) unit cell for H adsorption at the step (Fig.2a) is larger than the energy cost of removing CO (in a (2x1)-1CO structure) from the steps consistent with the experimental results of Fig.1 for Rh(553). For Rh(322), the calculations indicate that CO remains at the steps, again consistent with experiment.

The results based on the separate adsorption systems are confirmed by explicit calculations for CO-H co-adsorption systems at different coverages. In addition to this confirmation, the co-adsorption calculations provide more detailed information. We show in Fig. 3 the calculated stable CO-H co-adsorption structures for a CO coverage of 0.1 ML and H coverages of 0.1, 0.2, and 0.4 ML. As seen from Fig.3, all but one of the stable structures involve a co-adsorption of CO and H along the step, with the step-bridge sites being occupied by alternating CO and H. The exception (Fig.3c) is the high H coverage co-adsorption structure on Rh(553) where the large energy gain of the step "hydride" structure facilitates complete removal of CO from the steps. However, the next most stable co-adsorption structure in that system also involves alternating CO and H along the steps. The finding of bridge-step sites for CO in all stable structures for Rh(322) is consistent with the experimental results given in Fig.1

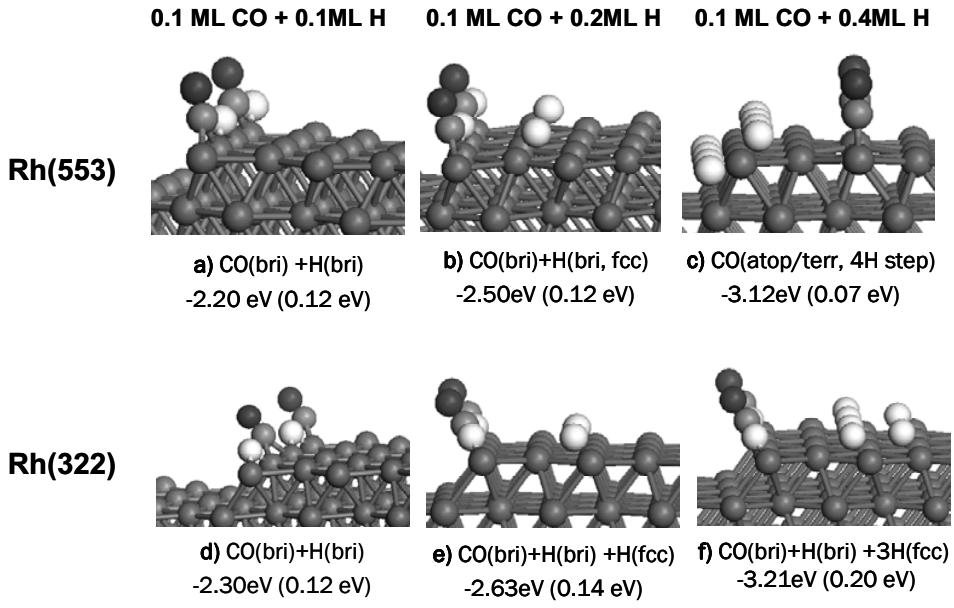

Figure 3. Adsorption energies per 2x1 unit cell of the depicted stable CO-H co-adsorption structures. Energies in parenthesis are the energy gain over the next most favorable co-adsorption structure

although these experimental results are valid for high H-coverage only. The results in Fig.1, however, contain no evidence for the calculated switch from atop to bridge sites at the steps of CO on Rh(553) at low H-coverage. In order to demonstrate that this calculational result is also found experimentally we show in Fig.4 C1s spectra as CO overlayer on Rh(553) and Rh(322) are exposed to small amounts of hydrogen. For Rh(553), Fig.4 shows the emergence of a C1s component at ~285.35 eV, that is at the binding energy expected for bridge bonded CO at the steps, and the subsequent disappearance of this component at higher hydrogen exposures in perfect agreement with the theoretical predictions of Fig.3. For Rh(322), Fig.4 shows that a hydrogen exposure as small as 0.1L leads to a complete conversion from atop to bridge sites at the steps. In passing we note that this high sensitivity to hydrogen indicates that some of the bridge adsorbed CO seen in the CO-only spectra in Fig.1 could be due to hydrogen contamination.

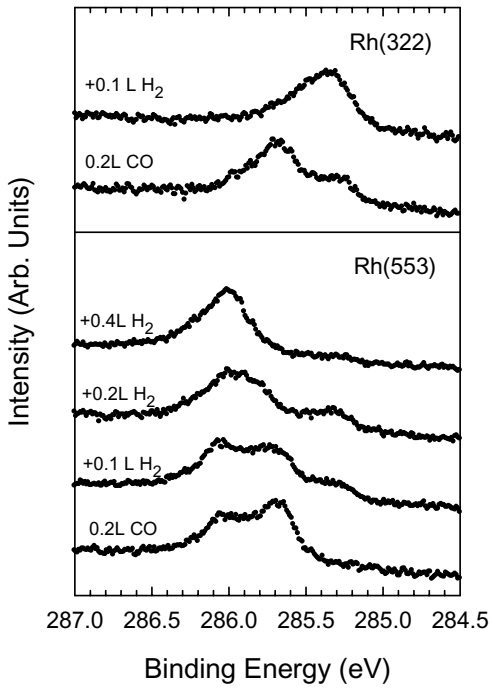

Figure 4. Lower panel: C1s spectra after 0.2 L CO exposure of Rh(553) at 273K (lower curve) and subsequent exposure to the H amounts indicated at 100K. Upper panel is as lower panel but for Rh(322). Photon energy 380 eV.

Summary and conclusions

From experiment as well as theoretical simulation it is found that CO at low coverage adsorbs at the steps on Rh(553) and Rh(322). For Rh(553), the step adsorption site is atop, whereas for Rh(322) both atop and bridge sites are taken. CO-adsorption with hydrogen leads to large changes. At high H-coverage CO is forced away from the steps on Rh(553) and for Rh(322) a site change from atop to bridge at the steps occurs. For lower H-coverage, CO remains at the steps also on Rh(553) but similar to the behavior on Rh(322) now switches to bridge sites. Whereas some of these H-induced site changes of the CO molecules could be understood from theoretical simulations for the separate CO and H adsorption systems, a detailed understanding required calculations for the co-adsorbed systems. Such calculations for CO-H co-adsorbed systems with increasing H-coverage reproduced the experimentally observed site changes.

Acknowledgements

This work was financially supported by the Swedish and Danish Research Councils and the Knut and Alice Wallenberg Foundation. X. F. Ma and W. X. Li acknowledge financial support from the National Natural Science Foundation of China and the Chinese Academy of Sciences "Bairen Project". Technical support by the MAX-lab staff is gratefully acknowledged.

References

1 R. Nyholm, J. N. Andersen, U. Johansson, B.N. Jensen, I. Lindau, Nucl. Instr. & Meth. in Phys. Res. **A 467-468** (2001) 520.

2 S. Doniach, M. Šunjić, J. Phys. **C 3** (1970) 285.

3 B. Hammer, K. W. Jacobsen, V. Milman, and M. C. Payne, J. Phys.: Condens. Matter **4** (1992) 453.

4 D. Vanderbilt, Phys. Rev. B **4**1 (1990) 7892.

5 M. Birgersson, C.-O. Almbladh, M. Borg, and J. N. Andersen, Phys. Rev B **67**, (2003) 045402.

6 J. G. Wang, W. X. Li, M. Borg, J. Gustafson, A. Mikkelsen,T. M. Pedersen, E. Lundgren, J. Weissenrieder, J. Klikovits, M. Schmid, B. Hammer, and J. N. Andersen, Phys. Rev. Lett. **95** (2005) 256102.

7 B. Hammer, L. B. Hansen, J. K. Nørskov, Phys. Rev. B **59** (1999) 7413.

8 A. Beutler, E. Lundgren, R. Nyholm, J. N. Andersen, B. J. Setlik, and D. Heskett, Surf. Sci. **396** (1998) 117 and M. Smedh, A. Beutler, T. Ramsvik, R. Nyholm, M. Borg, and J. N. Andersen, R. Duschek, M. Sock, F. P. Netzer, and M. G. Ramsey, Surf. Sci. **491** (2001) 99.

9 B. Tränkenschuh, N. Fritsche, T. Fuhrmann, C. Papp, J. F. Zhu, R. Denecke, and H.-P. Steinrück, J. Chem. Phys. **124** (2006) 74712 and B. Tränkenschuh, C. Papp, T. Fuhrmann, R. Denecke, and H.-P. Steinrück, Surf. Sci. **601** (2007) 1108.

Paper II

II

Mechanism of CO oxidation reaction on O-covered Pd(111) surfaces studied with fast x-ray photoelectron spectroscopy: Change of reaction path accompanying phase transition of O domains.

Ikuyo Nakai, Hiroshi Kondoh, Toru Shimada, Andrea Resta, Jesper N. Andersen and Toshiaki Ohta.

J. Chem. Phys. **124** 224712 (2006)

Mechanism of CO oxidation reaction on O-covered Pd(111) surfaces studied with fast x-ray photoelectron spectroscopy: Change of reaction path accompanying phase transition of O domains

Ikuyo Nakai, Hiroshi Kondoh,[a] and Toru Shimada
Department of Chemistry, Graduate School of Science, The University of Tokyo, 7-3-1 Hongo, Bunkyo-ku, Tokyo 113-0033, Japan

Andrea Resta and Jesper N. Andersen
Department of Synchrotron Radiation Research, Institute of Physics, Lund University, P.O. Box 118, S-221 00 Lund, Sweden

Toshiaki Ohta
Department of Chemistry, Graduate School of Science, The University of Tokyo, 7-3-1 Hongo, Bunkyo-ku, Tokyo 113-0033, Japan

(Received 9 February 2006; accepted 20 April 2006; published online 14 June 2006)

We studied the mechanism of CO oxidation on O-precovered Pd(111) surfaces by means of fast x-ray photoelectron spectroscopy (XPS). The oxygen overlayer is compressed upon CO coadsorption from a $p(2\times2)$ structure into a $(\sqrt{3}\times\sqrt{3})R30°$ structure and then into a $p(2\times1)$ structure with increasing CO coverage. These three O phases exhibit distinctly different reactivities. (1) The $p(2\times2)$ phase does not react with CO unless the surface temperature is sufficiently high ($<$290 K). (2) In the $(\sqrt{3}\times\sqrt{3})R30°$ phase, the reaction occurs exclusively at island peripheries. CO molecules in a high-density phase formed under CO exposure react with oxygen atoms, leading to quite a small apparent activation energy. (3) The reaction proceeds uniformly over the islands in the $p(2\times1)$ phase. © *2006 American Institute of Physics*. [DOI: 10.1063/1.2205856]

I. INTRODUCTION

The mechanism of CO oxidation on platinum-group metal surfaces has been extensively studied because it is one of the most fundamental surface reactions.[1–28] When adsorbed atomic oxygen is exposed to CO gas, an oxidation reaction occurs and generated CO_2 immediately desorbs into the gas phase. It has already been evidenced that adsorbed oxygen atoms react with adsorbed CO molecules (Langmuir-Hinshelwood mechanism) but do not directly react with impinging CO molecules (Eley-Rideal mechanism),[2,11,12]

$$\mathrm{CO(a)} + \mathrm{O(a)} \rightarrow \mathrm{CO_2(g)}. \quad (1)$$

The classical Langmuir-Hinshelwood reaction occurs between randomly distributed adsorbates, but in some cases, significant deviations from the simple kinetics have been found.[29] The deviations come from coverage dependence of activation energies and inhomogeneous distribution of reactants possibly due to the strong adsorbate-adsorbate interactions. Actually, we observed reaction site switching in the CO oxidation reaction on Pt(111) by monitoring the progress of the reaction by means of fast near edge x-ray absorption fine structure (NEXAFS) spectral measurement.[10] On the Pt(111) surface, oxygen atoms form an island structure. When the O-covered surface is exposed to CO gas, isolated oxygen atoms between islands react with CO at the initial stages of CO adsorption, whereas the reaction site switches to islands peripheries upon the CO saturation (or as the amount of CO increases). This switching of the reaction site is induced by compression of isolated oxygen atoms into islands by CO adsorption; the change in the spatial distribution of reactants caused by adsorbate-adsorbate interactions alters the reaction path. Such influences of the (dynamical) spatial distribution on the reaction mechanism may be essential also in other reactions. In order to understand this effect in more detail, we studied CO oxidation on a Pd(111) surface. The adsorption structure of O and CO on Pt(111) and Pd(111) surfaces is quite different. On both surfaces atomic oxygen forms a $p(2\times2)$ structure. While many diffusing isolated oxygen atoms are observed between islands on the Pt(111) surface,[7] they are not observed on Pd(111), and edges of islands formed on Pd(111) are much smoother than those on Pt(111).[16,17,30] When the $p(2\times2)$-O islands on Pd(111) are exposed to CO gas, they are compressed first into $(\sqrt{3}\times\sqrt{3})R30°$ domains and further into $p(2\times1)$ at higher CO exposure.[12,13,16,17,31,32] On the other hand, on Pt(111), no phase transition occurs for the O $p(2\times2)$ domains upon CO adsorption, but CO molecules occupy the atop site inside the O islands.[5–9] These observations indicate that O–O attraction and O–CO repulsion are stronger on Pd(111) than on Pt(111). Thus, the effect of CO adsorption on the spatial distribution and reactivity of atomic O is expected to play a more pronounced role in the CO oxidation reaction on Pd(111).

Although the presence of the $(\sqrt{3}\times\sqrt{3})R30°$ and $p(2\times1)$ O domains under CO coadsorption is well known for Pd(111), it has not been clear yet whether the compressed

[a]Author to whom correspondence should be addressed. Electronic mail: kondo@chem.s.u-tokyo.ac.jp

domains are pure oxygen domains or mixed O+CO domains. The $(\sqrt{3}\times\sqrt{3})R30°$ domain was revealed to be a pure oxygen phase by several techniques,[12,16,32] while both pure-phase[16,32] and mixed-phase[31] models have been proposed for the $p(2\times1)$ domain. Recently, a scanning tunneling microscopy (STM) study combined with density functional theory (DFT) calculations showed that it is a pure oxygen phase. Our x-ray photoelectron spectroscopy (XPS) and DFT results also support this conclusion.[33]

It is likely that the three types of oxygen domains exhibit different reactivities in the CO oxidation reaction. In isothermal kinetic experiments and temperature programmed desorption (TPD) measurements, variations in the reaction rate and activation energy were observed corresponding to compression from the $(\sqrt{3}\times\sqrt{3})R30°$ phase into the $p(2\times1)$ phase.[11–13,16,17] The $p(2\times2)$ phase is not reactive to CO.[11,12,16] The change in the reactivity has been attributed to the effects of local environments around the reactants and to consequent changes in the adsorbate-adsorbate interactions.[11–13,29] Very recently, Kim *et al.* found an interesting reactivity for the $p(2\times1)$ phase: consumption of O islands proceeds discontinuously.[17] Although these results from previous studies showed distinct reactivity for each of the three different O domains, a comprehensive understanding of the relationship between the phase transition of O domains by CO adsorption and the reactivity has not been obtained. Since the compression of domains is a dynamic phenomenon occurring under the supply of coadsorbates from the gas phase, it is important to observe the compression and the reaction under gas exposure. Moreover, it is suggested that in the CO oxidation reaction on Pt(111), weakly bound CO, which appears exclusively in the presence of gas-phase CO, is responsible for the reaction at island peripheries.[7–10,24] For these reasons, we conducted real-time monitoring of the surface during the reaction under the compression of O domains by XPS.

XPS is suitable for quantitative and chemical-state specific detection of adsorbed atoms and molecules. Thanks to recent development of synchrotron light sources and electron-energy analyzers, fast acquisition of XP spectra has become possible.[34] The typical acquisition time for monolayer adsorbates is ranging from several seconds to several tens of seconds. We monitored the progress of CO oxidation on the Pd(111) surface by means of fast XPS under various conditions and based on a kinetic analysis of these results we propose mechanisms for this reaction. The results reveal that the reaction sites and the types of reactive CO are significantly different for the three O phases.

II. EXPERIMENT

The experiments were carried out at the beamline I311 at MAX II (Lund, Sweden), which is an undulator-based vacuum-ultraviolet and soft x-ray beamline with a modified SX-700 monochrometer.[35] The XPS measurements were performed with a high-resolution electron-energy analyzer SES200 (SCIENTA). The base pressure of the ultrahigh vacuum chamber was below 8×10^{-11} Torr.

The reaction was monitored with real-time O 2*s* XPS. In general, O 1*s* XPS is used for studies of oxygen-containing adspecies,[9,34] but in the present case, the O 1*s* peak overlaps strongly with the Pd $3p_{3/2}$ line. This overlap also interferes with fast NEXAFS measurements,[10] which therefore is difficult to apply to this reaction.

A Pd(111) single crystal surface was cleaned with repeated cycles of sputtering and annealing at 1100 K. The cleanliness and ordering were checked with XPS and low-energy electron diffraction (LEED). A saturated $p(2\times2)$-O monolayer was prepared by exposing the clean Pd(111) surface to gaseous O_2 at 300 K. Then the atomic-oxygen precovered surface was exposed to gaseous CO at constant pressure and surface temperature. The titration process of O by CO was monitored with real-time O 2*s* XPS with an interval of 20 s. The photon energy used here was 160 eV.

Real-time observations of LEED and Pd 3*d* XPS were also conducted for several typical reaction conditions to obtain information on the phase transition of the O domains. Pd 3*d* exhibits characteristic surface core-level shifts for the three O adsorption phases.[33]

X-ray-induced reaction and desorption have been reported for several surface systems.[36–38] It is possible that the intense x-ray irradiation from an undulator causes acceleration or deceleration of the reaction or even creates undesirable side reactions such as dissociation of reactants. We compared the reaction rates under continuous x-ray irradiation with those under minimal x-ray irradiation by occasional measurement, and confirmed that x-ray irradiation does not affect the rate of this reaction. Dissociation of CO or oxidation of the substrate metal by x-ray irradiation was not observed, either.

We also conducted high-resolution XPS measurement under static conditions to investigate the coadsorption structure as a basis of the understanding of the reaction. The results will be presented elsewhere.[33]

III. RESULTS AND DISCUSSION

A. Typical spectra and kinetics

A typical series of the O 2*s* spectra is shown in Fig. 1(a). A peak observed at 20.6 eV, which decreases with time, corresponds to the O 2*s* level of surface atomic oxygen, while a growing peak around 27 eV is ascribed to the 3σ molecular orbital of adsorbed CO. No other species were observed on the surface during CO exposure. CO_2 produced by the reaction immediately desorbs at the reaction temperatures adopted here.

To extract the time evolution of coverages of O and CO (θ_O and θ_{CO}, respectively), we conducted curve-fitting analyses for the O 2*s* spectra. Since broad structures originating form valence structures appear in the vicinity of the O 2*s* XPS peaks, the curve fitting procedure was not straightforward. First, as shown in Fig. 1(b), the standard spectrum from a pure O or CO overlayer on Pd (111) is reproduced by a superposition of Gaussian peaks and a linear base line; here we focused only on the spectral shape, while we did not care

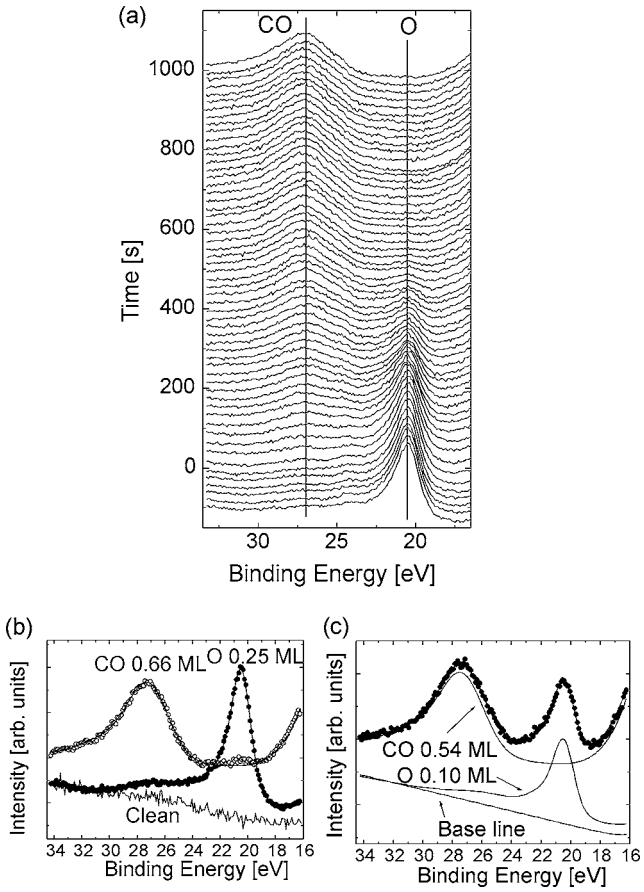

FIG. 1. (a) A typical series of O 2*s* spectra during the titration of an O overlayer by CO on Pd(111). (b) Standard spectra from O- and CO-saturated surfaces and clean surface. (c) An example of curve fitting for estimation of coverages of O and CO (θ_O and θ_{CO}, respectively). In this case, θ_O=0.10 ML and θ_{CO}=0.54 ML.

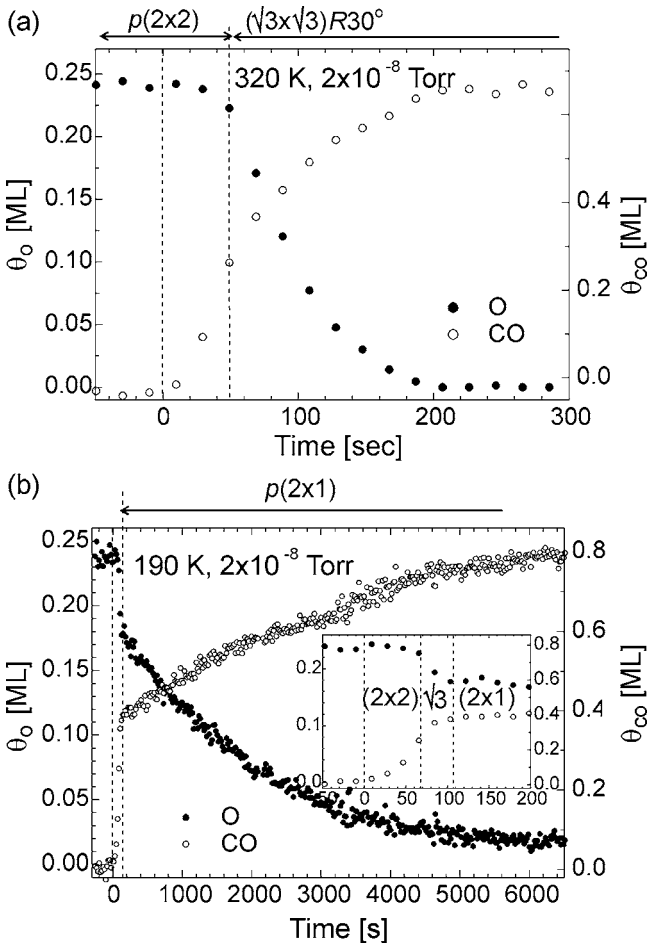

FIG. 2. Time evolution of coverages of θ_O (solid circles) and θ_{CO} (open circles) at 320 K (a) and 190 K (b). CO pressure is 2×10^{-8} Torr. The initial stage of (b) is shown in a large scale in the inset.

about the physical meanings for the fitted parameters. Each of the peaks from O and CO is assumed to consist of two Gaussian components. Second, in order to estimate the coverages of O and CO, each spectrum during the CO exposure was reproduced by a liner combination of the standard spectra of the O and CO after subtraction of a fixed base line [Fig. 1(c)]. Here, the shapes of standard spectra were basically unchanged but the binding energies of the Gaussian peak centers were changed to reproduce small peak shifts due to change in the adsorbate structure: for example, the transition from $p(2\times2)$ to $(\sqrt{3}\times\sqrt{3})R30°$ structure of atomic O. In addition, the intensity ratio of the two Gaussian components in the main peak of CO was varied to reproduce the change in the peak shape with the increase of its coverage.

Time evolutions of the coverage of the reactants at 320 and 190 K are shown in Fig. 2. The information on the phase transitions of the O domains monitored with LEED and Pd 3*d* XPS is also indicated in the figure. In both conditions, an "induction period" is observed at the initial stage where CO adsorption has already started but reaction does not occur. This induction period appears in the oxygen $p(2\times2)$ phase, which agrees with previously observed unreactivity of the $p(2\times2)$ phase.[11,12,16] The ignition of the reaction coincides with the completion of compression into the $(\sqrt{3}\times\sqrt{3})R30°$ phase. The induction period was not observed when the surface temperature is high (above 290 K) and the CO pressure is low (below 2×10^{-9} Torr). At relatively high surface temperatures, the hopping of the adsorbates is active. Thus, we tentatively attribute this process to the reaction between highly mobile CO molecules and fluctuating O atoms. Due to the low CO pressure and high temperature, the compression of O domains into the $(\sqrt{3}\times\sqrt{3})R30°$ phase occurs more slowly than the progress of this reaction.

At 190 K in Fig. 2(b), a sharp break is found in the curve of oxygen consumption at about 120 s, which corresponds to the transition from the $(\sqrt{3}\times\sqrt{3})R30°$ phase to the $p(2\times1)$ phase. The reaction is much faster in the former phase than in the latter one. This observation clearly indicates that these two domains display distinct reactivities. Note that though the former process is much faster than the latter one in this condition, the reaction rates of these two processes strongly depend on the surface temperature and CO pressure as discussed below.

While the reaction of the $p(2\times1)$ phase was dominant below 200 K, the reaction of the $(\sqrt{3}\times\sqrt{3})R30°$ phase was mainly observed above 200 K. Above 200 K, the consumption of the $(\sqrt{3}\times\sqrt{3})R30°$ domain was faster than the

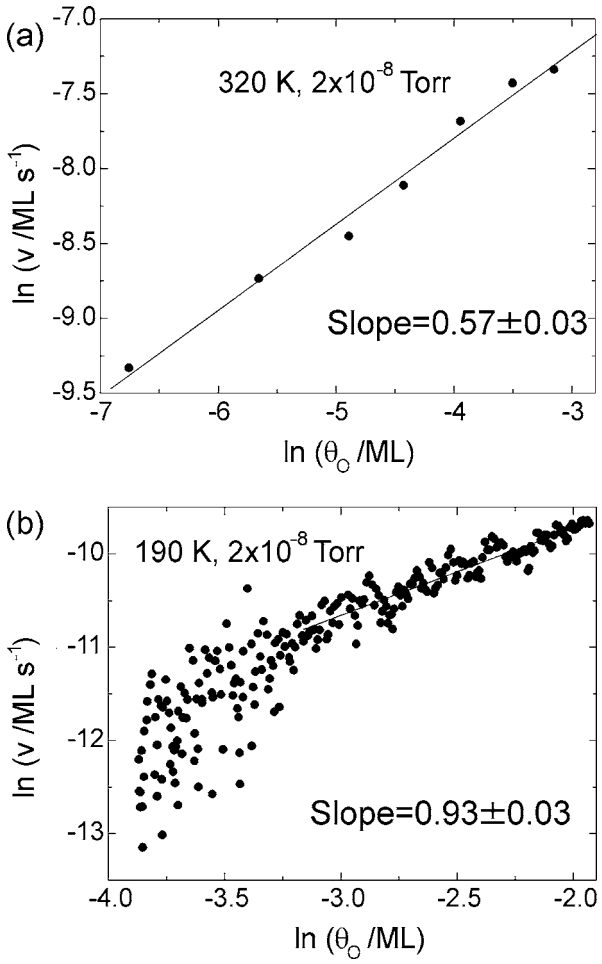

FIG. 3. Double logarithmic plots of reaction rate (ν) vs O coverage (θ_O): (a) and (b) correspond to Figs. 2(a) and 2(b). For (a) and (b), only the part of the $(\sqrt{3}\times\sqrt{3})R30°$ and $p(2\times1)$ phases is shown, respectively.

compression into $p(2\times1)$, and only the reaction in the $(\sqrt{3}\times\sqrt{3})R30°$ phase was observed; at higher temperatures the hopping of oxygen atoms is more active and the compression of the O domains by O–CO repulsion works less effectively. The reaction rate in the short-termed $(\sqrt{3}\times\sqrt{3})R30°$ phase at 190 K [Fig. 2(b)] is almost the same as the one in the reaction at 320 K where only $(\sqrt{3}\times\sqrt{3})R30°$ was observed [Fig. 2(a)].

The double logarithmic plots of the reaction rate with respect to the O coverage are shown in Fig. 3. They were plotted from the results shown in Fig. 2. The reaction rates were estimated by differentiation of the time evolution curve of the O coverage after a smoothing procedure.

According to the classical reaction rate law, reaction rate ν is expressed by the following equation:

$$\nu = k\theta_O^a \theta_{CO}^b. \tag{2}$$

As CO adsorption is expected to be already saturated at the given CO pressure and θ_{CO} can be regarded as a constant value throughout the reaction of each O phase, the slope of the double logarithmic plot indicates the reaction order with respect to atomic O, i.e., a.[10,11,17] The reaction orders for the $(\sqrt{3}\times\sqrt{3})R30°$ and $p(2\times1)$ phases were approximately 0.5 and 1 (half and first orders), respectively. The presence of

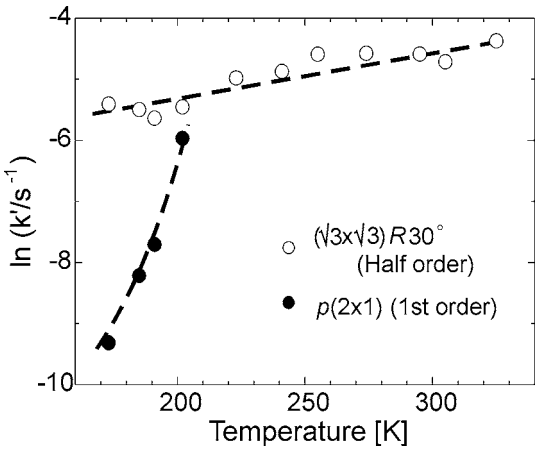

FIG. 4. Temperature dependence of reaction rate constants k' of the half-order reaction of the $(\sqrt{3}\times\sqrt{3})R30°$ phase (open circles) and the first-order reaction of the $p(2\times1)$ phase (filled circles) at $P_{CO}=2\times10^{-8}$ Torr. Here, to compare the rate constants with different units, the rate constants for the half-order reaction (in the unit of ML$^{1/2}$ s^{-1}) are converted into those for a first-order reaction (in the unit of s^{-1}) by assuming θ_O of 0.25 ML. The dashed lines are eye guides.

distinct reaction orders supports that different paths are involved in these reactions. As the O domain is compressed from $p(2\times2)$ into $(\sqrt{3}\times\sqrt{3})R30°$ and then into $p(2\times1)$ with the increase of the CO coverage, the reaction path is switched over.

B. Temperature dependence of the kinetics

Figure 4 shows the temperature dependence of the reaction rate constant k' at a CO pressure of 2×10^{-8} Torr. The reaction rate exhibits CO pressure dependence as shown later. Here, the "rate constant" k' is defined as the one including CO pressure,

$$\nu = k'\theta_O^a. \tag{3}$$

As shown in the figure, the first-order reaction displays strong temperature dependence, while the half-order reaction shows only very weak temperature dependence. The difference in the temperature dependence of the two reaction paths becomes more pronounced when the activation energies are estimated. Figure 5 shows the Arrhenius plots of the two reaction paths. The activation energies are estimated from the slopes of the plots to be 0.04±0.02 eV for the reaction of the $(\sqrt{3}\times\sqrt{3})R30°$ phase and 0.29±0.03 eV for the reaction of the $p(2\times1)$ phase. Here the different activation energies further confirm that the reaction paths are distinct for the two phases. The estimated activation energy for the $(\sqrt{3}\times\sqrt{3})R30°$ phase is extremely small for an elementary reaction path of CO oxidation reaction.[2–22]

C. Mechanism of the half-order reaction for the $(\sqrt{3}\times\sqrt{3})R30°$ phase

Characteristics of the reaction path for the $(\sqrt{3}\times\sqrt{3})R30°$ phase are summarized as follows:

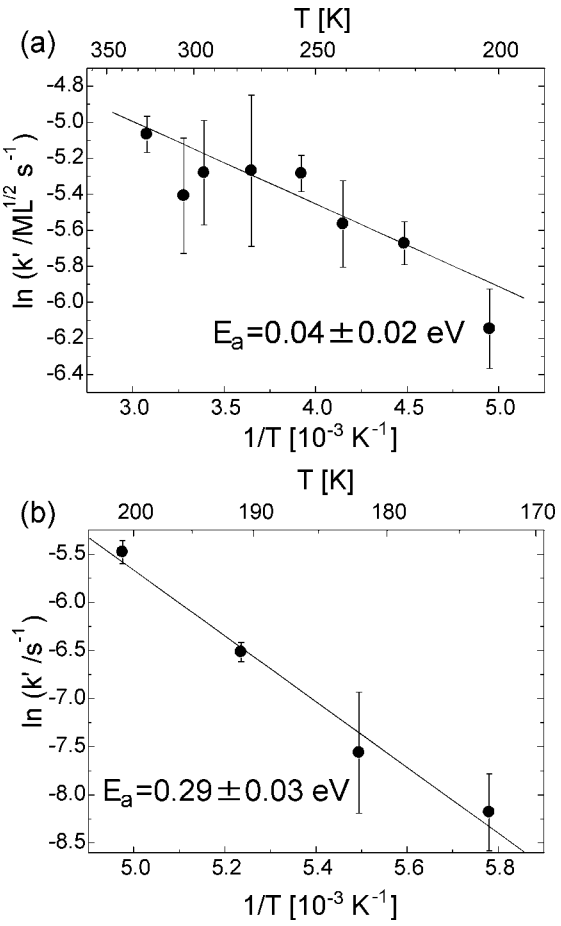

FIG. 5. Arrhenius plots for the half-order reaction of the $(\sqrt{3}\times\sqrt{3})R30°$ phase [(a) $P_{CO}=2\times10^{-8}$ Torr] and the first-order reaction of the $p(2\times1)$ phase [(b) $P_{CO}=5\times10^{-7}$ Torr].

(i) Half order with respect to θ_O.
(ii) Approximately first-order CO pressure dependence (Fig. 6).
(iii) Very small activation energy: 0.04±0.02 eV.

It has been established that the $(\sqrt{3}\times\sqrt{3})R30°$ phase is a

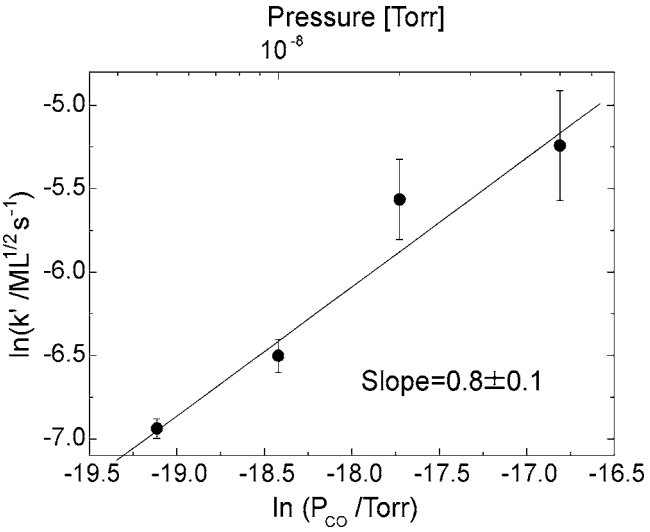

FIG. 6. CO pressure dependence of the reaction rate constant k' for the half-order reaction of the $(\sqrt{3}\times\sqrt{3})R30°$ phase at 240 K.

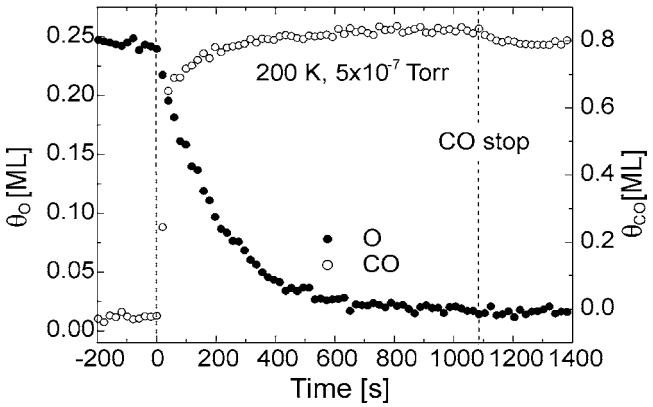

FIG. 7. Time evolution of θ_O and θ_{CO} at a relatively high CO pressure ($T=200$ K, $P_{CO}=5\times10^{-7}$ Torr). The absence of the induction period is due to quick CO adsorption under this condition. CO exposure was ceased at 1080 s.

pure oxygen domain.[12,16,32] The reaction order of 1/2 indicates that the reaction proceeds exclusively at island peripheries because the total length of peripheries of sufficiently large islands with smooth edges is approximately proportional to the square root of their area.

If an oxygen atom and a CO molecule adsorbed at adjacent sites at a domain boundary are involved in the reaction, the reaction rate would be independent of CO pressure after the saturation. However, it exhibits approximately first-order dependence on CO pressure. Moreover, as shown in Fig. 7, when the CO pressure is high enough, a part of adsorbed CO desorbs immediately as CO exposure is stopped. These observations suggest that in this reaction path, oxygen atoms at the peripheries of the $(\sqrt{3}\times\sqrt{3})$ domains do not react with stably adsorbed CO molecules which remain on the surface without the gas exposure. Instead, CO molecules in a high-density phase formed under CO gas exposure reacts with oxygen atoms at domain boundaries. Though the reaction order of 1/2 with respect to atomic O clearly shows that the reaction proceeds exclusively at peripheries of the $(\sqrt{3}\times\sqrt{3})R30°$ domains, the spatial distribution of the reactive high-density CO domains is not clear from the present results. They may be located exclusively at the peripheries of the oxygen domains, or they may be distributed uniformly on the surface and only the fraction in the vicinity of the peripheries contributes to the reaction.

If the population of a reactant (reactive CO at O island peripheries, in this case) is very small and in equilibrium with the gas phase, a steady-state approximation is valid and the apparent activation energy is expressed as the difference between the true activation energy of the elementary reaction path and the heat of adsorption of the reactive CO species.[39,40] The observed small activation energy, the large pressure dependence, and the desorption of CO after the stop of CO exposure are all explained by this mechanism. The proposed energy diagram is shown in Fig. 8. All the CO molecules desorbing after the stop of CO exposure in Fig. 7 may not necessarily be involved in the reaction; since the

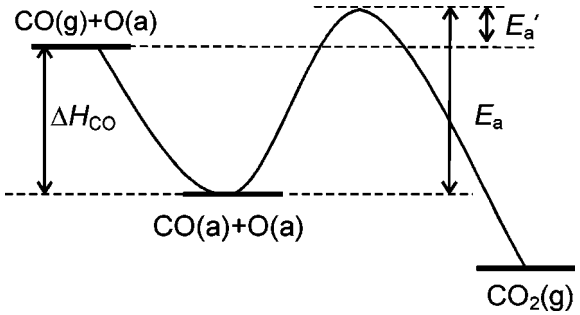

FIG. 8. Proposed energy diagram for the half-order reaction of the $(\sqrt{3}\times\sqrt{3})R30°$ phase.

reactive CO is not distinguished from the other CO with time-resolved XPS measurement, ΔH_{CO} of the reactive CO cannot be estimated accurately. If we assume that the desorption rate of the reactive CO is the same with that of the desorbing CO, ΔH_{CO} is estimated to be 0.58 eV from the rate of the desorption in Fig. 7 with a well-known universal preexponential factor for fast order desorption of 10^{13} s^{-1}. Then the activation energy of the reaction step E_a is estimated to be 0.62 eV. Note that chemisorption energy of CO is larger than 1.2 eV,[11,12,32,33] which indicates that the adsorption of desorbing species is very weak.

Then we examined what kind of CO desorbs after the stop of CO exposure. Figure 9(a) shows the O 2*s* spectra measured with and without CO exposure, which correspond to the data points at 800 and 1400 s in the plot in Fig. 7. Only in the spectrum with CO exposure, a shoulder structure is observed at the higher binding energy side. To identify the species which is responsible for the shoulder, we measured O 2*s* spectra for CO saturation at 90 and 240 K under static conditions without CO exposure [Fig. 9(b)]. While only hollow and bridge sites are occupied at 240 K, atop site is also occupied at 90 K.[33,41] In the 90 K spectrum, another component is observed at the higher energy side. It is ascribed to

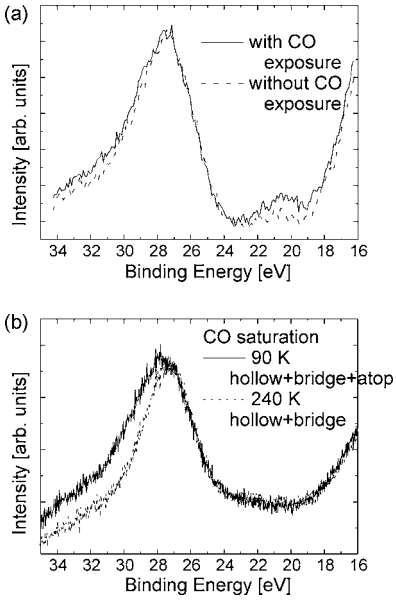

FIG. 9. (a) O 2*s* spectra measured with and without CO exposure which correspond to 800 and 1400 s in the plot in Fig. 7, respectively. (b) Static O 2*s* spectra from CO-saturated surfaces taken at 90 and 240 K.

atop-bonded CO. The C 1*s* spectra, which exhibit more pronounced chemical shifts for different adsorption sites of CO, support this assignment.[33] Its energy position is the same as the one observed in the spectrum measured under CO exposure in Fig. 9(a). Thus, the CO molecules which desorb after the stop of CO exposure in Fig. 7 are tentatively assigned to an atop species. Thus, the reactive high-density CO domains include atop species, though it is unclear which of the atop CO molecules or those on other adsorption sites in the high-density domains react with oxygen atoms at island peripheries.

D. Mechanism of the first-order reaction in the $p(2\times1)$ phase

Characteristics of the reaction of the $p(2\times1)$ phase are summarized as follows:

(i) First order with respect to θ_O.
(ii) Activation energy of 0.29 ± 0.03 eV.

To be a first-order reaction indicates a uniform reaction over the oxygen domain. The $p(2\times1)$-O phase consists of pure oxygen atoms, which was supported by recent STM,[16] LEED *I-V*, and DFT (Ref. 32) studies. Furthermore, our estimation of CO coverage from the C 1*s* XPS intensity and DFT calculation results are also consistent with the model in which CO exists only outside O domains.[33] Although no CO is stably adsorbed in the $p(2\times1)$-O domain, the consumption of oxygen actually proceeds over the islands. One can suppose that high-density CO domains formed only under CO exposure take part in the reaction, as observed in the reaction of the $(\sqrt{3}\times\sqrt{3})R30°$ phase. Desorption of CO, however, was not observed after stopping of the CO exposure, in contrast to the $(\sqrt{3}\times\sqrt{3})R30°$ phase (Fig. 7). We assume that weakly bound CO exists inside the O-$p(2\times1)$ domain but it cannot be detected by fast XPS. It was not observed with STM, either.[16,17] The lack of detection is probably due to its very small population or very short lifetime.

E. Comparison with STM results

The present results essentially agree with the result of the previous STM observations under similar conditions.[16,17] The reaction-site switching was observed in the same way. The largest disagreement lies in the reaction rate. The rate of the reaction of the $p(2\times1)$ phase is more than an order of magnitude higher than the present one. This may be partly because the reactivity in this reaction is very sensitive to the CO supply from the gas phase as mentioned above, which would seriously depend on the local geometry around the sample in the equipments. The preparation conditions of oxygen precovered surfaces were almost the same.

The greatest mystery is the nature of the reaction of the $p(2\times1)$ phase. We have concluded that the reaction proceeds over the domain judging from its reaction order of 1, but we could not detect the reactive CO. In the STM observation, an interesting reactivity was reported.[17] A $p(2\times1)$ island remains intact for a while under CO exposure, and once it starts to react, the entire island disappears in a very

short time: the reaction proceeds discontinuously. This reaction is started by a very small amount of weakly bound CO which cannot be detected with XPS or STM. One possible process is such that once the reaction occurs inside the island, very reactive sites are created around the site where the reaction initially occurred. Some experimental techniques which can detect the reactive species are necessary to understand the mechanism taking place in the $p(2\times1)$ phase thoroughly.

F. Comparison with the reaction on Pt(111)

The reaction path switching in the CO oxidation reactions on Pd(111) and Pt(111) upon CO adsorption indicates that the interactions between reactants, configuration of reactants, and the reaction sites dynamically affect one another and generate anomalies in the reactivity.

As mentioned in the Introduction, the O–O and O–CO interactions on Pt(111) and Pd(111) are quite different. The different adsorbate-adsorbate interactions lead to different ways of switching of reaction path. The variety of the reaction paths on Pd(111) is derived from the presence of compressed phases. Compression of O domains and phase separation between O and CO do not occur on Pt(111).

When a (2×2)-O overlayer on a close-packed surface is exposed to CO, a mixed (2×2)-(O+CO) overlayer is often observed, for instance, on Pt, Rh, Ru, and Ni;[42] the compression and phase separation are peculiar to Pd(111). In the (2×2)-O islands, O atoms occupy the fcc-hollow site, and CO molecules have to occupy other sites to form a mixed phase. According to a previous study on O+CO mixed overlayer on Pt(111) using DFT calculations,[25] the adsorption energy of CO on an atop site in the (2×2)-O domain is smaller only by 5% than in the case of adsorption on an oxygen-free atop site. In the case of Pd(111), the energetically most favorable site for CO is the fcc-hollow site of clean Pd(111) surface, and the adsorption energy on the atop site or the hcp-hollow site in the (2×2)-O domain is smaller by about 30% than the case of oxygen-free fcc-hollow site.[32,33,42] This is one reason why compression of O domains occurs on Pd(111) but not on Pt(111). Another reason is the difference in the O–O interaction. On Pd(111), the attractive interaction between adjacent O atoms in the $(\sqrt{3}\times\sqrt{3})R30°$ domain is comparable to that in the $p(2\times2)$ domain.[32,33] On the other hand, on Pt(111), the interaction between O atoms at the $(\sqrt{3}\times\sqrt{3})R30°$ position is repulsive.[43] The adsorbate-adsorbate interactions such as CO–O and O–O interactions are responsible for the ways of switching of reaction sites and reaction rates.

IV. CONCLUSIONS

The atomic oxygen overlayer on the Pd(111) surface is compressed by CO adsorption from a $p(2\times2)$ phase to $(\sqrt{3}\times\sqrt{3})R30°$ and $p(2\times1)$ phases. These phases exhibit quite distinct reactivities, and the reaction path is switched over with the compression. In the $(\sqrt{3}\times\sqrt{3})R30°$ phase, the reaction occurs exclusively at island peripheries between oxygen atoms and CO molecules in a high-density phase formed under CO exposure. The activation energy was estimated to be 0.61 eV. In the $p(2\times1)$ phase, the reaction occurs inside the oxygen islands with the activation energy of 0.29 eV. The $p(2\times2)$ phase does not react with CO, but when the CO pressure is low and the surface temperature is high, it react with diffusing CO.

ACKNOWLEDGMENTS

The authors acknowledge experimental help by Dr. Sven Stoltz and the MAX-lab staff and helpful discussions with Dr. Hideo Orita. The authors thank Dr. Sang Hoon Kim for showing us Ref. 17 before publication. The present work is supported by the Grant-in-Aid for Scientific Research (KAKENHI) in Priority Area "Molecular Nano Dynamics" from Ministry of Education, Culture, Sports, Science and Technology. The authors are grateful for the 21st century COE Program. One of the authors (I.N.) appreciates the JSPS Research Fellowship for Young Scientists.

[1] I. Langmuir, Trans. Faraday Soc. **17**, 621 (1921).
[2] C. T. Campbell, G. Ertl, H. Kuipers, and J. Segner, J. Chem. Phys. **73**, 5862 (1980).
[3] J. L. Gland and E. B. Kollin, J. Chem. Phys. **78**, 963 (1983).
[4] S. Akhter and J. M. White, Surf. Sci. **171**, 527 (1986).
[5] J. Yoshinobu and M. Kawai, J. Chem. Phys. **103**, 3220 (1995).
[6] F. Zaera, J. Liu, and M. Xu, J. Chem. Phys. **106**, 4204 (1997).
[7] J. Wintterlin, S. Völkening, T. V. W. Janssens, T. Zambelli, and G. Ertl, Science **278**, 1931 (1997).
[8] S. Völkening and J. Wintterlin, J. Chem. Phys. **114**, 6832 (2001).
[9] M. Kinne, T. Fuhrmann, J. F. Zhu, C. M. Whelan, R. Denecke, and H.-P. Steinrück, J. Chem. Phys. **120**, 7113 (2004).
[10] I. Nakai, H. Kondoh, K. Amemiya, M. Nagasaka, T. Shimada, R. Yokota, A. Nambu, and T. Ohta, J. Chem. Phys. **122**, 134709 (2005).
[11] T. Engel and G. Ertl, J. Chem. Phys. **69**, 1267 (1978).
[12] H. Conrad, G. Ertl, and J. Küppers, Surf. Sci. **76**, 323 (1978).
[13] T. Matsushima and H. Asada, J. Chem. Phys. **85**, 1658 (1986).
[14] J. Szanyi, W. K. Kuhn, and D. W. Goodman, J. Phys. Chem. **98**, 2978 (1994).
[15] U. Burghaus, I. Z. Jones, and M. Bowker, Surf. Sci. **454–456**, 326 (2000).
[16] J. Méndez, S. H. Kim, J. Cerdá, J. Wintterlin, and G. Ertl, Phys. Rev. B **71**, 085409 (2005).
[17] S. H. Kim, J. Méndez, J. Wintterlin, and G. Ertl, Phys. Rev. B **72**, 155414 (2005).
[18] T. Matsushima, T. Matsui, and M. Hashimoto, J. Chem. Phys. **81**, 5151 (1984).
[19] S. B. Schwartz, L. D. Schmidt, and G. B. Fisher, J. Phys. Chem. **90**, 6194 (1986).
[20] L. S. Brown and S. J. Sibener, J. Chem. Phys. **89**, 1263 (1988).
[21] L. S. Brown and S. J. Sibener, J. Chem. Phys. **90**, 2807 (1989).
[22] M. J. P. Hopstaken and J. W. Niemantsverdriet, J. Chem. Phys. **113**, 5457 (2000).
[23] G. W. Coulston and G. L. Haller, J. Chem. Phys. **95**, 6932 (1991).
[24] A. Alavi, P. Hu, T. Deutsch, P. L. Slivestrelli, and J. Hutter, Phys. Rev. Lett. **80**, 3650 (1998).
[25] M. Lynch and P. Hu, Surf. Sci. **458**, 1 (2000).
[26] A. Eichler and J. Hafner, Surf. Sci. **433–435**, 58 (1999).
[27] C. J. Zhang and P. Hu, J. Am. Chem. Soc. **123**, 1166 (2001).
[28] A. Eichler, Surf. Sci. **498**, 314 (2002).
[29] F. Zaera, Prog. Surf. Sci. **69**, 1 (2001).
[30] T. Mitsui, M. K. Rose, E. Fomin, D. F. Ogletree, and M. Salmeron, Surf. Sci. **511**, 259 (2002).
[31] G. Odörfer, E. W. Plummer, H.-J. Freund, H. Kuhlenbeck, and M. Neumann, Surf. Sci. **198**, 331 (1988).
[32] A. P. Seitsonen, Y. D. Kim, S. Schwegmann, and H. Over, Surf. Sci. **468**, 176 (2000).
[33] I. Nakai, H. Kondoh, T. Shimada, A. Resta, J. N. Andersen, H. Orita, and T. Ohta (unpublished).
[34] A. Baraldi, G. Comelli, S. Lizzit, M. Kiskinova, and G. Paolucci, Surf. Sci. Rep. **49**, 169 (2003).

[35] R. Nyholm, J. N. Andersen, U. Johansson, B. N. Jensen, and I. Lindau, Nucl. Instrum. Methods Phys. Res. A **467–468**, 520 (2001).
[36] K. Tanaka, E. O. Sako, E. Ikenaga, K. Isari, S. A. Sardar, S. Wada, T. Sekitani, K. Mase, and N. Ueno, J. Electron Spectrosc. Relat. Phenom. **119**, 255 (2001).
[37] A. Nambu, H. Kondoh, I. Nakai, K. Amemiya, and T. Ohta, Surf. Sci. **530**, 101 (2003).
[38] P. R. Norton, J. W. Goodale, and D. K. Creber, Surf. Sci. **119**, 411 (1982).
[39] A. J. Elliott, R. A. Hadden, J. Tabatabaei, K. C. Waugh, and F. W. Zemicael, J. Catal. **157**, 153 (1995).
[40] H. Celio, C. Scheer, and J. M. White, J. Am. Chem. Soc. **123**, 2990 (2001).
[41] S. Surnev, M. Sock, M. G. Ramsey, F. P. Netzer, M. Wiklund, M. Borg, and J. N. Andersen, Surf. Sci. **470**, 171 (2000).
[42] H. Over, Prog. Surf. Sci. **58**, 249 (1998).
[43] J. Wintterlin, R. Schuster, and G. Ertl, Phys. Rev. Lett. **77**, 123 (1996).

Paper III

Acetate formation during the ethanol oxidation on Rh(111).

A. Resta, J. Blomquist, J. Gustafson, H. Karhu,
A. Mikkelsen, E. Lundgren, P. Uvdal
and J. N Andersen.

Surf. Sci. **600** (2006) 5136.

III

Available online at www.sciencedirect.com
ScienceDirect
Surface Science 600 (2006) 5136–5141
SURFACE SCIENCE
www.elsevier.com/locate/susc

Acetate formation during the ethanol oxidation on Rh(1 1 1)

A. Resta [a,*], J. Blomquist [b], J. Gustafson [a], H. Karhu [a], A. Mikkelsen [a], E. Lundgren [a], P. Uvdal [b], J.N. Andersen [a]

[a] *Department of Synchrotron Radiation Research, Institute of Physics, Lund University, S-221 00 Lund, Sweden*
[b] *Chemical Physics, Department of Chemistry, P.O. Box 124, Lund University, S-221 00 Lund, Sweden*

Received 2 June 2006; accepted for publication 31 August 2006
Available online 25 September 2006

Abstract

The catalytic cracking of ethanol on clean and oxygen precovered Rh(1 1 1) surfaces has been studied by a combination of synchrotron based high-resolution core level spectroscopy and surface infrared spectroscopy. On the clean surface the decomposition of ethanol occurs without any formation of atomic oxygen. The presence of oxygen on the surface changes the reactivity significantly and acetate (CH_3COO) was identified as an important surface intermediate in the ethanol oxidation.

Keywords: Ethanol; Acetate; Surface; HRCLS; XPS; Infrared

1. Introduction

It has recently been shown that hydrogen may be efficiently extracted from ethanol by means of partial oxidation over a Rh based catalyst [1]. Such catalytic production of hydrogen from alcohols may present a viable route to a hydrogen-based economy exploiting renewable resources. Whereas also other metals catalyse this partial ethanol oxidation, Rh based catalysts appear to have particularly high efficiency and specificity [2]. However only a limited number of studies have addressed the detailed surface science aspects of the ethanol and ethanol/oxygen chemistry on Rh surfaces [3–5]. In the present study we have used high resolution core level spectroscopy (HRCLS) and surface infrared spectroscopy to study ethanol adsorption on clean and oxygen covered Rh(1 1 1) at temperatures around room temperature. A major aim of the study is to demonstrate that acetate constitutes an important intermediate in the partial oxidation of ethanol.

2. Experimental section

The HRCLS measurements were performed at beam line 1311 at MAX-lab, Lund, Sweden. The experimental system is described in details elsewhere [6]. For the present experiments we mainly used photon energies of 380 eV and 625 eV for the C1s and O1s regions, respectively. All spectra were collected in normal emission. The surface infrared spectroscopy experiments were performed in a separate system and made use of a Bruker IFS 66v/S spectrometer connected to a UHV chamber. A MCT (HgCdTe) detector and a resolution of 4 cm^{-1} was used. For the HRCLS experiment, the Rh(1 1 1) crystal was mounted on 0.5 mm tungsten wires in thermal contact with a liquid nitrogen reservoir. It could be heated by sending a current through these support wires or be cooled to 100 K. The same type of sample mounting was employed in the infrared experiment except that electron bombardment of the back side of the sample was used for heating. The temperature was measured by thermocouples spot-welded to the side of the crystal, Chromel–Alumel for the HRCLS experiments and Tungsten–Rhenium for the infrared measurements. The Rh(1 1 1) surface was cleaned by Ar^+ sputtering at a temperature of 900 K, and subsequently annealed at

* Corresponding author.
E-mail address: andrea.resta@sljus.lu.se (A. Resta).

0039-6028/$ - see front matter © 2006 Elsevier B.V. All rights reserved.
doi:10.1016/j.susc.2006.08.039

1400 K in order to restore the surface order. Any residual carbon contamination was removed by heating the crystal in 10^{-8} Torr O_2 followed by a flash to 1300 K in vacuum. In the HRCLS experiments, photoemission spectra for the likely contaminants were measured to check the cleanliness whereas in the infrared experiments the cleanliness was checked by Auger spectroscopy. The ordering of the surface was checked by low energy electron diffraction (LEED). The ethanol was 99.5% pure with dry residuals being less than 0.002% and was further cleaned by freeze-pump-thaw cycles. Gas exposures given in Langmuir (L) ($1\ L = 10^{-6}$ Torr s) are based on the gauge reading with no correction applied for the different sensitivities towards oxygen and ethanol [7].

3. Results and discussion

Adsorption of ethanol on Rh(1 1 1) at temperatures around 300 K results in C1s and O1s spectra with a general appearance as those shown in Fig. 1 for 2, 20, and 200 L. Adsorption of ethanol at lower temperatures followed by subsequent annealing at 300 K leads to similar spectra. From these C and O 1s spectra it is possible to identify some of the molecular fragments that form following ethanol adsorption at room temperature. Starting with the C1s spectra in Fig. 1a, the peaks at binding energies just above 286 eV and 285.4 eV, respectively, can by comparison to previously reported C1s binding energies for CO adsorption systems on Rh(1 1 1) [8] be identified as CO molecules in on-top and three-fold-hollow sites, respectively. In addition to the C1s binding energies, also the photoelectron diffraction induced variation of the intensity ratio between the two CO related peaks as function of the photon energy displays the characteristic fingerprint (see, e.g., Refs. [8,9]) for CO adsorbed on Rh(1 1 1) in on-top and threefold-hollow sites. Finally the O1s spectra of Fig. 1b contain two peaks at binding energies of 532.1 and 530.5 eV that coincide with the O1s binding energies of CO molecules in on-top and three-fold-hollow sites [9]. From the C1s spectra of Fig. 1a we estimate global CO coverages of 0.11, 0.13, 0.23 ML for the shown 2, 20, and 200 L exposures when using C1s spectra measured for the well-known $(\sqrt{3}\times\sqrt{3})$ R30°-1CO and (2×2)-3CO overlayers as calibrations. It should be noted that no emission peak is found in Fig. 1b at the expected O1s binding energy for atomic oxygen of 529.4 eV. In fact our data lack such emission attributable to atomic oxygen at all temperatures and ethanol exposures. This contrasts to the results of [4] which show the development of a strong O1s peak at 529.6 eV following ethanol exposure at 100 K. The spectra of Fig. 1 thus show that the C–C bond of the ethanol molecule can be broken by the interaction with the Rh(1 1 1) surface. Additionally, the lack of an O1s peak characteristic of atomic oxygen indicates that breaking of the C–O bond is very unlikely or that, if it occurs, the atomic oxygen immediately forms other molecules that either adsorb (CO) or desorb (e.g., H_2O, CO_2 [9,10]). Returning to the C1s spectra of Fig. 1a, all peaks not already accounted for as due to CO are found at binding energies between 284.5 eV and 283 eV. This C1s binding energy range is characteristic for hydrocarbons and surface carbon species on metal surfaces, see, e.g., [11–14]. Although the lowest binding energy component around 283 eV may be tentatively assigned to atomic carbon on the surface, we believe that the expected C1s binding energy shifts between various hydrocarbons are too small to warrant a detailed assignment in terms of specific hydrocarbon fragments.

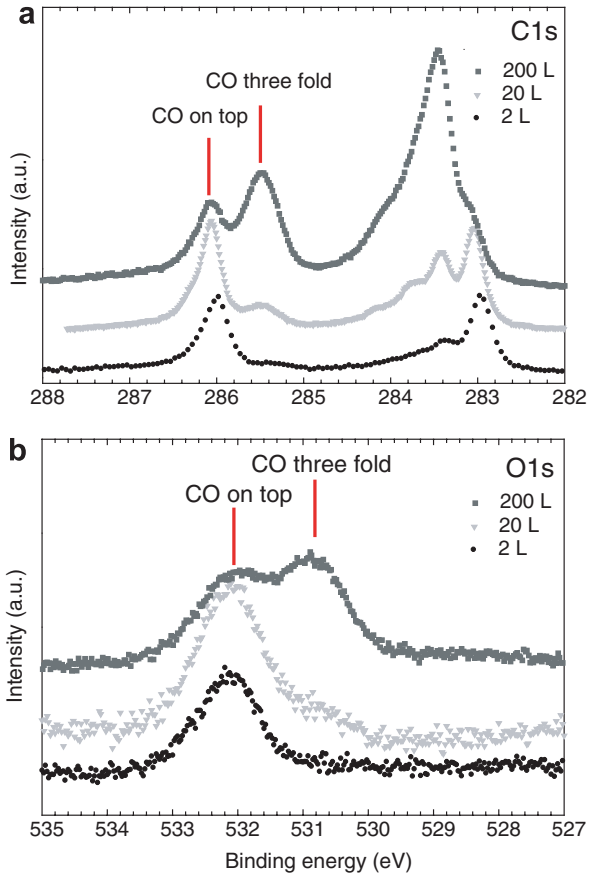

Fig. 1. C1s (a) and O1s (b) spectra measured after a clean Rh(1 1 1) surface has been exposed to the indicated amounts of ethanol at 300 K. Photon energies were 380 eV for C1s and 625 eV for O1s.

Fig. 2 shows typical C1s and O1s spectra when a Rh(1 1 1) surface covered by ~0.5 ML oxygen is exposed to ethanol at 300 K. Similar spectra result if instead the ethanol is dosed at lower temperature followed by a subsequent anneal at 300 K or if ethanol and oxygen are simultaneously dosed at 300 K. As seen by comparison to Fig. 1, the presence of oxygen on the Rh(1 1 1) surface results in major changes of the ethanol related C1s and O1s spectra. The C1s peak at 286 eV, that is present both with and without co-adsorbed oxygen, is on similar grounds as for ethanol adsorption on the clean Rh(1 1 1) surface attributed to CO adsorbed in on-top positions. The CO coverages estimated for this condition are 0.04 ML, 0.06 ML, 0.11 ML respectively for 2, 20 and 60 L. Whereas adsorbed CO is

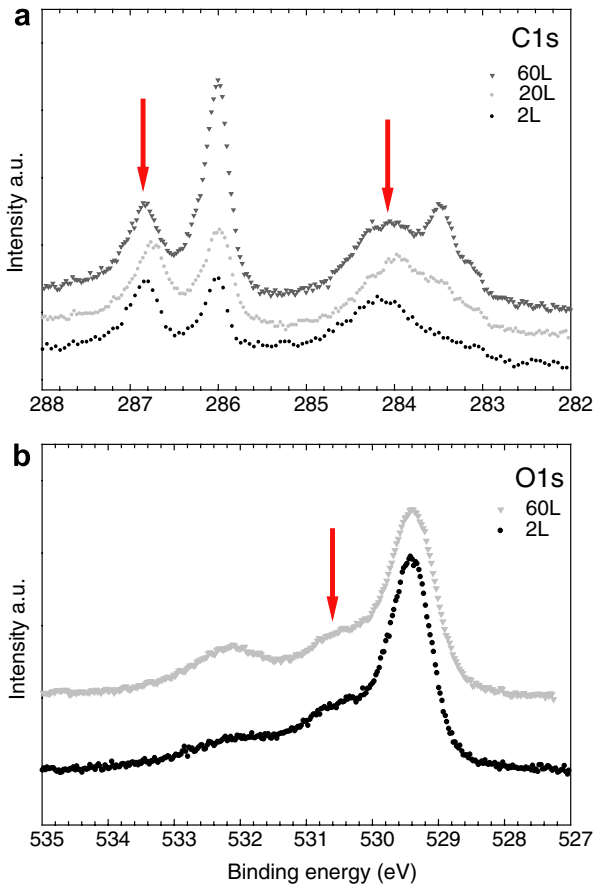

Fig. 2. C1s (a) and O1s (b) spectra measured after a Rh(1 1 1) surface precovered by ~0.5 ML of oxygen has been exposed to the indicated amounts of ethanol at 300 K. Photon energies were 380 eV for C1s and 625 eV for O1s. The arrows indicate emission attributed to adsorbed acetate (see text).

thus also found in the co-adsorbed system, the lack of any significant C1s emission at around 285.4 eV shows that the co-adsorbed oxygen strongly reduces the tendency for CO adsorption in three-fold-hollow sites. At binding energies below 285 eV, the co-adsorbed C1s spectra are much broader and featureless than on the clean surface. The relatively narrow peaks at 283 and 283.4 eV which dominate at low and high ethanol exposure, respectively, on the clean Rh(1 1 1) surface are much less prominent in the spectra from the co-adsorbed case. The only clearly distinguishable component that is common with and without predosed oxygen is the 283.4 eV peak which, however, has a significantly smaller intensity on the oxygen predosed surface. Instead much of the emission below 285 eV is found in a broad structure at binding energies around 284 eV. A most significant difference to the oxygen free case is the presence of a C1s peak at about 286.8 eV, that is, at even higher C1s binding energy than that of CO in on-top positions. We observe this 286.8 eV peak only when oxygen has been deliberately predosed on the surface (or if oxygen and ethanol are dosed simultaneously) although others [4] have reported its presence following only ethanol adsorption on the clean Rh(1 1 1) surface. The peak is furthermore found in a wide range of conditions regarding temperature, ethanol, and oxygen pressure when ethanol and oxygen are simultaneously dosed onto the surface. Under such exposure to an ethanol-oxygen mixture we find in general that as the temperature increases, the 286.8 eV peak increases in intensity relative to the 286 eV peak from CO in on-top positions. This dominance of the 286.8 eV over the 286 eV CO peak is illustrated by the C1s spectrum of Fig. 3a measured during exposure of Rh(1 1 1) at 400 K to a 1:1 ethanol:oxygen mixture with a total pressure of 5×10^{-8} Torr. In addition to the 286.8 eV peak and a weak peak at 286 eV from on-top adsorbed CO, Fig. 3 also contains a C1s peak at a binding energy around 284 eV. This peak has an intensity very similar to that of the 286.8 eV peak. Also a ~284 eV peak having roughly the same intensity as the 286.8 eV peak is found for all preparations where the latter peak can be distinguished. Additional surface infrared spectroscopy measurements on the molecule giving rise to the 286.8 eV C1s peak will be presented below. Whereas these vibrational spectroscopy results allow

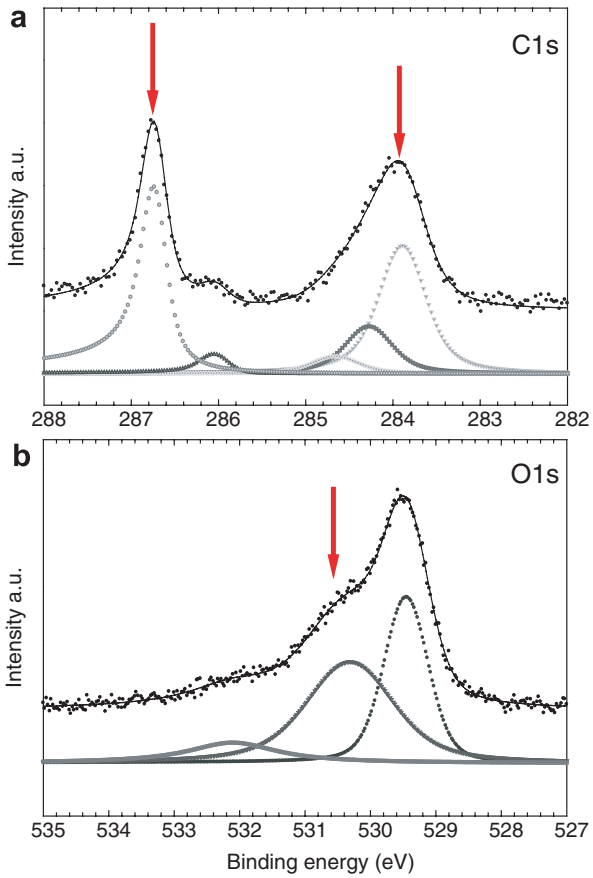

Fig. 3. C1s (a) and O1s (b) spectra (dots) measured after a Rh(1 1 1) surface has been exposed for ~300 s to a 1:1 ethanol:oxygen gas-mixture of total pressure 5×10^{-8} Torr at 393 K. The arrows indicate components attributed to acetate (see text). Decompositions of the spectra into components attributable to the various surface species (see text) are included.

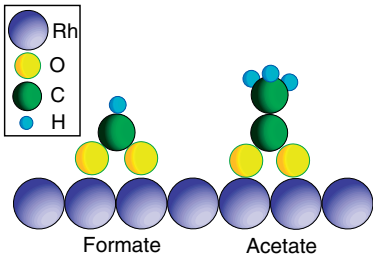

Fig. 4. Schematic adsorption geometry for formate and acetate on the Rh(1 1 1) surface.

identification of the molecule as acetate (CH_3COO), it is still useful to explore how a thorough analysis of the above HRCLS results leads to the same conclusion. First, the high binding energy of the 286.8 eV peak indicates that this carbon atom is part of a molecule in which it bonds to more than one oxygen atom. An alternative explanation to the high BE C1s peak, could be an interaction of CO with atomic oxygen on the surface. However, the C1s shift observed in CO–O coadsorption systems on Rh(1 1 1) [9] are only around 0.1 eV, making this explanation inconsistent with the observed 0.6 eV shift. For the present adsorption system, a carbon atom bonding to two oxygen atoms directly suggests that the molecule is either formate (HCOO) or acetate with both of these molecules bonding to the surface via the two oxygen atoms, see Fig. 4. Of these two alternatives, the acetate offers a simple and very direct explanation for the peak at ~284 eV as simply due to the methyl group of the molecule. Formation of acetate also explains why the 284 eV and the 286.8 eV components appear simultaneously and with about equal intensity for all preparations. In contrast, if the 286.8 eV peak is assigned to formate it becomes necessary to postulate that the 284 eV peak is due to the presence of additional hydrocarbon molecules on the surface and to explain why these hydrocarbons occur with roughly the same coverage as the formate molecules at all different preparation conditions. Finally, a more detailed analysis of the C1s line shapes also agrees with expectations for acetate formation. It is known that C1s emission from adsorbed hydrocarbon molecules contains fine-structure due to the intrinsic excitation of C–H vibrational modes in the photoemission process [11,15]. This manifests itself via the occurrence of a number of components separated in energy by the energy[1] of the vibrational mode. The intensities of these vibrational components follow a Poisson distribution characterised by a so-called S-factor (the intensity ratio between peaks corresponding to excitation of one and zero, respectively, vibration). For the case of adsorbed CH_n groups, the relevant C–H vibrational energy is around 380 meV and the S-factor is roughly proportional to n with a proportionality constant of about 0.12–0.13. Thus the S-factor provides a fingerprint for what CH_n [15] group is present. In Fig. 3 we show a decomposition of the 284 eV peak into three components using Doniach-Šunjić [16] line shapes convoluted with a Gaussian as basis functions. The vibrational components are separated in energy by 385 meV and have intensities that follow a Poisson distribution with an S-factor of 0.37. As seen, this decomposition provides a good description of the 284 eV peak strongly supporting that this emission is from a methyl group. The 286.8 eV peak is so narrow that it is not possible to include a vibrational component with an energy of around 380 meV even if an S-factor as low as 0.1 is used. This is consistent with the fact that the other C atom of the acetate molecules does not bond to any hydrogen atoms. Last on the C1s spectra we note that the current assignment of components is consistent with what has been observed for acetate on Cu(1 1 0) [17] and on Pd(1 1 0) [18].

We now turn to the O1s spectrum, Fig. 3b, measured under the same conditions as used for the C1s spectrum in Fig. 3a. This O1s spectrum may, as shown, be decomposed into three components at 529.5 eV, 530.5 eV, and 532.1 eV, respectively. Of these components, the 529.5 eV component is readily identifiable as due to emission from atomic oxygen present on the surface, and the 532.1 eV as due to emission from the small amount of CO molecules in on-top positions. The coverage of atomic oxygen obtained from Fig. 3b may be estimated to about 0.25 ML by comparison to O1s spectra from a (2×1) oxygen overlayer. In general we always find a significant coverage of atomic oxygen whenever a strong acetate signal is observed in C1s, see also the O1s spectra of Fig. 2b. This is in line with previous results [19] which demonstrate that predosed oxygen stabilizes acetate on Rh(1 1 1). The remaining component at 530.5 eV could, based on its binding energy, in principle be due to emission from CO in threefold-hollow sites. However, as seen from the lack of a C1s peak at 285.4 eV in the corresponding C1s spectrum of Fig. 3a, no such CO is present on the surface under the present conditions. Therefore, the emission around 530.5 eV in Fig. 3b can be safely identified as due to emission from the two oxygen atoms of the acetate molecule. Finally it may be noted that in experiments where the thermal evolution of ethanol layers adsorbed at 90 K is followed, Vesselli et al. [4] observe the simultaneous development of C1s components at 286.9 and 284.4 eV and an O1s component at 530.8 eV, which starts at a temperature just above 250 K. If the 286.9, 284.4 and 530.8 eV components of Vesselli et al. are identified as the present 286.8, 284, and 530.5 eV, respectively, components, the development reported (see Figs. 4 and 5 of [4]) by these authors can be simply interpreted as the formation of acetate during the annealing of the ethanol layer. When annealing ethanol overlayers deposited at 100 K we observe a similar behav-

[1] The vibrational energies relevant for core level photoemission from a specific atom in a molecule are those of the molecule with that particular atom in its core ionised state, i.e., the vibrational energies of the final state in core level photoemission. Thus the vibrational energies encountered in core level photoemission are in general slightly different from those measured by other vibrational techniques like infrared spectroscopy as the latter method probe the un-ionised ground state.

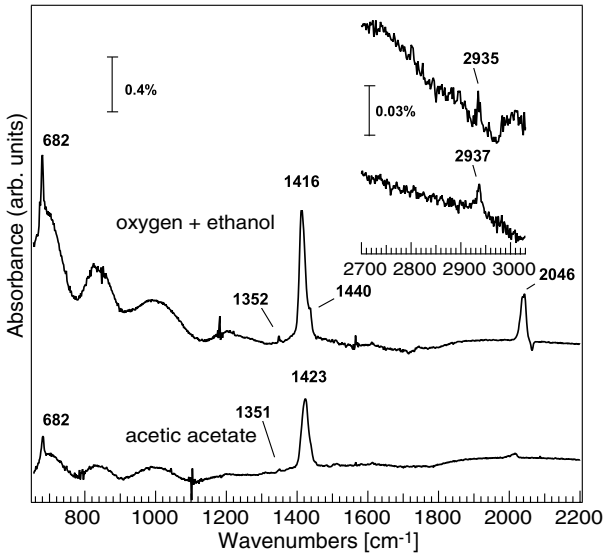

Fig. 5. Infrared absorbance spectra measured after exposure of Rh(1 1 1) to 14 L of a 1:1 ethanol: oxygen gas-mixture at 150 K followed by annealing for 30 s at 300 K (upper spectra) and to 0.15 L of acetic acid at 90 K followed by annealing at 250 K (lower spectra). Insert shows a detailed scan from 2700 to 3025 cm^{-1}.

iour, however, only if the surface is deliberately predosed with oxygen as mentioned previously.

The identification of acetate as a surface intermediate formed during the reaction between oxygen and ethanol on Rh(1 1 1) was conclusively made by surface infrared vibrational spectroscopy. For the surface infrared spectroscopy measurements, the Rh(1 1 1) surface was exposed to 14 L of a 1:1 ethanol:oxygen gas-mixture at a temperature of 150 K. Subsequently the sample was annealed at successively higher temperatures for 30 s after which the sample was cooled to 90 K and infrared absorption spectra were acquired. The spectrum shown in Fig. 5 was recorded after the sample was annealed to 300 K for 30 s and re-cooled to 90 K. For lower annealing temperatures, a rather large amount of ethanol/ethoxy (and possibly other fragments) makes the identification of acetate, less straightforward even though it starts to form at about 250 K. At temperatures above 300 K, the amount of CO increases and above 400 K no acetate is left on the surface. For reference, a spectrum obtained by exposing the clean surface to acetic acid (CH_3COOH) and subsequently heating to 250 K, where acetate is readily formed [20], is shown at the bottom of Fig. 5.

As expected the agreement between the two spectra is essentially one to one. The assignments are shown in Table 1. The small frequency difference, observed for the ν_s (OCO) mode, is attributed to differences in acetate coverages and to the presence of additional oxygen and carbon monoxide on the oxygen plus ethanol surface. The presence of carbon monoxide is seen by the intense ν_s mode at 2046 cm^{-1} attributed to carbon monoxide adsorbed in on-top position [21]. A formate species, HCOO, is expected to give a ν_s (OCO) mode at approximately 1350 cm^{-1} [22] inconsistent with formate being the dominant surface intermediate. The weak spectral feature, observed at 1352 cm^{-1}, assigned to the $\delta_s(CH_3)$, could of course be due to small amounts of formate formed during the decomposion of ethanol. The present assignment is however more straightforward and likely, particularly in the light of the reference spectrum of acetate together with the DFT calculations by York et al. [23]. In Table 1 we also include the DFT calculations, B3LYP/6-311 G(d), by York et al. of acetate adsorbed on Cu(1 1 0). The new scaling factor (0.9679) determined by Andersson and Uvdal [24] was used in Table 1 instead of the zero-point energy scaling factor (0.989) determined for the 6-311+G(3df,2p) basis set and incorrectly used in the work by York et al. The vibrational frequencies in Table 1 therefore differ from the ones published in [23]. The zero-point scaling factors are in general approximately 2% higher than the corresponding factors for the frequencies. By inspection of Table 1 it is clear that the agreement between the two experimental spectra and the calculated frequencies is good in spite of the different surface used for the calculations. The good agreement may indicate that acetate is coordinated to the Rh(1 1 1) surface in the same manner as on the ten atom copper cluster used by York et al. to model the Cu(1 1 0) surface. That is, the O–C–O plane of the adsorbate is oriented perpendicular to the surface and in the bridge plane with each oxygen coordinated to one metal atom, Fig. 4. It may appear a bit

Table 1
Assignment of vibrational modes of acetate, CH_3COO; on Rh(1 1 1)

Mode	Experimental (cm^{-1}) Ethanol + oxygen	Experimental (cm^{-1}) Acetic acetate	Calculation[a] B3LYP/6-311 G + (d)[a] Acetate Cu_{10}	Experimental[a] (cm^{-1}) Acetate Cu(1 1 0) [23]
δ_s (OCO)	682	682	661	678
δ_s (CH_3)	1352	1351	1353	1335
ν_s (OCO)	1416	1423	1403	1434
δ_{as} (CH_3)	1440	not obs	1456	1391
ν_s (CH_3)	2935	2937	2971	2932

Acetate is formed either from reaction between oxygen and ethanol or directly from acetic acid; CH_3COOH.

[a] From DFT calculation of a CH_3COO–Cu_{10} cluster representing the Cu(1 1 0) surface by York et al. [23], using the B3LYP method and 6-311G + (d) basis set. In the present work a new scaling factor, 0.9679; determined by Andersson and Uvdal [24] was used, see text for details.

surprising that our experimental data for acetate agrees better with the calculations for the Cu(1 1 0) model cluster than the corresponding experimental data [23] for the Cu(1 1 0) surface. The agreement between the Cu(1 1 0) surface and the calculations is about 5% in the work by York et al. whereas on the Rh(1 1 1) surface it is within 1%. The most important reason for this is that an incorrect scaling factor was used for the Cu_{10} cluster calculations. As seen in Table 1 the agreement between the calculations and the experiments by York et al. is essentially the same as for the Rh(1 1 1) system, or almost within 1% for all modes but the δ_s (OCO) mode, provided that the correct scaling factor is used.

4. Conclusions

The adsorption of ethanol on clean and oxygen covered Rh(1 1 1) and the reactions occurring at temperatures around 300 K have been investigated by a combination of HRCLS and infrared spectroscopy. The results provide information on ethanol decomposition on clean Rh(1 1 1) as well as on the ethanol oxidation reaction on this surface. For ethanol adsorption on the clean surface, C1s spectra demonstrate the formation of CO in on-top and three-fold-hollow sites and several hydrocarbon fragments most likely including also atomic carbon. The O1s spectra reveal only emission that can be assigned to the oxygen atoms of adsorbed CO but no emission attributable to adsorbed atomic oxygen. From this we conclude that the C–C bond of the ethanol molecule is preferentially broken at this temperature whereas the C–O bond stays intact. If the Rh(1 1 1) surface is precovered by ~0.5 ML of oxygen or if ethanol and oxygen are simultaneously dosed, the C1s spectra still show the formation of CO however the CO molecules are now found to reside exclusively in on-top sites. The C1s spectra also show that the presence of oxygen changes the distribution of hydrocarbon fragments. Most importantly they show the formation of a new rather stable intermediate fragment with a high C1s binding energy of 286.8 eV. It was found that a broader peak at about 284 eV binding energy appeared simultaneously with the 286.8 eV peak and that these two peaks had about equal intensity. From the simultaneous appearance of the two peaks, the high binding energy of the 286.8 eV peak, and a detailed analysis of the C1s line-shapes it was argued that the molecular fragment formed is acetate (CH_3COO–Rh) bonding to the Rh substrate via the two oxygen atoms. This acetate species was conclusively identified by infrared measurements of the vibrational modes. The acetate structure and coordination with respect to the surface was suggested based upon comparison to DFT calculations by York et al. [23] of the vibrational modes of a CH_3COO–Cu_{10} cluster model of the Cu(1 1 0) surface. We find that acetate forms under many different pressure and temperature conditions as long as sufficient oxygen is present on the surface and therefore we suggest that acetate is an important intermediate in the oxidation of ethanol on Rh(1 1 1) necessary for Rh-catalyzed hydrogen-extraction from ethanol.

Acknowledgements

This work has been financially supported by the Swedish Research Council. The support by the MAX-lab staff is gratefully acknowledged.

References

[1] G.A. Deluga, J.R. Salge, L.D. Schmidt, X.E. Verykios, Science 303 (2004) 993.
[2] H. Idriss, Platinum Metals Rev. 48 (2004) 105.
[3] C.J. Houtman, M.A. Barteau, J. Catal. 130 (1991) 528.
[4] E. Vesselli, A. Baraldi, G. Comelli, S. Lizzit, E. Rosei, Chem. Phys. Chem 5 (2004) 1133.
[5] D.C. Papageorgopoulos, Q. Ge, D.A. King, J. Phys. Chem 99 (1995) 17645.
[6] R. Nyholm, J.N. Andersen, U. Johansson, B.N. Jensen, I. Lindau, Nucl. Instrum. Methods Phys. Research A 467–468 (2001) 520.
[7] J.E. Bartmess, R.M. Georgiadis, Vacuum 33 (1983) 149.
[8] A. Beutler, E. Lundgren, R. Nyholm, J.N. Andersen, B.J. Setlik, D. Heskett, Surf. Sci. 396 (1998) 117.
[9] A.J. Jaworowski, A. Beutler, F. Strisland, R. Nyholm, B. Setlik, D. Heskett, J.N. Andersen, Surf. Sci. 431 (1999) 33.
[10] S. Schwegmann, H. Over, V. De Renzi, G. Ertl, Surf. Sci. 375 (1997) 91.
[11] M. Wiklund, A. Beutler, R. Nyholm, J.N. Andersen, Surf. Sci. 461 (2000) 107.
[12] R. Larciprete, A. Goldoni, A. Groso, S. Lizzit, G. Paolucci, Surf. Sci. 482 (2001) 134.
[13] C.M. Whelan, R. Neubauer, D. Borgmann, R. Denecke, H.P. Steinruck, J. Chem. Phys. 115 (2001) 8133.
[14] Handbook of X-ray Photo Emission Spectroscopy (Perkin Elmer; 1978).
[15] J.N. Andersen, A. Beutler, S.L. Sorensen, R. Nyholm, B. Setlik, D. Heskett, Chem. Phys. Lett 269 (1997) 371.
[16] S. Doniach, M. Šunjić, J. Phys. C 3 (1970) 285.
[17] J. Hasselström, O. Karis, M. Weinelt, N. Wassdahl, A. Nilsson, M. Nyberg, L.G.M. Pettersson, M.G. Samant, J. Stöhr, Surf. Sci. 407 (1998) 221.
[18] R.P. Holroyd, R.A. Bennett, I.Z. Jones, M. Bowker, J. Chem. Phys. 110 (1999) 8703.
[19] G. Hoogers, D.C. Papageorgopoulos, Q. Ge, D.A. King, Surf. Sci. 340 (1995) 23.
[20] M. Bowker, Cataly. Today 15 (1992) 77.
[21] K.J. Lyons, J. Xie, W.J. Mitchell, W.H. Weinberg, Surf. Sci. 325 (1995) 85.
[22] R.B. Barros, A.R. Garcia, L.M. Ilharco, Surf. Sci. 591 (2005) 142.
[23] S.M. York, S. Haq, K.V. Kilway, J.M. Phillips, F.M. Leibsle, Surf. Sci. 522 (2003) 34.
[24] M.P. Andersson, P. Uvdal, J. Phys. Chem. A 109 (2005) 2937.

Paper IV

Step induced efficient dehydrogenation of ethanol on Rh.

Andrea Resta, Johan Gustafson, Rasmus Westerström, Anders Mikkelsen, Edvin Lundgren, Jesper N Andersen, Ming-Mei Yang and Wei-Xue Li

In manuscript

IV

Step induced efficient dehydrogenation of ethanol on Rh

Andrea Resta, Johan Gustafson, Rasmus Westerström, Anders Mikkelsen, Edvin Lundgren and Jesper N Andersen

Department of Synchrotron Radiation Research, Institute of Physics, Lund University, Box 118, S-22100, Lund, Sweden

Ming-Mei Yang and Wei-Xue Li

Center for Theoretical and Computational Chemistry, Dalian Institute of Chemical Physics, Chinese Academy of Sciences, 457 Zhongshan Road, Dalian 116023, China

Abstract

We have investigated the decomposition of ethanol on the Rh(111) and Rh(553) surfaces at room temperature using high resolution core level spectroscopy and density functional theory (DFT) based simulations. A detailed analysis of the C1s core level spectra, including analysis of the vibrational fine-structure and comparison to calculated C1s binding energy shifts, shows that ethanol decomposes into CO, ethylidyne (C_2H_3), methylidyne (CH), atomic carbon, and hydrogen. At low ethanol exposures, CH is the dominating hydrocarbon on Rh(111) whereas on Rh(553) atomic C dominates and only a small CH amount is found. At higher ethanol exposures we find a similar behavior, where atomic C dominates over hydrocarbons on Rh(553), while on Rh(111) atomic carbon remains a minority species. The increased dehydrogenation efficiency of the steps on Rh(553) is confirmed by calculated adsorption energies for the various species as well as of the activation barriers for CH dehydrogenation.

I: Introduction

Hydrogen is being considered as a possible major energy sources for the future, to be used in fuel cells where the hydrogen is oxidized into H_2O and electricity is produced. Storage of pure hydrogen, however, implies severe safety-related problems and it has therefore been suggested to store and transport the hydrogen in the form of a more stable hydrogen-containing compound from which the hydrogen is extracted in close proximity to its use in e.g. fuel cells. One such H-containing compound under consideration is ethanol for which it has recently [1, 2, 3, 4] been demonstrated that Rh-ceria based catalytic extraction of hydrogen by partial oxidation is possible at relatively low temperatures.

However, little is known about the reasons for the efficiency of the Rh-ceria based catalysts used for H_2 production. This applies not only to the partial-oxidation reaction but even to the fundamental steps of ethanol adsorption and fragmentation on Rh surfaces. As edges and corners constitute a significant fraction of the surface area in the small Rh particles typically used in real catalysts, it is important to investigate what influence the presence of under-coordinated Rh atoms has on ethanol adsorption and fragmentation. We have therefore undertaken a study of the room temperature adsorption behavior of ethanol on both the flat Rh(111) and the vicinal Rh(553) surfaces where the steps on the latter surface is used to mimic the under-coordinated atoms present at the edges and corners of small Rh-particles. Our results show a significantly different fragmentation behavior of ethanol on these two surfaces demonstrating a large influence of the under-coordinated steps atoms. On both surfaces, we find that predominantly the C-C as opposed to the C-O bond of the ethanol molecule is broken due to the interaction with Rh. On the flat Rh(111) surface, hydrocarbons constitute a large fraction of the final decomposition products indicating non-complete dehydrogenation whereas on Rh(553) an atomic carbon species is found to dominate over hydrocarbon fragments indicating a much more complete dehydrogenation at the steps. The increased dehydrogenation at the steps is shown to be the result of both a significantly lower energy barrier for CH dissociation as well as the dehydrogenation becoming exothermic at the steps.

In addition to providing information on ethanol adsorption and decomposition on Rh(111) and Rh(553), the present study also demonstrates that High Resolution Core Level Spectroscopy (HRCLS) has a large potential for identifying hydrocarbon fragments on surfaces when including a detailed analysis of the C1s vibrational fine structure and comparison to theoretical simulations of surface structures and C1s binding energies. This large potential of HRCLS is not restricted to the present Rh surfaces.

II: Experimental and calculational details

The measurements were performed at beam line I311 at the synchrotron radiation source MAX II in Lund, Sweden. We refer the reader to ref. [5] for a detailed description of the beam line. Experimental procedures were as described in ref. [6]. In short, the surfaces were cleaned by a combination of Ar^+ sputtering and annealing in O_2 and in vacuum. The surface cleanness was checked by HRCLS and the long range order by low energy electron diffraction (LEED). The HRCL spectra were recorded at normal emission and at liquid nitrogen temperatures in order to reduce thermal broadenings.

Ethanol exposures are given in Langmuir (L) (1 L =10^{-6} torr sec) based on the gauge reading with no correction applied for the sensitivity towards ethanol [7]. Ethanol pressures in the low 10^{-8} torr range were typically used except for the lowest exposures. The ethanol was 99.5% pure with dry residuals less than 0.002% and was further purified by freeze-pump-thaw cycles.

The HRCL spectra were decomposed using Doniach-Šunjić line shapes [8] convoluted with Gaussian functions that represent unresolved vibrations and the experimental broadening. A linear background was included in the fits. For the case of hydrocarbons it has long been known [9] that intrinsic excitation of C-H stretch vibrations in the photoemission process gives rise to higher binding energy satellites in the C1s spectra also for the case of chemisorbed molecules see e.g. refs. [10, 11, 12]. The energy separation of the vibrational satellites is in all cases close to 400 meV and the intensity distribution closely follows a Poisson distribution as expected from a linear coupling model [13]. For the decomposition of hydrocarbon spectra we therefore used vibrational components with an energy splitting of close to 400 meV and the additional constraint that the intensities of these components follow a Poisson distribution.

For the slab-based calculations of surface structures we used Density Functional Theory (DFT) as implemented in the DACAPO package [14]. Ion-cores were described by ultrasoft pseudopotentials [15]. In order to describe core ionized C atoms, we employed a pseudopotential constructed for a C atom where a 1s electron had been promoted to a 2p valence level [16,17]. The one-electron wave functions were expanded in a plane wave basis with an energy cutoff of 25 Ry. For the exchange and correlation functional we used the Generalized Gradient Approximation (GGA) as implemented in the PW91 form [18]. For Rh(111) we used a three-layer slab and for Rh(553) a slab containing three (111) Rh layers and allowed the first two of these as well as the adsorbates to relax geometrically. The slabs were separated by vacuum of thickness equivalent to five (111) Rh layers. Energy barriers were found by constrained relaxation with care being taken that the pathways were continuous. Sampling of k-space was done using a (2x4x1) mesh for the (5x2) and (1x2) unit cells used for Rh(111) and Rh(553), respectively. The theoretical lattice constant was used for Rh. Finally, the C1s core level binding energy shifts were calculated as total energy differences between systems where the appropriate C-atoms had been core-ionized.

III: Results and Discussion

C1s spectra measured after representative room temperature ethanol exposures ranging from 0.1 to 30 L on Rh(111) and Rh(553) are shown in Figs. 1a and b, respectively, together with decompositions into a number of components.

III-1: C1s results, overview

The C1s peaks at binding energies above 285 eV can all be assigned to CO molecules adsorbed in different sites on the two surfaces. For Rh(111) the components at ~286 eV and ~285.4eV are assigned to CO molecules in on-top and three-fold-hollow adsorption sites, respectively, based upon their binding energies, as discussed in more detail in [6]. The shoulder at ~286.3 eV on the high binding energy side of the on-top

peak is due to the intrinsic excitation of the C-O stretch vibration in the photoemission process [19] and not to CO in a different configuration. For Rh(553), the C1s components at binding energies similar to those found on Rh(111) are interpreted as

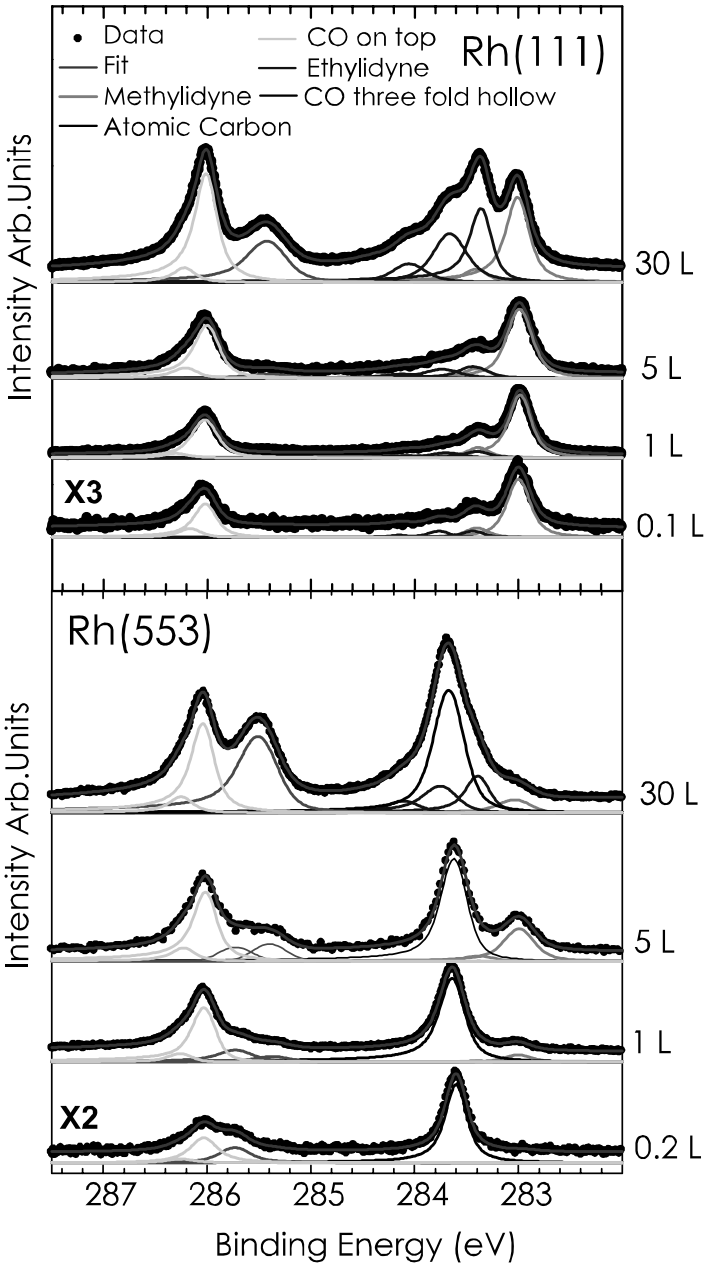

Figure 1. C1s spectra and their decompositions after ethanol exposures at room temperature between 0.1 L and 30 on a) Rh(111) and b) Rh(553). The photon energy is 380 eV.

due to CO molecules in on-top and three-fold-hollow sites on the 111 terraces of the surface. In addition, a C1s component at ~285.7 eV is clearly visible for CO exposures up to 1L. This component can, by comparison to C1s spectra measured after CO exposure of Rh(553) [20], be ascribed to CO molecules adsorbed on-top the Rh atoms at the steps of the (553) surface. For the sake of simplicity we have only included an explicit component for this step-adsorbed CO at the lower ethanol

exposures whereas at higher exposures we have included it as an additional broadening of the on-top component.

As discussed previously [6], the above assignments on Rh(111) are supported by corresponding O1s spectra. We find the O1s spectra for Rh(553) to be very similar to those for Rh(111). In particular we find a similar lack of any emission around 529.5 eV which could be ascribed to atomic oxygen. From this, and the appearance of CO on the surface, we therefore conclude that the C-C bond of the ethanol molecule is broken upon adsorption on Rh surfaces at 300K, whereas the C-O bond is left intact.

The remaining C1s components are all found at binding energies between ~283 and ~284.5 eV, that is, in the binding energy range expected for hydrocarbons and/or for C-species adsorbed on metallic surfaces [11, 21, 22, 23]. Assigning these components to specific molecular fragments is in general difficult due to the large number of possible C-H containing fragments, the close-lying and even overlapping C1s binding energies, and the possibility that some of the components are not due to chemical shifts but instead to the excitation of C-H vibrations in the photoemission process. In the present case we, however, believe that several fragments can be unambiguously identified.

III-2: Rh(111), the hydrocarbon region

We start with the Rh(111) surface and ethanol exposures of up to 5 L as shown in Fig. 1a. For these exposures, the C1s spectra below 285 eV binding energy contain two main components, one at 283.0 eV and one at 283.4 eV. In addition, a broad shoulder is visible, in particular at 5L exposure, on the high binding energy side of the 283.4 eV component. In a previous publication [6] it was tentatively suggested that the 283 eV component was due to atomic C on the surface. Here we show that instead this component is the adiabatic peak from CH (methylidyne) fragments on the surface and that part of the 283.4 eV peak is due to excitation of the C-H stretch vibration of the CH molecule. *A priori* the emission at 283.4 eV could be either a chemically shifted C1s component or, as it is shifted ~400 meV from the 283.0 eV component, a vibrational shake-up [10, 11, 12] of the C-H stretch in the molecular fragment corresponding to the 283.0 eV component, or a combination of these two possibilities. In order to distinguish between these possibilities we performed experiments where fully deuterated ethanol was used as this should reduce [10, 13] the C-H vibrational energies by a factor of $\sqrt{((13/14)* 2)} = 1.36$. As seen from Fig. 2, deuteration causes the 283.4 eV peak to split into two components, one at just above 283.4 eV and one at 283.3 eV. The 283.3 eV component can be identified as due to the excitation of a C-D stretch vibration as the 0.3 eV shift from the 283.0 eV peak is very close to the expected (0.4/1.36) eV = 0.294 eV. The component at just above 283.4 eV in the deuterated spectra is due to a chemically shifted component. We thus can conclude that the 284.4 eV emission in the non-deuterated spectra of Fig. 1 and 2 is due to a C-H vibrational satellite of the 283.0 eV peak and that also part of the intensity comes from a chemically shifted component at that energy.

In identifying that the 283.0 eV component corresponds to methylidyne we make use of the correlation [10, 11, 12, 24] between the intensity ratio (the so-called S-factor) of the first vibrational level and the adiabatic C1s peak and the number of H-atoms bonding to the C-atom. For free molecules [24] and for CH_2 and CH_3 groups in molecules chemisorbed on surfaces [10, 11], the S-factor is found to depend almost

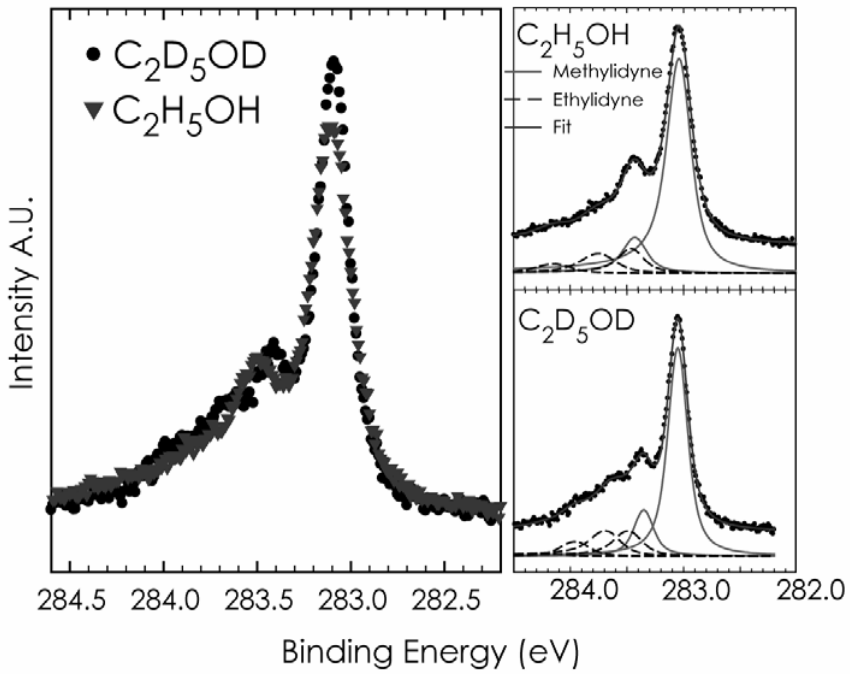

Figure 2: C 1s spectra after an exposure at room temperature of 0.5 L of ethanol (red triangles) and deuterated ethanol (black dots). Decomposition of the C 1s spectra after an exposure of 0.5 L normal and deuterated ethanol, respectively.

linearly on the number of H-atoms bound to the C atom with a proportionality factor of around 0.13 per H-atom whereas for CH species chemisorbed on Pt(111), a slightly larger S-factor of ~0.17 has recently been reported [12]. In the present case, extraction of the S-factor is made difficult by the presence, as described above, of another chemical component overlapping the first C-H vibrational component. However, for the deuterated spectra this difficulty is less severe due to the lowering of the C-D vibrational energy which allows separation of the C-D component and quite unambiguous determination of its S-factor as being ~0.22, see Fig.2. As the S-factor (for the harmonic approximation) increases by close to a factor of $\sqrt{((13/14) * 2)}$ from H to D, the 0.22 determined for the deuterated species corresponds to about 0.16 for the non-deuterated case. Using the latter S-factor for the non-deuterated spectra results in fits where the intensities of the additional chemically shifted component at just above 283.4 eV are very similar to those found for the deuterated case, see Fig.2, demonstrating the internal consistency of the assignment and the S-factors. We thus conclude that methylidyne is found on the surface and gives rise to an adiabatic C1s peak at 283.0 eV binding energy and a vibrational satellite at 283.4 eV with intensity around 0.16 times that of the adiabatic peak.

The presence of methylidyne on the surface is further supported by our theoretical calculations which, as described below, show that the dehydrogenation of CH to C on Rh(111) is not thermodynamically preferred and that the activation barrier for this endothermic reaction is about 1 eV. These conclusions are further supported by other recent calculations, which show methylidyne to be the most stable CH_x ($1 \leq x \leq 4$) molecule on Rh(111) with a high activation barrier for further dehydrogenation [25, 26].

We now turn to the 30 L exposure spectrum in Fig.1a and use this high exposure spectrum to demonstrate that the C1s intensity at ~283.4 eV not accounted for by the methylidyne vibration as well as the shoulders at 283.74 and 284.14 eV are due to ethylidyne.

On Rh(111) the ethylidyne (CCH_3) molecule is adsorbed with the molecular axis normal to the surface plane in a three-fold-hollow site with the CH_3 group furthest from the surface. The two C-atoms of the molecule have different C1s binding energies. The inner C-atom gives rise to C1s peaks at 283.45 and 286.46 eV [10, 11] for the (2x2)-Rh(111)-1CCH_3 and the c(4x2)-Rh(111)-1CO+1CCH_3 structures, respectively. The adiabatic C1s binding energy of the outer C-atom is for these two structures found [10, 11] at 284.07 and 283.64 eV, respectively. Furthermore, the fact that the outer C-atom is part of a methyl group gives rise to additional C-H vibrational fine-structure components with splittings of ~400 meV and an S-factor of ~0.4 [10, 11]. Finally, the strong variation with photon energy of the outer to inner C-atom intensity has been found to provide a reliable fingerprint for the presence of ethylidyne molecules on the surface also when co-adsorbed with CO [10, 11]. For the present spectra we interpret the 283.4 eV component as due to the inner C-atom, the 283.74 eV component as the adiabatic peak of the outer C-atom, and the 284.14 eV component as the first C-H vibration of the outer C-atom of ethylidyne formed on the surface. Using this assignment we obtain an outer to inner C-atom intensity ratio variation versus photon energy as shown in Fig. 3. Clearly, this intensity variation is very similar to the one found for the c(4x2)-Rh(111)-1CO+1CCH_3 overlayer, also shown in Fig.4. In particular we also in the present system find the almost complete suppression of emission from the outer C-atom at 350 eV photon energy very characteristic of ethylidyne on Rh(111). Furthermore, use of an S-factor of 0.4 characteristic of a methyl group (and inclusion of the next C-H vibrational feature at 284.53 eV) provides good fits of the spectra. We therefore, based upon the C1s binding energies, the S-factor, and the intensity variation with photon energy assign

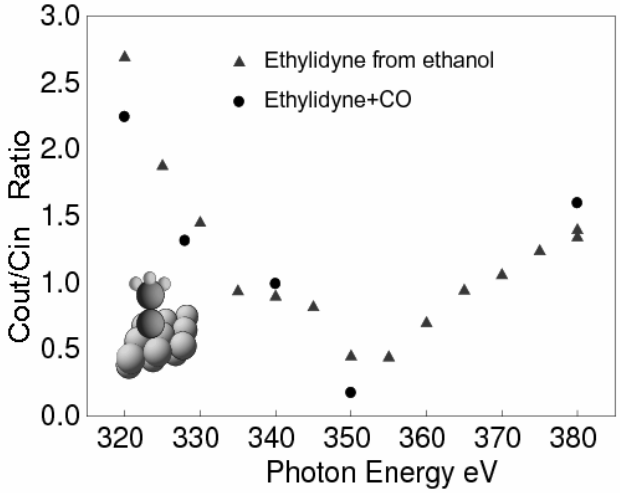

Figure 3: Comparison of the C1s intensity ratio between the outer (C_{out}) and the inner (C_{in}) C-atom of ethylidyne versus photon energy for the present system (red triangles) and ethylidyne co-adsorbed with CO (black dots) from ref. 11.

the 283.4 eV emission as well as the shoulders at 283.74 and 284.14 eV to ethylidyne.

Returning to the lower ethanol exposures in Fig.1a and 2 we point out that the just discussed C1s components from ethylidyne have been included in the decompositions of the low coverage spectra. In addition to the fact that this provides a good description of the measured spectra, the inclusion is also justified by the fact that spectra measured at a photon energy of 350 eV (not shown) show less emission on the high energy side of the 283.4 eV component in agreement with the behaviour of ethylidyne. Finally, it should also be noticed that the outer to inner C intensity ratio is slightly larger for the lower exposures. In addition to the difficulties in determining the exact intensity for the inner C-atom, this behaviour could also be caused by the existence of additional low intensity C1s components due to, e.g., molecular fragments formed at steps and other surface defects, not taken into account in the fitting procedure.

Summing up the Rh(111) results, the decomposition of ethanol at temperatures around 300K results in the formation of CO, methylidyne, and ethylidyne. This, and the fact that no signal attributable to atomic O is observed [6], leads us to conclude that predominantly the C-C bond of the ethanol molecule is broken by the interaction with the Rh-surface.

III-3: Rh(553), the hydrocarbon region

We now turn to Rh(553) and the ~283eV to ~284.5 eV region, see Fig.1b, in order to investigate the influence of the under-coordinated Rh step atoms on the formation of hydrocarbon and/or C-species.

A dramatic difference is seen when comparing the low ethanol exposure spectra of Fig. 1b for Rh(553) to those for Rh(111) in Fig.1a and 2. Instead of the dominating component at 283 eV and a weak emission at ~283.4 eV found for Rh(111), the Rh(553) C1s spectra are dominated by a component at ~283.55 eV and a weak component at ~283 eV. The dominating component at 283.55 eV is very narrow in energy, has a very small asymmetry, and does not exhibit any satellites that can be attributed to C-H vibrations. This immediately suggests that it is due to some form of atomic C on the surface although the binding energy, ~0.55 eV higher than that of CH on Rh(111), is surprisingly high. However, as discussed below, theoretical calculations of the C1s binding energy supports that this component is due to atomic carbon on the surface. The weak component at ~283 eV is in analogy with the Rh(111) results interpreted as due to a small amount of methylidyne on the surface presumably adsorbed on the (111) terraces of the surface. Thus, in contrast to the situation on Rh(111), the decomposition of ethanol on the stepped Rh(553) surface does not stop at the formation of CH but instead continues to almost complete dehydrogenation of the fragments. This conclusion is supported by the theoretical simulations as discussed below.

The 283.56 eV component remains dominant also at higher ethanol exposures. At the highest exposures, see the 30L spectrum of Fig.2, this component broadens and a shoulder develops towards lower binding energy. This behaviour can be reproduced if the aforementioned C1s components characteristic of ethylidyne are included. Thus at higher coverages, ethylidyne also forms on Rh(553), most likely on the 111-type terraces of the surface albeit in much smaller quantities than on Rh(111). The ~283 eV component ascribed to methylidyne increases between the 1 and 5L exposures and

thereafter decreases. From measurements at intermediate exposures we found that the 283eV intensity reaches within 90% of its maximum intensity after ~2L exposure, goes through a maximum at ~5L, and drops below the 90% limit at ~10L. As evidenced by the spectra in Fig.1b, the intensity decrease with exposure is slower than the initial increase. The initial increase of the 283eV component may be rationalized as caused by an increasing deactivation of the steps by the 283.55 eV C-species causing the methylidyne dissociation to become less efficient. The decrease of the 283eV component at higher ethanol exposures is accompanied by the appearance of the ethylidyne components and is therefore interpreted as due to conversion of methylidyne to ethylidyne at higher coverages.

In summary, the decomposition of ethanol on Rh(553) at temperatures around 300K results in the formation of CO, a dominating atomic C-species, a minor amount of methylidyne, and after high ethanol exposures the formation of ethylidyne. As also found for Rh(111), the lack of an O1s component from atomic O-species indicates a predominant C-C bond breaking of the ethanol molecules.

III-4: Comparison to theoretical results

Comparing the experimental results from Rh(111) and Rh(553) we find that the presence of the under-coordinated step atoms on Rh(553) significantly influences the molecular fragments present after ethanol decomposition at room temperature. Based on the interpretations of the experimental data given in sections III-2 and 3, we propose that a major reason for the differences is that Rh(553), in particular at low ethanol exposures, very efficiently dissociates CH whereas on Rh(111) the majority of the CH molecules remain intact. We have investigated this issue of CH stability further by DFT based simulations. In addition to supporting the above interpretation of a high CH dissociation efficiency at the steps, these calculations also provide an explanation to the high C1s binding energy found for the atomic C-species on Rh(553).

In Table I we give the adsorption energies (relative to CH in gas-phase) for fcc and hcp adsorption of CH in a (5x2)-1CH structure on Rh(111) and for CH in various adsorption sites in a (1x2)-1CH structure on Rh(553). Our designations for the various adsorption sites on the Rh(553) surface are shown in Fig.4. Table I also gives the calculated C1s chemical shifts using as reference the C1s binding energy of CH adsorbed in an hcp site in the Rh(111)-(5x2)-1CH structure. On Rh(111), the hcp site is preferred by the CH molecules, whereas on Rh(553) the two three-fold sites on the upper side of the step and the terrace hcp site all are within 50 meV in adsorption energy. It is therefore not possible to unambiguously choose between these three adsorption sites on the Rh(553). For all of these three sites on Rh(553), the C1s binding energy is within 0.13 eV of the value for CH on Rh(111) which on one hand supports the interpretation that the minority 283.0 eV component on Rh(553) is due to CH, but on the other hand also precludes use of the C1s binding energy for distinguishing between the three adsorption sites. Table I also shows that a CH molecule adsorbed in the hcp site below the step would actually exhibit a C1s shift of 0.55 eV relative to the (111) hcp site and would therefore be a candidate for the 283.55 eV component. However, in addition to the fact that the calculated adsorption energy for such an adsorption site is 0.14 eV less favourable than the highest adsorption energy, such a suggestion is inconsistent with the experimental observation that the 283.55 eV component is not accompanied by a C-H vibrational satellite. In

Table I: The CH adsorption energy (E_{ads}) with respect to the CH radical in gas phase and the C1s core level shifts (CLS) relative to CH in the hcp site on Rh(111) for Rh(111)-(5x2)-1CH and Rh(553)-(1x2)-1CH structures, respectively. See Fig.4 for the site-nomenclature used.

Surface	Site	E_{ads} (eV)	CLS (eV)
Rh(111)	Hcp	-6.54	0.00
-"-	Fcc	-6.34	-0.16
Rh(553)	Fcc(up)	-6.58	-0.13
-"-	Terrace(hcp)	-6.55	0.00
-"-	Hcp(up)	-6.53	-0.03
-"-	Hcp(low)	-6.44	0.55
-"-	Fcc(low)	-6.39	0.04
	Terrace(fcc)	-6.28	-0.14
	Bridge(step)	-6.16	-0.12

Table II: The C adsorption energy (E_{ads}) per C-atom with respect to a C atom in gas phase and the C1s core level shifts (CLS) relative to CH in the hcp site on Rh(111) for Rh(111)-(5x2)-1C and Rh(553)-(1x2)-2C structures, respectively, where in the latter case the two C-atoms are placed in equivalent sites along the step. See Fig.4 for the site nomenclature used.

Surface	Site	E_{ads} (eV)	CLS (eV)
Rh(111)	Hcp	-7.18	0.03
Rh(553)	Hcp(low)	-7.20	0.47
-"-	Fcc(up)	-6.88	0.33
-"-	Hcp(up)	-6.83	0.23
-"-	Terrace(hcp)	-6.72	0.05
-"-	Terrace(fcc)	-6.42	0.01
	Fcc(low)	-6.38	0.06
	Bridge(step)	-5.97	0.08

Table II we give the adsorption energy per C atom (relative to a C atom in gas-phase) for a (5x2)-1C structure with the C-atom in the (stable) hcp site on Rh(111) and for various adsorption sites in a (1x2)-2C structure on Rh(553) where the two C atoms

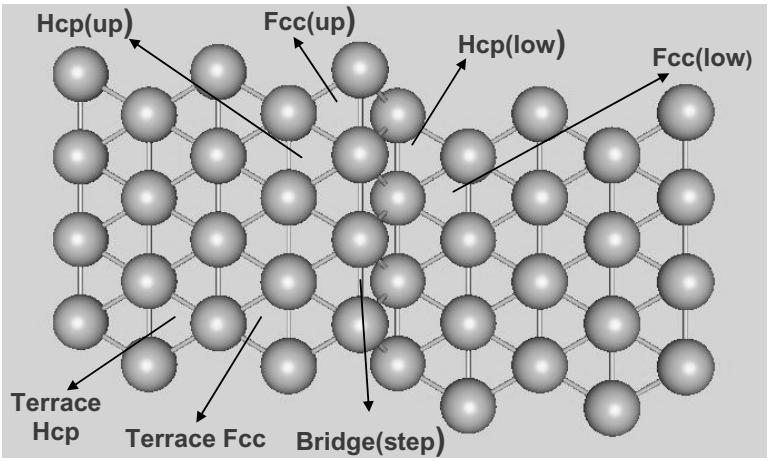

Figure 4: Top-view of the Rh(553) surface. The designations used for the various adsorption sites considered are shown.

have been placed in equivalent sites along the step. For Rh(553), the hcp(low) site is seen to be preferred by at least 0.32 eV per C-atom over other sites and furthermore to give a C1s binding energy shift of 0.47 eV relative to CH in hcp sites on Rh(111). Thus this adsorption site for C provides a straightforward explanation for the dominating 283.55 eV peak in the experimental C1s spectra for Rh(553). In passing we note that calculations using a (1x2)-1C structure with the C-atom in an hcp(low) site give a C1s shift of 0.46 eV, i.e. very similar to that in Table II, and additionally show that the C-C interaction in the (1x2)-2C structure is repulsive and quite large, 0.68 eV per unit cell. Calculations for a number of C-CH co-adsorption systems show that the hcp(low) site is preferred by C also in such systems and most importantly that the C1s binding energy of the C atom is only weakly influenced by the co-adsorbed CH. For most co-adsorption geometries, keeping the atomic C in the stable hcp(low) site, we find a small attractive interaction. However, if the CH is placed in an adjacent hcp(low) site a strong repulsive interaction of 0.72 eV results. Thus C-CH co-adsorption in hcp(low) sites is excluded. Based on the above we therefore assign the 283.55 eV C1s peak on Rh(553) to C-atoms situated in the hcp site at the bottom of the steps.

We now turn to the issue of dissociation of CH on the two surfaces and show in Fig. 5 the result of an extensive search for low energy reaction paths for the dissociation of CH on Rh(111) and Rh(553). As seen, clear differences exist between the two surfaces. The 0.96 eV barrier for dissociation on the Rh(111) surface is reduced to only 0.59 eV on Rh(553) for a reaction path that starts out at the fcc(up) site and ends at the hcp(low) site. These energy barriers on their own would be sufficient for explaining why dissociation at room temperature occurs on Rh(553) and not on Rh(111). In addition to this, Fig.5 shows that CH dissociation on Rh(111) is endothermic whereas it becomes slightly exothermic on Rh(553). Thus not only kinetics but also energetics favour the observed behaviour of CH dissociation at the steps of the Rh(553) surface and stability of CH on the flat Rh(111) surface. We are not aware of any other calculations of CH dissociation for vicinal Rh substrates, but note that a recent calculation [27] for Ni found a similar behaviour with the slightly

endothermic dissociation of CH on Ni(111) becoming exothermic on the stepped Ni(211) surface.

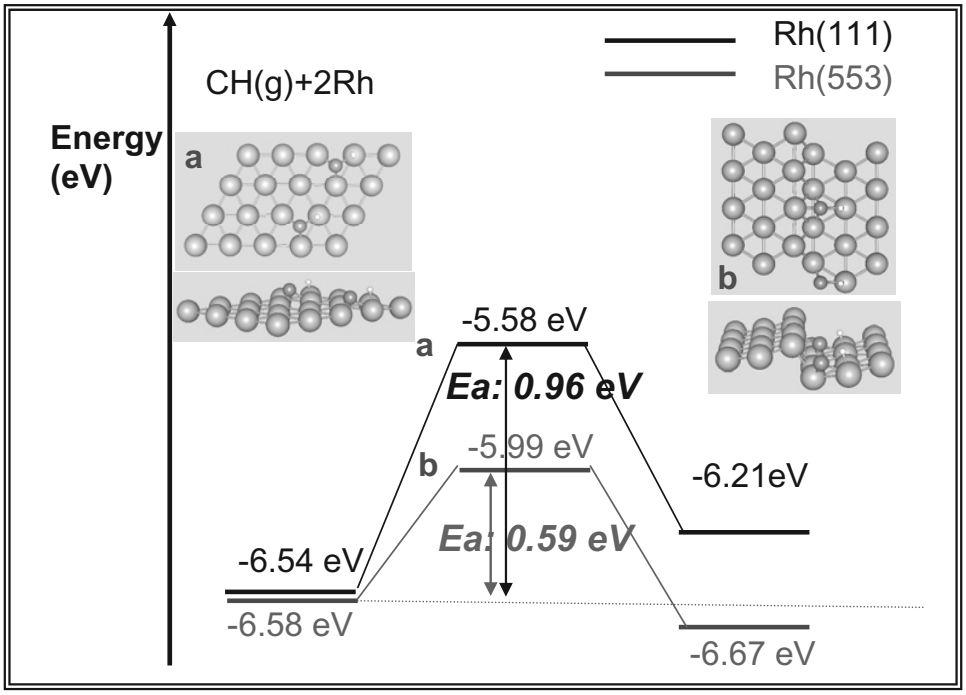

Figure 5: Adsorption energies on Rh(111) (red) and Rh(553) (black) relative to CH in gas phase of: left: CH, middle: the transition state, and right: C and H. The dissociation barriers for the two surfaces are shown. The geometry prior to (upper) and after (lower) the dissociation is shown in a) for Rh(111) and b) Rh(553).

IV: Summary and conclusions

The adsorption of ethanol at room temperature on the Rh(111) and its vicinal surface Rh(553) has been investigated by a detailed analysis of high resolution core level spectroscopy data including comparison to calculated C1s binding energy shifts. Extensive DFT-based simulations of adsorption structures and transition states were used to address issues related to the different stability of CH fragments on the two surfaces.

Both surfaces were found to predominantly dissociate the carbon-carbon bond and preserve the carbon-oxygen bond leading to adsorbed CO but no adsorbed atomic O. In addition to CO significant amounts of methylidyne and ethylidyne are formed on Rh(111), the latter presumably via a reforming reaction. On Rh(553), the dominant surface species in addition to CO was shown to be atomic C adsorbed in the hcp sites on the lower side of the steps. The surprisingly high C1s binding energy of such C-atoms was reproduced by the calculations. In agreement with the experimental results DFT-based simulations demonstrated that the activation barrier for CH dissociation was lowered from 0.96 eV on Rh(111) to only 0.59 eV at the Rh(553) steps and furthermore that the CH dissociation changes from endothermic on Rh(111) to exothermic on Rh(553). These significant differences in kinetic barriers as well as energetics show that ethanol adsorption and decomposition on small Rh particles with their large concentration of low-coordinated edge and corner atoms are not well-

described by the flat Rh(111) surface. The under-coordinated atoms at steps are necessary in order to obtain complete dehydrogenation of ethanol.

Acknowledgements

This work has been financially supported by the Swedish Research Council and by the Knut and Alice Wallenberg Foundation. Support by the MAX-lab staff is gratefully acknowledged. Wei-Xue Li gratefully acknowledges financial support from the National Natural Science Foundation of China (No. 20503030) and the Chinese Academy of Sciences "Bairen Project".

References

1 G. A. Deluga, J. R. Salge, L. D. Schmidt, X. E. Verykios. Science **303** (2004) 993

2 S. Cavallaro, V. Chiodo, A. Vita, S. Freni. J. of Power Sources **123** (2003) 10–16

3 Hyun-Seog Roh, Yong Wang, David L. King, Alexandru Platon, and Ya-Huei Chin, Cat. Let. **108** (2006) 15

4 F. Frusteri, S. Freni, L. Spadaro, V. Chiodo, G. Bonura, S. Donato, S. Cavallaro. Cat. Com. **5** (2004) 611–615

5 R. Nyholm, J. N. Andersen, U. Johansson, B.N. Jensen, I. Lindau, Nucl. Instr. & Meth. in Phys. Res. A 467-468, (2001) 520.

6 A. Resta, J. Blomquist, J. Gustafson, H. Karhu, A. Mikkelsen, E. Lundgren, P. Uvdal and J.N. Andersen, Surf. Sci. **600**, (2006), 5136.

7 J. E. Bartmess, R. M. Georgiadis, Vacuum **33**, (1983) 149.

8 S. Doniach, M. Šunjić, J. Phys. C **3** (1970) 285

9 U. Gelius, S. Svensson, H. Siegbahn, E. Basilier, Å. Faxälv, K. Siegbahn, Chem. Phys. Lett. **28** (1974) 1.

10 J.N. Andersen, A. Beutler, S.L. Sorensen, R. Nyholm, B. Setlik, D. Heskett, Chem. Phys. Lett. **269** (1997) 371

11 M. Wiklund, A. Beutler, R. Nyholm, J.N. Andersen, Surf. Sci **461** (2000) 107

12 T. Fuhrmann, M. Kinne, C.M. Whelan, J.F. Zhu, R. Denecke, H.-P. Steinrück, Chem. Phys. Lett. **390** (2004) 208.

13 S. Cederbaum, W. Domcke, J. Chem. Phys. **64** (1976) 603

14 Hammer, K. W. Jacobsen, V. Milman, and M. C. Payne, J.Phys.: Condens. Matter **4**, (1992), 453.

15 D Vanderbilt, Phys. Rev. B **41**, (1990) 7892.

16 M. Birgersson, C.-O. Almbladh, M. Borg, and J. N. Andersen, Phys. Rev B **67**, (2003) 045402.

17 J. G. Wang, W. X. Li, M. Borg, J. Gustafson, A. Mikkelsen,T. M. Pedersen, E. Lundgren, J. Weissenrieder, J. Klikovits, M. Schmid, B. Hammer, and J. N. Andersen, Phys. Rev. Lett., **95** (2005) 256102

18 J. P. Perdew, J. Chevary, S. Vosko, K. A. Jackson, M. R. Pederson, D. Singh, and C. Foilhais, Phys. Rev. B **46**, (1992) 6671.

19 M. Smedh, A. Beutler, T. Ramsvik, R. Nyholm, M. Borg, J.N. Andersen, R. Duschek, M. Sock, F. P. Netzer, M.G. Ramsey, Surf. Sci. **491** (2001) 99

20 Jesper N. Andersen, Andrea Resta, Edvin Lundgren, Johan Gustafson, Xiu-Fang Ma, Wei-Xue Li, Jianguo Wang and Bjørk Hammer, to be published

21 R. Larciprete, A. Goldoni, A. Groso, S. Lizzit, G. Paolucci, Surf. Sci. **482** (2001) 134

22 C.M. Whelan, R. Neubauer, D. Borgmann, R. Denecke, H.P. Steinruck, J. Chem. Phys. **115** (2001) 8133

23 Handbook of X-ray Photo Emission Spectroscopy (Perkin Elmer; 1978).

24 S. J. Osborne, S. Sundin, A. Ausmees, S. Svensson, S.L. Sorensen, L. J. Saethre, O. Svaeren, J. Végh, J. Karvonen, S. Aksela, A. Kikas, J. Chem. Phys. **106** (1997) 1661.

25 B. S. Bunnik , G. J. Kramer, J. Cat. **242** (2006) 309.

26 Ming-Mei Yang, Xinhe Bao, and Wei-Xue Li, J. Chem. Phys. **127** (2007), 024705

27 H. S. Bengaard, J. K. Nørskov, J. Sehested, B. S. Clausen, L. P. Nielsen, A. M. Molenbroek, J. R. Rostrup-Nielsen, J.Cat. **209** (2002) 365.

Paper V

Step dependent hydrocarbon decomposition.

A. Resta, E. Lundgren and J. N Andersen

In manuscript

V

Step dependent hydrocarbon decomposition

A. Resta, E. Lundgren and J. N Andersen.
Department of Synchrotron Radiation Research, Institute of Physics
Lund University, Box 118, SE-221 00 Lund, Sweden.

Abstract

We have studied the formation of ethylidyne from adsorbed ethylene upon annealing and the subsequent decomposition of ethylidyne at higher temperatures on Rh(111), Rh(322) (A-step), and Rh(553) (B-step) by high resolution core level spectroscopy. By a detailed analysis of the C1s spectra, including analysis of the vibrational fine-structure, we are able to distinguish between chemically different C atoms in small hydrocarbons adsorbed on these surfaces. We use this to monitor the ethylidyne formation and the subsequent decomposition and show that the ethylidyne backbone decomposes into methylidyne, and atomic C at increasing temperatures. The onset temperatures for formation and decomposition of ethylidyne, as well as the relative amounts of the various decomposition products, are shown to depend on the exact geometry of the surface.

The A-steps are found to promote ethylidyne decomposition at low temperatures but the resulting dissociation products adsorb strongly at the steps and thereby prevent further decomposition. On the B-steps, the decomposition temperature is slightly higher, but the decomposition products are more easily released from the steps, resulting in a continuous dissociation process. Our results nicely illustrate the Sabattier principle.

Introduction

The concept of active sites in catalysis has been discussed for almost a century [1]. More recent studies using modern experimental and theoretical techniques have studied the details of the atomic scale dissociation and the reaction pathways on such sites, in particular at steps of vicinal surfaces [2, 3, 4, 5, 6]. Because of the under-coordinated atoms at the steps, various properties in the vicinity of steps are distinctly different from those at the terraces. For instance, the steps introduce new diffusion barriers for the adsorbates, changing the surface mobility at the steps [7, 8], or they may significantly change the adsorption energy [6, 9, 10].

In the light of this knowledge, we have studied the temperature induced formation of ethylidyne from adsorbed ethylene and the subsequent decomposition of the ethylidyne on Rh(111), Rh(322) (A-step), and Rh(553) (B-step) by advanced high resolution core level spectroscopy. We show that the temperature dependence of the ethylidyne decomposition differs amongst the surfaces, and that the presence of steps clearly promotes decomposition. In addition, we show that although the decomposition at low ethylidyne coverage occurs at lower temperatures on A- than on B-steps, the resulting products adsorb strongly on the A-steps and poison the enhanced step activity, whereas on the B-steps the products are more easily released, ensuring the continuation of the catalytic activity. The results illustrate not only the reaction capabilities of the under-coordinated step atoms, but also how the reactivity of an active site is a delicate balance between the strength of the adsorption and activation energies, which both depends on the local geometrical arrangement of the atoms.

Experimental details and decomposition procedure

The experiments were performed at beam line I311 at MAX II in Lund, Sweden [11]. The HRCL C1s spectra were recorded using normal emission keeping the sample at 90K in order to reduce the thermal broadening. The excitation energy used for the C1s was 380 eV unless otherwise stated. The sample mounting, the cleaning procedure and the control of surface cleanliness and ordering have been described elsewhere [12, 13]. High purity (99.8%) ethylene was introduced into the vacuum chamber via a leak valve. Exposures are given in Langmuir (1L = 10^{-6}torr sec) based on the pressure gauge reading.

The spectra were decomposed using Doniach-Sunjic line shapes [14] convoluted with a Gaussian distribution, which represents unresolved vibrations and the experimental broadening. A linear background was included in the fits. For the vibrational components caused by the C-H stretch vibration in the C 1s spectra we used an energy shift of 390 meV [15, 16] and constrained the intensities to follow a linear coupling model [17, 18]. For the decomposition of photoemission spectra from samples containing both ethylidyne and methylidyne at intermediate temperatures, we used a methylidyne line-shape from methylidyne overlayers obtained by decomposition of ethylidyne on Rh(111) at higher temperature.

The spectra are collected in normal emission with respect to the macroscopic surface. The angle between the macroscopic (553) and (322) surfaces, respectively, and their (111) terraces is ~12 degrees. This angle will affect the photoelectron diffraction of the C1s emission, which is known [15, 16] to be strong for the present system in the used photon energy range, and thereby also the C1s intensity. Therefore the C1s area obtained for the vicinal surfaces can not be compared to the C1s area from the (111) surface in order to estimate the coverage. Thus ethylidyne coverages are not given for the vicinal surfaces. For Rh(111), the ethylidyne coverages are obtained by using the (2x2) saturation structure at 0.25 ML [19,20] as reference.

Results

Rh(111), Rh(553), and Rh(322): Ethylidyne formation

It is known from literature that ethylene adsorbed at low temperature on Rh(111) forms ethylidyne when annealed [19, 20]. The first step in the present experiments is to study at which temperature ethylidyne is formed on the Rh(111), Rh(322), and Rh(553) surfaces. We have previously studied the system extensively [15, 16] by high resolution core level spectroscopy and have shown that the ethylidyne may be identified by the presence of two C1s components from the inner (lower binding energy) and the outer (higher binding energy) C atoms. In addition, the component from the outer atom contains vibrational components at higher binding energies, due to the excitation of the C-H stretch vibration of the methyl group during the photoemission process. Thus the CH_3 group of the ethylidyne has a clear signature in the C1s spectra.

The formation temperature of ethylidyne is here detected by the appearance of the CH_3 signature, during the sequential annealing. The results are summarized in Fig 1. It can be seen that the ethylidyne formation (the appearance of the CH_3 signal at 284.1 eV) depends on the presence of steps and occurs at lower temperatures for the stepped surfaces. The results are also given in the column “Formation Temperature” of Table 1.

Rh(111), Rh(553), and Rh(322): Ethylidyne formation after different exposures

Fig. 2a shows C1s spectra from Rh(111) for different ethylene exposures at 90 K and subsequent annealing at 242 K, which is the lowest temperature at which the conversion of ethylene to ethylidyne is completed. In all spectra only the signal from ethylidyne is observed, no decomposition to any intermediate can be detected. In particular, it is important to note that also for the low exposures only ethylidyne can be observed in the C1s spectra. It is also interesting to note that the chemical shift between the inner and the outer carbon of the ethylidyne changes with coverage from 0.61 eV at 0.25 ML to 0.33 eV at 0.03 ML, as summarized in Table 1. This coverage dependence of the C1s shift between the inner and outer C atom is almost entirely caused by a shift of the absolute C1s binding energy of the outer C atom presumably caused by an increasing interaction between these C-atoms as the distance between the ethylidyne molecules decreases with increasing coverage.

Fig. 2b shows the corresponding C1s spectra from the Rh(553) surface using an annealing temperature of 214 K, i.e. lower than that used for Rh(111). At 214 K, the C1s signal from the outer ethylidyne C-atom attains its maximum indicating that the highest ethylidyne coverages are obtained for annealing at this temperature. In addition to the signal from ethylidyne, a small component towards lower binding energy can also be seen in the 0.2 and 1L situations, indicating the onset of ethylidyne decomposition already at 214K.

It can also be seen in Fig. 2b that, as on the (111) surface, the binding energy position of the outer carbon is affected by the surface coverage, see also Table 1. The shift between the inner and outer C atoms is, however, 0.09 eV larger on Rh(553) than on Rh(111) for the highest coverage. Following the argumentation for the (111) surface, a larger shift could indicate that the ethylidyne density is either higher on the (111) terraces on the Rh(553) surface than on the Rh(111) surface, or that the steps themselves affect the outermost carbon atom in such a way that its C1s binding energy increases.

Turning to the Rh(322) surface, Fig. 2c shows the development of the C1s spectra as function of the ethylidyne coverage. First, it is important to note that no ethylidyne can be observed for the lowest ethylene exposure (0.2 L) at 214 K, in contrast to the (553) and (111) surfaces. Only the decomposition products, methylidyne and atomic C, can be observed (see below for the assignment) on Rh(322). At low coverages, all ethylene is directly transformed into methylidyne and atomic C, even at temperatures as low as 150 K (not shown). The observations from Fig. 2c suggest that the A-steps immediately decompose the ethylene at low temperatures, as opposed to the B-steps on the (553) surface. At higher coverages, an ethylidyne signature starts to appear in the C1s spectra, however the signals from methylidyne and the atomic C from the initial decomposition at low coverages are always present.

A binding energy shift between the inner and outer carbon atoms can also for Rh(322) be seen as the coverage is increased (see Table 1). This is similar to what was observed in the case of Rh(553) and Rh(111), again suggesting an increasing ethylidyne density on the surface affecting the C 1s binding energy of the outer ethylidyne carbon atom or an influence of the steps themselves.

Rh(111), Rh(553), and Rh(322): Peak assignments for decomposition products

In order to extract information about the identity of the decomposition products and decomposition temperatures, all components in the C1s spectra must be identified. The decomposition products on the surfaces can be more easily identified by fully decomposing the ethylidyne for the lowest ethylene exposure (0.2 L), see Fig 3.

In the case of the Rh(111) surface, the spectrum in Fig. 3a measured after an anneal at 342K has all the characteristics of methylidyne on Rh(111) [21]. The main peak at ~283 eV is the adiabatic component and the small peak at ~283.4 eV is the vibrational satellite from excitation of the C-H stretch vibration. From Fig 3a, the decomposition parameters for the methylidyne can be extracted and used to describe the methylidyne component in all spectra C1s spectra shown in the present paper. In this way, we can follow the decomposition process of ethylidyne as the annealing temperature is varied.

A similar fitting procedure as on the Rh(111) surface can also be used for the vicinal surfaces. However, an additional intense component at 283.58 eV has to be included for both surfaces, see Figs. 3b and c. This binding energy is close to that found for atomic carbon on the (111) surface [22]. In addition, no satellite peaks are present on the high binding energy side of the component where C-H vibrations should be found, excluding that this C atom has any bonds with H-atoms. These observations lead us to conclude that the 283.58 eV component observed on the vicinal surfaces is due to atomic carbon. This assignment is also confirmed by explicit calculation of the C1s binding energy for atomic C on Rh(553) in ref. 21. We thus conclude that atomic carbon is produced to a much higher extent on the vicinal surfaces as the ethylidyne is decomposed than on the flat (111) surface. A very similar observation of enhanced atomic C formation has recently been made for the decomposition of ethanol on Rh(553) [21] where theoretical calculations additionally showed that CH is thermodynamically stable over atomic C and H on Rh(111) but not on the steps of the Rh(553) surface.

Being armed with the knowledge that methylidyne and atomic carbon appears as decomposition products of ethylidyne on the studied Rh surfaces, we may follow the detailed temperature dependence of the ethylidyne decomposition on flat and stepped Rh surfaces.

Rh(111), Rh(553), and Rh(322): Decomposition of ethylidyne

Fig. 4a shows the development of the C1s spectra after 10 L exposure of ethylene as the Rh(111) sample is annealed at different temperatures. Only ethylidyne can be observed after annealing at 242K and at room temperature. At 342 K, an additional component at 283.05 eV can be observed, which corresponds to the above described emission from methylidyne. Fig. 5a shows the area underneath the methylidyne component as function of the annealing temperature. The inset shows typical C1s components for the fitting procedure of the experimental spectra, including two components from the carbons of the ethylidyne, one component for the methylidyne plus two vibrational components for ethylidyne and one for methylidyne. Two different regimes can be observed in Fig. 5a, one at lower temperature where only ethylidyne is observed, and one where the decomposition process into methylidyne occurs. It can clearly be seen that for all initial ethylene coverages, the ethylidyne decomposition into methylidyne starts at a temperature close to 295 K and that the decomposition is independent of the initial ethylidyne coverage.

The decomposition of ethylidyne into methylidyne on the (553) surface is shown in Fig. 4b from a 10 L ethylene exposure. Here we see that the C1s peak due to methylidyne appears already at a temperature of 242K. The more efficient decomposition is assigned to the step atoms on the Rh(553) surface. Further, a significant amount of atomic carbon is found on the surface as the ethylidyne is decomposed, therefore also this component must be included in the fitting procedure. The complete dehydrogenation of the hydrocarbons leading to atomic C is also

assigned to occur at step atoms in agreement with the conclusions of ref. 21. Fig. 5b shows that for all initial ethylene coverages, ethylidyne decomposition on Rh(553) starts at a well defined temperature. The behavior is similar to what was observed on the (111) surface, except that the onset temperature for ethylidyne decomposition is 100K lower than on the (111) surface. Also in the case of Rh(553), the decomposition temperature does not depend on the ethylidyne coverage.

Turning to the decomposition of ethylidyne into methylidyne and atomic carbon on the Rh(322) surface, a similar analysis as for the two previous surfaces leads to a surface coverage dependence of the decomposition temperature for this surface. Fig.4c shows the development of the C1s spectra of an ethylidyne overlayer produced by 10L ethylene exposure at 90 K and subsequent annealing. A decomposition temperature of ~300 K is found for this high coverage overlayer, see Fig.5c, which is comparable to the temperature for Rh(111) and significantly higher than for Rh(553). The similarity to Rh(111) is also illustrated by the observation that for high ethylene exposures of Rh(322), ethylidyne is, as on Rh(111), still present at 342 K, whereas on (553) ethylidyne completely decomposes at that temperature. However, for a 1 L ethylene exposure, the ethylidyne decomposition temperature changes to ~210 K. In the experiment for the lowest ethylene exposure (0.2 L) ethylidyne does not even form, indicating very low activation energy for the decomposition of the ethylene or ethylidyne into methylidyne and atomic carbon. This is summarized in Fig.5c which demonstrates that on Rh(322), the conversion of the ethylidyne into methylidyne strongly depends on the coverage.

An interesting observation is that the shift between the inner and outer carbon in the ethylidyne decreases as the decomposition procedure proceeds for Rh(553) and Rh(322) but not for Rh(111). As discussed previously, such shifts are related to the ethylidyne coverage and, as discussed further below, we believe that the present observation contains information on the decomposition process on a more mesoscopic length scale.

Discussion

It is interesting to discuss the differences between the surfaces and their ability to decompose ethylidyne at different coverages and temperatures. Our measurements show that at low exposures, ethylidyne decomposes at lower temperatures on the Rh(322) surface than on the (553), while higher temperatures are needed to decompose ethylidyne at high exposures on the (322) than on the (553).

Comparing the plots of the degree of decomposition of the ethylidyne on the (111), (553) and (322) surfaces in Fig. 5, it is clear that the (111) and (553) surfaces have a coverage independent such temperature. However, the almost 100K lower temperature needed on Rh(553) suggests that the B-steps are highly efficient in dissociating the ethylidyne. At first glance, the Rh(322) appears to be even more efficient, however this is only so at low coverages. At higher coverages, the decomposition temperature is in fact similar to that of Rh(111), strongly suggesting that a continued efficient step induced dissociation is inhibited by the dissociation products, or a self-poisoning effect. It is likely that the decomposition products methylidyne and carbon, attach at the step edges on both the (553) and the (322). However, in the case of the (322), the active sites, the step-atoms, remain blocked for further decomposition even though the sample is annealed at higher temperatures. Therefore, the observed difference in behavior of the two vicinal surfaces can be explained by higher adsorption energy of the decomposition products on the A-steps

than on the B-steps. Much higher temperatures are therefore needed on the (322) surface to sustain ethylidyne decomposition.

A second interesting phenomenon observed in this adsorption system concerns the binding energy shift of the outermost carbon atom in the ethylidyne. The measurements show that for all surfaces, the shift between the inner and outer carbon atoms increases with increasing ethylidyne coverage. The three surfaces show a different behavior as the ethylidyne layer is decomposed into methylidyne and atomic carbon. On the Rh(111) surface, no shift between the inner and outer carbon can be detected. Assuming that the shift is due to an increase/decrease in the layer density, no shift indicates that the local density for the majority of the ethylidyne molecules has not been changed. This will occur if the decomposition instead of happening homogeneously over the whole surface takes place via a nucleation and growth mode as this will create 2-dimensional islands of decomposition products, see Fig. 6a. Such islands only influence the small fraction of intact ethylidyne molecules at their perimeter. Turning to the vicinal surfaces, a clear shift can be observed as the ethylidyne layer is decomposed. The reason for this difference is most likely that the decomposition occurs along the steps thereby creating 1-dimensional islands of decomposition products. The change of dimensionality in itself will result in a larger degree of intermixing between remaining ethylidyne molecules and decomposition products leading to a larger fraction of the ethylidyne molecules being affected than for the Rh(111) case. For example, under the reasonable assumption that only two rows of ethylidyne can adsorb along the steps, as shown in Fig.6b, decomposing all molecules at the steps will cause all remaining ethylidyne molecules to be affected, Fig.6b.

Finally, our study shows that both A- and B-steps produce fully dehydrogenated carbon species at 342K whereas CH is still stable on the flat Rh(111) surface at this temperature. This confirms experiments and calculations previously presented for methylidyne dehydrogenation from ethanol decomposition on Rh(553) and Rh(111). In that study it was shown that the methylidyne dehydrogenation is endothermic with a high activation energy on Rh(111), but exothermic and with a lower activation energy on Rh(553)[21].

Summary:

We have studied the ethylene exposure and subsequent chemical transformation into ethylidyne, methylidyne and atomic carbon on the Rh(111), Rh(553) and Rh(322) surfaces. Our study demonstrates the complexity of the system and the potential of HRCLS to disentangle the presence of the different species on the surface. We show that the A-step promotes ethylidyne decomposition at low temperatures (low activation energy), but the resulting dissociation products adsorb strongly at the steps, preventing further decomposition. On the B-steps, the dissociation temperature is slightly higher (higher activation energy), but the products are removed more easily from the steps, resulting in a continuous dissociation process. Our results nicely illustrate the Sabattier principle, a delicate interplay between the adsorption energies and activation energies to promote or poison a catalytic reaction.

Acknowledgments

This work was financially supported by the Swedish Research Council and by the Knut and Alice Wallenberg Foundation. Support by the MAX-lab staff is gratefully acknowledged.

References

[1] H.S. Taylor Proc. Royal Soc. London A **108** (1925) 105
[2] T. Zambelli, J. Wintterlin, J. Trost, G. Ertl Science **273** (1996) 1688
[3] S. Dahl, A Logadottir, R. C. Egeberg, J.H. Larsen, I. Chorkendorff, E. Törnqvist, J.K. Nørskov. Phys. Rev. Lett. **83** (1999) 1814
[4] B. Hammer Phys. Rev. Lett. **83** (1999) 3681
[5] P. Gambardella, Ž. Sljivancanin, B. Hammer, M. Blanc, K. Kuhnke and K. Kern. Phys. Rev. Lett. **87** (2001) 056103
[6] J. G. Wang, W.X. Li, M.Borg, J. Gustafson, A. Mikkelsen, T. M. Pedersen, E. Lundgren, J. Weissenrieder, J. Klikovits, M. Shmid, B. Hammer and J. N Andersen. Phys. Rev. Lett. **95** (2005) 256102
[7] Sondan Durukanoğlu, Oleg S. Trushinand, Talat S. Rahman Phys. Rev. B **73** (2006) 125426
[8] J. Ma, L. Cai, X. Xiao, M.M.T. Loy Surf. Sci. **425** (1999) 131
[9] B.Hammer, O.H. Nielsen and J.K.Nørskov. Cat. Lett. **46** (1997) 31
[10] B. Tränkenschuh, C. Papp, T. Fuhrmann, R. Denecke, H.-P. Steinrück Surf. Sci. **601** (2007) 1108
[11] R.Nyholm, J. N. Andersen, U. Johansson, B.N. Jensen, I. Lindau. Nuclear Instruments and Methods in Physics Research A **467-468** (2001) 520
[12] J. Gustafson, M. Borg, A. Mikkelsen, S. Gorovikov, E. Lundgren, J.N. Andersen. Phys. Rev. Lett. **91** (2003) 056102.
[13] A. Resta, J. Blomquist, J. Gustafson, H. Karhu, A. Mikkelsen , E. Lundgren, P. Uvdal, J.N. Andersen Surf. Sci. **600** (2006) 5136
[14] S. Doniach, M. Sunjic. Phys. C **3** (1970) 285
[15] J. N. Andersen, A. Beutler, S. L. Sorensen, R. Nyholm, B. Setlik and D. Heskett. Chem. Phys. Lett **269** (1997) 371
[16] M. Wiklund, A. Beutler, R. Nyholm, J.N. Andersen. Surf. Sci. **461** (2000) 107
[17] S. Cederbaum, W. Domcke. J. Chem. Phys. **64** (1976) 603
[18] S. J. Osborne, S. Sundin, A. Ausmees, S. Svensson, L. J. Saethre and O. Svaeren, S. L. Sorensen, J. Végh, J. Karvonen, S. Aksela, A. Kikas J. Chem. Phys. **106** (1997) 1661
[19] L. Dubois, D.G. Castner, G. A. Somorjai. J. Chem. Phys. **72** (1980) 5234
[20] R.J. Koestner, M.A. Van Hove and G.A. Somorjai. Surf. Sci. 121 (1982) 321
[21] Andrea Resta, Johan Gustafson, Rasmus Westerström, Anders Mikkelsen, Edvin Lundgren, Jesper N Andersen, Ming-Mei Yang and Wei-Xue Li. In Manuscript.
[22] A. Resta et. al., Unpublished.

Table 1:

Summary of some properties of the investigated adsorbate systems. **(a)** Ethylene exposure (L). **(b)** Ethylidyne surface coverage (ML) (only valid for the (111) surface, see text). **(c)** Inner-outer C1s shift in (eV). **(d)** Ethylidyne formation temperature (K) (defined as the temperature at which the C1s signal from the outer carbon can be observed). **(e)** Decomposition temperature (start, defined as the intersection of the lines in Figure 5). **(f)** Decomposition temperature (end, defined as the temperature when the C1s signal from the outer carbon atom can not be detected)

	Rh(111)					Rh(553)				Rh(322)			
(a)	(b)	(c)	(d)	(e)	(f)	(c)	(d)	(e)	(f)	(c)	(d)	(e)	(f)
10	0.25	0.61	200	295	>342	0.69	168	210	342	0.59	184	305	>342
1	0.20	0.54	200	298	>342	0.51	168	205	342	0.37	184	210	342
0.2	0.03	0.33	184	300	318	0.33	168	205	318	-	-	-	-

Figure 1: Annealing series of adsorbed ethylene after a 10 L exposure for: **(a)** Rh(111), **(b)** Rh(553), and **(c)** Rh(322). The signature of the CH_3 group is indicated. A summary for the three different coverages on the three different surfaces can be found in Table 1.

Figure 2: The development of the C1s region as the Rh surfaces are exposed to the indicated amounts of ethylene. Note the coverage dependent change in the shift between inner carbon (283.46 eV) and outer carbon for all three surfaces. **(a)** Rh(111) after an anneal at 242K. **(b)** Rh(553) after an anneal at 214K. Note the component at lower binding energy (283.01 eV) indicating that the ethylidyne has started to decompose. **(c)** Rh(322) after an anneal at 214K. Note that no ethylidyne is formed at 214K after 0.2L exposure.

Figure 3: The C1s region from 0.2 L of ethylene on the Rh surfaces annealed at 342 K. Here the ethylidyne is fully decomposed on all three surfaces, yielding emission only from the decomposition products. **(a)** On Rh(111) the signal is dominated by methylidyne [21], however a small amount of atomic carbon at 283.58 eV can also be detected. **(b)** On Rh(553), the emission is dominated by methylidyne and atomic carbon (see text). **(c)** On Rh(322), the emission is also dominated by methylidyne and atomic carbon (see text). The bottom spectra in each figure are from ethanol on Rh(111) annealed at 900K forming atomic carbon [22].

Figure 4: The decomposition of the ethylidyne formed from a 10L ethylene exposure as the Rh surfaces are annealed at successively higher temperatures. The new component at 283.01 eV indicates that ethylidyne has started to decompose. **(a)** On Rh(111) the decomposition starts around 298K. Note that no shift between the inner and outer carbon atom in the ethylidyne atom can be observed during the decomposition **(b)** On Rh(553), the decomposition starts above 214K. Here a shift between the inner and outer C can be observed. **(c)** On the Rh(322) surface the decomposition starts above 300 K. Here a shift between the inner and outer C can also be observed.

Figure 5. The area underneath the methylidyne component plotted versus the annealing temperature for the three indicated ethylene exposures of **(a)** Rh(111), **(b)** Rh(553), and **(c)** Rh(322). The inserts show examples of fits of the C1s spectra. Note that the onset temperature for decomposition as defined by the sudden increase of the methylidyne amount is coverage independent for Rh(111) and Rh(553) but not for Rh(322). The straight lines are fits to the data points below and above, respectively, the onset temperature.

Figure 6: Schematic illustration of the overall morphology, as suggested by the C1s spectra, of the partly decomposed overlayers on **(a)** Rh(111) and **(b)** Rh(553) as illustrative example for the vicinal surfaces. See also text.

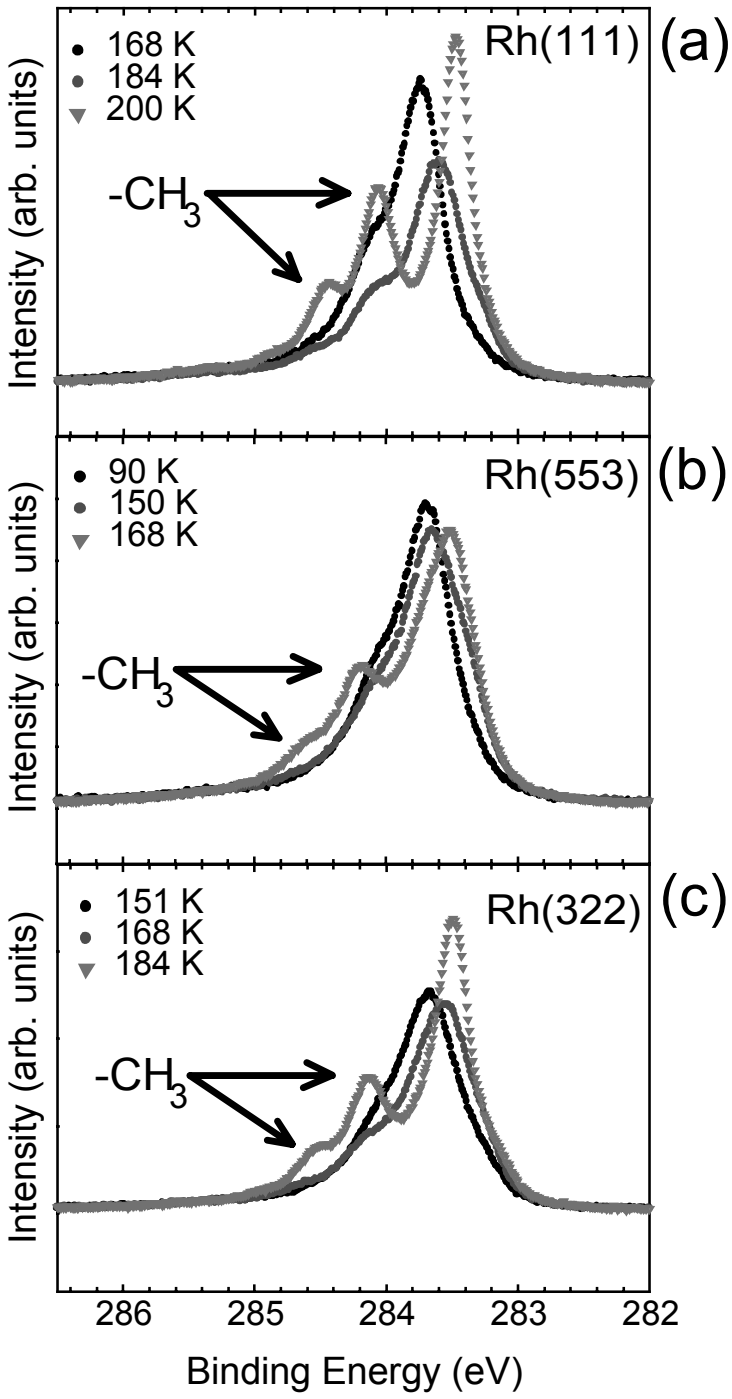
168 K
184 K
200 K
Rh(111)
(a)
-CH3
Intensity (arb. units)
90 K
150 K
168 K
Rh(553)
(b)
-CH3
Intensity (arb. units)
151 K
168 K
184 K
Rh(322)
(c)
-CH3
Intensity (arb. units)
286
285
284
283
282
Binding Energy (eV)

Figure 1

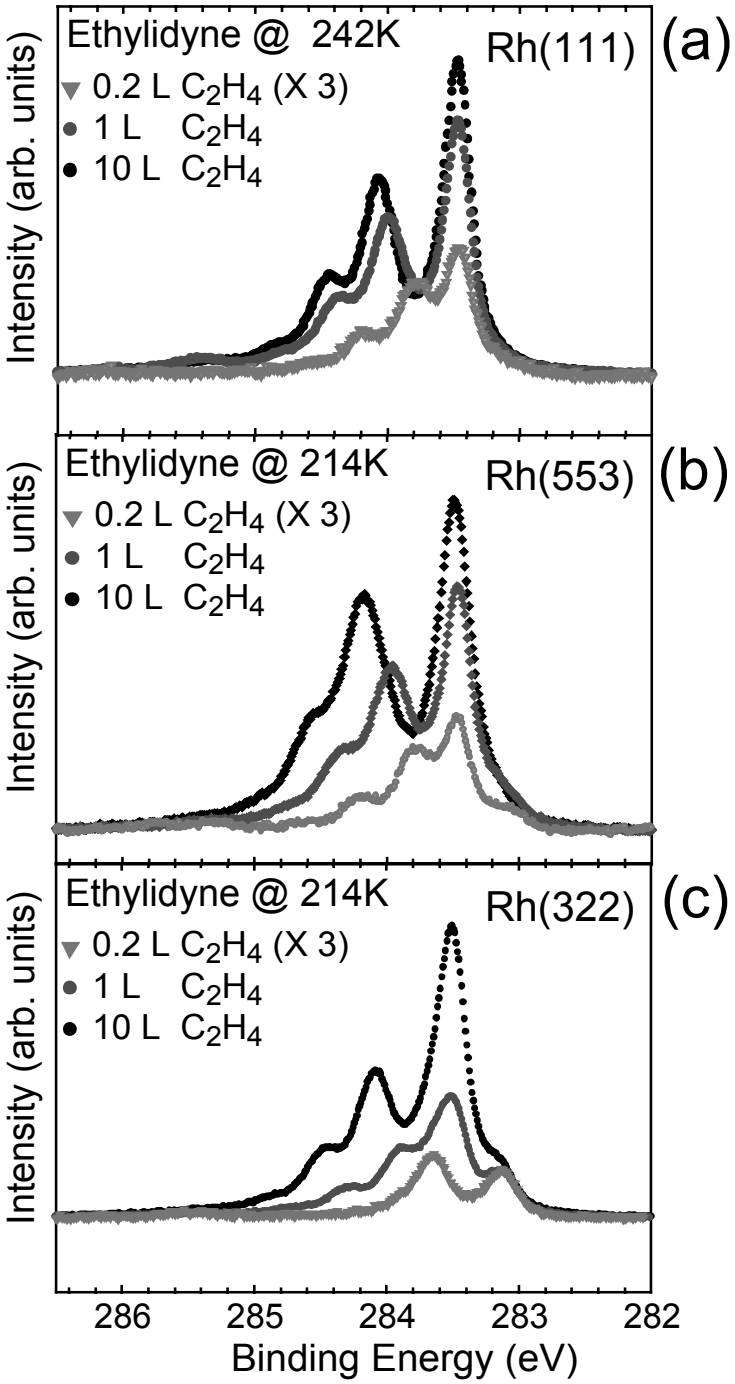
Ethylidyne @ 242K
Rh(111)
(a)
0.2 L C2H4 (X 3)
1 L C2H4
10 L C2H4
Intensity (arb. units)
Ethylidyne @ 214K
Rh(553)
(b)
0.2 L C2H4 (X 3)
1 L C2H4
10 L C2H4
Intensity (arb. units)
Ethylidyne @ 214K
Rh(322)
(c)
0.2 L C2H4 (X 3)
1 L C2H4
10 L C2H4
Intensity (arb. units)
286
285
284
283
282
Binding Energy (eV)

Figure 2

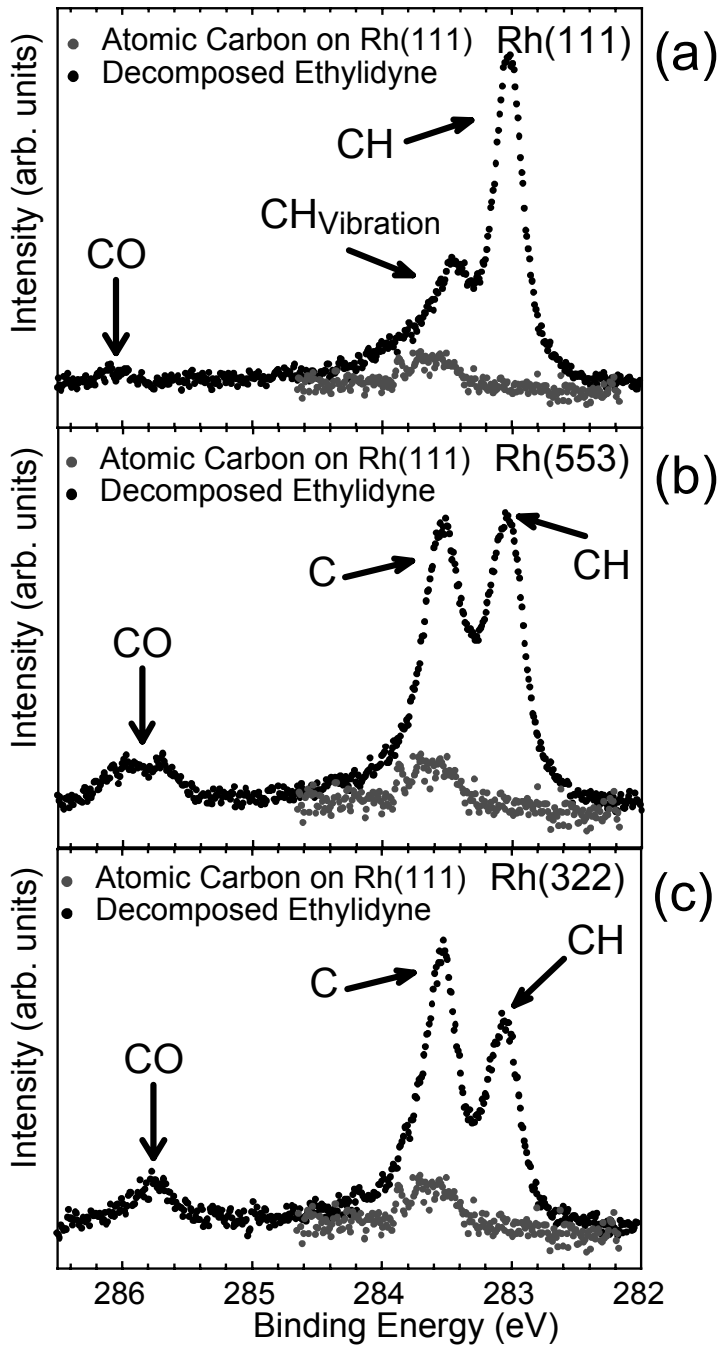
Atomic Carbon on Rh(111)
Decomposed Ethylidyne
Rh(111)
(a)
CH
CH$_{Vibration}$
CO
Intensity (arb. units)
Atomic Carbon on Rh(111)
Decomposed Ethylidyne
Rh(553)
(b)
C
CH
CO
Intensity (arb. units)
Atomic Carbon on Rh(111)
Decomposed Ethylidyne
Rh(322)
(c)
CH
C
CO
Intensity (arb. units)
286
285
284
283
282
Binding Energy (eV)

Figure 3

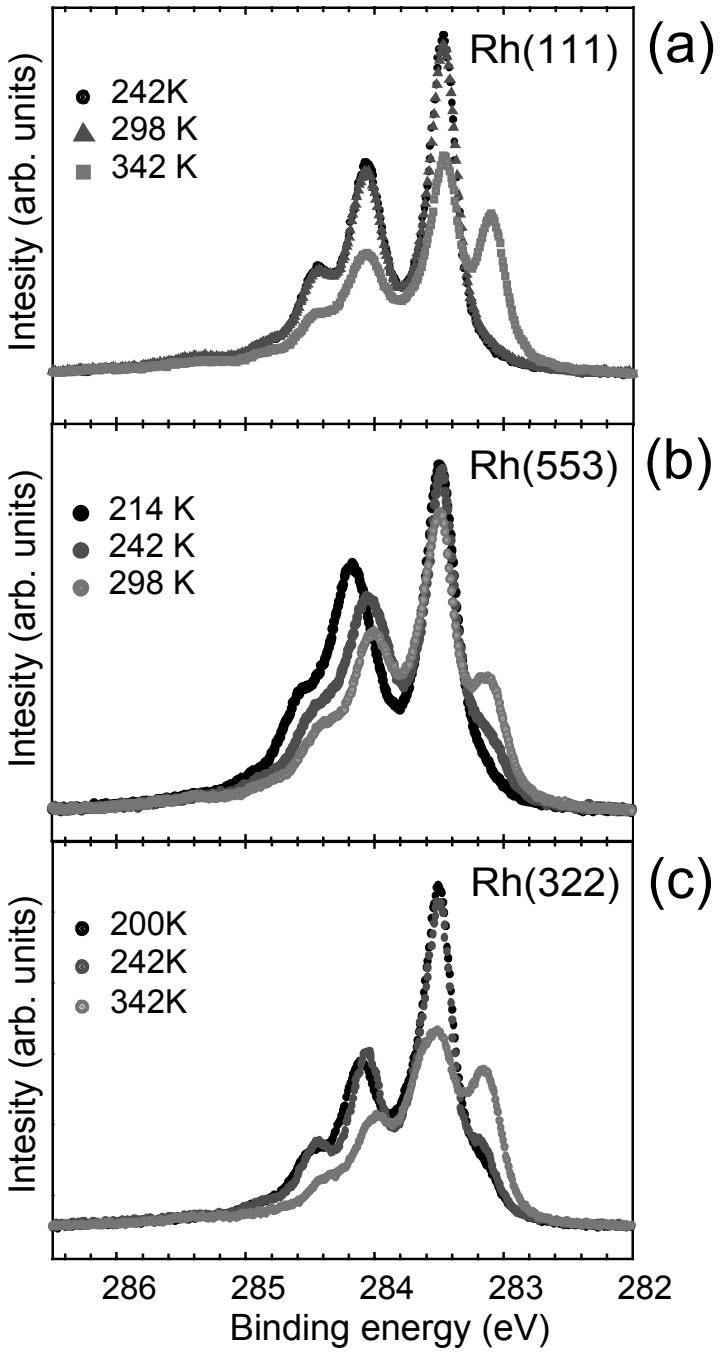
Rh(111)
(a)
242K
298 K
342 K
Intesity (arb. units)
Rh(553)
(b)
214 K
242 K
298 K
Intesity (arb. units)
Rh(322)
(c)
200K
242K
342K
Intesity (arb. units)
286
285
284
283
282
Binding energy (eV)

Figure 4

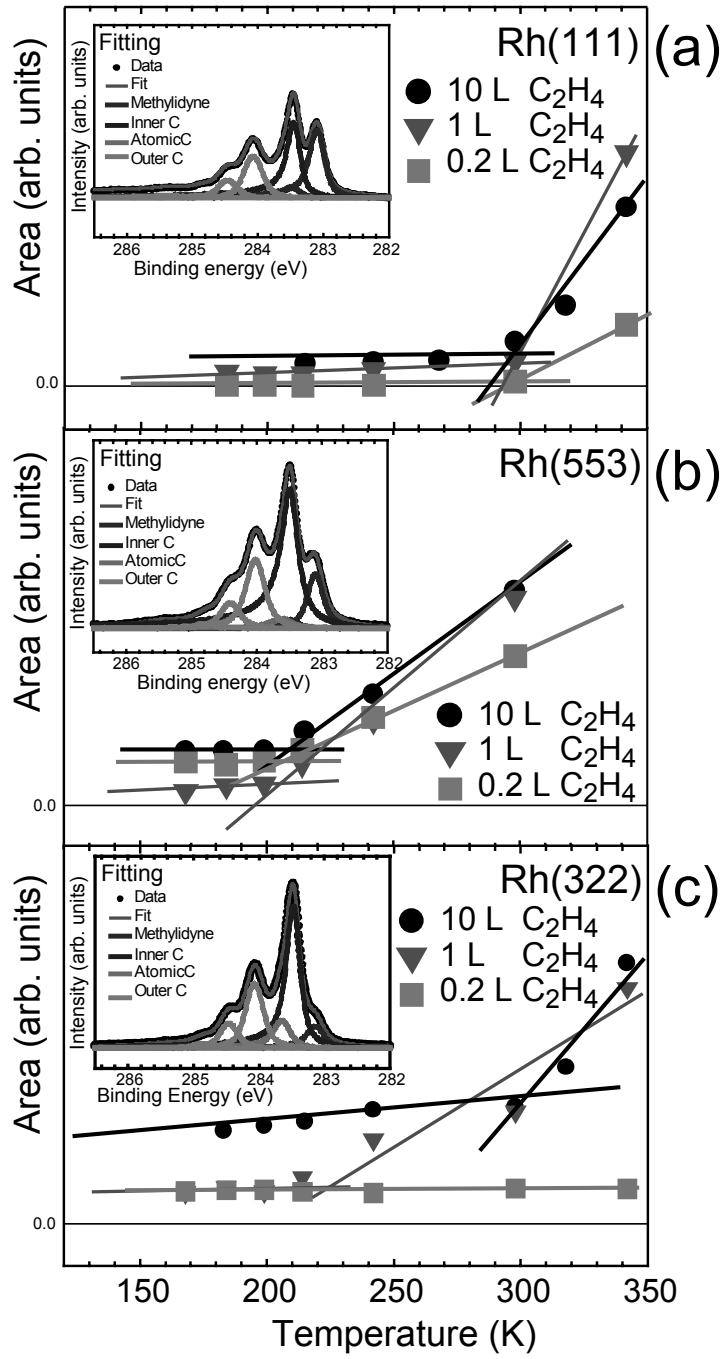
Rh(111)
(a)
10 L C2H4
1 L C2H4
0.2 L C2H4
Fitting
Data
Fit
Methylidyne
Inner C
AtomicC
Outer C
Intensity (arb. units)
Binding energy (eV)
Area (arb. units)
0.0
Rh(553)
(b)
Rh(322)
(c)
Binding Energy (eV)
150
200
250
300
350
Temperature (K)

Figure 5

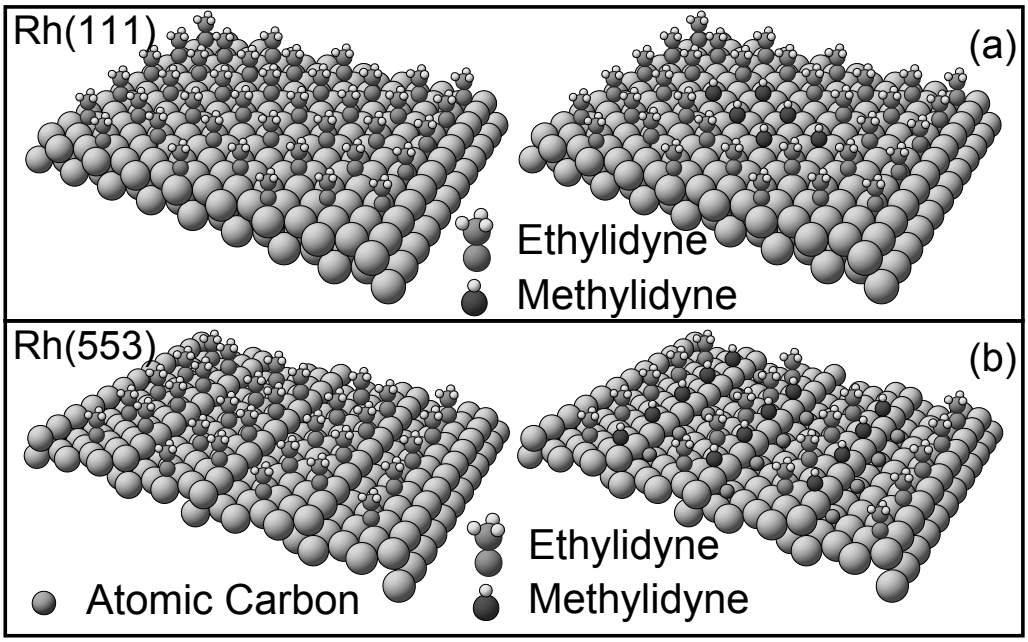
Rh(111)
(a)
Ethylidyne
Methylidyne
Rh(553)
(b)
Ethylidyne
Methylidyne
Atomic Carbon

Figure 6

Paper VI

Kinetics of the reduction of the Rh(111) surface oxide: Linking spectroscopy and atomic-scale information.

J. Klikovits, M. Schmid, J. Gustafson, A. Mikkelsen, A. Resta,
E. Lundgren, N. Andersen and P. Varga.

J. Phys. Chem. B **110** 9966 (2006)

VI

Kinetics of the Reduction of the Rh(111) Surface Oxide: Linking Spectroscopy and Atomic-Scale Information

J. Klikovits,*,† M. Schmid,† J. Gustafson,‡ A. Mikkelsen,‡ A. Resta,‡ E. Lundgren,‡ J. N. Andersen,‡ and P. Varga†

Institut für Allgemeine Physik, Technische Universität Wien, Wiedner Hauptstrasse 8-10, 1040 Wien, Austria, and Department of Synchrotron Radiation Research, Institute of Physics, Lund University, Box 118, S-22100 Lund, Sweden

Received: February 24, 2006

The reduction of the surface oxide on Rh(111) by H_2 was observed in situ by scanning tunneling microscopy (STM) and high-resolution core level spectroscopy (HRCLS). At room temperature, H_2 does not adsorb on the oxide, only in reduced areas. Reduction starts in very few sites, almost exclusively in stepped areas. One can also initiate the reduction process by deliberately creating defects with the STM tip allowing us to examine the reduction kinetics in detail. Depending on the size of the reduced area and the hydrogen pressure, two growth regimes were found. At low H_2 pressures or small reduced areas, the reduction rate is limited by hydrogen adsorption on the reduced area. For large reduced areas, the reduction rate is limited by the processes at the border of the reduced area. Since a near-random distribution of the reduction nuclei was found and the reduction process at defects starts at a random time, one can use Johnson−Mehl−Avrami−Kolmogoroff (JMAK) theory to describe the process of reduction. The microscopic data from STM agree well with spatially averaged data from HRCLS measurements.

1. Introduction

Oxidized surfaces are of great interest in the field of catalysis, since oxide formation cannot be neglected under realistic catalytic conditions. Oxide formation changes the properties of a surface, and it was found that in many cases catalytic properties can be attributed to oxides rather than to the pure metal surfaces.[1,2] Besides the formation of superstructures by oxygen adsorption and bulk oxides, oxidation of a metal surface often leads to complex two-dimensional structures, which are different from bulk oxides.[3−7] In the case of Rh(111), the structure of the three-layer surface oxide has already been solved by a combination of experimental and theoretical methods.[7] It was found that the Rh surface oxide is kinetically stable and hinders the formation of a bulk oxide. The reduction of the surface oxide on Rh(111) by CO at 100 °C has been studied recently, showing that the surface oxide provides a source of oxygen in the CO_2 formation process, which is an interesting aspect for catalysis.[8] Using hydrogen for the reduction gives us the opportunity to observe the reduction process in situ not only with high-resolution core level spectroscopy (HRCLS) but also by scanning tunneling microscopy (STM) at room temperature, since the reduction proceeds already at room temperature. This approach of using microscopic and macroscopic measurements gives us a good understanding of the reduction process. Linking results from HRCLS and STM was achieved by using the Johnson−Mehl−Avrami−Kolmogoroff (JMAK or Avrami) theory.[9−12] JMAK theory has been successfully used to describe various phase transitions and is appreciated for its simplicity and its applicability for two as well as three dimensions. Nevertheless, JMAK theory has to be modified for many practical applications, since the strict requirements are rarely met. Extensions to Avrami kinetics include the description of the phase transition occurring in a finite volume,[13,14] the formation of anisotropic particles,[14,15] and a nonrandom distribution of nuclei[14,16] as well as transient nucleation and size-dependent growth rates[14] including two nucleation stages during a phase change.[17] Considering a nonrandom distribution of nuclei and two nucleation stages during the phase change will be important for describing the reduction of the surface oxide layer on Rh(111) by hydrogen with the aid of JMAK theory. Our study provides a further step in the strive for linking atomic-scale information and macroscopic behavior, up to now dominated by application of density functional theory (DFT) derived reaction rates to homogeneous systems.[18]

2. Experimental Section

All STM and HRCLS experiments for the reduction of the surface oxide with hydrogen were performed at room temperature, and the reduction could be monitored in situ in both cases. The STM images were performed in Vienna in an ultrahigh vacuum (UHV) chamber with a base pressure of about 5×10^{-11} mbar. The H_2 pressure values and gas doses given in this work are corrected for the low ionization probability of H_2 in the ionization gauge (0.5 with respect to N_2). Even with the aid of a liquid-nitrogen cooled Ti-covered cryopanel, it took several minutes to reduce the pressure below 10^{-10} mbar after having dosed H_2 at 1×10^{-7} mbar. The HRCLS measurements were done at beam line I311 at MAXII in Lund, Sweden. The photon energy for the measurement of the O1s core levels was 625 eV.

The Rh(111) single crystal was cleaned by cycles of Ar^+ ion sputtering and was subsequently annealed at 900 °C. No contaminants such as O, C, or S could be detected by Auger

* Corresponding author. E-mail: klikovits@iap.tuwien.ac.at. Telephone: +43-1-58801-13453. Fax: +43-1-58801-13499.
† Technische Universität Wien.
‡ Lund University.

10.1021/jp0611875 CCC: $33.50
Published on Web 05/02/2006

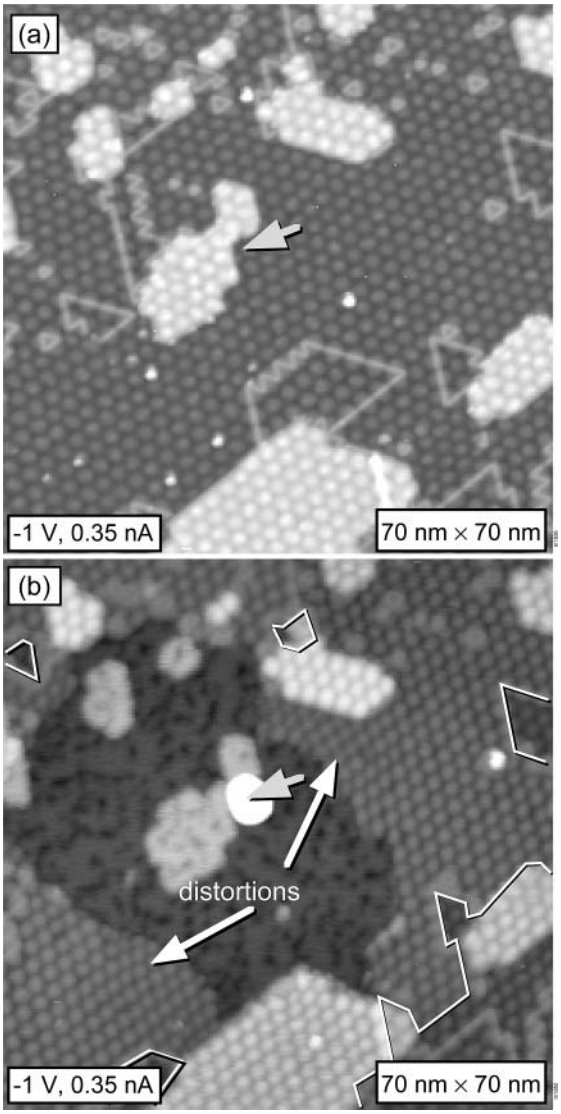

Figure 1. STM constant current topographs. The unperturbed surface oxide on Rh(111) with its characteristic moiré pattern and domain boundaries (bright lines) is shown in part a. A tip-induced defect is placed at the position of the arrow in part a. Frame b shows the same area during reduction at 1×10^{-8} mbar H_2. Reduction starts on the left side of the defect. In the reduced areas, holes of 1 ML depth can be observed. Oxide areas remaining dark at this stage of the reduction process are marked by lines in part b.

electron spectroscopy. Surface oxide formation was done at an oxygen pressure of about 5×10^{-6} mbar at 380 °C for 10 min. By using an oxygen doser with a microcapillary plate placed in front of the sample, the effective oxygen pressure at the sample surface was increased by a factor of approximately 50, resulting in an oxygen dose of about 10^5 L (1 Langmuir $= 10^{-6}$ Torr s). After this procedure, STM revealed that the whole surface was covered by the surface oxide having no defects except for step edges and islands, which form during oxide formation.

3. Results

3.1. Qualitative Observations by STM. Before reduction, the whole surface is covered by the three-layer oxide,[7] which can be easily identified by its hexagonal moiré pattern forming a (9×9) superstructure on the Rh(111) surface (Figure 1). During oxide formation, monolayer-high islands form by excess Rh, because the Rh density in the surface oxide is lower than in the metal by almost 21% [(8×8) RhO_2 units occupy the space of (9×9) Rh atoms in the metal] (Figure 1). At the borders between different (9×9) domains, domain boundaries are formed, due to a different stacking with respect to the Rh-(111) surface. In our STM images, domain boundaries are displayed as bright lines (Figure 1).

All reduction experiments with H_2 were performed at room temperature so that the reduction process could be monitored locally by STM. For large-area scans, we used a lock-in amplifier to do STM dI/dV spectroscopy to distinguish between the surface oxide and the reduced surface. As the oxide has a different density of states than the reduced area, at a gap voltage of about 2 V, reduced areas appear at different brightness than the oxide (see Figure 2). Lock-in dI/dV images show an inverted contrast compared to the STS (scanning tunneling spectroscopy) spectrum, which comes from a 180° phase shift in our lock-in spectroscopy measurements. Furthermore, a tip-dependent topographic contrast makes steps and highly stepped areas appear bright in Figure 2b. The advantage of lock-in spectroscopy measurements is that we can easily identify reduced areas and monitor the progression of the reduction even if the surface roughness is high. From the different sizes of reduced areas in Figure 2b, we conclude that the reduction starts in different locations at different times. The size of the image (1500 nm × 1500 nm) and the low number of reduced areas indicate that the probability that a reduction process starts in a rather flat area, such as that shown, is very low. The sites where the reduction starts are located almost exclusively in stepped areas, indicating that multiple steps provide suitable defects for initializing the reduction. In areas with few steps, the number of reduction nuclei can be as low as two per square micrometer (Figure 2). Even if we had the resolution to find the initiation of the reduction on any nucleus in such a huge image as that in Figure 2, taking the image would take too much time (several minutes), giving us no chance to observe the reduction process from the beginning.

A good way to observe the reduction from the very beginning is to create a defect deliberately by slightly crashing the tip into the sample, which can be seen in Figure 1b. For the same H_2 pressure, the size of the defect has an influence on when the reduction starts, since bigger defects offer a higher number of possible reduction nuclei. Unfortunately, the size and shape of the defect is not perfectly reproducible. In most experiments, the reduction was nucleated at a single nucleus on one side of the defect, causing the reduced area to expand more rapidly in the direction away from the defect. On reduced areas, we observe a metallic Rh(111) surface exhibiting many holes of 1 ML depth, providing a good possibility to distinguish reduced areas from the oxide in STM images. The formation of these holes (see Figure 1) is due to the lower Rh area density in the oxide than in the metal. After nucleation, the reduced area expands from the defects and its shape is roughly circular, except for the effect of the defects, acting as barriers for further reduction.

Before the reduction starts, the brightness of the oxide is uniform. During reduction, the brightness (apparent height) of the oxide adjacent to a reduced area increases (Figures 1b and 3). Domain boundary lines (bright lines in the STM images) or islands separate the brighter area from the darker. Also, the spectroscopy images of large reduced areas show a brightness contrast outside the border of the reduced area (Figure 4). This band of different brightness can be 10 nm wide or more and varies depending on the surrounding oxide. If the density of islands and domain boundary lines is high, the width of the band is lower.

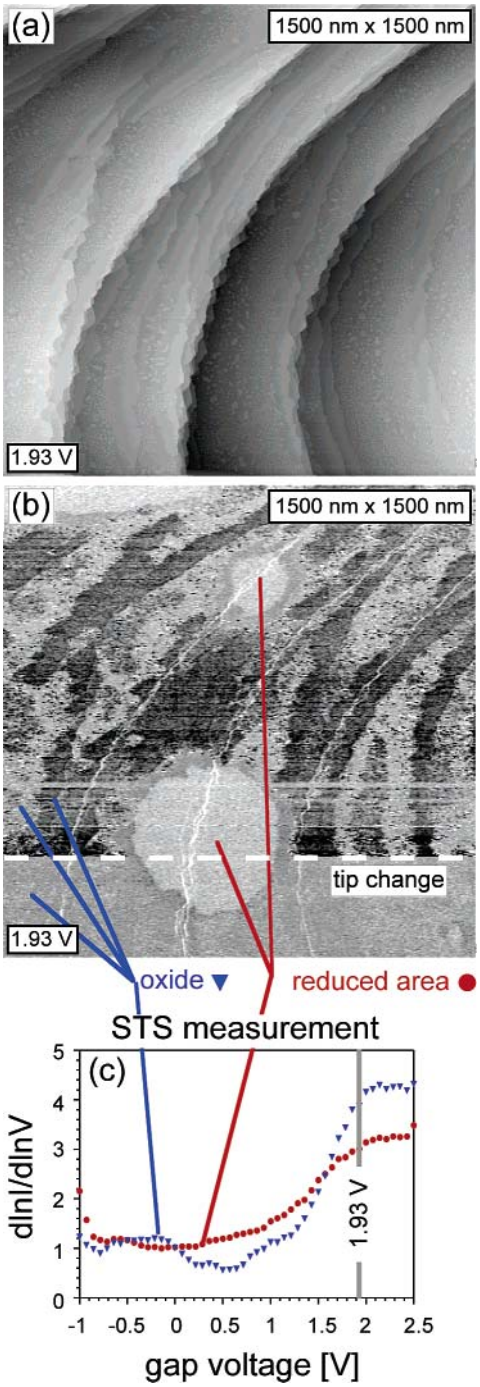

Figure 2. (a) STM image of a 1500 nm × 1500 nm area. (b) Lock-in dI/dV spectroscopy of the same area. Reduced areas are displayed brighter in part b, corresponding to a lower density of states in the tunneling spectrum (c).

During the reduction process, also, the oxide structure at the border of the reduced area is changed slightly. The moiré pattern appears locally distorted close to the reduced area (Figure 1b). The distortions in the moiré pattern indicate that the size of the surface oxide unit cell has increased. Distortions in the moiré pattern are not equally distributed along the border of the reduced area.

3.2. Kinetics of the Reduction. STM allows us to study the kinetics of the reduction in detail. For this purpose, as described above, we create a defect with the STM tip and follow the evolution of the reduced area at constant H_2 pressure. We find that the reduced area grows with an increasing rate. For low H_2 pressures and small reduced areas, growth of the reduced area is proportional to the already reduced area, indicating that the reduction process is limited by hydrogen adsorption in the reduced area (Figure 5a). This results in an exponential increase of the reduced area with the H_2 dose, shown in Figure 5b. We will refer to this behavior as the "first growth regime". For this experiment, a relatively low hydrogen pressure was chosen (5×10^{-9} mbar). At higher pressures or large reduced areas, further growth of the reduced area is proportional to the perimeter of the reduced area, which means that the reduction is limited by the processes at the border of the reduced area ("second growth regime", Figure 6b). For a H_2 pressure of 4×10^{-8} mbar, the reduction speed depends on hydrogen adsorption only in the beginning, i.e., below a reduced area of 700 nm^2 (the first growth regime). For higher pressures, the second growth regime starts at a smaller reduced area than for lower pressure (compare Figures 5a and 6a).

The equation for the linear fit in the first growth regime is the following: $\mathrm{d}A \approx 0.22[\mathrm{L}^{-1}]A\ \mathrm{d}D$, where A stands for the already reduced area, and dA, for the growth of the reduced area after an additional H_2 dose dD. This equation proved to be valid for all pressures studied (5×10^{-9} to 1×10^{-7} mbar). In other words, the initial reduction speed of a single reduced patch [nm^2 s^{-1}] in Figure 6a scales with the H_2 pressure. The reduction speed is independent of the H_2 pressure for large reduced areas (second growth regime) as in Figure 6b, where the reduction speeds at 2×10^{-8} and 4×10^{-8} mbar are compared. In the second growth regime, the radius of the reduced area grows constantly with time by approximately 0.11 nm s^{-1}. This growth speed can be influenced by sample preparation. In Figure 7b, 0.21 ML of the Rh(111) surface were removed by Ar-ion bombardment before oxide formation at 380 °C. The number of islands and domain boundary lines has decreased (compare insets in Figure 7a and b), but some holes are visible in the inset in Figure 7b. Due to the different preparation, the radius of the reduced areas grows by only 0.053 nm s^{-1} (second growth regime). Reduction speed is also influenced by other factors, such as the presence of step edges, which decrease the reduction speed significantly in the step-up direction (Figure 4) but have hardly any effect in the step-down direction.

Since the number of nuclei strongly depends on the local step density, for comparison with spatially averaging methods, a preparation with better-defined density of nucleation sites is required. Therefore, we have created a surface with a high number of randomly distributed defects (Figure 8). These defects were formed on the surface by 2 keV Ar^+ sputtering for 5 s with an ion current of 2.6 nA mm^{-2}, corresponding to a dose of 8×10^{16} m^{-2}. Thus, the sputter-induced defect density on the surface was approximately 0.005 ML if we assume that every Ar ion creates one defect. Unlike the reduction displayed in Figure 2, the reduction starts also on terraces now as shown in Figure 8. In rather flat surface areas, the number of reduction nuclei is increased roughly by a factor of 10 after defect creation by sputtering (compare Figures 2b and 8b). Nevertheless, also for the sputtered surface, the reduction proceeds faster in stepped areas. In Figure 8a, the reduction process is far more advanced in the highly stepped part than in the flat part in the center.

We have also studied the reduction of an even rougher surface, which was prepared by cleaning the Rh(111) crystal by Ar-ion sputtering and oxide formation at 380 °C without additional annealing. The rough unreduced surface is fully oxide covered with a high step density everywhere on the surface. For the reduction at 1×10^{-7} mbar, this high step density results in a high density of randomly distributed reduction nuclei

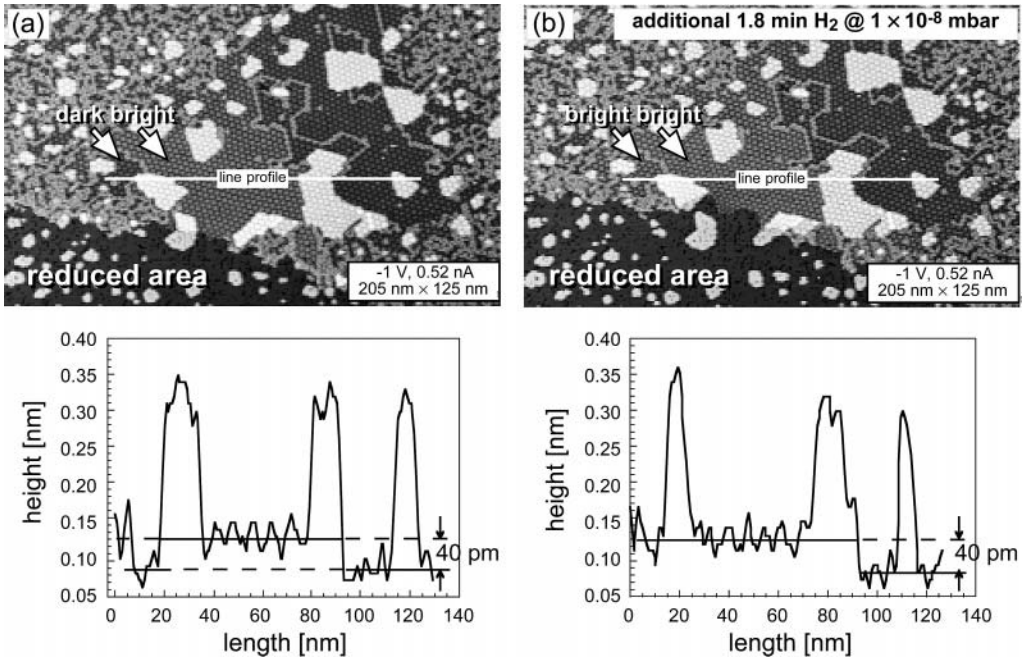

Figure 3. Oxide next to the reduced area appearing brighter in STM topography (apparent height difference about 40 pm). Domain boundaries stop the spread of brighter areas. In part b, after removal of domain boundaries by reduction, another dark patch becomes bright (arrows).

(Figure 9). The density of the nuclei is about 5 times higher than on the surface in Figure 8b. Since a realistic surface exhibits a high number of intrinsic defects, considering reduction with H_2, it is far from being chemically as inert as the surface oxide on a perfect single crystal.

Studying the late stages of reduction of the rough surface (Figure 9) by STM is rewarding, because it has an almost completely random distribution of reduction nuclei, in sharp contrast to surfaces where nucleation is strongly influenced by an inhomogeneous distribution of steps (cf. Figure 8a). The results shown in Figure 9 indicate that nucleus-free areas of the surface can delay the end of the reduction, even in the case of a random distribution of nuclei. It is easy to imagine that the complete reduction of the surface is considerably delayed in the case of an inhomogeneous distribution of defects, leading to large areas where nucleation does not occur.

3.3. HRCLS Measurements. HRCLS measurements were done to describe the macroscopic behavior of the reduction process by monitoring the O1s peaks. Before studying the reduction of the surface oxide, we have also investigated how the (2×1) oxygen adatom structure on Rh(111) was reduced by H_2 (Figure 10a). We find no OH or H_2O peaks during reduction of the (2×1) structure by H_2, which indicates that the formation of H_2O from OH and its desorption are not rate-limiting steps in the reduction process.

Figure 10b shows a O1s core level spectrum obtained during the reduction of the surface oxide. The O1s peak at a binding energy of 528.8 eV is the surface component, coming from the upper layer of the trilayer oxide, and the peak at 529.7 eV, the interface component, comes from the lower oxygen layer.[7,8] During the whole reduction process, the intensity ratio of these two surface oxide components stays constant. There is hardly any evidence for atomic oxygen on the reduced areas during the reduction. Only a small peak at about 529.5 eV might be fitted to the HRCLS data (Figure 10c and d), which exhibits its maximum at the beginning of the reduction, where no atomic oxygen can be expected on the surface. We thus attribute it to imperfect fitting of the two O1s components of the surface oxide.

The reduction of the surface oxide is slow at the beginning and end and exhibits its maximum rate after a considerable delay, a behavior usually associated with autocatalytic reactions. The reduction process is much faster if we place additional defects by sputtering (Figure 10d), but the slow induction period at the beginning is hardly changed. Low rates at the beginning of the reduction have also been found for reduction of the surface oxide on Rh(110)[19] and of Rh_2O_3 layers[20] by H_2. During the reduction process, we find an additional peak at about 531.5 eV (labeled "OH"). This peak, which is negligible before and after the reduction, slowly increases in intensity during the reduction until the maximum reduction rate is reached. The peak becomes much stronger for the surface with sputter-induced defects and is roughly proportional to the reduction rate (slope of the oxide intensities). This peak cannot be explained by OH or H_2O formation on the reduced Rh surface, since the O1s respective binding energy on Rh(111) determined by adsorption of H_2O should lie at about 530.5 and 532.5 eV (Figure 11).

4. Discussion

4.1. Qualitative Description of the Reduction Process. We have observed that the reduction speed is very slow in the beginning of the reduction. Therefore, we can argue that no significant amounts of hydrogen adsorb on the surface oxide. This is similar to the reduction with CO, which also does not adsorb on the oxide.[8] The reduction process can start on defects only. Two adsorption sites in direct proximity are required for dissociative adsorption of a H_2 molecule. Therefore, active sites are rare on a fully oxide-covered surface and located almost exclusively in stepped areas. During the reduction process, hydrogen adsorption and dissociation occurs on the previously reduced areas. From the HRCLS measurements, we have to conclude that the reduced area is essentially free of adsorbed oxygen, OH, and water. There is no indication that oxygen is moving to the reduced area as in the case of the reduction by CO at 100 °C, where reduction proceeds through CO_2 formation in the oxide-free areas.[8] Therefore, we conclude from the absence of atomic oxygen that the active sites for reduction are located at the border of the reduced area and that hydrogen

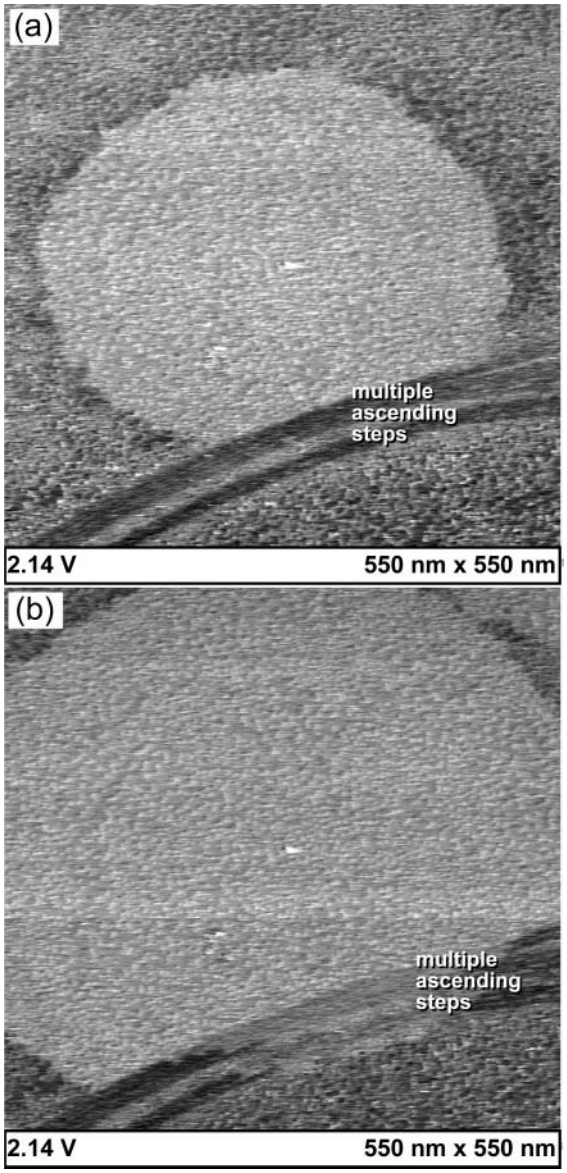

Figure 4. Successive lock-in d*I*/d*V* images of the same area. Reduced areas appear bright, and a dark ring around the reduced area is observed. The reduction is clearly slowed at ascending step edges. Multiple steps appear dark.

attacks the oxide at its border removing oxygen from both layers of the oxide.

The reduction is not isotropic at the very beginning since islands and ascending step edges slow the reduction process. For explaining the observation that only ascending steps have this effect in contrast to descending steps (Figure 4), we have to assume that the border of the oxide provides fewer active reduction sites on ascending steps than on descending steps or planes. A reason for fewer active sites at ascending steps might be that hydrogen attacks the oxide from the upper oxygen layer rather than from the lower layer and that hydrogen has difficulty in reaching the upper sites at an ascending step. The rate at which oxide is removed by H_2 is not only decreased by ascending step edges but is also affected by oxide preparation. For the reduction in Figure 7b, a decreased reduction speed in the second growth regime by roughly a factor of 2 compared to Figure 7a was measured. A clear difference between the two preparations is the density of the domain boundaries, which is lower in Figure 7b. Unfortunately, the number of domain boundaries cannot explain a decreased reduction speed, since

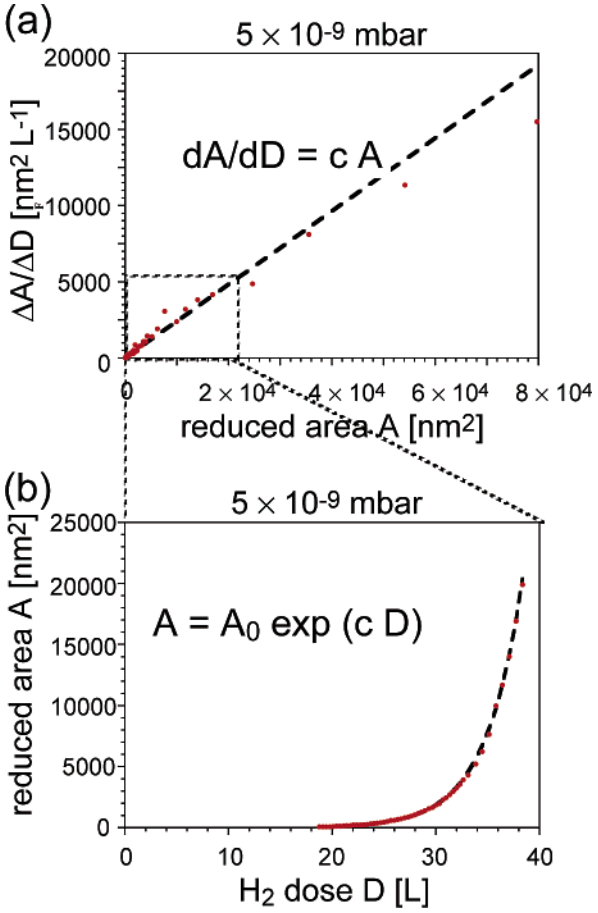

Figure 5. (a) Growth rate and (b) area of a single reduced patch at 5 × 10^{-9} mbar H_2 monitored by STM. Reduction starts at a tip-induced defect. The dashed line marks the fit for this growth regime.

STM measurements indicate that domain boundaries do not affect the growth rate of reduced areas (see Figure 3). Surprisingly, the slower reduction speed occurs for the preparation with fewer islands, in contrast to what we expected.

4.2. Reduction Rate of a Single Reduced Patch. We have described the reduction process quantitatively for a single reduced area (Figures 5−7), and we can use the data obtained to estimate the sticking probability of H_2 on the reduced area. The density for oxygen atoms in the RhO_2 surface oxide is 1.58 times the density of Rh atoms in the (111) layer of the Rh substrate. Since two hydrogen atoms are required to form H_2O from one oxygen atom of the surface oxide, we would need 3.16 ML of adsorbed hydrogen to remove a whole layer of the surface oxide. Comparing this value with the initial growth rate (first growth regime), we can determine the sticking coefficient of H_2 in the reduced areas to be 0.36. This estimate of the sticking coefficient is slightly above the zero-coverage sticking coefficient of 0.3 as determined in ref 21 but agrees within the error bars of our experiment. Since the $(1 - \theta)^2$ behavior of the H_2 sticking coefficient[22] would lead to a further reduction of the sticking coefficient at nonzero coverage, we must conclude that the reduced area is nearly free of adsorbates at the beginning of the reduction (first growth regime).

For large reduced areas (second growth regime), we expect a high hydrogen coverage on the reduced areas. Because of the low ratio of perimeter versus reduced area, the consumption of hydrogen at the border of the reduced area is low compared to adsorption in the second growth regime. Thus, the hydrogen coverage will increase and the sticking coefficient decreases proportional to $(1 - \theta)^2$ (ref 22). Part of the hydrogen from the

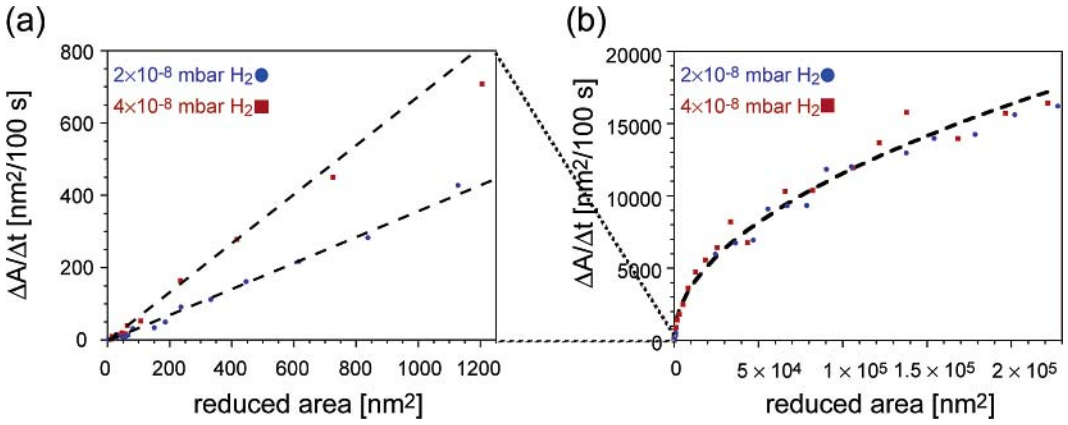

Figure 6. Comparison of the reduction speed over time for 2×10^{-8} mbar H_2 and 4×10^{-8} mbar H_2. (a) Initial reduction speed (first growth regime, linear fit) that scales with the pressure. (b) Reduction speed for large reduced areas (second growth regime, square root fit) that is pressure-independent.

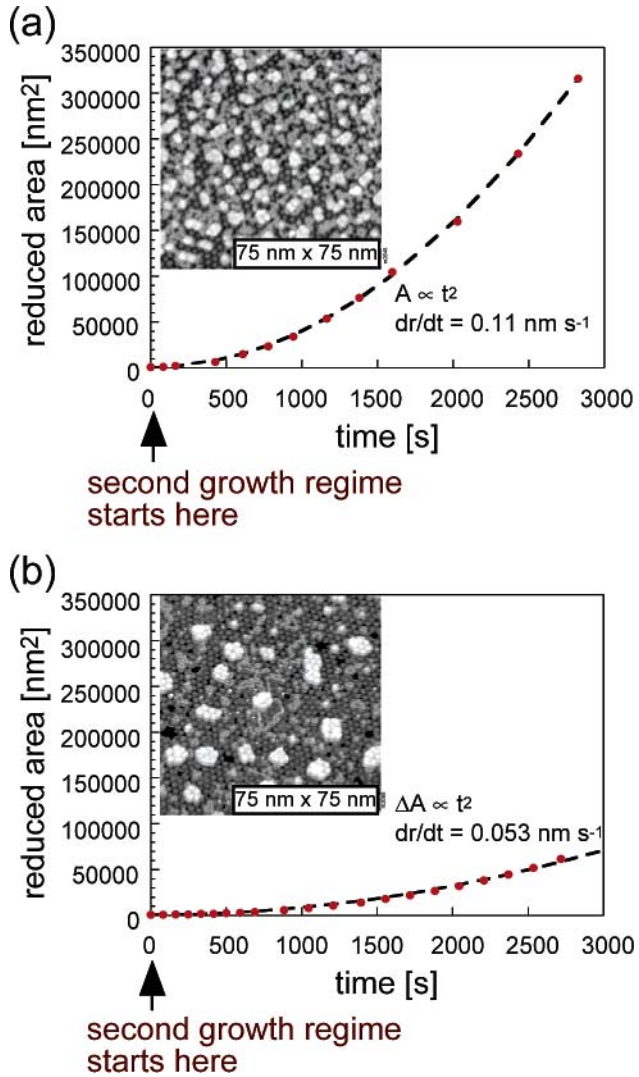

Figure 7. Growth of a single reduced patch at 1×10^{-7} mbar H_2 for (a) the normal preparation of the oxide and (b) a smoother surface oxide created by removal of 0.21 ML before oxidation. Surface b has fewer domain boundaries, fewer islands, but slightly more holes (inset).

gas phase is unused in the reduction process because it cannot adsorb on the hydrogen-covered reduced surface. Therefore, reduction at 2×10^{-8} mbar uses hydrogen two times more efficiently than at 4×10^{-8} mbar in the second growth regime (Figure 6b).

The transition between the two growth regimes, adsorption-limited growth and border-limited growth, depends on the pressure. For a study of this dependence, we employ the initially linear relationship between the growth rate of the reduced area and that of the area itself, both determined from STM measurements. The transition to the second growth regime can be seen as a departure from the linear relationship. The reduced areas A_t where the transition occurs are plotted in Figure 12 and decrease with increasing pressure. Our data are in good agreement with a $1/p^2$ behavior, where p denotes the pressure. The second growth regime starts as soon as more hydrogen is adsorbed on the reduced area than hydrogen is used in the reduction process at the border. The transition occurs when the growth rates calculated for the two growth regimes become equal (1):

$$\frac{dA}{dt} = pc_1A_t(p) = c_2\sqrt{A_t(p)} \qquad (1)$$

where c_1 and c_2 are constants. The limiting factor for the reduction rate in the first growth regime is hydrogen adsorption on the left-hand side of eq 1. The length of the border limits the reduction rate in the second growth regime on the right-hand side of eq 1. Solving eq 1 for $A_t(p)$ directly leads to the $1/p^2$ behavior observed.

4.3. Hydrogen-Induced Changes to the Oxide. Besides the distortions of the moiré pattern mentioned in section 3.1, we observed areas of different brightness near the reduced area in the STM topography data (Figures 1b and 3) as well as in tunneling spectroscopy (Figure 4). These changes in brightness in the oxide occur only during the reduction process, and we therefore argue that diffusion of a hydrogen containing species into, or possibly onto, the oxide occurred while dosing H_2. The diffusion of this "mystery species" is considerably slowed by domain boundaries within the oxide (Figures 1 and 3) as well as by islands and step edges. It seems that unfavorable sites at domain boundaries and steps hinder diffusion of the mystery species.

These rings of different brightness around the reduced areas, due to diffusion of a mystery species, can be related the "OH" component at about 531.5 eV in the HRCLS measurements. For early reduction, the perimeter of the reduced areas increases as the reduction proceeds. This leads to an increasing overall area containing the "OH" species. In late stages of reduction, many reduced areas coalesce, and thus, the border length between the oxide and the reduced area decreases again. This means that the total area of the diffusion zone near the border

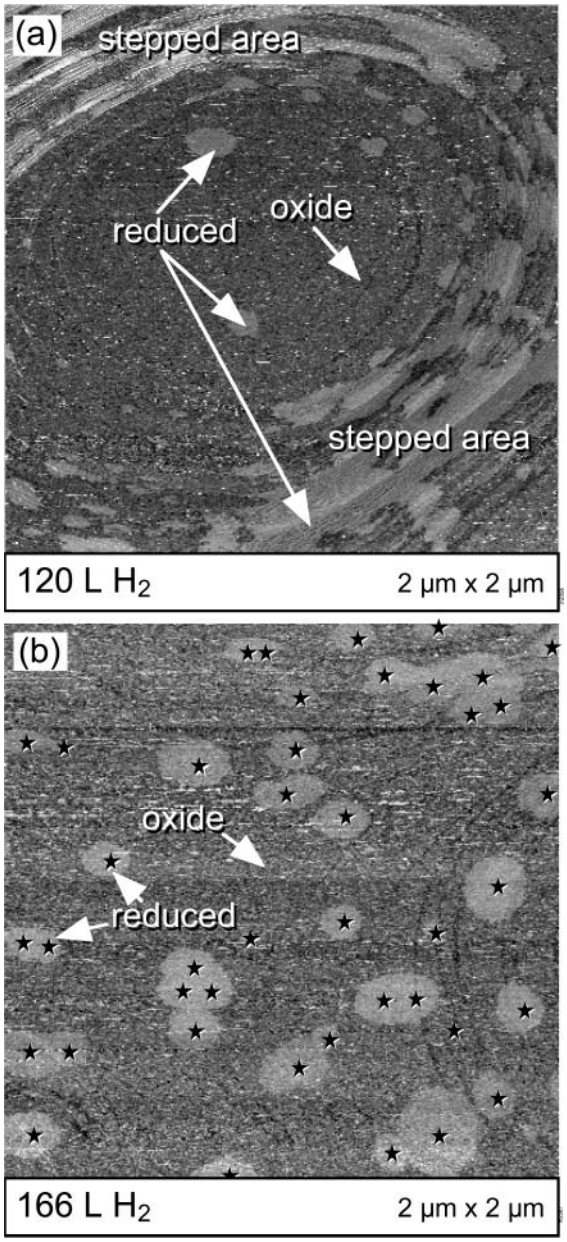

Figure 8. Reduction of a surface sputtered with 8×10^{16} Ar^+-ions m^{-2} at 1×10^{-7} mbar H_2. A stepped (a) and a flat area (b) of the same surface are shown. Despite sputter-induced nuclei, the reduction in stepped areas (a) nucleates faster than in part b (nuclei marked with black stars). Flat areas would considerably delay the end of the reduction process without sputter-induced defects.

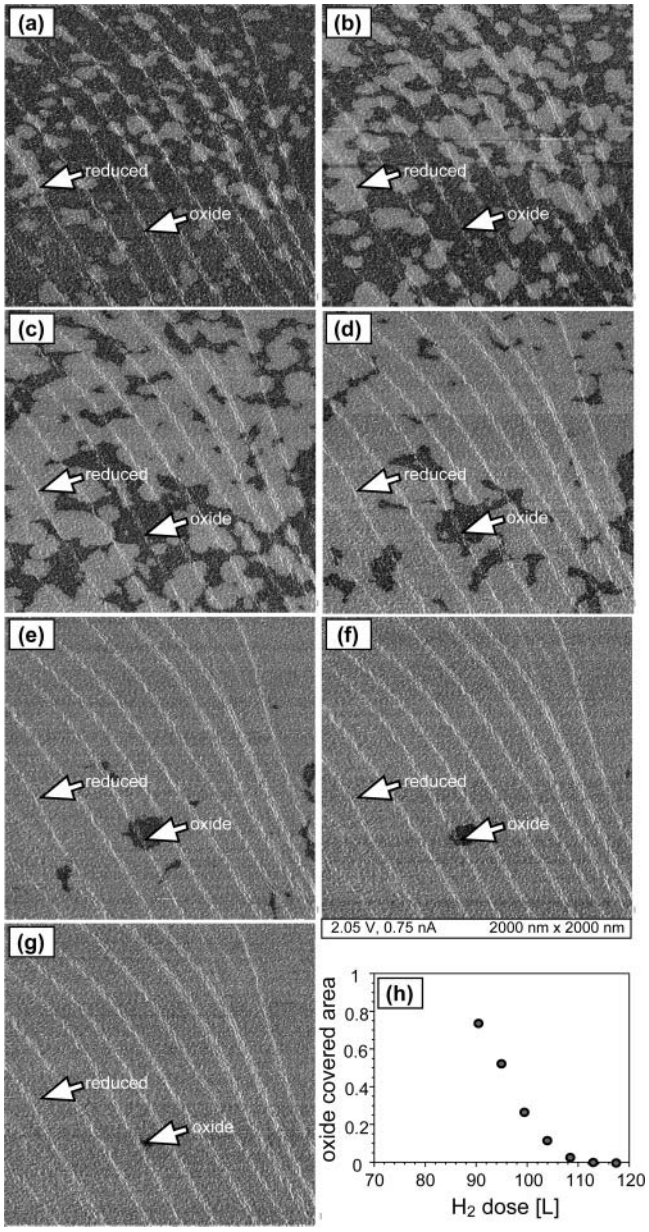

Figure 9. Reduction of a rough, fully oxidized surface. Each image has been taken after an additional H_2 pulse of 4.5 L (1 min, 1×10^{-7} mbar). Although quantitative comparison with reduction at constant H_2 pressure is not possible, the qualitative behavior can be seen well. The dots in part h indicate the oxide area fraction in each spectroscopic STM image. The right arrow marks an area free of reduction nuclei due to statistical fluctuations, indicating that the removal of the last remnants of oxide takes considerable time, due to the linear decrease of its radius with time.

also decreases. Therefore, diffusion of a hydrogen-containing species into (or onto) the oxide can give a reasonable explanation of why we observe a maximum of the "OH" peak when the reduction rate is fastest, i.e., when the border around the reduced area has its maximum length. By sputtering the oxide surface prior to reduction, the intensity of the "OH" peak is clearly increased (compare Figure 10c and d). The stronger "OH" component is attributed to a higher number of reduced patches, which start growing at the additional sputter-induced defects, resulting in a longer border of the reduced areas. Again, this is exactly what we expect from the band around the reduced areas. Our HRCLS measurements indicate that the diffusing "OH" species affects the surface oxygen layer as well as the oxygen interface layer in the oxide to the same extent, since the ratio of both oxygen peaks remains perfectly constant for the whole reduction process (Figure 10c and d). Therefore, we can exclude a chemisorbed species (e.g., H_{ads}) on top of the surface oxygen layer of the oxide as the "OH" component. A possible explanation for the "OH" species might be weakly H-bonded H_2O, which probably would not cause a shift in the O1s core levels of the surface component. H-bonded H_2O was also suggested for H_2O adsorption on Rh(111)−O−(1 × 1), but it desorbs at 150 K in this case.[23] Thus, it is questionable whether H-bonded H_2O on the surface oxide can be a possible solution for the "OH" species observed by HRCLS and the mystery species inferred from the STM images. The true identity of this species remains unknown.

4.4. Avrami Kinetics (JMAK Theory). In section 4.2, we have obtained a good description of the microscopic behavior of the reduction from STM measurements. Using JMAK

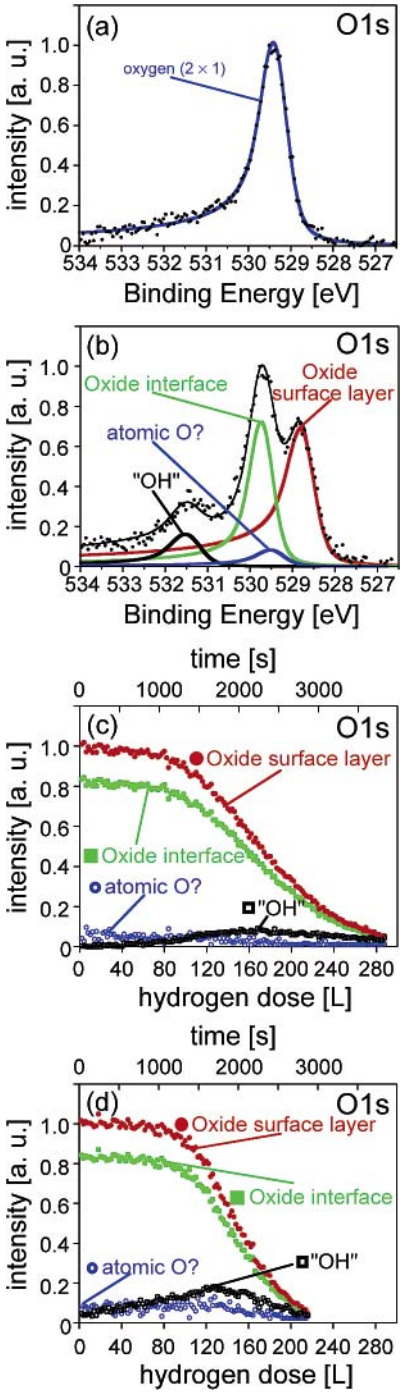

Figure 10. Photoemission spectra taken during reduction of (a) the (2 × 1) adatom oxygen structure on Rh(111) and (b) the (9 × 9) surface oxide by H_2 at 1×10^{-7} mbar. (c and d) Evolution of the peak intensities of (c) an untreated and (d) a presputtered surface oxide.

theory,[9−12] we can combine our microscopic data with the macroscopic data from the HRCLS measurements. JMAK theory is applicable for 2D and 3D growth and requires that (1) the initiation of the reduction at a defect occurs randomly in time, (2) defects are randomly distributed across the surface, (3) reduced patches have a circular (2D) or spherical (3D) shape, and (4) the growth of the radius of the reduced patch with time can be described by a simple power law. Large-area scans indicate that the first requirement is fulfilled on the unmodified oxide (see Figure 2b). With additional nuclei created by slight sputtering (about 3×10^5 defects on a 2000 nm × 2000 nm area were formed by sputtering corresponding to a defect density of 0.005 ML), we see that only a negligible number of the

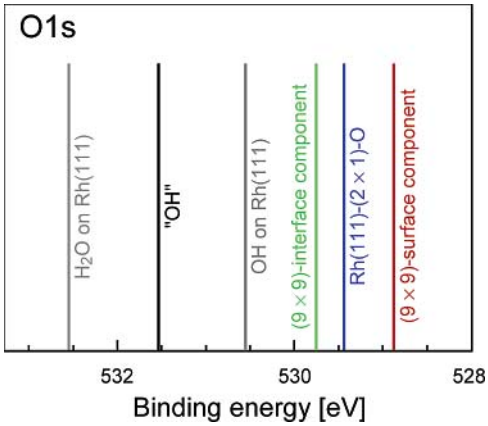

Figure 11. O1s core level shifts on Rh(111). Binding energies of the two surface oxide components, the unknown "OH" species, chemisorbed O, OH, and H_2O on Rh(111) are shown.

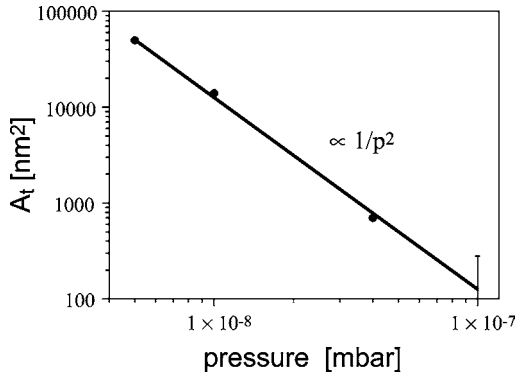

Figure 12. Area at the transition from adsorption-limited to border-limited growth. The transition is pressure-dependent, and the area at the transition scales with $1/p^2$.

sputter-induced defects has transformed into reduction nuclei during the whole reduction process. As a reasonable simplification, we can assume that the reservoir of possible nuclei is not depleted. This again indicates that the first requirement is fulfilled. Concerning requirement 2, a random distribution of defects, we must note that on a surface with not completely randomly distributed defects it would take more time until the surface is fully reduced.[14,16] For the analysis, we use sputtered surfaces as shown in Figure 8, where we found reduction nuclei also on terraces. In our case, the second requirement is not fulfilled perfectly well, but we can make a rough estimate of the number of defects that become reduction nuclei per second on a given area (dN/dt). The shape of single reduced patches is nearly circular (Figures 2, 4, and 8), so the third requirement is also fulfilled. The fourth requirement that the radius of a reduced area grows according to a power law with time is not completely fulfilled because we observe two growth regimes in our microscopic measurements. The reduction speed in the first regime is limited by H_2 adsorption on the reduced area and in the second regime by the processes at its border. No distinction between the two growth regimes is made by JMAK theory, so an empirical growth function for both regimes is required.[17] In our case, the radius of a single reduced area grows constantly with time only in the second regime. By extrapolating the second growth regime back to a reduced area size of zero for a single reduced area, we can estimate that the first growth regime lasts about 575 ± 200 s for a H_2 pressure of 1×10^{-7} mbar (see Figure 13). For different pressures, this time scales roughly with a factor of $1/p$ where p denotes the ratio of the pressures. During this period, the reduction is extremely slow compared to the

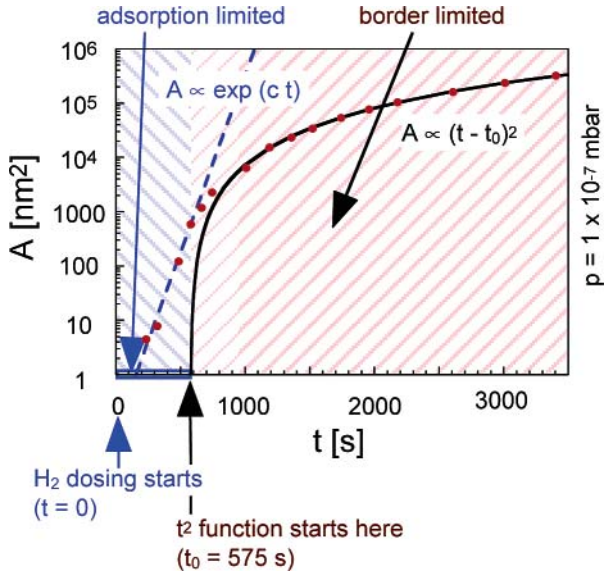

Figure 13. Area of a single reduced patch vs time at 1×10^{-7} mbar H_2. The fit curves for the two growth regimes are shown as a dashed and a full line, respectively. The quadratic function for the second growth regime can be extrapolated back to zero area.

second growth regime, which is not limited by hydrogen adsorption. As a simplification, we introduce a delay time t_0 in which we assume that the reduced area does not grow at all instead of growing very slowly. With these assumptions, the growth function, i.e., the radius of a given reduced patch as a function of time τ since nucleation, becomes the following:

$$r(\tau) = \begin{cases} 0 & \text{for } \tau \le t_0 \\ \text{const} \times (\tau - t_0) & \text{for } \tau > t_0 \end{cases} \quad (2)$$

The equation for the fraction of the transformed area for 2D JMAK growth is then given by

$$F(t) = \begin{cases} 0 & \text{for } t \le t_0 \\ 1 - \exp(-c \times (t - t_0)^3) & \text{for } t > t_0 \end{cases} \quad (3)$$

where $F(t)$ stands for the fraction of reduced area and c is proportional to the product of the nucleation rate dN/dt and the reduction speed of a single reduced patch in the second growth regime:[16]

$$c = \frac{\pi}{3}\left(\frac{dr}{d\tau}\right)^2 \frac{dN_p}{dt} \quad (4)$$

We have determined dN/dt by counting the number of reduced patches per area (see Figure 8b), taking phantom nuclei into account.[9,12] Including phantom nuclei in JMAK theory means that we include the possibility that a defect in an already reduced area would otherwise turn into a nucleus. So, we have to calculate dN_p/dt, where dN_p stands for dN devided by the fraction of nonreduced area. Furthermore, we have to keep in mind that it takes some time until the nucleus of a reduction becomes visible in our STM measurements. In the present case, we can assume that this time roughly matches the delay time t_0. So, we can make an estimate, namely, $t \rightarrow t - t_0$, when counting the nuclei (black stars in Figure 8b). By this procedure, we have determined the nucleation rate in a flat as well as a highly stepped surface area. In the flat area, the formation of nuclei is dominated by sputter-induced defects (Figure 8b). In stepped areas, the defect density is higher because of defects at steps (Figure 8a), but the evaluation is much more difficult for Figure 8a and can be only roughly estimated as an upper limit due to the frequent coalescence of reduced areas in the stepped regions. Table 1 gives the resulting constants from the STM measurement.

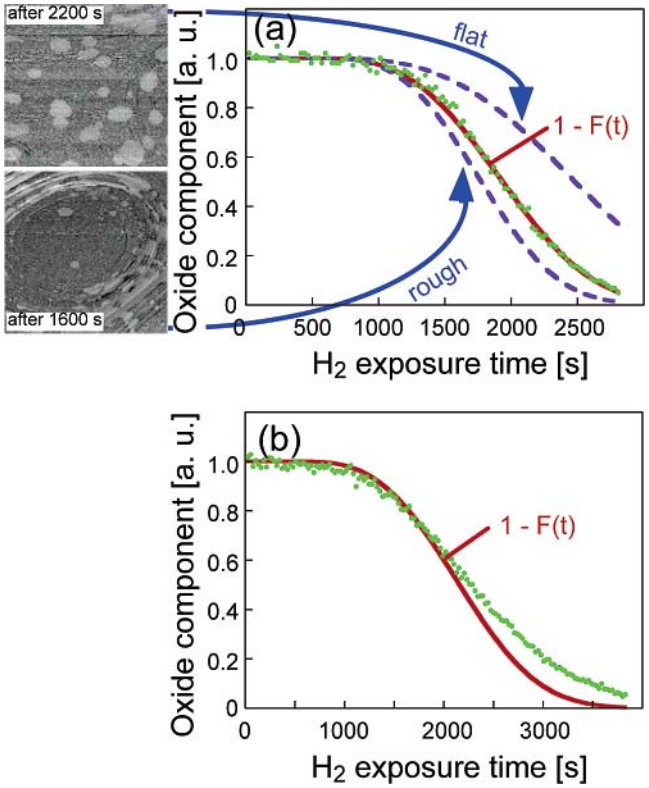

Figure 14. Decay of the oxidized area observed by HRCLS (green dots) and fit function (red) based on JMAK theory with a delay time t_0. In part a, curves calculated from STM-deduced parameters (Table 1) are shown for flat and rough areas. Part b shows that, without sputter-induced defects, JMAK theory does not describe the data due to a nonrandom defect distribution.

TABLE 1: Parameters Used in the JMAK Equation Deduced from STM and HRCLS Measurements at a Hydrogen Pressure of 1×10^{-7} mbar

	HRCLS	STM	
		flat area	rough area
dr/dτ (nm s^{-1})	na	0.11	
$\Delta N/\Delta t$ (10^{-9} nm^{-2} s^{-1})	na	7.8	≈31.5
c (10^{-10} s^{-3})	2.5	1.0	≈4.0
t_0 (s)	530	575 ± 200	

Equation 3 was also applied as a fit function to the HRCLS curve (Figure 14a). The parameters from the curve fit can be compared with our STM data. These values are shown in Table 1, and we can see good agreement. HRCLS averages over stepped and flat surface areas. Therefore, the HRCLS-determined value of the constant c, which is proportional to the nucleation rate, must lie between the values for c determined by STM in flat and highly stepped areas. Furthermore, we used two different Rh(111) crystals in our STM and HRCLS experiments, which may have a different step density. So, we have to expect slightly different quantitative results for the two Rh(111) crystals.

For the surface without sputter-induced defects, a fit of the HRCLS oxide component with eq 3 is much worse (Figure 14b). The initial delay time has been fixed at $t_0 = 575$ s for the fit. A better, but unphysical, fit could be obtained with lower values of t_0. We attribute the poor fit to the fact that the reduction starts almost exclusively in areas with multiple steps. Without

sputter-induced defects, we are far from having a random defect distribution. We find flat areas with a very low defect density (see Figure 2b). Judging from STM measurements, areas without nuclei can be almost up to a square micrometer in size and will not get reduced, until already reduced areas that started to grow at far-away nuclei swallow them. This takes a long time, and the end of the reduction process will be considerably delayed compared to a random distribution of nuclei (compare Figure 10c and d).[14,16]

For H_2 pressures far below 1×10^{-7} mbar, we have a major contribution of the first growth regime and, so, we expect stronger deviations from JMAK theory.

5. Conclusions

The reduction of the surface oxide on Rh(111) by H_2 was studied by STM and HRCLS. Our results show that hydrogen cannot adsorb on the oxide. Therefore, reduction can only start at defects. These defects are located at steps, but we can also place defects artificially, either by crashing the tip deliberately into the surface or by slightly sputtering the surface after oxide formation. During the reduction, hydrogen attacks the oxide at its border. As a consequence, we found two growth regimes depending on the size of the reduced area and on hydrogen pressure. During the early phase of reduction, the reaction is limited by hydrogen adsorption on the already reduced area. This leads to an exponential growth of the reduced area with time. Later on, the processes at the border of the reduced area limit the reduction speed (second growth regime) resulting in a constant speed of the reaction front. We conclude from the kinetics that the hydrogen adatom coverage on the reduced areas is low in the first growth regime and near saturation coverage in the second growth regime (late phase of reduction). There is no evidence for adsorbates other than hydrogen on the reduced areas, but we have evidence for diffusion of a hydrogen-containing species from the reduced areas into (or onto) the oxide.

By using JMAK theory, we can describe coalescence of reduced patches, thereby, connect microscopic and macroscopic measurements, and achieve a good understanding of the processes that lead to the reduction kinetics observed by spatially averaging techniques. JMAK theory requires that the radius of the reduced areas grows linearly with time. This is fulfilled in the second growth regime only, where the processes at the border of the oxide are rate-limiting. Therefore, JMAK theory requires an extension for taking also the adsorption-limited growth regime into account. The parameters obtained from microscopic STM measurements are in good agreement with parameters obtained from fitting JMAK theory to our macroscopic HRCLS measurements.

Acknowledgment. This work was financially supported by the Austrian Fonds zur Förderung der wissenschaftlichen Forschung (FWF) under project number S9003, the Swedish Research Council, and the European Union under Contract No. NMP3-CT-2003-505670 (NANO2). Technical assistance by the MAX-lab staff is gratefully acknowledged.

References and Notes

(1) Over, H.; Kim, Y. D.; Seitsonen, A. P.; Wendt, S.; Lundgren, E.; Schmid, M.; Varga, P.; Morgante, A.; Ertl, G. *Science* **2000**, *287*, 1474.
(2) Hendriksen, B. L. M.; Frenken, J. W. M. *Phys. Rev. Lett.* **2002**, *89*, 046101.
(3) Kresse, G.; Schmid, M.; Napetschnig, E.; Shishkin, M.; Köhler, L.; Varga, P. *Science* **2005**, *308*, 1440.
(4) Lundgren, E.; Kresse, G.; Klein, C.; Borg, M.; Andersen, J. N.; De Santis, M.; Gauthier, Y.; Konvicka, C.; Schmid, M.; Varga, P. *Phys. Rev. Lett.* **2002**, *88*, 246103.
(5) Gustafson, J.; Mikkelsen, A.; Borg, M.; Andersen, J. N.; Lundgren, E.; Klein, C.; Hofer, W.; Schmid, M.; Varga, P.; Köhler, L.; Kresse, G.; Kasper, N.; Stierle, A.; Dosch, H. *Phys. Rev. B* **2005**, *71*, 115442.
(6) Reuter, K.; Scheffler, M. *Appl. Phys. A* **2004**, *78*, 793.
(7) Gustafson, J.; Mikkelsen, A.; Borg, M.; Lundgren, E.; Köhler, L.; Kresse, G.; Schmid, M.; Varga, P.; Yuhara, J.; Torrelles, X.; Quirós, C.; Andersen, J. N. *Phys. Rev. Lett.* **2004**, *92*, 126102.
(8) Lundgren, E.; Gustafson, J.; Resta, A.; Weissenrieder, J.; Mikkelsen, A.; Andersen, J. N.; Köhler, L.; Kresse, G.; Klikovits, J.; Biedermann, A.; Schmid, M.; Varga, P. *J. Electron Spectrosc. Relat. Phenom.* **2005**, *144*−*147*, 367.
(9) Avrami, M. *J. Chem. Phys.* **1939**, *7*, 1103. Avrami, M. *J. Chem. Phys.* **1940**, *8*, 212.
(10) Johnson, W. A.; Mehl, R. F. *Trans. Am. Inst. Min. Eng.* **1939**, *135*, 416.
(11) Kolmogoroff, A. N. *Bull. Acad. Sci. USSR (Cl. Sci. Mater. Nat.)* **1937**, *3*, 355.
(12) Tomellini, M.; Fanfoni, M. *Phys. Rev. B* **1996**, *54*, 9828.
(13) Weinberg, M. C. *J. Non-Cryst. Solids* **1991**, *134*, 116.
(14) Weinberg, M. C.; Birnie, D. P., III; Shneidman, V. A. *J. Non-Cryst. Solids* **1997**, *219*, 89.
(15) Birnie, D. P., III; Weinberg, M. C. *J. Chem. Phys.* **1995**, *103*, 3742.
(16) Sessa, V.; Fanfoni, M.; Tomellini, M. *Phys. Rev. B* **1996**, *54*, 836.
(17) Tomellini, M. Fanfoni, M. *Surf. Sci.* **1996**, *349*, L191.
(18) Gross, A. *Surf. Sci. Rep.* **1998**, *32*, 291.
(19) Dudin, P.; Barinov, A.; Gregoratti, L.; Kiskinova, M.; Esch, F.; Dri, C.; Africh, C.; Comelli, G. *J. Phys. Chem. B* **2005**, *109*, 13649.
(20) Williams, C. T.; Chen, E. K.-Y.; Takoudis, C. G.; Weaver, M. J. *J. Phys. Chem. B* **1998**, *102*, 4785.
(21) Beutl, M.; Lesnik, J.; Rendulic, K. D. *Surf. Sci.* **1999**, *429*, 71.
(22) Yates, J. T.; Thiel, P. A.; Weinberg, W. H. *Surf. Sci.* **1979**, *84*, 427.
(23) Gibson, K. D.; Viste, M.; Sibener, S. J. *J. Chem. Phys.* **2000**, *112*, 9582.

Paper VII

The surface oxide as a source of oxygen on Rh(111).

E. Lundgren, J. Gustafson, A. Resta, J. Weissenrieder,
A. Mikkelsen, J. N. Andersen, L. Köhler, G. Kresse,
J. Klikovits, A. Biederman, M. Schmid, and P. Varga.

J. Electron Spectrosc. Relat. Phen. **144-147** 367 (2005)

VII

Available online at www.sciencedirect.com
SCIENCE DIRECT®
Journal of Electron Spectroscopy and Related Phenomena 144–147 (2005) 367–372
JOURNAL OF ELECTRON SPECTROSCOPY and Related Phenomena
www.elsevier.com/locate/elspec

The surface oxide as a source of oxygen on Rh(1 1 1)

E. Lundgren[a,*], J. Gustafson[a], A. Resta[a], J. Weissenrieder[a], A. Mikkelsen[a], J.N. Andersen[a], L. Köhler[b], G. Kresse[b], J. Klikovits[c], A. Biederman[c], M. Schmid[c], P. Varga[c]

[a] *Department of Synchrotron Radiation Research, Institute of Physics, Lund University, Box 118, S-221 00 Lund, Sweden*
[b] *Institut für Materialphysik and Centre for Computational Materials Science, Universität Wien, A-1090 Wien, Austria*
[c] *Institut für Allgemeine Physik, Technische Universität Wien, A-1040 Wien, Austria*

Available online 26 February 2005

Abstract

The reduction of a thin surface oxide on the Rh(1 1 1) surface by CO is studied in situ by photoemission spectroscopy, scanning tunneling microscopy, and density functional theory. CO molecules are found not to adsorb on the surface oxide at a sample temperature of 100 K, in contrast to on the clean and chemisorbed oxygen covered surface. Despite this behavior, the surface oxide may still be reduced by CO, albeit in a significantly different fashion as compared to the reduction of a phase containing only chemisorbed on surface oxygen. The experimental observations combined with theoretical considerations concerning the stability of the surface oxide, result in a model of the reduction process at these pressures suggesting that the surface oxide behaves as a source of oxygen for the CO-oxidation reaction.

Keywords: PES; DFT; STM; Rh; O; CO

1. Introduction

Because of the importance for commercial applications, the catalytic activity of the late transition metals has been studied for many years. By using model systems, such as single crystal surfaces under ultra high vacuum (UHV) conditions, and carefully controlling the reactant gas abundance on the surface, significant progress has been made in the understanding of adsorbate–adsorbate and adsorbate–metal interactions. A common model system to study has been the CO reactivity with O chemisorbed on close-packed late transition metal surfaces. In recent years however, it has been discussed in the literature that on Ru, Pt and Pd surfaces [1–3], it is not the chemisorbed atomic oxygen adsorbed on the surface, but rather the oxides formed on the surfaces under such conditions, that are the most efficient phase in oxidizing CO. In the case of Ru, it has been shown that whereas metallic Ru is not active in CO oxidation, RuO_2, which forms under high partial O pressure on the Ru(0 0 0 1) surface, is the most active catalyst known for this reaction. The reason for the high activity could be shown to be due to the details of the surface structure of the RuO_2(1 1 0) surface, indicating that the formed oxide also provide one of the reactant species, namely oxygen (Mars-van-Krevelen mechanism). The RuO_2(1 1 0) surface provides catalytically active sites, so-called coordinatively unsaturated sites (CUS), onto which impinging molecules readily adsorb and later react [4]. Thus, on Ru the mechanism for the increased CO-oxidation activity due to the geometrical details of the formed RuO_2 is in general understood, in contrast to the situation for Pd, Pt and Rh which are not as thoroughly investigated on the atomic scale at or after exposure to higher O partial pressures. One reason for the difference in knowledge is the higher partial oxygen pressures needed to form the bulk oxides on the latter materials. Another reason is that on Pd and Rh, the formation of thicker oxides has turned out to be more complicated than initially believed. On several of these surfaces, at intermediate O partial pressures, so-called tri-layer surface-oxides form [5–8] prior to the onset of the growth of thicker oxides. Some of these thin, intermediate oxides display properties which are not found in the corresponding bulk oxides [6],

* Corresponding author. Tel.: +46 46 2224154; fax: +46 46 2224221.
E-mail address: edvin.lundgren@sljus.lu.se (E. Lundgren).

0368-2048/$ – see front matter © 2005 Elsevier B.V. All rights reserved.
doi:10.1016/j.elspec.2005.01.004

and in the case of Rh(1 1 1) as well as on Pd(0 0 1) [8,9], the presence of a surface oxide kinetically hinders the formation of the respective bulk oxides.

The role of the surface oxides in the catalytic activity of these metals is at present not clear. This statement is in particular valid at pressures and temperatures approaching those found in a more realistic environment of a catalyst. It is however clear that the surface structure on the atomic scale of the surface oxides does not exhibit any obvious CUS sites (see, e.g., inset in Fig. 1), suggesting a different interaction with an impinging or adsorbed reducing molecule than in the RuO_2(1 1 0) case. Therefore, it is of interest to study the interaction of a tri-layer surface oxide and a reducing molecule, and eventually try to elucidate the importance of this interaction in a more realistic environment.

In the present contribution we have investigated the reduction by CO of the (9 × 9) tri-layer surface-oxide formed on Rh(1 1 1) at elevated O partial pressures and sample temperatures. We show that CO does not adsorb on the (9 × 9) surface oxide. The reduction of the (9 × 9) phase is initially slower than the CO reduction of the p(2 × 1) chemisorbed phase, however the reduction speed is observed to increase as more of the metal surface is exposed. We propose a model explaining the observed behavior using experimental evidence as well as theoretical considerations based on density functional theory. The observed CO-oxidation behavior of the surface oxide is in good agreement with previous experiments [10], in which the onset of oxidation of Rh reduces rather than stops the reactivity.

2. Experiment and theory

The PES measurements were performed at beam line I311 at MAX II in Lund, Sweden [11]. All spectra were recorded using a normal emission angle using photon energies of 625 eV (O 1s) and 400 eV (C 1s). Scanning tunneling microscopy (STM) measurements were done in Vienna at room temperature using the same instrument as in Refs. [6,8]. The cleaning procedure of the Rh(1 1 1) surface has been described elsewhere [8]. The p(2 × 1) ($\theta = 1/2$ ML (MonoLayers, 1 ML equals the number of atoms in one Rh(1 1 1) layer) oxygen induced structure could be formed by exposing the Rh(1 1 1) surface to 100 L of oxygen at a temperature of 300 K, while the (9 × 9) structure could be formed by exposing the Rh(1 1 1) surface to 60,000 L (1 L = 10^{-6} mbar for 1 s) of oxygen at a sample temperature of 800 K [8].

The density functional calculations were performed using the Vienna ab initio simulation package (VASP) [12]. The interaction between the core and the valence electrons was treated by the projector augmented wave method [13], and the valence wave functions were expanded in a plane wave basis set with a plane wave cutoff of 250 eV. The generalized gradient approximation (GGA) was applied throughout this work [14]. With this setup, the lattice constant of Rh was determined to be $a_0 = 3.84$ Åin excellent agreement with previous DFT-GGA calculations ($a_0 = 3.83$ Å, e.g. Ref. [15]). The Rh substrate was modelled by six layer thick slabs, and the Brillouin zone integration was performed with grids corresponding to 24 × 24 k-points in the primitive surface cell.

3. Results and discussion

The CO adsorption at 100 K on the clean Rh(1 1 1) surface and on the (9 × 9) structure is shown in Fig. 1. While on the clean surface a strong C 1s peak is observed indicating the existence of suitable adsorption sites, no such peak is discernible after an even higher CO exposure onto the (9 × 9) surface. The measurements in Fig. 1 indicate that there is only an extremely small number of sites on the (9 × 9) phase onto which the CO can adsorb with an adsorption energy comparable to the clean surface. In catalytic reactions based on the usual Langmuir–Hinshelwood mechanism the activity is closely related to the adsorption ability of the gas phase reactants onto the surface. In this picture, Fig. 1 suggests a low CO oxidation reactivity of the surface oxide. However, a high activity also requires low barriers resulting in that intermediate adsorption energies are desirable [16]. Thus, in order to study the reactivity of a particular structure, the interaction between the adsorbed CO and O should be studied. Co-adsorbing CO at room temperature with chemisorbed O such as the p(2 × 1) structure, results in a mixed layer in which the CO preferably takes the on-top sites and the O the fcc-hollow sites [17]. Thus, also in the presence of chemisorbed oxygen, the adsorption ability of CO is significantly higher than that on the (9 × 9) structure, indicating a lower reactivity for the (9 × 9) structure.

More information about the in situ CO interaction with a chemisorbed oxygen phase such as the p(2 × 1) and a surface oxide such as the (9 × 9) structure can be obtained by

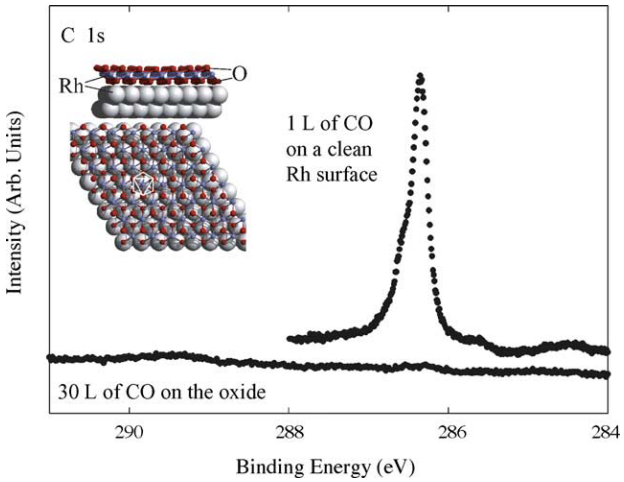

Fig. 1. Comparison of CO adsorption (1 L at 100 K) on the clean Rh(1 1 1) surface and on the (9 × 9) surface oxide (30 L at 100 K). No CO is observed to adsorb on the (9 × 9) phase at this temperature. The inset displays a side view of the (9 × 9) structure.

the measurements shown in Fig. 2. Fig. 2a shows the reduction of the p(2 × 1) structure in a CO partial pressure of 2×10^{-8} mbar and a sample temperature of 375 K. The left panel of Fig. 2a shows a two-dimensional plot of the O 1s region compiled from spectra recorded during the CO exposure with one spectrum per 24 s. The O 1s component at a binding energy of around 530 eV corresponds to the chemisorbed O atoms in fcc hollow sites, while the component at 532.4 eV reflects the O in the CO adsorbing in on-top sites. In the right panel of Fig. 2a, some selected O 1s spectra during the reduction are shown. The area underneath the chemisorbed O component directly reflects the reduction rate. The corresponding measurements from the reduction of the (9 × 9) structure using the same sample environments as in the p(2 × 1) is shown in Fig. 2b. The O 1s fingerprint from the (9 × 9) structure is somewhat more complicated due to the two components at 529 eV (surface component) and 530 eV (interface component) from the two different oxygen layers in the tri-layer structure of the (9 × 9) structure, yielding a ratio between the area underneath each component of 1:1. Nevertheless, the reduction can be monitored, and although CO does not adsorb to a high degree on this surface as was shown above, eventually, the structure can be reduced.

By performing a fit of the recorded PES spectra shown in the left panel of Fig. 2 using the components as shown in the right panel, we can extract details on the reduction process of the two different oxygen prepared samples. The result from this procedure is shown in Fig. 3. Starting with the reduction of the p(2 × 1) structure in Fig. 3a, it can be seen that the amount of chemisorbed O decreases immediately when the sample gets exposed to the CO gas, indicating that the O on the surface in the (2 × 1) structure reacts with the impinging CO forming CO_2. It can be seen that the rate of the decrease of the chemisorbed O 1s signal is reduced in a decreasing fashion with time, i.e. the CO-oxidation reaction rate decreases linearly. The reason for this is presumably simply due to the reduced number of O atoms on the surface, yielding a progressively lower probability for the CO-oxidation reaction. The behavior observed is in good agreement with that expected from a Langmuir–Hinshelwood mechanism, in which the reactants adsorb on the surface either molecularly or dissociatively, diffuse on the surface and react occasionally on the surface. It should also be noted that each coincidence not necessarily leads to a reaction. The complete disappearance of the chemisorbed O component is observed to occur only very slowly, reflecting the larger diffusion distances involved as the number of O atoms are reduced, or a change in the activation barrier of the CO_2 formation barrier as the CO and O concentrations are changing on the surface. However, finally, almost all the chemisorbed O atoms has been removed by the CO.

Turning to the reduction of the (9 × 9) structure, a very different development of the O 1s components due to the surface oxide can be seen in Fig. 3b. Initially the decrease of the O 1s signal is very slow, indicating that the reduction rate or the CO-reaction rate is low, confirming the CO adsorption behavior observed in Fig. 1. The slow decrease in the surface

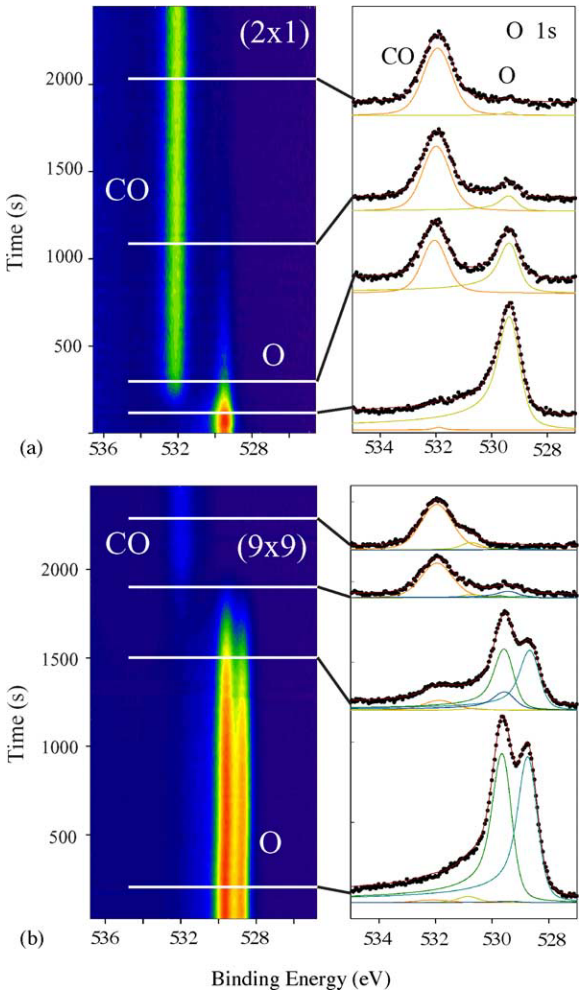

Fig. 2. CO induced reduction using a CO partial pressure of 2×10^{-8} mbar and a sample temperature of 375 K of (a) the p(2 × 1) structure and (b) the (9 × 9) structure. Left panels show the evolution of the O 1s binding energy region as a function of time, while right panels show some selected spectra during the reduction process.

oxide O 1s signal also indicates that neither the Eley–Ridal mechanism (in which gas phase molecules should react directly with molecules adsorbed on the surface, in this case the oxygen atoms in the (9 × 9) structure) or the Mars-van-Krevelen mechanism is of a significant importance on the surface of the (9 × 9) structure at these pressures and sample temperatures. We would have expected a more immediate response in the decrease of the O 1s signal in both cases.

We believe that the reason for observing a slow decrease of the signal at all—despite that we know that CO does not adsorb on the surface—are defects. A small number of defects on the (9 × 9) structure exposing oxygen undercoordinated Rh atoms will be attractive adsorption sites for CO molecules. From these sites, the CO may react with the O atoms in the nearby oxide, resulting in CO_2 and a larger area of the unreconstructed surface. From our measurements, this process seems to be initially rather slow. The process however eventually leads to an increase of the unreconstructed

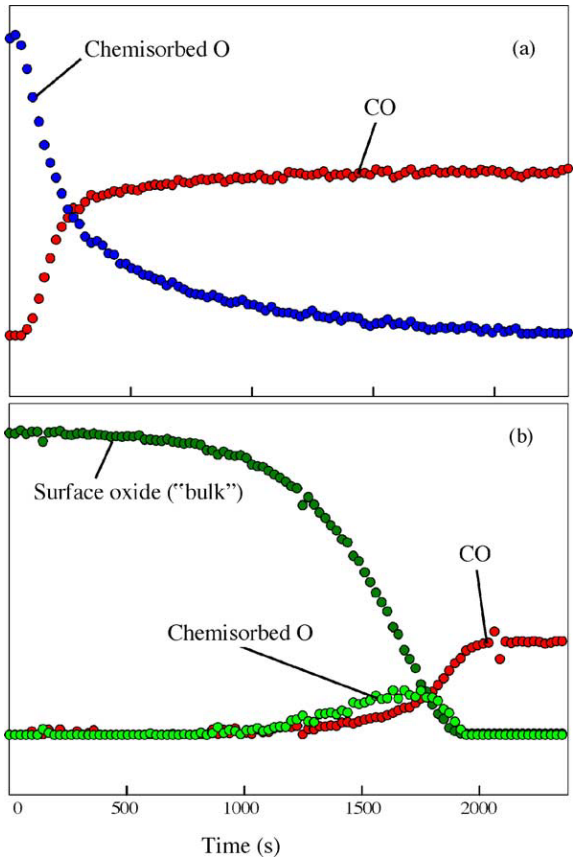

Fig. 3. The extracted area underneath the O 1s components as a function of time during the reduction after a fitting procedure from (a) the p(2 × 1) structure with components due to the chemisorbed O and the CO. (b) The (9 × 9) structure with components due to the (9 × 9) bulk oxygen component, chemisorbed oxygen, and CO. In the fit of the (9 × 9), the ratio of the surface and the bulk oxygen area was locked as 1:1 as obtained by spectra prior to CO exposure.

surface area (i.e., no surface oxide, but with adsorbed CO and, possibly, O).

The notion that the reduction process of the (9 × 9) structure by CO starts at defects on the surface is supported by the STM images shown in Fig. 4. From these images, reduced areas can be seen which preferably starts at steps. We find that reduction can start at both types of steps, those present on the Rh(1 1 1) before oxidation [long steps in Fig. 4(b)] and those bounding islands formed by excess Rh during surface oxide formation [e.g., black arrow in Fig. 4(b)]. In the reduced areas, small holes can be seen due to the difference in Rh density between the (9 × 9) and a (1 1 1) Rh plane. We also observe that the reduced areas exhibit a (2 × 2) surface structure, see inset in Fig. 4(a). We find that the corrugation between the bright protrusions using a high tunneling resistance (−0.5 to −1 V, 0.5 nA) in the (2 × 2) is approximately 0.5 Å. While CO molecules usually appear as protrusions under such tunneling conditions, we have never observed oxygen adatoms appearing as protrusions at these rather high tunneling voltages. We therefore attribute the protrusions to CO molecules. We note, however, that CO molecules on Rh are usually very mobile at room temperature, in contrast to the well-defined protrusions observed. This indicates that the CO is stabilized on the surface by the repulsive interaction with O, causing high diffusion barriers for the CO. The (2 × 2) could therefore be either a (2 × 2)-1CO–1O or (2 × 2)-1CO–2O. Considering the structures given in Ref. [17], CO would probably be less mobile in the (2 × 2)-1CO–2O, so we consider this structure most likely for the areas where CO is perfectly stationary (sharp in the STM images). On the terraces which are fully reduced, the CO seems to be more mobile—this could mean a structure with less O, though not necessarily an ordered one. Less O on these terraces would be consistent with the fact that the supply of oxygen from the (9 × 9) on these terraces has ceased (see below). A (2 × 2)-1CO–2O structure would be also consistent with the PES observations

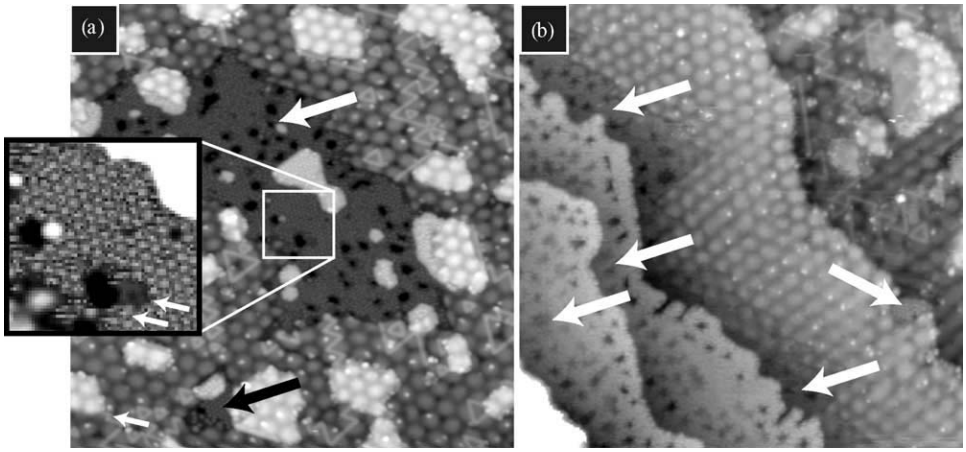

Fig. 4. Room-temperature STM images (50 nm × 50 nm) of a Rh(1 1 1) surface completely covered by the O–Rh–O (9 × 9) surface oxide after reduction for 1300 s at 375 K in 2 × 10⁻8 mbar CO. Frame (a) shows two reduced areas (arrows) within a large terrace still fully covered by the surface oxide (appearing as a hexagonal network-like pattern). At the same time, the surface oxide is completely absent on many of the terraces in the more stepped parts of the sample (white arrows), as shown in frame (b).

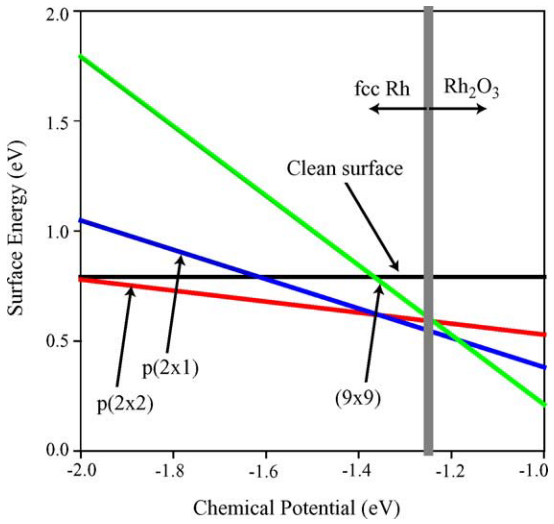

Fig. 5. Theoretical zero temperature phase diagram showing the stability of the (9 × 9), the p(2 × 1), p(2 × 2), as well as, of the clean surface.

where approx. twice as much adsorbed O as CO is found [Fig. 3(b)].

To understand the increased catalytic reactivity of the surface oxide the theoretical phase diagram, shown in Fig. 5, is helpful. Below a chemical potential of −1.2 eV, oxygen is simply chemisorbed on the otherwise unreconstructed surface either in a low coverage p(2 × 2)-1O phase or in the higher coverage p(2 × 1)-1O phase; at more oxidizing conditions ($\mu_O > -1.2$ eV) the surface oxide is stable. For finite temperatures, instead of sharp boundaries between the three domains smoother transitions with intermediate disordered phases may occur, but the picture remains essentially the same. When the surface oxide is now reduced by carbon monoxide, patches of the surface oxide and the unreconstructed surface—covered partly by atomic oxygen—must be simultaneously present at the surface. This is oxygen and CO—must be simultaneously present at the surface. Ignoring the more weakly bound CO, this is only possible if the chemical potential of oxygen is exactly −1.2 eV, i.e. at the crossing point of the energy lines of the p(2 × 1)-1O phase and the surface oxide. This behavior is similar to a temperature driven melting transition in a solid, where the liquid and the solid coexist only at *one* specific temperature (at a given pressure). In the present case the chemical potential plays the role of the temperature and remains constant, as long as both phases coexist on the surface. Microscopically we can understand the behavior as follows (see Fig. 6): carbon monoxide and oxygen coexist at patches which are not covered by the surface oxide. Eventually they react, decreasing the oxygen and CO content locally. But at the boundaries of these patches the surface oxides immediately decomposes in order to increase the oxygen content in the depleted areas. Therefore, the surface oxide indeed acts as *an efficient source for atomic oxygen* keeping the chemical potential of oxygen essentially constant, until it has entirely "evaporated". On the unreconstructed surface, however, the chemical potential

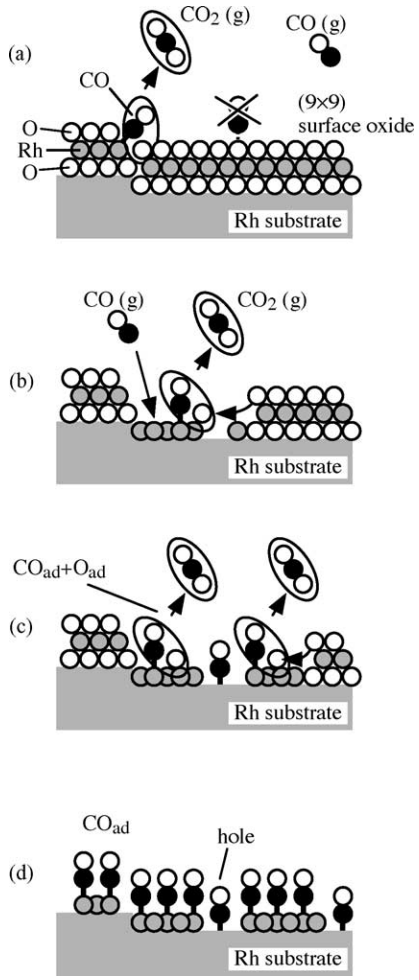

Fig. 6. Schematic illustration of the reduction process of the (9 × 9) structure. (a) The initial adsorption of CO at defects and reaction with nearby O in the surface oxide. (b) The CO may easily adsorb and react on the exposed Rh in partly reduced areas. (c) Co-adsorbed O as well as O in the surface oxide participate in the reaction at a later stage in the reduction process. (d) In the final stage only CO is left on the surface.

of oxygen is progressively reduced, as oxygen reacts with carbon monoxide. Since the driving force for oxidation is directly proportional to the chemical potential of oxygen on the surface, the reaction is faster on the oxide precovered surface (at least once sufficient surface area is available to adsorb carbon monoxide).

After around 1500 s, the reduction rate seen in Fig. 3(b) becomes roughly constant. Simultaneously the amount of chemisorbed oxygen on the Rh(1 1 1) surface continues to increase, but finally starts to disappear *without a noticeable decrease of the reaction rate*. At this stage, the major difference between the two initial surface preparations is most likely the number of defects on the surface. Since the Rh density in the (9 × 9) layer is 19% smaller than in a Rh(1 1 1) plane, reduction of the oxide results in a metal surface with a high density of defects, such as steps, kinks and corners. These sites could be responsible for the observed differences at the final reduction stage, since they

are known to be favorable sites for adsorption and reactions [18–20].

4. Summary

In summary we have shown that CO does not easily adsorb on the (9×9) surface oxide at 100 K, and argued that the reason for this is the low availability of suitable adsorption sites. The CO reduction process at a CO pressure of 2×10^{-8} mbar and sample temperature of 375 K of the (2×1) and the (9×9) oxygen induced structures on the Rh(1 1 1) surface was studied by in situ time-resolved PES. The measurements demonstrate significant differences in the reduction rate; for the (2×1) a traditional Langmuir–Hinshelwood mechanism was observed while for the (9×9) a more complicated reduction process was observed, involving both defects and the stability of the (9×9) structure with respect to the clean surface, as calculated by DFT.

Acknowledgements

This work was financially supported by the Swedish Research Council, the Austrian *Fonds zur Förderung der wissenschaftlichen Forschung* and the European Union under contract no. NMP3-CT-2003-505670 (NANO2). Support by the MAX-lab staff is gratefully acknowledged. The authors thank Herbert Over for stimulating discussions.

References

[1] H. Over, Y.D. Kim, A.P. Seitsonen, S. Wendt, E. Lundgren, M. Schmid, P. Varga, A. Morgante, G. Ertl, Science 287 (2000) 1474.
[2] B.L.M. Hendriksen, J.W.M. Frenken, Phys. Rev. Lett. 89 (2002) 046101.
[3] B.L.M. Hendriksen, J.W.M. Frenken, Surf. Sci. 552 (2004) 229.
[4] H. Over, A.P. Seitsonen, E. Lundgren, M. Schmid, P. Varga, J. Am. Chem. Soc. 123 (2001) 11807.
[5] C.I. Carlisle, D.A. King, M.-L. Bocquet, J. Cerdá, P. Sautet, Phys. Rev. Lett. 84 (2000) 3899.
[6] E. Lundgren, G. Kresse, C. Klein, M. Borg, J.N. Andersen, M. De Santis, Y. Gauthier, C. Konvicka, M. Schmid, P. Varga, Phys. Rev. Lett. 88 (2002) 246103.
[7] M. Todorova, E. Lundgren, V. Blum, A. Mikkelsen, S. Gray, J. Gustafson, M. Borg, J. Rogal, K. Reuter, J.N. Andersen, M. Scheffler, Surf. Sci. 541 (2003) 101.
[8] J. Gustafson, A. Mikkelsen, M. Borg, E. Lundgren, L. Köhler, G. Kresse, M. Schmid, P. Varga, X. Torrelles, C. Quiros, J.N. Andersen, Phys. Rev. Lett. 92 (2004) 126102.
[9] E. Lundgren, J. Gustafson, A. Mikkelsen, J.N. Andersen, A. Stierle, H. Dosch, M. Todorova, J. Rogal, K. Reuter, M. Scheffler, Phys. Rev. Lett. 92 (2004) 046101.
[10] C.H.F. Peden, D.W. Goodman, D.S. Blair, P.J. Berlowitz, G.B. Fischer, S.H. Oh, J. Phys. Chem. 92 (1988) 1563.
[11] R. Nyholm, J.N. Andersen, U. Johansson, B.N. Jensen, I. Lindau, Nucl. Instrum. Meth. A 467 (2001) 520.
[12] G. Kresse, J. Furthmüller, Comput. Mater. Sci. 6 (1996) 15.
[13] G. Kresse, D. Joubert, Phys. Rev. B 59 (1998) 1758.
[14] J.P. Perdew, J.A. Chevary, C.H. Vosko, K.A. Jackson, M.R. Pederson, D.J. Singh, C. Fiolhais, Phys. Rev. B 46 (1992) 6671.
[15] M.V. Ganduglia-Pirovano, M. Scheffler, Phys. Rev. B 59 (1999) 15533.
[16] B. Hammer, J. Norskov, Surf. Sci. 343 (1995) 211.
[17] A.J. Jaworowski, A. Beutler, F. Strisland, R. Nyholm, B. Setlik, D. Heskett, J.N. Andersen, Surf. Sci. 431 (1999) 33.
[18] T. Zambelli, J. Wintterlin, J. Trost, G. Ertl, Science 273 (1996) 1688.
[19] B. Hammer, Phys. Rev. Lett. 83 (1999) 3681.
[20] J. Gustafson, M. Borg, A. Mikkelsen, S. Gorovikov, E. Lundgren, J.N. Andersen, Phys. Rev. Lett. 91 (2003) 056102.

...mindful that are not enough in quantity and quality.

Acknowledgements

These four years flew away in whirlwind of facts, experiences and persons that at this point of the story deserve at least to be mentioned....
Starting from Mamma and Papá, permanent imprint of my origins and always present even if far away... Thank You! To my sister and her husband that keept me up to date on what was going on down there...

Thanks to my two advisors Jesper and Edvin, sources of inspirations that wisely drove me through the magic world of synchrotron radiation up to the end of this thesis!
Thanks to Anders and Stacey, always available for good scientific tips!
Thanks to Johan and Rasmus, good fellows during the MAX lab nights...
to Lassana, Suomi and Elizabeta for the stimulating discussions, scientific and not...
to Evren and Cristina, fresh air for the department...
to Emilie, Jessica, Joakim, Kees Jan, Achim for the chat when one does not feel as work...
to the department that keeps all this possible every day...

to all the MAXlab staff of course! that had builded an environment where promptness is daily experience!

To Ida, sun from the north...
to Anders, clever and teaser informer...
to Alex, Bigos and chalk pusher...
to Emma, strong with smile and marvelous dancer...
to Ana, who adopted me...at least for a while!!
to Tompa, for the enriching talks and...yes I'm almost removing my freewheel!
to Hanna, sweet heart and fantastisk svenska lärare!
to Flavius, inspiring climber and bright mind...
to the brave Marie...
to Zinaida, sharp!
to Joseph, also because we start this adventure together!
to Johanna, always challenging...
to Aldana and Henrik for the nice dinners and the cozy chats...
to Sofia for the talks in front of wine glasses...
to everyone that makes me smiling here in Skåne...

few lines to the Italians that despite my terrible written language kept replying to mails!

Grazie a Rude che sa stupire...
a Lucio, tuttologo in assistenza da remoto...
a Sara che sa discutere anche per e-mail...
a Peo che mi pungola il lato idiota...
a Sergio, uomo in carriera con la birra in mano...
a Pane, alti e bassi ma sempre al confronto...
a Davide, Neo-papá con pruriti alpinistici...
a ‘‘The emigrant abstinence group’’ preziosa quotidiana presenza di menti allo sbaraglio!!
a ...tutti coloro che ad ogni rientro mi accolgono con il sorriso!
a ...

Thanks!